FEDERAL UNIVERSITY OF PARANÁ
POST-GRADUATE PROGRAM IN MECHANICAL ENGINEERING

FELIPE REZENDE DE LOYOLA

A NUMERICAL-EXPERIMENTAL STUDY OF TAYLOR-COUETTE FLOWS OF FABRIC-WATER SUSPENSIONS

CURITIBA
2017

FELIPE REZENDE DE LOYOLA

UM ESTUDO NUMÉRICO-EXPERIMENTAL DE ESCOAMENTOS DE TAYLOR-COUETTE DE SUSPENSÕES DE TECIDO E ÁGUA

A NUMERICAL-EXPERIMENTAL STUDY OF TAYLOR-COUETTE FLOWS OF FABRIC-WATER SUSPENSIONS

Tese de doutorado submetida ao Programa de Pós-graduação em Engenharia Mecânica da Universidade Federal do Paraná como requisito parcial para a obtenção do grau de Doutor em Engenharia Mecânica, na área de concentração de Fenômenos de Transporte e Engenharia Térmica

Doctoral thesis submitted to the Post-Graduate Program in Mechanical Engineering of the Federal University of Paraná in partial fulfillment of the requirements for the degree of Doctor of Science in Mechanical Engineering, in the realm of Transport Phenomena and Thermal Engineering

Advisor: Professor Christian Johann Losso Hermes, Dr.Eng.
Co-advisor: Professor Waldyr de Lima e Silva Junior, Ph.D.

CURITIBA

2017

L923n Loyola, Felipe Rezende de
A numerical-experimental study of Taylor-Couette flows of fabric-water suspensions / Felipe Rezende de Loyola. – Curitiba, 2017.
249 f. : il. color. ; 30 cm.

Tese - Universidade Federal do Paraná, Setor de Tecnologia, Programa de Pós-Graduação em Engenharia Mecânica, 2017.

Orientador: Christian Johann Losso Hermes – Co-orientador: Waldyr de Lima e Silva Junior,.
Bibliografia: p. 225-234.

1. Reômetros. 2. Reologia. 3. Fluidodinâmica computacional. 4. Máquinas de lavar roupas. 5. Escoamento. I. Universidade Federal do Paraná. II.Hermes, Christian Johann Losso. III. Silva Junior, Waldyr de Lima e . IV. Título.

CDD: 531.1134

MINISTÉRIO DA EDUCAÇÃO
UNIVERSIDADE FEDERAL DO PARANÁ
PRÓ-REITORIA DE PESQUISA E PÓS-GRADUAÇÃO
Setor TECNOLOGIA
Programa de Pós Graduação em ENGENHARIA MECÂNICA
Código CAPES: 40001016040P5

TERMO DE APROVAÇÃO

Os membros da Banca Examinadora designada pelo Colegiado do Programa de Pós-Graduação em ENGENHARIA MECÂNICA da Universidade Federal do Paraná foram convocados para realizar a arguição da Tese de Doutorado de **FELIPE REZENDE DE LOYOLA**, intitulada: "**A NUMERICAL-EXPERIMENTAL STUDY OF TAYLOR-COUTTE FLOWS OF FABRIC-WATER SOLUTIONS**", após terem inquirido o aluno e realizado a avaliação do trabalho, são de parecer pela sua Aprovação.

Curitiba, 09 de Junho de 2017.

CHRISTIAN JOHANN LOSSO HERMES
Presidente da Banca Examinadora (UFPR)

LUCIANO KIYOSHI ARAKI
Avaliador Interno (UFPR)

MARCIO AUGUSTO VILLELA PINTO
Avaliador Externo (UFPR)

VIVIANA COCCO MARIANI
Avaliador Externo (PUC/PR)

FERNANDO TADEU BOÇON
Avaliador Externo (UFPR)

I dedicate this thesis to my parents, Luciano and Maria Estela, to my brothers, and my girlfriend Beatriz.

ACKNOWLEDGEMENTS

I first thank my advisor Prof. Christian Hermes for the continuous support of my education for the last four years, for his motivation, patience, and knowledge. His guidance helped me not only with this thesis but also in my life.

Besides my advisor, I would like to thank my co-advisor Prof. Waldyr for all the support, and also my thesis committee: Prof. Viviana Mariani, Prof. Fernando Bóçon, Prof. Luciano Araki and Prof. Marcio Pinto.

My sincere thanks also go to Prof. Shinji Tamano and Prof. Yohei Morinishi, for offering me a one-year study opportunity at Flow Design Laboratory in Nagoya Institute of Technology and for their kind support.

I thank also my fellow labmates at the Laboratory of Thermophysics and Thermodynamics (LT^2): Valter Sales, Ricardo Yee, Rafael Ribeiro, Silvia Negrelli, Vanessa Haluch, Felipe Zanotto, Dirceu Machado and Luiz Campos for their support and friendship. I would also like to thank my friends from all over the world that I had get along with during my one-year period in Japan.

I thank also my beloved girlfriend Beatriz Yasuda for her utmost understanding and encouragement in all these years.

I would like to thank all my friends: Bruno, Willian, Pedro Murakami, Braulio, Rodrigo, Luiz Henrique, Yuri, Maura, Pedro Tanaka, Tony, Ciro, André, Adolfo, Diogo, Augusto, among others for their support and all the fun we have had in the last four years.

I thank also my cousins, in particular, Eduardo Graminho for his support during my stay in Japan.

I thank the Post-Graduate Program in Mechanical Engineering (PGMec) for the commitment and support in the last four years.

I thank the Federal University of Paraná (UFPR) for the resources for this research. I thank CAPES and the Brazilian Government for the financial support.

Finally, I must express my very profound gratitude to my parents Luciano and Maria Estela, to my brothers Fernando, André and Rafael, and my grandparents Rubens and Vera for providing me with unfailing support and continuous encouragement throughout this process. Such an accomplishment would not have been possible without them.

Thanks for all your encouragement!

"*All men are the same except for their belief in their own selves, regardless of what others may think of them*"

(Miyamoto Musashi)

RESUMO

Escoamentos periódicos de fluidos newtonianos e não-newtonianos estão presentes em um grande número de aplicações, particularmente em lavadoras domésticas de eixo vertical. O processo de lavação depende do transporte de massa e quantidade de movimento do agitador para o fluido. Nesses casos, o escoamento segue o padrão de Taylor-Couette, cuja característica é um escoamento confinado entre dois cilindros rotativos. O presente trabalho está focado na simulação numérica de escoamentos periódicos e em regime permanente de fluidos newtonianos e não-newtonianos (fluidos de Herschel-Bulkley) com base nas equações tridimensionais de conservação de massa e de quantidade de movimento. Uma geometria simplificada é utilizada como domínio físico para as análises numéricas. Além disso, o perfil de rotação (deslocamento angular e velocidade) foi imposto externamente ao modelo como condições de contorno, já que o padrão de escoamento é dependente deste parâmetro, bem como das propriedades reológicas do fluido. As simulações foram baseadas no Método dos Volume Finitos, utilizando o algoritmo PRIME para o acoplamento de pressão-velocidade e a técnica BiCGSTAB, que usa o algoritmo de Thomas como pré-condicionador, para a solução numérica das equações. Além disso, testes experimentais foram realizados para a obtenção das propriedades reológicas das misturas de água e tecidos. Esses experimentos recaem no problema inverso de Couette, onde as curvas de taxa de deformação e tensão de cisalhamento são obtidas a partir dos resultados de torque e velocidade angular. Os resultados numéricos foram verificados contra os resultados experimentais e também contra resultados obtidos na literatura aberta apresentando uma concordância satisfatória para as velocidades e torques tanto para os fluidos newtonianos como para os não-newtonianos.

Palavras-Chave: Reometria. Misturas água-tecido. CFD. Lavanderia. Escoamentos periódicos.

ABSTRACT

Periodic flows of Newtonian and non-Newtonian fluids are present in a wide range of applications, particularly in household vertical axis washing machines. The washing process relies on the mass and momentum transport from the agitator to the fluid stream. In such cases, the flow follows a pattern that recalls the Taylor-Couette one, whose main feature is the confinement between two rotating cylinders. The present study concerns the numerical simulation of steady-state and periodic flows of Newtonian and non-Newtonian (Herschel-Bulkley) fluids based on the three-dimensional conservation equations of mass and momentum. A simplified Taylor-Couette geometry is used as the physical domain for the numerical analyses. In addition, the agitation profile (angular swept and speed) was imposed externally as boundary condition as the flow patterns rely on it, and also on the rheological properties of the fluid. Simulations were carried out by means of a homemade finite-volume-based code (which used the PRIME method for the sake of velocity-pressure coupling, and the BiCGSTAB solver together with the Thomas algorithm as a preconditioner, for solving the linear set of equations). Furthermore, experimental tests were carried out in a purpose-built facility in order to gather the rheological properties of the fabric-water suspensions. The experiments rely on the Couette inverse problem, in which the shear curves are obtained from the torque and velocity data. The simulation model was verified against experimental and numerical data obtained in-house or elsewhere indicating a satisfactory agreement between numerical and experimental torques and velocities.

Keywords: Rheometry. Fabric-water suspensions. CFD. Laundry. Periodic Flows.

LIST OF FIGURES

LIST OF TABLES

LIST OF ABBREVIATIONS

Abbreviation	Description
BCE	Before Common Era
BiCGSTAB	Biconjugate Gradient Stabilized method
CFD	Computation Fluid Dynamics
CMC	Caboxymethylcellulose
CTDMA	Cyclic Tridiagonal Matrix Algorithm
DAQ	Data Acquisition System
FDM	Finite Difference Method
FEM	Finite Element Method
FVM	Finite Volume Method
GNF	Generalized Newtonian Fluid
MRI	Magnetic Resonance Imaging
NNF	Non-Newtonian Fluid
PIV	Particle Image Velocimetry
PMMA	Polymethyl Methacrylate
PRIME	Pressure Implicit Momentum Explicit
RMS	Root Mean Square
S.S.	Semi-Synthetic
SSE	Sum of Square Errors
TDMA	Tridiagonal Matrix Algorithm – Thomas Algorithm

LIST OF SYMBOLS

Roman Symbols

Symbol	Description	Unit
A	Area	[m²]
B	Source term	[kg·m/s^2]
D	Diffusive mass flow rates through the faces	[kg/m^2·s]
det	Tensor determinant	
Ec	Eckert number	[-]
ERR	Error	[-]
F	Advective mass flow rates through the faces	[kg/m^2·s]
g	Gravity acceleration	[m/s²]
Gr	Grashof number	[-]
h	Fluid height column	[m]
H	Cylinder height	[m]
$\mathcal{J}$	Interpolation Function	[-]
J	Total flux	[kg/s^2·m]
k	Radius ratio	[-]
K	Yield stress fluids exponential growth of stress	[-]
m	Flow consistency index (Power-Law model)	[Pa·s^n]
n	Flow behavior index (Power Index)	[-]
n	Number of nodal points	
p	Pressure	[Pa]
Pe	Péclet number	[-]

q	Control volume index	[-]
Q	Number of control volumes along the coordinate direction	[-]
r	Radial position	[m]
r_0	Plug radius	[m]
R	Radius	[m]
Re	Reynolds number	[-]
t	Time	[s]
T	Torque	[N·m]
tr	Trace of tensor	
Ta	Taylor number	[-]
Tol	Tolerance	[-]
V	Volume	[m³]
v	Velocity	[m/s]
v_r	Radial velocity component	[m/s]
v_θ	Tangential velocity component	[m/s]
v_z	Axial velocity component	[m/s]
v_{max}	Maximum velocity (ωR_{inn})	[m/s]
$\dot{W}$	Power	[W]
ws	Windows Size	[-]
z	Axial position	[m]

Greek symbols

Symbol	Description	Unit
$\bar{\bar{\dot{\gamma}}}$	Rate of strain tensor	[1/s]
$\dot{\gamma}$	Shear rate	[1/s]
Γ	Cylinder aspect ratio (δ/H)	[-]
Γ	General diffusivity	[Pa·s]
δ	Radius gap	[m]
δ_θ	Distance from the nodal point P to nodal points at east or west	[-]
δ_r	Distance from the nodal point P to nodal points at north or south	[m]
δ_z	Distance from the nodal point P to nodal points at top or bottom	[m]
Δt	Time step	[s]
ε	Control volume surface position	[m]
η	Rheological dynamic viscosity (Apparent viscosity)	[Pa·s]
θ	Angular position	[-]
κ	Inverse radius ratio (R_{out}/R_{inn})	[-]
λ	Relaxation time	[-]
μ	Dynamic viscosity	[Pa·s]
μ_m	Measurement uncertainty	[-]
μ_P	Process uncertainty	[-]
μ_T	Torque uncertainty	[-]
ρ	Density	[kg/m^3]
σ	Normal stress	[Pa]
ς	Mesh concentration factor	[-]

$\bar{\bar{\tau}}$	Shear stress tensor	[Pa]
τ	Shear stress tensor magnitude	[Pa]
τ_0	Yield stress	[Pa]
ψ	Stream function	[m²/s]
ω	Inner cylinder angular velocity	[rad/s]

Subscripts

Symbol	Description
b, B	Bottom surface border and nodal point
c	Critical
e, E	East surface border and nodal point
final	Final time
i, j and k	Nodal points indices
in	Entering control volume
inn	Inner cylinder
liq	Liquid
loaded	Loaded torque value
mass	Mass conservation
max	Maximum value
momentum	Momentum conservation
n, N	North surface border and nodal point
nb, NB	Neighborhood surfaces and nodal points
net	Net torque value
out	Outer cylinder, leaving control volume

P	Center nodal point
r	Radial coordinate (position)
θ	Angular coordinate (position)
s, S	South surface border and nodal point
t, T	Top surface border and nodal point
unloaded	Unloaded torque value
w, W	West surface border and nodal point
z	Axial coordinate (position)

Superscripts

Symbol	Description
0	Previous time

TABLE OF CONTENTS

1 INTRODUCTION

1.1 GENERAL VIEW

The efforts of the mankind to improve the washing processes date back to prehistory, when fur and leather, used as clothing, were washed in lakes by rubbing through friction of stones. Since then, the human habits have changed significantly in the pioneer civilizations, especially the Romans (from ~500 to 476 BCE), when cities had supplied water and the use of detergents as soap was disseminated (STALMANS, 2008).

The laundry techniques had undergone little progress in the Middle Ages (476-1453), when the concern for hygiene and, consequently, public health, had lessened in Europe due to the superstitious fear that water could bring diseases (STALMANS, 2008). In Arab countries, on the other hand, the production of soaps had advanced, especially in Mediterranean countries during the Renaissance years (1453 to ~1700). Furthermore, following the development of sciences and arts, there was a greater dissemination of the direct relationship between hygiene and health relation. Consequently, laundries which provided water came up in major European cities, as shown in Figure 1, which depicts an illustration of a popular alchemy guide (TRISMOSIN, 1582). According to Stalmans (2008), the dirty water, from laundry applications, used to be sold to the less fortunate.

During the Industrial Revolution, particularly in 1744, the Swedish chemist Karl W. Scheele pointed out that chlorine has not only a bleaching effect but also acts as a disinfectant when present in an aqueous solution containing sodium hydroxide (NaOH). A few years later (1783), Scheele discovered glycerin, which would revolutionize the manufacturing of soap and detergents in industrial scale. Likewise, in the late eighteenth century, the first washboards came up, thus producing a better washing effect with less human effort.

FIGURE 1 - ENGRAVING OF WOMEN WASHING CLOTHES.

SOURCE: TRISMOSIN (1582).

The widespread use of disinfectants took place nearly a century later the germ theory was published by Louis Pasteur (1880), which associated infectious diseases to micro-organisms. Moreover, in the mid-nineteenth century, in addition to the advances in Chemistry, households started to be water supply. Consequently, the first mechanical devices to aid the laborious process of cloth washing came onto the market, which consisted of a cylindrical tank that was rotated by means of manual action.

The first washing machine was designed by Jacob Schaeffer in 1767. It was made of wood and comprised of a four-blade agitator operated manually, as depicted in Figure 2. In 1851 James King patented the first drum-type washing machine. A few years later, in 1858, Hamilton Smith designed a washing machine with mechanical actuation, which was improved and marketed by William Blackstone in 1874, whose company is still open these days (VAN DEN BREKEL, 1987). Also, according to Sérgio et al. (2003), approximately two thousand patents related to washing machines have been requested in the U. S. and U. K. between 1850 and 1870.

FIGURE 2 - SCHEMATIC SKETCH OF THE WASHING MACHINE DESIGNED BY JACOB SCHAEFFER.

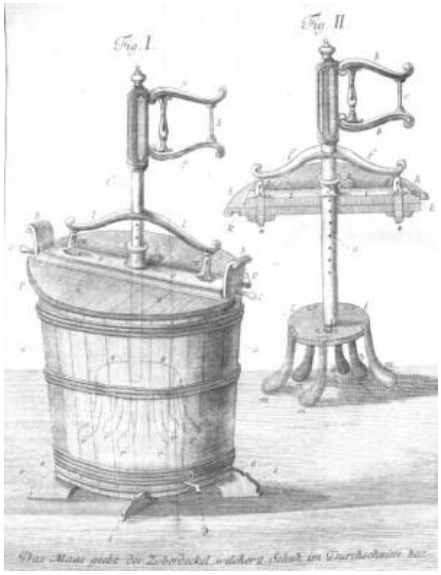

SOURCE: SCHAEFFER (1767).

In the early twentieth century, the first electrically-driven washing machine was developed. One of the first vertical axis washing machines with electric actuator produced in large scale, named Thor, is illustrated in Figure 3. Only in the 1920s, the first horizontal axis washing machine was released on the market. Since then, a series of improvements have been implemented, such as water heating, additives dispenser (e.g., detergent, softener, bleach) and spinning.

FIGURE 3 - THOR, ONE OF THE FIRST WASHING MACHINES WITH ELECTRICAL ACTUATION - 1911 MODEL.

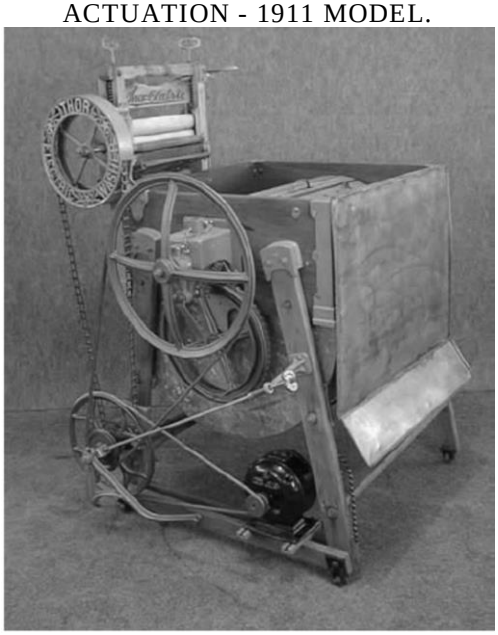

SOURCE: MAXWELL (2009).

Currently, a washing machine is a household appliance whose main purpose is to remove the dirt from a given amount of fabric (natural or synthetic) by means of mechanical, thermal, and chemical processes occurring simultaneously during the washing cycle (VAN DEN BREKEL, 1987). Such an apparatus may be mounted with either horizontal or vertical axis, where the former is more likely found in European countries, and the latter in Australasia and the Americas, including Brazil (BANSAL, VINEYARD and ABDELAZIS, 2011).

Therefore, a vertical axis washing machine, with top loading, is comprised of a structure that supports a water reservoir (outer bowl), wherein a perforated drum (spin bowl) that rotates without angular restrictions is placed, and an agitator – responsible for moving the set formed by fabric, water, additives, and the spin bowl itself. The agitator is connected to an electric motor by a transmission so that the torque and the angular velocity can be both controlled. Finally, the tank is filled with water through a hydraulic system comprising a pump, a suction valve, and a water level sensor, as shown in Figure 4.

FIGURE 4 - SCHEMATIC REPRESENTATION OF A VERTICAL AXIS WASHING MACHINE.

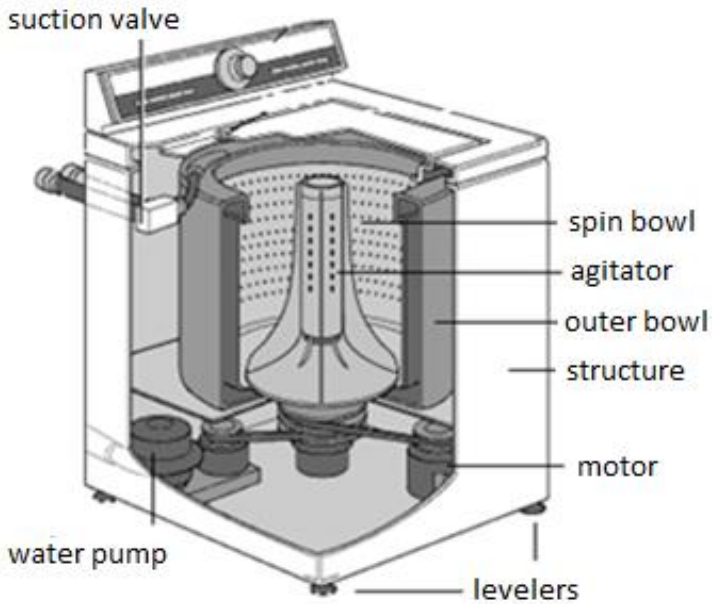

SOURCE: ADAPTED FROM HTTP://WWW.HOMETIPS.COM, 2015.

In general, the washing process depends on a wide set of parameters, such as the spin bowl and agitator geometries, the agitation profile (i.e., temporal variation of torque, angular swept and speed), water level, temperature of the mixture formed by water, fabric, additives, detergent, among others (VAN DEN BREKEL, 1987). In addition, the washing process relies on the mass and momentum transport from the agitator to the fluid stream. Essentially, there is a periodic circular flow between two concentric cylinders, where the inner cylinder (spin bowl)

rotates while the outer cylinder (outer bowl) remains stationary. Because not only of the geometry but also of the fluid characteristics, the flow pattern is quite complex. Most of the information concerning this kind of flow is of empirical nature, which does not provide a deep understanding of the mechanical interactions, the flow pattern, and the chemical reactions. However, a satisfactory level of understanding can be obtained by means of an analysis of fluid flows in cylindrical cavities, which follows a pattern that refers to the well-known Taylor-Couette one, whose main characteristic is the confinement between two rotating cylinders (DONNELLY, 1991).

The Taylor-Couette flow, although may appear to be simple, is quite complex: when one limits the radius ratio ($k = R_{inn}/R_{out}$), and the angular velocity of the inner cylinder exceeds a critical figure, hydrodynamic instabilities take place.

A typical Taylor-Couette domain is shown in Figure 5. The inner radius can be denoted as kR, whereas k is the radius ratio. The height of the fluid column is denoted by h, whereas the total height is denoted by H. In this case, the outer cylinder is held stationary while the inner one rotates independently with an imposed angular velocity ω. The radius gap (δ), radius ratio (k) and aspect ratio (Γ) are defined as follows:

$$\delta = R_{out} - R_{inn} \tag{1.1}$$

$$k = \frac{R_{inn}}{R_{out}} \tag{1.2}$$

$$\Gamma = \frac{H}{\delta} \tag{1.3}$$

where the dimensionless flow parameters are the rotational Reynolds number and Taylor number. The former is the ratio between inertial and viscous forces acting in the flow. Whereas the later relates the same forces taking the above geometrical parameters in consideration. Regarding the Newtonian fluids:

$$Re = \frac{\rho(\omega R_{inn})\delta}{\mu} \tag{1.4}$$

$$Ta = \left(\frac{\rho\omega}{\mu}\right)^2 R_{inn}\delta^3 = \left(\frac{1}{k} - 1\right) Re^2 \tag{1.5}$$

where ρ denotes the density (kg/m³) and μ denotes the dynamic viscosity (Pa·s) of the fluid.

FIGURE 5 - SCHEMATIC REPRESENTATION OF THE PHYSICAL DOMAIN.

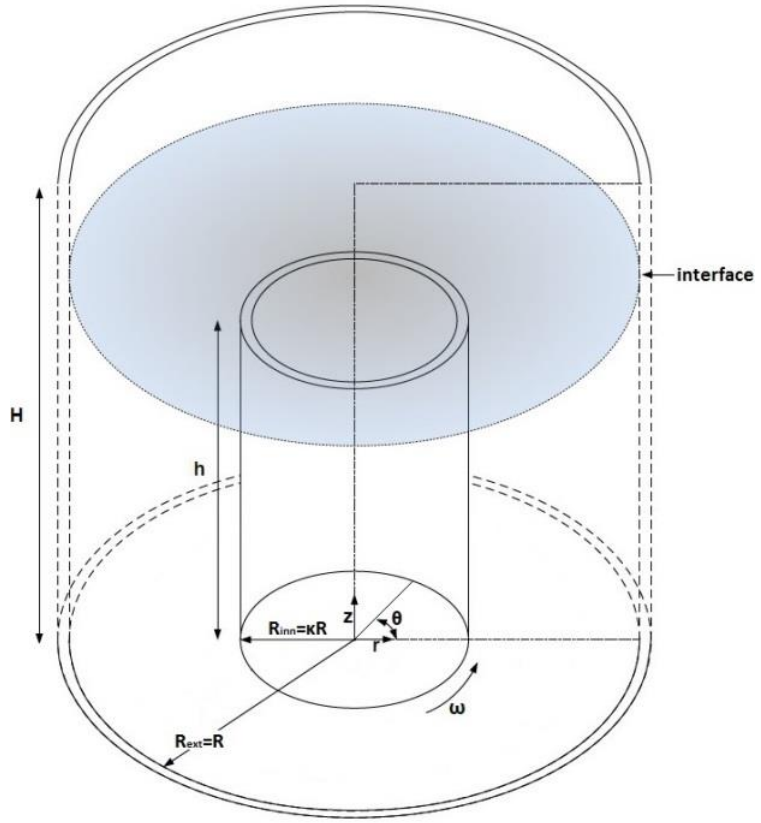

The flow is considered unstable when the viscous forces are not able to dissipate the disturbance caused by the inertial forces, which occurs when a critical value of the dimensionless number (either Reynolds or Taylor) is reached.

Many scientists have studied the physics of confined flow between two rotating cylinders, aiming at the instabilities due to the turbulence that occurs when an angular velocity of the cylinders is exceeded (NEWTON, 1946) (STOKES, 1880) (STOKES, 1905) (MALLOCK, 1888) (COUETTE, 1888) (COUETTE, 1890) (RAYLEIGH, 1914), (see Figure 6). However, only in 1923, G. I. Taylor developed a theory concerning the stability of the Couette flow (TAYLOR, 1923). His study was a milestone in the realm of fluid dynamics (DONNELLY, 1991) because: (i) held a convincing proof of the no-slip condition, (ii) provided evidence that the Navier-Stokes equations could predict accurately the flows of Newtonian fluids, and (iii) applied the linear stability theory to predict the experimental results, characterizing the transition from the stable flow to the unstable one (DONTULA, MACOSKO and SCRIVEN, 2005) (PIAU and PIAU, 2005).

FIGURE 6 - MALLOCK'S APPARATUS USED IN PIONEERING INVESTIGATIONS OF THE FLUID FLOW OF THE BETWEEN CONCENTRIC CYLINDERS.

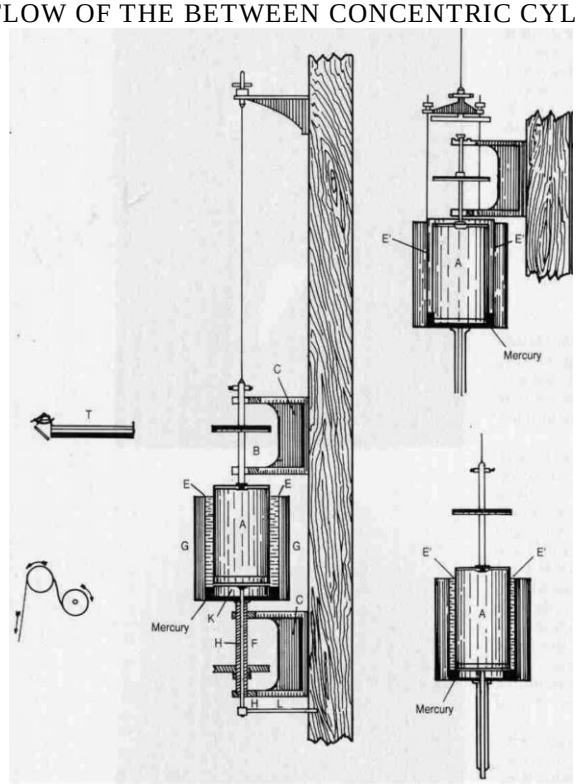

SOURCE: DONNELLY (1991).

The present study has focused the flow of fabric-water suspensions in simplified Taylor-Couette cylindrical geometries through experimental measurements and numerical simulations carried out by means of a purpose-built testing facility and a tailor-made computational model, respectively. The numerical front is regarded with the computer simulation of flows of homogeneous Newtonian and non-Newtonian fluids based on the three-dimensional conservation equations of mass and momentum in cylindrical coordinates, whilst the experimental front is conducted for different mixtures of fabrics in water.

1.2 LITERATURE

Since the present work is aimed at understanding the rheological behavior of fabric-water suspensions inside a cylindrical cavity (a simplified geometry that emulates a washing machine), the literature review spanned different fronts.

Firstly, a brief review of the literature in the realm of laundry/washing processes was conducted. It was found that the literature is still scarce in this field, especially regarded with numerical simulations of fabric-water suspensions (AKCABAY, DOWLING and SCHULTZ, 2014). Next, a literature review of the Taylor-Couette flows of Newtonian and non-Newtonian

fluids was performed to get a better understanding of the main and secondary flows behaviors, as well as the conditions which lead to unstable flows. The main flow is described by the tangential velocity only, which is transmitted from the cylinder to the fluid stream. The secondary flow is the fluid circulation inside the cavity in both the radial and the vertical directions. Finally, a comprehensive literature review of rheometry in cylindrical cavities (also called Couette geometries) was carried out. In this part, the focus was on the experimental measurement and numerical reduction of raw data (torque and angular velocity).

1.2.1 Laundry/ Washing Processes

In a pioneering work, Van den Brekel (1987) studied the momentum and mass transfer in a horizontal axis washing machine. The author focused especially on the chemical aspects of the washing process. A simplified model suited for the drum dynamics, responsible for the movement of the fluid stream and the mass transfer between water and fabric, was developed and validated against experimental data obtained in-home. Moreover, based on a simplified simulation model, Van den Brekel concluded that the advection caused by the flow of water-detergent mixture between basket and tank outweighs the diffusive transport, while the opposite is observed for the fabric.

Two decades later, aiming at advancing the knowledge about the mechanical aspects of the washing process, Akcabay (2007) put forward two and three-dimensional models to solve the flows of fabric-water suspensions. The fabric was modeled as an elastic plate, while the water flow was modeled by means of the Navier-Stokes equations. The fabric-water coupling was performed by the Peskin's immersed boundary method (PESKIN, 2002). The numerical results have not been validated against experimental data. His research was also published in Akcabay, Dowling, and Shultz (2014).

Calvimontes (2009) sought to understand the wetting phenomena on rugged surfaces. The author performed a topographic characterization of polyester and cotton fabric. The influence of the morphology of yarns and fibers on the wettability was additionally studied. He observed that the polyester fabric parameters strongly affect the capillarity. Another front of research was on the effect of the washing cycles on topography, spreading, wetting and dirt accumulation in cotton fabric. For doing so, he proposed a mathematical model to represent the fabric surface so that the changes in the topography can be predicted.

Eger (2010) analyzed numerically the flow mixing in alternated motion focusing on vertical drum washing machines. A turbulent three-dimensional model was implemented into a commercial CFD software to simulate the water flow in a simplified geometry in which the drum (outer bowl) rotates. An experimental rig was built so that velocity was measured to validate the model. The following parameters were analyzed: water level, rotational velocity, and geometry. Finally, a comparison between numerical and experimental data showed a satisfactory level of concordance, according to the author. Numerical analyses including fabric-water suspensions were not performed.

Janáčová et al. (2011) analyzed the washing process in a vertical axis washing machine for the reducing the water consumption. A lumped model based on the fundamental principles was designed to predict the diffusive mass transfer along a homogeneous fabric-water suspension. The authors determined the optimal operation cost in terms of a dimensionless parameter introduced by them, called the soak number.

Yee (2013), Machado (2014) and Zanotto (2015) advanced in their undergraduate term papers – all carried out at the Laboratory of Thermodynamics and Thermophysics of the Federal University of Parana – different work fronts concerning both the experimental analysis and numerical flow simulations of vertical axis washing machines. Yee performed numerical simulations using a commercial CFD software to evaluate the flow of water in complex washing machine geometries, whereas Machado designed and constructed an experimental apparatus to gather data to validate the numerical simulations. The numerical and experimental data for power and torque were compared when a satisfactory level of agreement was observed. Zanotto, on the other hand, adapted the purpose-built facility introduced by Machado to perform experimental tests using fabric-water suspensions confined in two concentric cylinders, supporting the present work. All the three prior studies have been used as the baseline for this thesis work.

Campos and Hermes (2016) investigated experimentally and numerically the transient detergent transport between the compartments and through the garments during the washing process in a household top-load washing machine. The experimental results were used in the numerical model as closing parameters, thus providing the model with a semi-empirical character. The model prediction and the experimental results agreed quite well for the time evolution of the detergent concentration within the different compartments of the washing machine. The authors pointed out that the detergent insertion and the agitation level were the most influencing washing parameters.

The review of the literature on laundry points out that studies in the open literature that sought to understand chemical and mechanical phenomena present in the fabric washing are quite scarce. Additionally, there is no evidence in the literature of a computational fluid dynamics models considering the presence of fabric during the washing process that was validated against experimental data. Finally, there is no information regarded with the rheology of fabric-water suspensions. The present work is aimed at filling those gaps.

1.2.2 Taylor-Couette Literature

Figure 7 shows a steadily increasing number of published papers in the main areas of the present work over the years from 1900 up to 2016. One can note that the rheology and yield stress fronts experienced a notable growth in the last decades. Rheometry, which is a sub-area of rheology, has also shown a significant growth in this period. Figure 8 depicts the interest on the non-Newtonian fluid models that are subject matter for the present work. The figure shows that the Bingham fluid was the most cited model but there had been a great interest in the Herschel-Bulkley and Casson fluids in the last two decades.

FIGURE 7 - NUMBER OF PUBLICATIONS CONCERNING THE LITERATURE FRONTS REVIEWED IN THE PRESENT WORK.

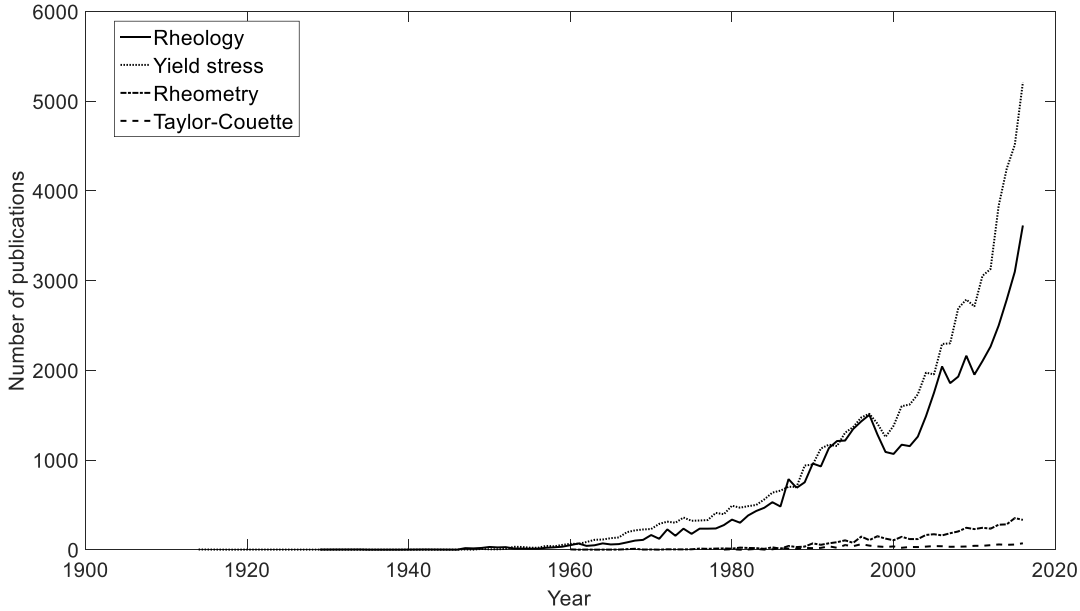

SOURCE: DATA OBTAINED FROM SCIENCE DIRECT (2017).

FIGURE 8 - NUMBER OF PUBLICATION CONCERNING SOME YIELD STRESS MODELS.

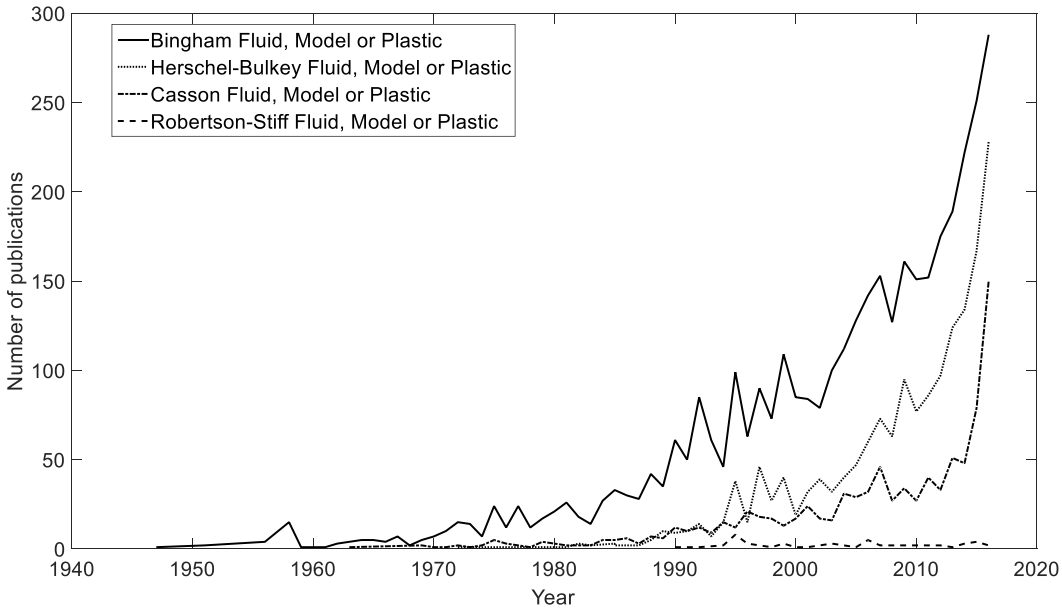

SOURCE: DATA OBTAINED FROM SCIENCE DIRECT (2017).

The literature concerning Taylor-Couette flows is quite broad, since it covers different aspects of the flow (i.e., flow regimes, instabilities, fluid type, etc). Among the classical works concerning the instabilities in Taylor-Couette flows, one can mention the pioneering studies by Chandrasekhar (1953), Di Prima and Swinney (1985) and Andereck, Liu and Swinney (1986). Chandrasekhar (1953) performed a numerical study based on the flow stability equations and studied cases where the gap between cylinders was narrow and both cylinders were rotated in the same direction. The author produced a table of critical Taylor numbers in which the flow regime changed to turbulent. Di Prima and Swinney (1985) conducted a comprehensive review of many works concerning instability and transition in circular flows between concentric cylinders. Table 1 shows some of the works cited by them and presents some critical values for the following dimensionless parameter, $\mathrm{Re}\left(\frac{\delta}{R_{inn}}\right)^{1/2}$, where δ (R_{out} - R_{inn}) denotes the radius gap, considering different radius ratios. The Reynolds number for a fluid flow between concentric cylinders is calculated as follows:

$$\mathrm{Re} = \frac{\rho\omega_{inn}R_{inn}\delta}{\mu} = \frac{\omega_{inn}R_{inn}\delta}{\nu} \tag{1.6}$$

TABLE 1 - CRITICAL VALUES FOR TAYLOR-COUETTE FLOWS.

k	Reference	$Re\left(\frac{\delta}{R_{inn}}\right)^{1/2}$	k	Reference	$Re\left(\frac{\delta}{R_{inn}}\right)^{1/2}$
1.000	Walowit et al, 1964	41.18	0.600	Walowit et al, 1964	58.56
0.975	Donnelly et al., 1965	41.79	0.500	Donnelly et al., 1965	68.19
0.963	Donnelly et al., 1965	42.09		Sparrow et al, 1964	68.19
0.950	Donnelly et al., 1965	42.44		Walowit et al, 1964	68.18
	Sparrow et al, 1964	42.44			
	Walowit et al, 1964	42.45	0.400	Walowit et al, 1964	83.64
			0.360	Donnelly et al., 1965	97.72
0.925	Donnelly et al., 1965	43.13	0.350	Sparrow et al, 1964	95.38
0.900	Donnelly et al., 1965	43.87	0.300	Walowit et al, 1964	118.89
	Walowit et al, 1964	43.88	0.280	Donnelly et al., 1965	120.43
0.875	Donnelly et al., 1965	44.66	0.250	Sparrow et al, 1964	136.40
0.850	Donnelly et al., 1965	45.50			
0.800	Walowit et al, 1964	47.37	0.200	Donnelly et al., 1965	176.26
0.750	Donnelly et al., 1965	49.52		Walowit et al, 1964	176.33
	Sparrow et al, 1964	49.53	0.150	Sparrow et al, 1964	250.10
			0.100	Sparrow et al, 1964	423.48
0.700	Walowit et al, 1964	52.04		Walowit et al, 1964	422.79
0.650	Donnelly et al., 1965	55.01			

SOURCE: ADAPTED FROM DI PRIMA AND SWINNEY (1985).

Dou, Khoo, and Yeo (2008) summarized some classic experimental studies on Taylor-Couette flows considering the geometric aspects of the experimental apparatuses, as presented in Table 2. Attention should be also given to the work of Andereck et al. (1986), who have shown, by means of the map depicted in Figure 9, the flow regimes in case of fluid flow between two independent rotating coaxial cylinders as a function of the Reynolds numbers relative to the inner cylinder (R_0) and the outer cylinder (R_1). Their experimental facility had a radius ratio (k) of 0.884 and cylinder aspect ratios ($\Gamma = \delta/H$) varying from 20 to 48. During their experiments, both the top and bottom surfaces were fixed, while that inner cylinder was put to rotate with gradually increasing speed in order to achieve flow transition.

TABLE 2 - CRITICAL VALUES FROM KEY EXPERIMENTAL STUDIES ON TAYLOR-COUETTE FLOW.

Author	Year	R_{inn} (cm)	R_{out} (cm)	H (cm)	k	Re_c
Taylor	1923	3.8	4.035	0.235	0.94	169
		3.55	4.035	0.485	0.88	120
		3	4.035	1.035	0.74	95
Coles	1965	10.155	11.52	1.365	0.88	116
Snyder	1968	6.023	6.281	0.258	0.96	217
		5.032	6.281	1.249	0.80	94
Gollub and Swinney	1975	2.224	2.54	0.316	0.88	128
Andereck et al.	1986	5.25	5.946	0.696	0.88	120

SOURCE: ADAPTED FROM DOU ET AL. (2008).

FIGURE 9 - TAYLOR-COUETTE FLOW MAP AS A FUNCTION OF REYNOLDS NUMBERS OF THE INNER AND THE OUTER CYLINDERS.

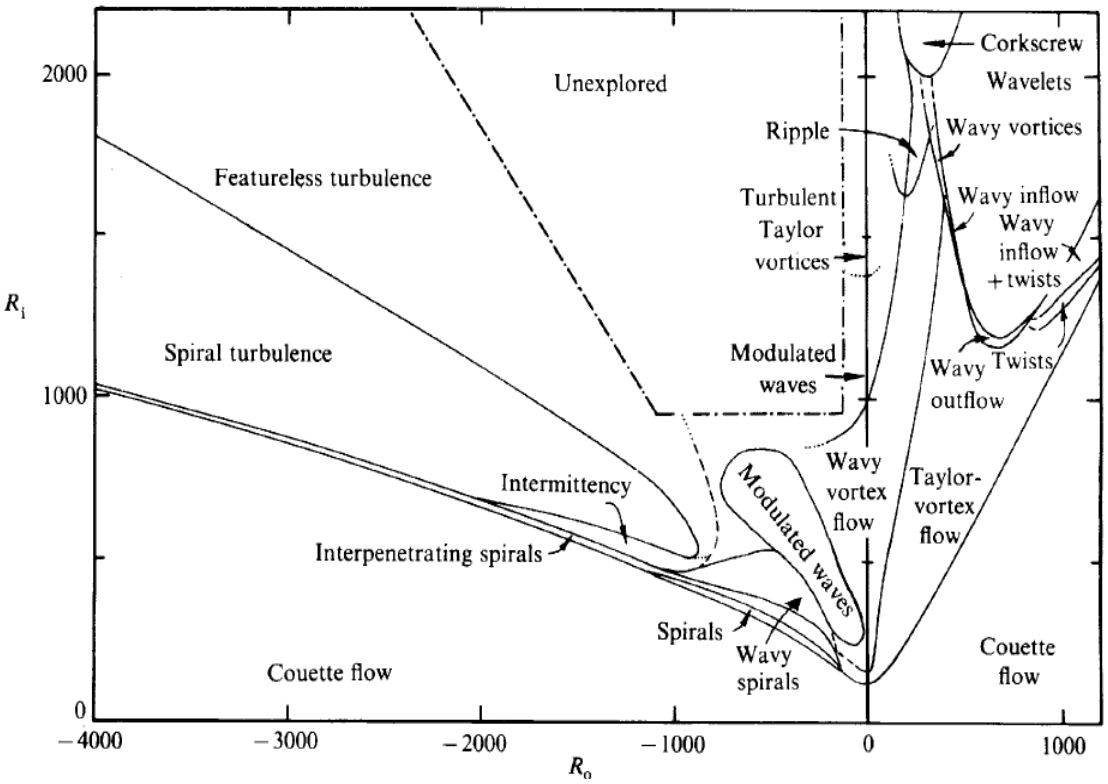

SOURCE: ANDERECK ET AL. (1986).

Both Tables 1 and 2 shows that the critical Reynolds number values change according to the geometry parameters (cylinders radius and column height). Figure 9 also shows different wave regimes (instabilities) in a Taylor-Couette flow by changing the velocities and rotation directions of both inner and outer cylinders.

Table 3 summarizes some of the key studies regarding Taylor-Couette flows of Newtonian fluids. The radius ratio (k) is used as a comparison parameter. Wu and Swift (1989),

for instance, performed an experimental work focusing on Taylor-Couette secondary flows, where inner and outer cylinder rotation were both modulated according to a sinusoidal pattern. The model was validated against data from the literature when it was observed that the outer cylinder modulation leads to large critical Reynolds numbers, whereas the inner cylinder modulation led to the opposite behavior.

TABLE 3 - KEY TAYLOR-COUETTE STUDIES CONCERNING NEWTONIAN FLUIDS.

Authors	Year	Origin	Approach	Validation	k
Meyer-Spasche and Keller	1980	Germany	Numerical	Yes	0.5 and 0.95
Marcus	1984	United States	Numerical	Yes	0.5 to 0.9
Wu and Swift	1989	United States	Numerical	Yes	0.88 and 0.95
Escudier et al.	1995	England	Experimental	-	0.506
Weisberg et al.	1997	United States	Experimental	-	0.9051
Takeda et al.	1999	Swiss	Experimental	-	0.904
Watanabe et al.	2003	Japan	Numerical and Experimental	Yes	0.675, 0.839 and 0.931
Djeridi et al.	2004	France	Experimental		0.857
Huang et al.	2007	Singapore	Numerical	Yes	0.5
Watanabe and Toya	2012	Japan	Numerical and experimental	Yes	0.667

Weisberg et al. (1997) conducted an experimental work to generate Taylor vortices in a flow produced from an imposed periodical axial velocity (v_z) applied in the inner cylinder simultaneously to the rotational velocity. Water and Kalliroscope AQ-1000 solution was employed as the working fluid, in such a way that the flakes enabled the flow visualization. From the axial velocity and Taylor number, the authors could establish a flow stability criterion.

Takeda et al. (1999) performed an experimental work concerning the measurement of axial velocity by means of ultrasonic Doppler method. The experimental apparatus had a radius ratio of 0.904, where flows with the Reynolds number varying from 9 up to 40 times the critical value were tested. Water and glycerin solutions (30 wt.%) were used as the working fluid. Fast Fourier Transform (FFT) techniques were applied in order to observe the density, power, and energy spectral distributions. By doing so, the authors confirmed part of the flow regimes depicted by Andereck et al. (1986).

Watanabe et al. (2003) performed an experimental and numerical research to evaluate the influence of the cylinder surface characteristics, the concentration of the fluid (glycerine solution), and the aspect ratio of the flow pattern in a Taylor-Couette flow. The authors used highly repellent wall coatings to figure out the effect of the cylinder surface on the laminar drag

reduction with fluid slip. Furthermore, through PIV (Particle Image Velocimetry) techniques, they visualized the velocity profile close to the inner cylinder using smooth and highly repellent walls. They found that the intervals of Taylor cell vortices (of secondary flow) become slightly irregular when a highly repellent wall was used. The numerical results concerning the velocity profile and the Taylor cells visualization, when the slip velocity boundary condition was applied, agreed with the experimental counterparts.

Djeridi et al. (2004) conducted an experimental study of two-phase Taylor-Couette flows of air-water-glycerin mixtures. Their apparatus had a radius ratio of 0.857, where the air was introduced into the flow in two different ways: through free surface or by cavitation through a pressure drop. They found that in the case of low Reynolds numbers, air bubbles were trapped inside the core of the Taylor-cells. On the other hand, for higher Reynolds number the air bubbles migrated to the region near the inner cylinder.

Watanabe and Toya (2012) performed a numerical-experimental study regarding Taylor-Couette flows with the free top surface. A finite-difference scheme was employed to solve the governing equations, while the pressure equation was solved through the marker-and-cell (MAC) method. The experimental apparatus had a radius ratio of 0.667 and water-glycerin mixtures were used as working fluid, while aluminum flakes were applied to visualize the flow. The reason to make use of low Reynolds numbers was to ensure axisymmetric flow. Moreover, the study focus was on the recirculation cells in the axial direction due to the increase of the aspect ratio ($\Gamma = \delta/H$). The interface curves between the flow transition regimes were plotted as function of Reynolds number and aspect ratio as the number of recirculation cells increased

Similarly, a summary of key numerical-experimental studies found in the open literature concerning Taylor-Couette flows of non-Newtonian fluids is found in Table 4, some of them used in the present work for the sake of code verification.

For instance, Chow and Fuller (1985) draws attention to some experimental results regarding collagen solutions obtained by means of an apparatus where the inner diameter of the outer cylinder was 2.54 cm, and two different gap sizes were applied during the tests: 0.5 and 1.0 mm, corresponding to aspect ratios (k) of approximately 0.96 and 0.92, respectively. Birefringence techniques in bicolor flow experiments, where the outer cylinder was rotated while the inner one was kept stationary, were applied and proven to be suitable for measuring the changes of non-Newtonian flows in which fast transients were observed. Nevertheless, the techniques failed in observing the flow as a whole.

One year later Sinevic et al. (1986) conducted an experimental work using three different test rigs: two with different aspect ratios (0.908 and 0.702) and one with four vertical strip baffles with 1.4 cm on the outer cylinder inner liner. The tests were performed with Newtonian fluid (corn syrup) and non-Newtonian fluids (carboxymethyl cellulose solutions - CMC and Carbopol). A strain gauge was used for the torque measurements, and small polystyrene particles were used for the flow visualization. They pointed out that the presence of the vertical strip baffles increased the value of the critical Taylor number, thus making it less dependent on the rheological properties of the fluids while increasing the vortex numbers.

Lockett et al. (1992) handled computer simulations by means of finite element techniques in two different geometries: aspect ratios of 0.95 (narrow gap) and 0.5 (wide gap). Two models of inelastic non-Newtonian fluids were used and compared with literature values, namely Power-Law and Bingham model. Also, two different dimensionless parameters (critical Taylor number and wavenumber) were applied to compare the differences between the radius gaps and the fluid flows, where a good agreement with the literature data was found in the narrow gap case, while it was also detected that the critical values were more dependent on the rheological parameters in the wide gap case.

Jastrzębski et al. (1992) performed some numerical simulations to ascertain the critical values of the Taylor number and the vortex number in the axial direction. Four different radius ratio values were applied (0.90, 0.80, 0.66 and 0.5), where the first two were considered as narrow gap geometries and the latter ones as a wide gap geometry. Also, different values of the Power-Law index (n) ranging from 0.25 (shear-thinning) to 1.75 (dilatant) were tested. It was observed that in all simulations, the greater the Power-Law index (n) the greater was the critical Taylor number. Furthermore, pseudoplastic fluid flows showed a tendency to destabilize the rotational flow, while for dilatant fluids the tendency for stabilization was noted. Also, it was observed that for $k > 0.6$ the theoretical stability limit was in good agreement with the experiments, while for $k<0.6$ the critical Taylor number was found to be lower than that predicted by theory.

TABLE 4 - KEY TAYLOR-COUETTE STUDIES CONCERNING NON-NEWTONIAN FLUIDS.

Authors	Year	Origin	NNF Model	Approach	Validation	k
Chow and Fuller	1985	United States	Collagen solution	Experimental	-	0.96 and 0.92
Sinevic et al.	1986	England	Corn syrup, CMC solutions, and Carbopol	Experimental	-	0.908, 0.702 and with vertical strip baffles
Lockett et al.	1992	England	Power-law and Bingham	Numerical	Yes	0.95 and 0.5
Jastrzębski et al.	1992	Poland	Power-Law	Numerical	Yes	0.5 0.66 0.8 and 0.9
Escudier et al.	1995	England	Xanthan gum solution and Laponite/CMC aqueous blend	Experimental	-	0.506
Coronado et al.	2002	Brazil	Carreau	Numerical	Yes	0.6 to 0.9
Escudier et al.	2002	England	Cross, Carreau and Herschel-Bulkley models	Numerical	Yes	0.2 to 0.8 (eccentric annulus)
Smieszek and Egbers	2005	Germany	Silicone oil and Boger fluid (viscoelastic)	Experimental	-	0.5
Amoura et al.	2006	Algeria	Carreau	Numerical	Yes	0.5
Jeng and Zhu	2010	China	Bingham	Numerical	Yes	0.5
Alibenyahia et al.	2012	Algeria	Bingham, Carreau, and Power-law	Numerical	Yes	0.4 to 0.9
Khali et al.	2013	Algeria	Power-law	Numerical	Yes	0.5

Escudier et al. (1995) performed an experimental work in a concentric annular geometry with a radius ratio (k) of 0.506 and a very large aspect ratio (Γ), wherein the inner cylinder rotates where the outer one is held stationary. Velocity measurements were carried out by means of a laser Doppler anemometer for an aqueous solution of Glucose, which is a Newtonian fluid. They found that for Taylor numbers above the critical value the components of the tangential velocity have periodic structures of the same wavelengths as those of the axial components. Moreover, the maximum axial velocity and velocity gradient were found to be closer to the core, whilst the radial location of zero axial velocity in the vortex interior moves towards the outer wall with an increasing Taylor number. Furthermore, they performed similar measurements for an aqueous solution of Xanthan gum (very shear-thinning and slightly elastic), where it was found that the asymmetry of the maximum axial velocities was higher than the Newtonian fluid with a significant radial shift in the location of the vortex eye towards the core, while the vortices exhibited a slow axial drift in the direction opposite to the centre body rotation vector. Finally, measurements were made using a Laponite/CMC aqueous blend

(shear-thinning and thixotropic fluid), where they found that the shear-thinning aspect of the fluid rheology was more significant than either thixotropy or viscoelasticity for both non-Newtonian fluids.

Coronado et al. (2002) performed a numerical work in which the effect of the viscoplastic properties of high concentration suspensions on the onset of the Taylor vortices was determined theoretically through the critical values of the Taylor number for Newtonian and non-Newtonian fluids. The differential equations were solved by the Galerkin finite-element method and the resulting set of nonlinear algebraic equations, by Newton iteration. The Newtonian fluid flow simulations were validated against experimental data of the literature with radius ratio (k) ranging from 0.4 to 1. Also, the Carreau non-Newtonian model was applied to simulate pseudoplastic flows, where the results showed that for shear-thinning fluids the vortex tends to occur in lower angular velocities regions.

Escudier et al. (2002) presented results of extensive numerical calculations carried out using a finite-volume method for fully developed laminar flow of an inelastic shear-thinning Power-Law fluid, as well as Cross, Carreau and Herschel-Bulkley fluid models. The simulations took place in a concentric and eccentric annulus with inner cylinder rotation, when the results were compared with other numerical studies covering a wide range of parameters (Power-Law index n, radius ratio δ, eccentricity, Reynolds, and Taylor numbers).

Smieszek and Egbers (2005) performed an experimental work using a silicone oil as reference fluid (Newtonian fluid) and a viscoelastic Boger fluid in a wide-gap Taylor-Couette system ($k = 0.5$) to investigate the pattern formation and stability of the flow through a PIV (Particle Image Velocimetry), which was used to visualize and measure the flow fields. The results showed that the transition sequence of the Boger fluid resembles the Newtonian fluid at lower rotation rates for the inner cylinder. They also demonstrated that the aspect ratio (Γ) strongly affects the fluid flow behavior, where for aspect ratios lower than 4.48 the wavy vortex flow is inhibited by the Boger fluid flow.

Amoura et al. (2006) performed a numerical work focused on the flow characteristics and the heat transfer mechanism of a non-Newtonian flow in a Taylor-Couette geometry, where the vortex generation can enhance the heat transfer. The Carreau model was adopted to model the rheological fluid behavior. The authors considered a geometry with a radius ratio of 0.5 and Power-Law index (n) spanning from 0.6 and 1. The heated inner cylinder rotated while the cooled outer cylinder was at the rest. Also, the horizontal axis was assumed to be adiabatic. The governing equations were solved by means of the finite element method while some

dimensionless numbers (Reynolds, Grashof, and Weissenberg numbers) were evaluated. The results show that the non-Newtonian effects are important on the structure of the flow and on the heat transfer.

Jeng and Zhu (2010) performed a numerical study regarding the Taylor-Couette flow of a Bingham fluid where the cylinders were assumed to rotate independently and there was an imposed axial sliding. The applied numerical methods were based on the expression of the deviation field in terms of complete sets of orthogonal function and Chebyshev series, where the Galerkin projection was used to eliminate the pressure term. Thus, the numerical method was compared with literature data using the friction coefficient as a reference with $\tau_0 = 0$ referring to Newtonian fluids. For $\tau_0 > 0$, the Papanastasiou method was adopted (PAPANASTASIOU, 1987). They also showed that when the outer cylinder was held stationary the vortices were squeezed toward the inner cylinder and the friction factor was augmented. However, when the outer cylinder rotates in the same direction of the inner cylinder, the vortex flow is initially strengthened with an increase of the yield stress, but after that, it is weakened when the yield stress is raised large enough, while the annular unyielded regions emerge and stick to the outer cylinder. Finally, in the case where there was an imposed axial sliding of the inner cylinder, spiral vortices were formed with spiral unyielded regions being obtained.

Alibenyahia et al. (2012) conducted a numerical analysis of the three-dimensional stability of the Taylor-Couette flow of non-Newtonian fluids. Three different models were used: Bingham, Carreau, and Power-Law fluids. The authors explored a wide range of rheological, geometrical, and dynamical parameters using a pseudo-spectral method to solve the eigenvalue problem of the governing equations and validating the code against Newtonian fluid flows found in the literature for different aspect ratios. In all cases, it was observed that along the increasing shear viscosity in the inner cylinder a stabilizing effect in the pseudoplastic is observed, thus delaying the onset vortices, and confirming that the viscosity gradient near the inner cylinder has the highest stabilizing effect, while the gradients far from the cylinders produce almost no effect. Also, in the axisymmetric case, they showed that the shear-thinning delayed the appearance of the vortices, but no instability was found in the non-axisymmetric case.

Khali, Nebbali, and Bouhadef (2013) performed a numerical investigation concerning the flow of a Power-Law non-Newtonian fluid flow in a Taylor-Couette geometry by means of a DQ29 lattice Boltzmann model developed from the Bhatangar-Gross-Krook (LBGK)

approximation. Two different cases were evaluated: counter and co-rotating cylinders while the end walls are held at rest. The code was validated against an analytical solution of azimuthal velocity and an available literature database. It was observed that in the counter-rotating case the increasing of the inner cylinder velocity tends to increase the vorticity for the shear-thinning fluids, while that for shear-thickening its influence is lowered. Moreover, in the co-rotating case, the increasing of the inner cylinder velocity favors the number of vortices cells for shear-thinning fluids, while that for shear-thickening fluids it leads to a higher stability.

Finally, Table 5 summarizes the key features of various studies concerned with viscometry in both experimental and numerical counterpoints. For instance, Nguyen and Boger (1985) proposed the vane method as an alternative for measuring the yield stress. By means of a four-blade vane and assuming that the stress is uniformly distributed on a cylindrical sheared surface, thus computing the yield stress from a maximum torque and vane dimensions using the red mud as working fluid. Moreover, the authors proposed two methods of analysis: one assuming an approximate distribution for the end shear, and a second one considering only the wall shear stress. Finally, they proved that the assumption of a uniform stress distribution along a cylindrical yield surface is reasonable for this purpose. Both methods agreed well with the results obtained with the conventional method widely employed.

Darby (1985) used the Power-Law approximation to evaluate the error in calculating the shear rate in a Couette viscometer. The author applied the dimensionless forms of the Bingham and Casson fluids constitutive equations to evaluate the error in the shear rate and viscosity computation, which depends on the gap width and the yield stress value. Furthermore, he concluded that the maximum error for the Bingham fluid occurs at the point where the stress at the outer cylinder coincides with the yield stress, while for Casson fluids it shifts to slightly higher stress levels as the gap increases. Also, the error in the viscosity is lower than that in the shear rate due to the shear-thinning nature of the fluids. Finally, he concluded that the approximation leads to a reasonably accurate evaluation of the shear rate.

In a follow-up study, Nguyen and Boger (1987) proposed a two-step procedure in order to obtain the shear stress-shear rate curves from the torque-angular velocity curves in concentric cylinders' rheometers. Thus, they employed the Casson constitutive equation in order to proceed a numerical analysis of the errors embedded in the using of different equations to obtain the shear rate values in two cases: partially sheared and fully sheared flows. Finally, they performed some tests to stipulate the errors when the assumption of time-independent yield stress fluid is used to characterize thixotropic fluids.

TABLE 5 - SOME VISCOMETRY STUDIES CONCERNING DIFFERENT FLUID MODELS.

continue

Authors	Year	Approaches	Fluid model	Real fluid	k (ratio)	Comments
Nguyen and Boger	1983	Experimental	Several	Red mud	Several (depending on the vane dimension)	Also, contains a review concerning different vane method papers
Hanks	1983	Numerical	Casson		Several	Only numerical experimentation
Dzuy and Boger	1985	Experimental	Several	Red mud	Several (depending on the vane dimension)	Comparison between different methods to obtain yield stress in vane geometry
Darby	1985	Numerical	Bingham and Casson		Several	Error analysis from using local Power-Law approximation
Nguyen and Boger	1987	Numerical and Experimental	Casson	Red mud	0.88	
Borgia and Spera	1990	Numerical and Experimental	Herschel-Bulkley	Clay slurry	0.11	Shear-rate recovered by Krieger-Elrod-Pawlowski series
Barnes and Carnali	1990	Numerical and Experimental	Power-Law fluid	Clay-in-water suspension and aqueous polymer solution		
Yan and James	1997	Numerical	Herschel-Bulkley, Casson and viscoelastic		0.51	Modeled the viscoelastic fluid as a Maxwell type
Yeow et al.	2000	Numerical	Casson, purely NNF	Synthetic Couette viscometry data, CMC solutions	Several	Compared the results obtained from Tikhonov regularization with experimental database
Saak et al.	2001	Experimental		Cement-based materials	0.92 (concentric cylinder) and 0.5 (vane)	

TABLE 5- SOME VISCOMETRY STUDIES CONCERNING DIFFERENT FLUID MODELS.

continuation

Authors	Year	Approaches	Fluid model	Real fluid	k (ratio)	Comments
Leong and Yeow	2003	Numerical and Experimental		Tomato ketchup, red gum honey, French salad dressing and creamy mayonnaise	Several	Solved Couette inverse problem (with wall sleep) from raw data of other authors using Tikhonov regularization
James et al.	2004	Numerical	Power-Law, Cross model, and Carrier-Yasuda	2% Keltrol solution, 2% Benecel solution, orange juice, and chicken soup	Eccentric	Finite difference solution
Yeow et al.	2004	Numerical		Blood, bentonite suspensions and CMC solutions	Several (narrow gaps)	Solved Couette inverse problem (with wall sleep) from raw data of other authors using Tikhonov regularization
Ancey	2005	Numerical	Casson	Commercial hair gel (Baudez et al., 2004) and granular suspensions (Ancey, 2001)	0.51 and 0.24 (Baudez et al., 2004) and 0.3 (Ancey, 2001)	The author developed the wavelet-vaguelette decomposition in order to solve the Couette inverse problem
Kelessidis and Maglione	2006	Experimental	Casson and Robertson-Stiff	Bentonite Suspensions	0.936	
Estellé et al.	2008	Numerical	Bingham	Tomato ketchup and bentonite suspensions	0.96, 0.50 and 0.33	
Kelessidis and Maglione	2008	Numerical	Herschel-Bulkley	Several	Several (narrow gaps)	

TABLE 5- SOME VISCOMETRY STUDIES CONCERNING DIFFERENT FLUID MODELS.

continuation

Authors	**Year**	**Approaches**	**Fluid model**	**Real fluid**	**k (ratio)**	**Comments**
Ovarlez et al.	2008	Experimental	Herschel-Bulkley	Dense emulsions	0.68	
Chatzmina et al.	2009	Numerical	Herschel-Bulkley		0.833 and 0.952	
Ahuja and Singh	2009	Numerical and Experimental	Stokesian dynamics	PMMA (Polymethylmethacrylate) particles and water-glycerol	0.876	Wall slip velocity measurements with smooth and serrated walls
Coussot et al.	2009	Experimental	Herschel-Bulkley	Carbopol solution (hair gel)	0.69	Compared the results with a cone and plate rheometer
Potanin	2010	Numerical	Casson and Thixotropic models	Toothpastes	0.51	
Kelessidis et al.	2010	Experimental	Herschel-Bulkley	Water-glycerol solution (Newtonian) and water-bentonite suspension (non-Newtonian)	0.94	End-effect analysis
Laskar and Bhattacharjee	2011	Experimental	Bingham	Concrete	0.454	Vane method, including bottom and top resistance

TABLE 5- SOME VISCOMETRY STUDIES CONCERNING DIFFERENT FLUID MODELS.

conclusion

Authors	Year	Approaches	Fluid model	Real fluid	k (ratio)	Comments
Koos et al.	2012	Experimental		Nylon, polystyrene, and SAN (styrene acrylonitrile) water suspensions	0.834	Rough and smooth wall
Ihle et al.	2013	Experimental	Bingham	Copper concentrates	0.44	Particle migration and loading speed and times influence
Konijin et al.	2014	Experimental	Power-Law	Glycerine with solid spherical DynoAdd particles	0.88	
Marchesini et al.	2015	Numerical and Experimental	SMD function	Water-based Carbopol dispersions	0.941	Smooth, grooved and vane-in-cup geometries were applied in experiments
Wallevik et al.	2015	Numerical and Experimental	Bingham and Herschel-Bulkley	Vegetable oil and Cement-based materials	0.922(a), 0.576(b) and 0.922(c)	Smooth wall - (a) and (b) and sandblast wall (c)
Heirman et al.	2008 (a) and 2009 (b)	Numerical and Experimental	Bingham and Herschel-Bulkley	Self-compacting concrete	0.690	Mineral additions and chemical admixtures were used in (b)

Barnes and Canali (1990) performed a numerical simulation of the vane-in-cup rheometer geometry and compared the results with the conventional bob-in-cup (circular Couette) geometry, thus showing that for a sufficiently Power-Law fluid (index less than 0.5) the assumption of the fluid trapped between the vane blades acting as a solid cylinder is valid. Furthermore, experimental tests with two different fluids: 5.5% sodium carboxymethylcellulose (CMC) solution and a 4.2% Veegum PRO clay suspension were carried out. Even though both fluids were thought to have yield stress, the results showed that there was an absence of a true

yield stress. Both fluids were compared with the results of the vane-in-cup and bob-in-cup geometries and showed equivalent rheometric curves at very low shear rates, but a loss of viscosity was found for both fluids for larger shear rates, which was faster in the bob-in-cup case. Finally, the authors assigned this loss to the fact that there was an apparent slip due to the formation of a thixotropic layer at the bob and vane surfaces.

Snabre and Mills (1999) presented a Kelvin Voigt model (BITBOL and MILLS, 1984) to describe the deformation and stable orientation of a viscoelastic particle in a simple shear flow. Thus, by relating the maximum packing concentration of the suspension they made use of a viscosity law for concentrated suspensions of hard particles. The rheological law described the viscosity of viscoelastic suspensions such as red cells and granted information about the non-linear viscoelastic properties of the fluid.

Yeow et al. (2000) solved the Couette inverse problem by means of the Tikhonov regularization. They demonstrated that the method is not dependent on the small gap assumption and is also applied to yield stress fluids. Hence, by solving a synthetic Couette viscometry data (using the Casson constitutive equation) and using the torque-velocity curves from CMC (carboxymethyl cellulose) solution and mineral suspension (SCA330) found in the open literature, the authors proved that the Tikhonov regularization is suitable for solving the Couette inverse problem independently of the radius gap and the presence of a yield stress. When comparing the curves obtained by the method and the experimental data a good agreement was found.

Saak et al. (2001) compared the measurements of wall slip on the yield stress and modulus of cement paste through a rotational rheometer with smooth-walled concentric cylinders and a vane. Also, they showed that the use of vane prevented the wall slip from appearing. The slip layer, which occurred in the smooth-walled surface cylinders, developed when the shear stress approached the yield point. Finally, oscillatory tests were conducted for both geometries and they showed good agreement with the literature at a stress below the yield point.

Similarly, Yeow et al., (2004) applied Tikhonov regularization to obtain the shear stress and shear rate curves from raw data from elsewhere considering the slip velocity in narrow-gap rheometers. They compared the results obtained via the regularization with the curves from the other authors and obtained a good concordance between the counterparts, proving that the Tikhonov is also a reliable method for processing Couette viscometry when slip is present.

James et al. (2004) described a numerical method to determine the apparent viscosity of shear-thinning liquids on wide-gap double concentric cylinders geometries. The authors explained the errors associated when the narrow-gap approach is used in a wide-gap geometry and by means of a numerical procedure which gives the best agreement between experimental torque data and the numerical simplified simulation. The model was validated against two shear-thinning liquids with no particles and then presented results for orange juice and chicken soup.

Ancey (2005) employed a numerical method, called wavelet-vaguelette decomposition (WVD), which was not being used in rheometry techniques so far. In order to solve the Couette inverse problem and derive the flow curve of shear stress in function of shear-rates, this method is more accurate and presents faster convergence. Furthermore, the author used raw data from other data to compare the solution of the Couette inverse problem with Tikhonov method. Also, according to Ancey, no prior knowledge of the shear rate characteristics is needed.

Kelessidis and Maglione (2006), similarly to Joye (2003), performed a numerical and an experimental work in order to obtain the best way to describe some aqueous bentonite solution using the Casson and Robertson-Stiff fluid models. The authors used some sample raw rheological data found in the literature and also performed some experiments in a small-gap Couette geometry using different bentonite suspensions. Moreover, the authors performed the non-linear regression data to obtain the stress-shear rate curves using true (analytical) shear rates and Newtonian shear rates for both methods. Finally, the results fitted well the experimental data and it was observed that true shear rates were always higher than the Newtonian shear rates for both methods, where the fitted rheological model parameters presented small differences between the two different shear rates. However, the true (or analytical) shear rates should be applied whenever it is possible.

Kelessidis and Maglione (2008) presented a methodology to solve the Couette inverse problem of a Herschel-Bulkley fluid, so enabling the computation of the three model parameters and the true shear-rates. They used data found in the literature of narrow-gap (oil field rheometer) for different fluids, thereby comparing the errors with the Newtonian fluid approach and realizing that the computed Herschel-Bulkley shear-rates are higher than the Newtonian ones. The methodology was compared with some others found in the literature (power series approximation and Tikhonov regularization) with nearly identical results.

Ovarlez et al. (2008) studied the behavior of dense emulsions flows for four different oils droplet sizes: 0.3, 1, 6.5 and 40 μm. Hence, they carried out some experiments in a wide-

gap Couette geometry and coupled the macroscopic rheometric experiments and local velocity and concentration measurements through MRI (magnetic resonance imaging) techniques. Moreover, in order to minimize some undesirable effects, they carried out some experiments to make sure that there was no particle migration and wall slip effects. Finally, they found that all the emulsions behaviors were consistent with the Herschel-Bulkley model.

Heirman et al. (2008) studied the shear thickening flow behavior of powder type self-compacting concrete (SCC) through a wide-gap (k = 0.69) Taylor-Couette geometry. In order to obtain the flow curve $\tau(\dot{\gamma})$ from torque measurements by means of the integration method for the Bingham and Herschel-Bulkley fluids the Couette inverse problem for Herschel-Bulkley fluid was approached by decoupling the flow resistance and the Power-Law behavior after exceeding the flow resistance the integration was validated by experimental verification, despite the fact that the Herschel-Bulkley fluid flow does not have an analytical solution. Similarly, the authors (2009) studied the influence of mineral additions and chemical admixtures (chemicals used to aid the properties of concrete or cement) on the shear thickening flow behavior of powder type self-compacting concrete (SCC) and found that the addition of mineral and chemical admixtures modify the intensity of shear thickening.

Chatzimina et al. (2009) studied the effect of the errors introduced when the Newtonian fluid and the Power-Law non-Newtonian fluid assumptions were used to calculate the wall shear-rate of the rotating inner cylinder in a Couette geometry. They found that the errors, when compared to the numerical (and analytical in some cases) solution of a Herschel-Bulkley fluid flow, were greater the wider was the gap between the cylinders. The errors were proved to be dependent also on the power index (n) and the yield stress.

Coussot et al. (2009) measured the flow characteristics of a Carbopol gel using an MRI velocimetry for a wide range of shear rates. Those measurements revealed an excellent agreement with the measurements made in a cone and plate viscometry, both represented through the Herschel-Bulkley model.

Ahuja and Singh (2009) presented a simple experimental method for measurement of wall-slip velocity in a cylindrical Couette geometry. The authors have used a serrated cup and a serrated rotor to avoid the slip velocity and then realized the tests again with a smooth rotor to compare the results. Two different concentrations of suspensions of PMMA (Polymethyl methacrylate) spheres were used as working fluids and it was found that higher wall slip velocities were observed at higher concentrations, which varies linearly with the shear rate. Also, the authors have performed some Stokesian dynamic simulations in similar conditions to

the experimental tests, which found similar viscosities for both smooth and serrated rotor for low concentration values, but the difference was more significant the higher was the concentration, which is in concordance with the experimental observations.

Kelessidis et al. (2010) realized an experimental and numerical analysis in order to quantify the magnitude of end-effects in oil-field direct indicating viscometers (with a narrow-gap) for Newtonian (water-glycerol) and non-Newtonian (water-bentonite suspension) fluids. Considering the end-effects on the manufacturing rheometers they estimated the errors associated and the embedded correction. Finally, it was detected and additional end-effect from the top section of the bob (inner cylinder), which is higher for non-Newtonian fluids.

Laskar and Bhattacharjee (2011) advanced a mathematical relationship between torque and angular speed in a concrete rheometer with vane geometry. The resistance of the concrete below and above the vane as well as other end effects were evaluated too, thus resulting in an expression that computes the total shear stress during the flow. Besides, an experimental test was carried out using a cement mixture, which behaves like a Bingham fluid, and the curves obtained were evaluated with the expression showing a good agreement with values of yield stress and plastic viscosity obtained elsewhere. Moreover, they showed the importance of taking into account the resistance of the fluid at the top and bottom of the vane geometry.

Koos et al. (2012) performed some experimental measurements of the rheological behavior of some Nylon, polystyrene, and SAN (styrene acrylonitrile) water suspensions at moderate Reynolds and Stoke numbers. Experiments were held on a coaxial double cylinder geometry with the smooth and rough wall. Despite prior works had shown that the shear stress changes non-linearly with the shear rate, in the range of conditions that the authors performed the tests, it was observed a linear dependence of them on both smooth and rough walls, despite that the effective viscosity is larger for rough walls. In addition, the authors also performed some measurements of the wall slip for the smooth wall geometry.

Ihle et al. (2013) performed an experimental work using two copper sulfides concentrate samples as working fluid. Also, the cylinder wall had a sand-blasted surface to prevent slip. The authors carried out two different test types: the generation of angular velocity ramp and individual torque measurements with constant angular velocities. They noticed that hydrodynamic segregation and angular velocities played a more significant role than the sample loading time. Furthermore, the impact of the sample loading time may have a greater importance for small loading times.

Konijn et al. (2014) realized experiments with cylindrical rheometers using a nearly-buoyant suspension (glycerin and DynoAdd spherical particles). They studied the effects of (i) solid fraction, (ii) diameter of the solid spherical particles, (iii) viscosity of the suspending liquid and (iv) shear rate on the suspension viscosity. The suspension was well-described by the Power-Law fluid. Finally, they concluded that the suspension viscosity is not a function of the solid fraction only, but also depends on shear-rate, particle diameter and viscosity of the suspending liquid.

Wallevik et al. (2015) evaluated the errors that arise when some mistakes are made on the regression of the raw data from the rheometers. The authors discussed some errors occurring by using equations for Newtonian fluids when analyzing data from non-Newtonian fluid (vegetable oil) and using the small-gap interpretation into a wide-gap of a coaxial double cylinder rheometer. The errors of an incorrect rheological model, thixotropy, plug flow appearance and particle migration were also evaluated. Finally, the authors discussed the use of numerical simulations to obtain the rheological parameters of cement-based materials.

Marchesini et al. (2015) performed experimental and numerical tests using Carbopol dispersions as working fluid in a coaxial double concentric cylinder rheometer and compared the results of both counterparts for three different arrangements of cylinders' walls: smooth walls, grooved walls, and vane-in-cup geometry. In the experimental tests, where the outer cylinder rotated while the torque needed to hold still the inner cylinder was measured the grooved wall presented better results than the other geometries because it performed better in preventing the wall slip condition, which occurs in lower shear stresses. Furthermore, the bidimensional numerical simulations were carried out in a commercial CFD software using the finite volume technique and presented good agreement in higher shear-rates, while, contrary to a prior work (BUSCALL, MCGOWAN and MORTON-JONES, 1993), it was found that the wall slip was higher in the outer cylinder surface for lower shear-rates. Finally, numerical results showed that the kinematics was more affected in the vane-in-cup geometry which could lead to experimental errors in viscosity measurements.

Finally, one can note that, among all these works found in the literature, there is not a single one concerning the study of Taylor-Couette flows with fabric-water suspensions as working fluids. This arrangement is an emulation of the complex geometry that occurs on top-loading household washing machines. Moreover, there are no studies aimed at modeling the fabric-water suspension as non-Newtonian fluid either. These characters, which are some of the objectives of the present work, give to this thesis an unprecedented nature.

1.3 OBJECTIVES AND METHODOLOGY

The key objective of the present work is to understand the fluid flow between two concentric cylinders, using as the working fluid a mixture of fabric and water, which is treated as a non-Newtonian fluid (suspension) and is different from the other authors works found in the literature. Moreover, the specific objectives as follows:

- Development of a computational code based on the finite volume approach, in 2 and 3 dimensions, to predict the fluid flow of NNF on Taylor-Couette geometries, comparing the results with numerical and experimental datasets;
- Design and construct an experimental facility to gather a reliable database for water and fabric-water flows in terms of power and torque values for different rotation profiles and amounts of fabric;
- Obtain the shear stress and shear rate curves of the fabric-water suspension by testing different NNF models by means of rheometry techniques applied to the experimental database;
- Verify the hypothesis of generalizing the whole fluid suspension as a homogeneous non-Newtonian and non-thixotropic mixture. In other words, the time dependence of the fluid thermophysical properties are negligible;
- Conduct experimental tests in periodic regime – similar agitation profiles used in actual washing machines – and compare the results with the ones obtained from the steady-state approach.

1.4 THESIS STRUCTURE

This thesis is organized as follows: Chapter 1 introduced the main objectives and the methodology of the present work, as well as a comprehensive literature review. Chapter 2, in turn, introduces the theoretical fundamentals regarding the flow of Newtonian and non-Newtonian fluids confined between two concentric cylinders, as well as the rheometry techniques that have been applied in the experimental work. Chapter 3 depicts the numerical methodology used to solve the model and the structure of the homemade finite-volume code. Chapter 4 presents the experimental work, whereas Chapter 5 depicts the code-verification for both Newtonian and non-Newtonian fluids flows, including (but not limited to) comparisons

between the experimental and numerical results, and numerical experimentation concerning yield stress fluids and periodic unsteady flows. Finally, Chapter 6 summarizes the achievements of the present thesis and provides the reader with some recommendations for future endeavors in the field.

2 THEORETICAL BACKGROUND

In this chapter, the first-principles are introduced with the purpose of modeling the flow of both Newtonian and non-Newtonian fluids in cylindrical coordinates. In addition, some key generalized empirical fluid models are presented. Finally, the physical domain and the mathematical model adopted in this thesis are discussed.

2.1 FLUID MODEL

A fluid is called Newtonian when the shear stress magnitude (τ) is directly proportional to its shear rate, as follows in tensor notation:

$$\bar{\bar{\tau}} = \mu\bar{\bar{\dot{\gamma}}} \tag{2.1}$$

where the dynamic viscosity (μ) is a thermophysical property of the fluid that relates the shear stress to the shear rate. Newtonian fluids examples include water, air, and glycerin.

The viscosity of the non-Newtonian fluid differs from the Newtonian one as it is dependent on the shear rate. Unlike a Newtonian fluid, the relation between the shear stress and the shear rate is not linear and can be even time-dependent (thixotropic fluids). In general, the behavior of a non-Newtonian fluid can be described through an apparent viscosity (η), also known as rheological dynamic viscosity, for the Generalized Newtonian Fluid models (which can describe the non-Newtonian fluid behavior through a modification in the Newtonian fluid constitutive equation),

$$\bar{\bar{\tau}} = \eta\bar{\bar{\dot{\gamma}}} \tag{2.2}$$

The curve of the shear stress and viscosity as a function of the shear rate for a Newtonian fluid and different non-Newtonian fluid models is illustrated in Figure 10. One can note in Figure 10 three different behaviors for the non-Newtonian fluids: (i) shear-thinning Power-Law fluid, (ii) shear-thickening Power-Law fluid, and (iii) yield stress Bingham fluid. Both Power-Law-fluid and Bingham fluid are empirical models applied to the so-called Generalized Newtonian Fluid, which is a well-known rheological model. It should also be mentioned that

the Generalized Newtonian Fluid model has been extensively used to model non-Newtonian fluids in engineering complex problems (BIRD, ARMSTRONG and HASSAGER, 1987).

FIGURE 10 - PROPERTIES BEHAVIORS OF NEWTONIANS AND SOME NON-NEWTONIAN FLUIDS.

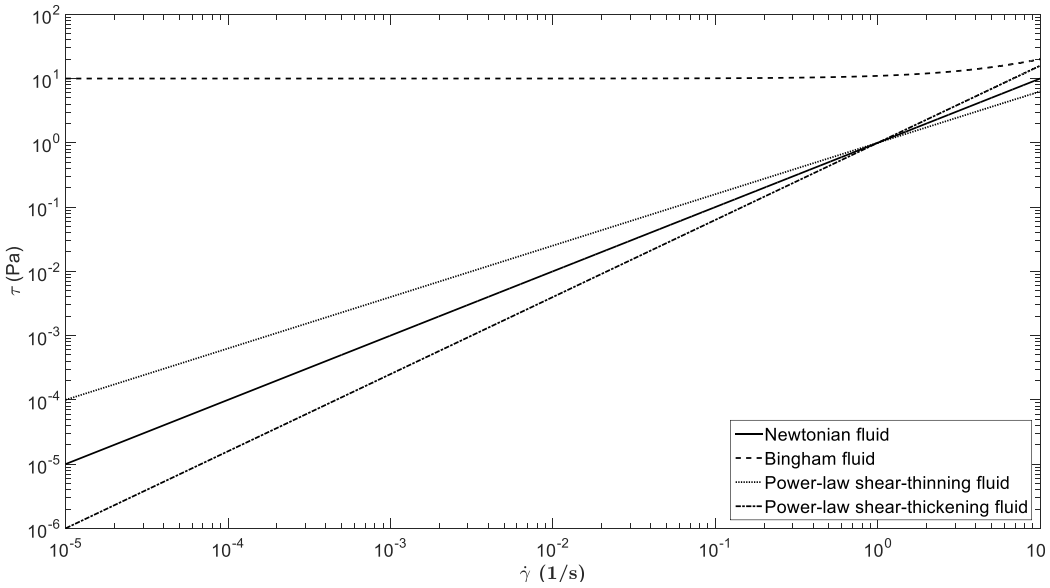

(A)

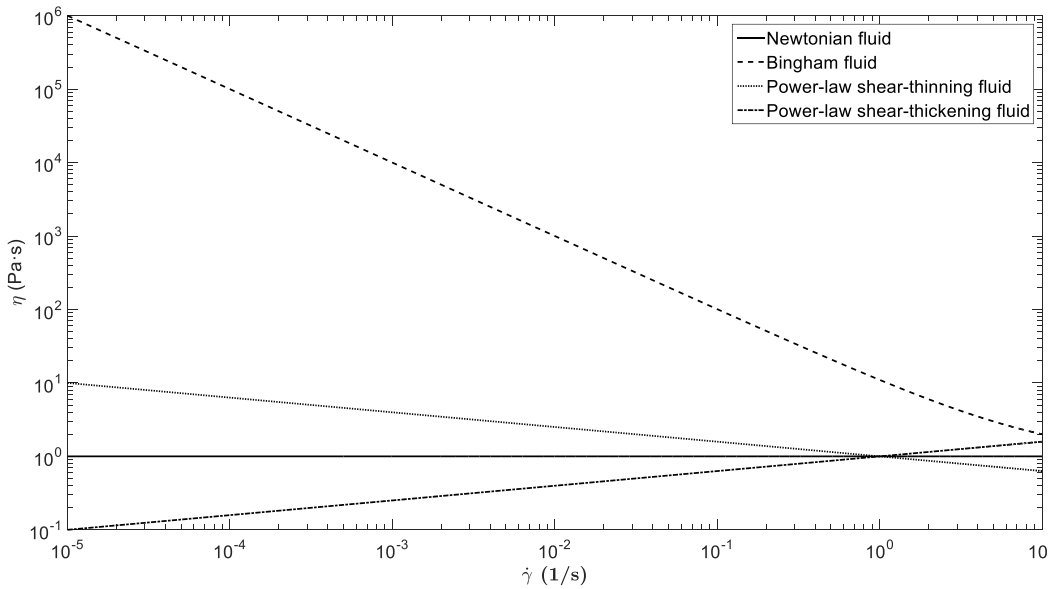

(B)

(A) SHEAR STRESS AND (B) APPARENT VISCOSITY. M = 1 PA·S, N = 0.8 (SHEAR-THINNING FLUID), N = 1.2 (SHEAR-THICKENING FLUID) AND T0 = 10 PA.

The Generalized Newtonian fluid (GNF) is a simple model used to describe a collection of non-Newtonian fluids by means of a constitutive equation based on a generalized form of the Newtonian fluid model. Even though the GNF cannot characterize the time-dependent aspects of the fluid, it is widely used in engineering because leads to reliable results.

In the model, the apparent viscosity (η) is a scalar dependent on the shear rate tensor $\bar{\bar{\dot{\gamma}}}$, especially on the tensor independent combinations, also known as invariants, (SCHOWALTER, 1978), as follows:

$$\mathrm{I} = \sum_{i} \dot{\gamma}_{ii} = \mathrm{tr}\left(\bar{\bar{\dot{\gamma}}}\right) \tag{2.3}$$

$$\mathrm{II} = \sum_{i}\sum_{j} \dot{\gamma}_{ij}\dot{\gamma}_{ji} = \frac{1}{2}\left[\mathrm{tr}\left(\bar{\bar{\dot{\gamma}}}^{2}\right) - \left(\mathrm{tr}\left(\bar{\bar{\dot{\gamma}}}\right)\right)^{2}\right] \tag{2.4}$$

$$\mathrm{III} = \sum_{i}\sum_{j}\sum_{k} \dot{\gamma}_{ij}\dot{\gamma}_{jk}\dot{\gamma}_{ki} = \det\left(\bar{\bar{\dot{\gamma}}}\right) \tag{2.5}$$

where i, j and k denote the three-dimensional coordinates indices.

For an incompressible fluid and steady-state shear flow, the apparent viscosity is dependent only on the second invariant (BIRD, ARMSTRONG and HASSAGER, 1987). Thus, the magnitude of the tensor is reduced to:

$$|\dot{\gamma}| = \sqrt{\frac{1}{2}\sum_{i}\sum_{j} \dot{\gamma}_{ij}\dot{\gamma}_{ji}} = \sqrt{\frac{1}{2}\mathrm{II}} \tag{2.6}$$

Some of the empirical viscosity models used to describe the behavior of the apparent viscosity $\eta(\dot{\gamma})$ curve, which is used in the present work, are introduced as follows:

2.2 POWER-LAW MODEL

The Power-Law model, developed by Oswald (1925) and de Waele (1923), is the most well-known and widely used non-Newtonian empirical viscosity model in engineering works (BIRD, ARMSTRONG and HASSAGER, 1987). The model can be described by the following constitutive equation:

$$\bar{\bar{\tau}} = (m|\dot{\gamma}|^{n-1})\bar{\bar{\dot{\gamma}}} \tag{2.7}$$

where m represents the flow consistency index ($Pa \cdot s^{n}$), and n represents the Power-Law index (dimensionless). One can note that when n = 1 and m = μ (Newtonian dynamic viscosity) the

model describes the Newtonian fluid. However, if n < 1, the fluid is called shear-thinning (or pseudoplastic) and if n > 1, the fluid is called shear-thickening (or dilatant).

2.3 YIELD STRESS FLUIDS

Yield stress fluids, also known as viscoplastic fluid, are characterized by the presence of a yield stress τ_0, below which there is no deformation of the fluid flow (BARNES, 1999). Above the yield stress, the fluid will deform according to different constitutive equations (MITSOULIS, 2007). The most well-spread constitutive equations concerning yield stress fluids are the ones due to Bingham (1916), (1922) (mudflow in drilling engineering and in the handling of slurries), Herschel-Bulkley (1926) (complex fluids, like self-compacting concrete) and Casson (1959) (printing inks, drilling fluids). These models are respectively as follows:

a) Bingham Fluid

$$\begin{cases} \bar{\bar{\dot{\gamma}}} = 0 & (|\tau| \leq \tau_0) \\ \bar{\bar{\tau}} = \left(\mu + \frac{\tau_0}{|\dot{\gamma}|}\right)\bar{\bar{\dot{\gamma}}} & (|\tau| > \tau_0) \end{cases} \tag{2.8}$$

b) Herschel-Bulkley Fluid

$$\begin{cases} \bar{\bar{\dot{\gamma}}} = 0 & (|\tau| \leq \tau_0) \\ \bar{\bar{\tau}} = \left(m|\dot{\gamma}|^{n-1} + \frac{\tau_0}{|\dot{\gamma}|}\right)\bar{\bar{\dot{\gamma}}} & (|\tau| > \tau_0) \end{cases} \tag{2.9}$$

c) Casson Fluid

$$\begin{cases} \bar{\bar{\dot{\gamma}}} = 0 & (|\tau| \leq \tau_0) \\ \bar{\bar{\tau}} = \left(\sqrt{\mu} + \sqrt{\frac{\tau_0}{|\dot{\gamma}|}}\right)^2 \bar{\bar{\dot{\gamma}}} & (|\tau| > \tau_0) \end{cases} \tag{2.10}$$

Another viscosity model that has been used, mostly for cement slurries and drilling fluids, is the Robertson-Stiff fluid model, which is also a three-parameter model and is represented as follows (ROBERTSON and STIFF, 1976) (bentonite suspensions, drilling fluids, and cement slurries):

$$\bar{\bar{\tau}} = m\left(\dot{\gamma}_0 + \bar{\bar{\dot{\gamma}}}\right)^n \tag{2.11}$$

where $\dot{\gamma}_0$ is a shear rate correction factor (s^{-1}).

The behavior of the shear stress (a) and viscosity (b) related to the shear rate for all the above-mentioned yield stress fluid models are illustrated in Figure 11. One can notice that

despite the Robertson-Stiff fluid does not have a yield stress (τ_0) embedded in its model, the $\dot{\gamma}_0$ parameter can be used to model the yield stress behavior.

FIGURE 11 - YIELD STRESS FLUID BEHAVIOR.

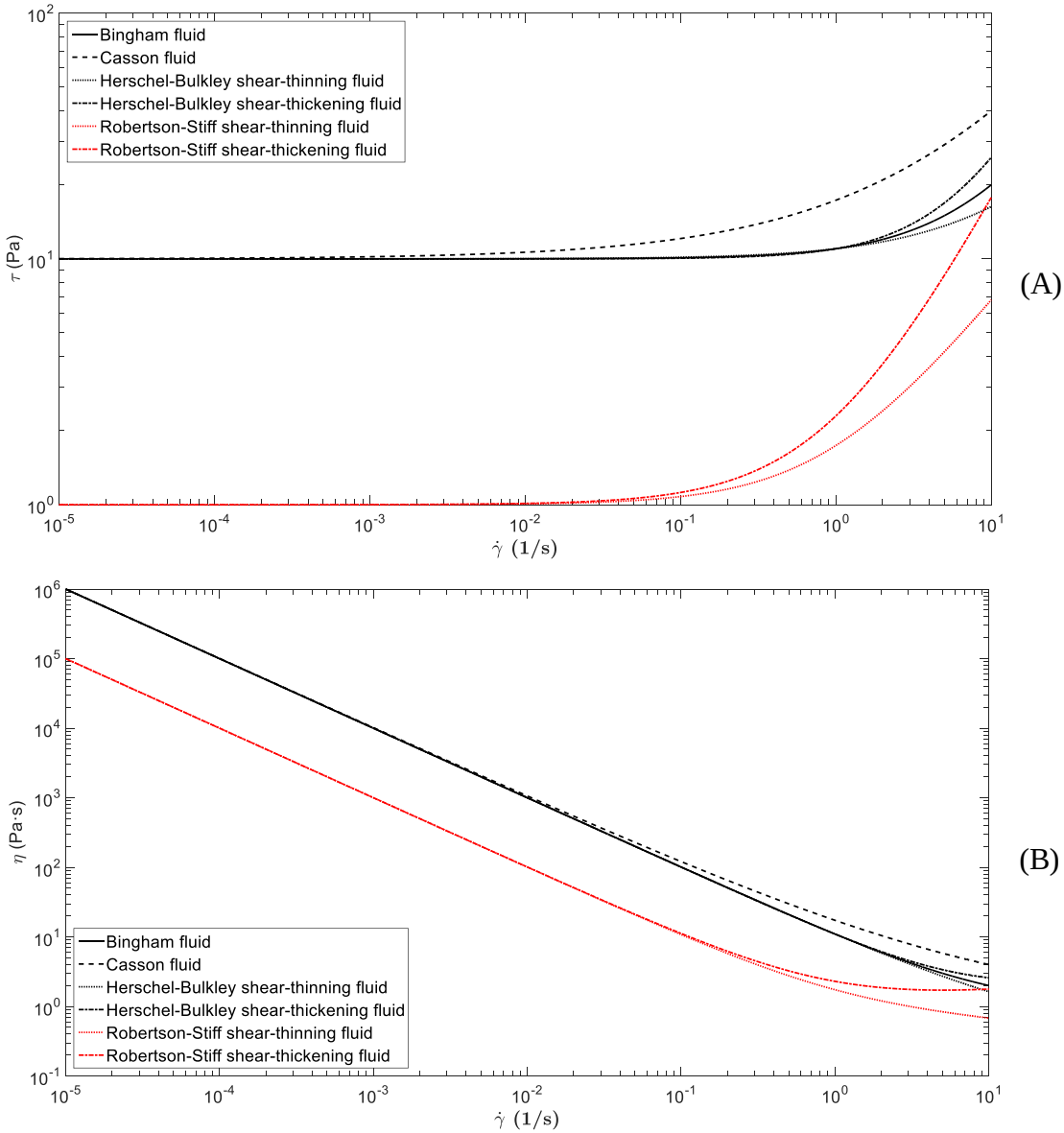

(A) SHEAR STRESS AND (B) APPARENT VISCOSITY. FOR M = M = 1 PA·S, N = 0.8 (SHEAR-THINNING FLUID), N = 1.2 (SHEAR-THICKENING FLUID) AND T0 = 10 PA.

One can also note that, as there is no flow when the shear stress is below yield stress, two different regions take place, the unyielded and the flow region. This discontinuity may lead to numerical problems of convergence when a simulation is conducted. Papanastasiou (1987) proposed a modification in the viscosity of yield stress fluid models to avoid this discontinuity by introducing a parameter K, which controls the exponential growth of the stress

(MITSOULIS, 2007). These modifications applied to the Bingham fluid, Herschel-Bulkley fluid and Casson fluid constitutive equations lead to:

a) Bingham Fluid

$$\bar{\bar{\tau}} = \left(\mu + \frac{\tau_0}{|\dot{\gamma}|}[1 - \exp(-K|\dot{\gamma}|)]\right)\bar{\bar{\dot{\gamma}}} \tag{2.12}$$

b) Herschel-Bulkley Fluid

$$\bar{\bar{\tau}} = \left(m|\dot{\gamma}|^{n-1} + \frac{\tau_0}{|\dot{\gamma}|}[1 - \exp(-K|\dot{\gamma}|)]\right)\bar{\bar{\dot{\gamma}}} \tag{2.13}$$

c) Casson Fluid

$$\bar{\bar{\tau}} = \left(\sqrt{\mu} + \sqrt{\frac{\tau_0}{|\dot{\gamma}|}}\left[1 - \exp\left(-\sqrt{K|\dot{\gamma}|}\right)\right]\right)^2 \bar{\bar{\dot{\gamma}}} \tag{2.14}$$

Hence, the apparent viscosities for the above-mentioned fluid models are given as follows:

a) Bingham Fluid

$$\eta = \mu + \frac{\tau_0}{|\dot{\gamma}|}[1 - \exp(-K|\dot{\gamma}|)] \tag{2.15}$$

b) Herschel-Bulkley Fluid

$$\eta = m|\dot{\gamma}|^{n-1} + \frac{\tau_0}{|\dot{\gamma}|}[1 - \exp(-K|\dot{\gamma}|)] \tag{2.16}$$

c) Casson Fluid

$$\sqrt{\eta} = \sqrt{\mu} + \sqrt{\frac{\tau_0}{|\dot{\gamma}|}}\left[1 - \exp\left(-\sqrt{K|\dot{\gamma}|}\right)\right] \tag{2.17}$$

The behavior of the Papanastasiou-Herschel-Bulkley fluid compared with the Herschel-Bulkley fluid, concerning different values for the K-parameter, are depicted below for the apparent viscosities (Figure 12) and shear stresses (Figure 13) for both shear-thinning and shear-thickening Herschel-Bulkley fluids.

FIGURE 12 - PAPANASTASIOU-HERSCHEL-BULKLEY APPARENT VISCOSITIES BEHAVIORS.

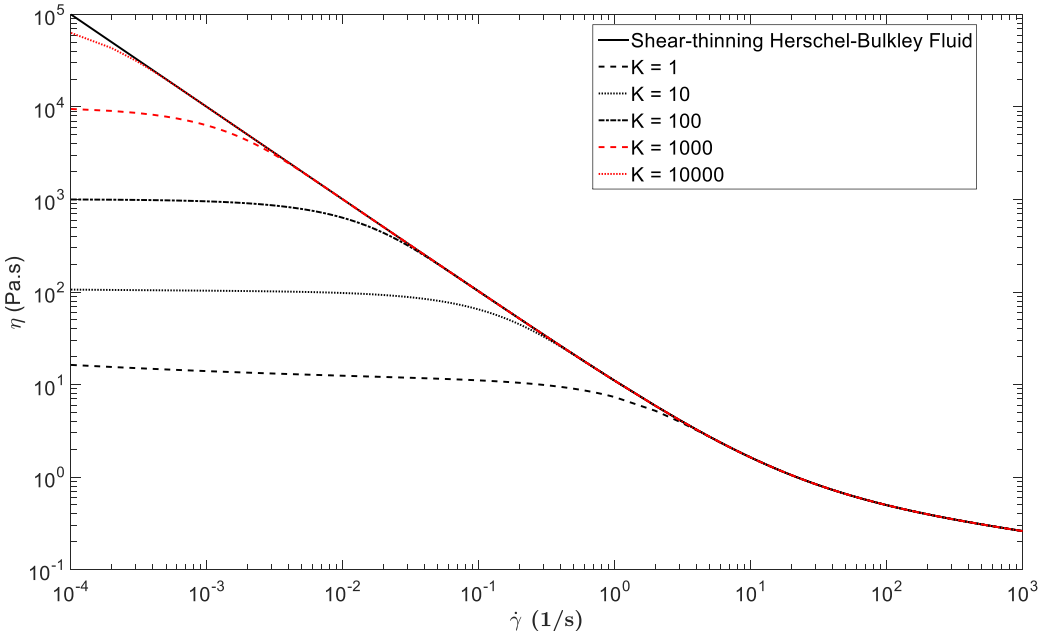

(A)

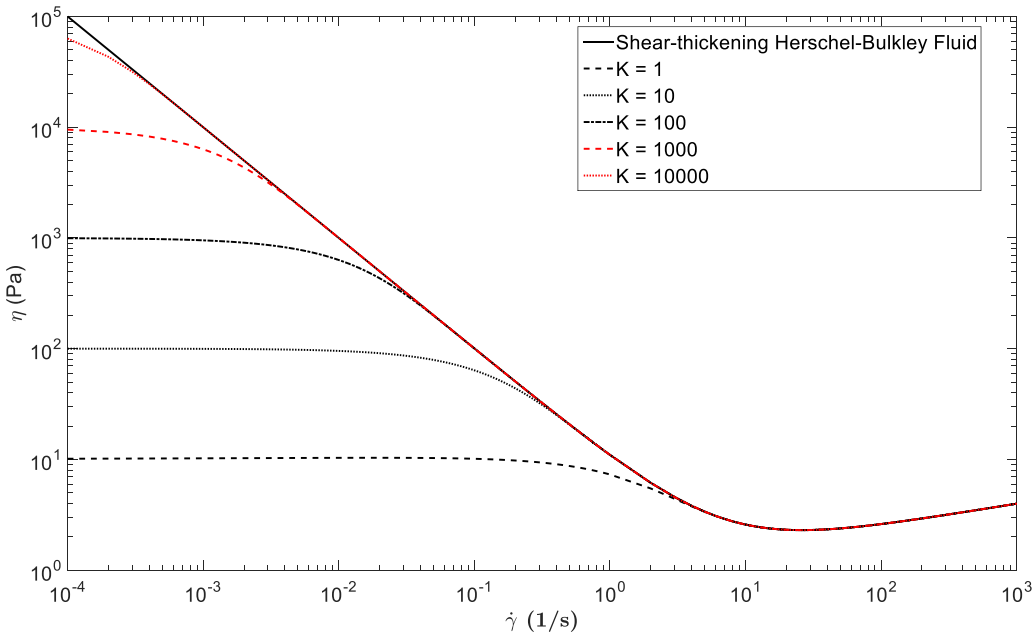

(B)

(A) SHEAR-THINNING AND (B) SHEAR-THICKENING.

FIGURE 13 - PAPANASTASIOU-HERSCHEL-BULKLEY SHEAR STRESS BEHAVIOR.

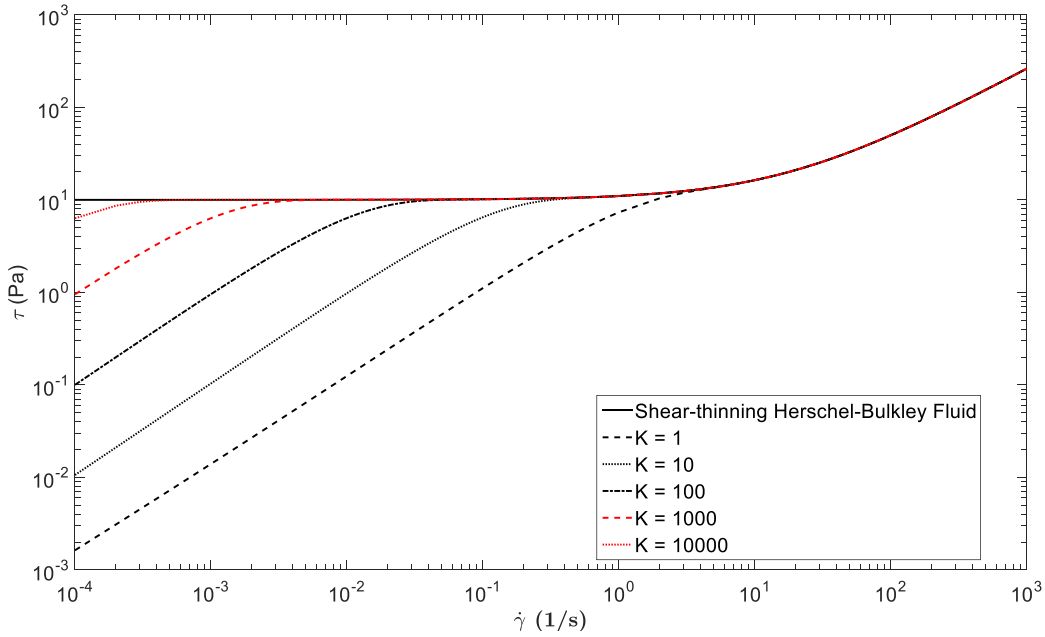

(A)

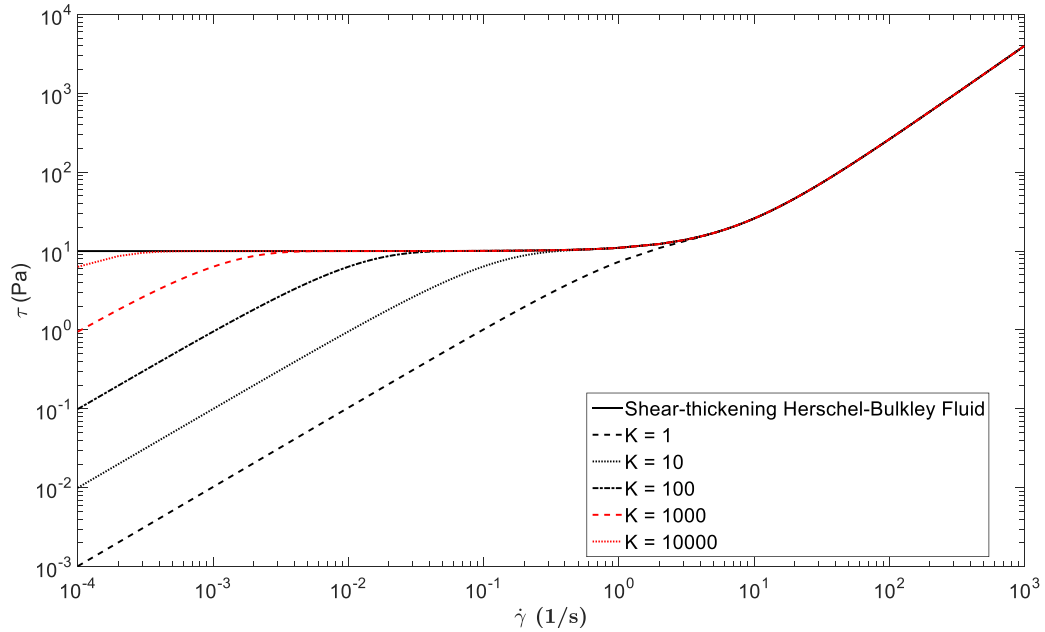

(B)

(A) SHEAR-THINNING AND (B) SHEAR-THICKENING.

The K-parameter can be adopted for adjusting the fluid behavior for very low shear rates domain, or else to enable a faster convergence for numerical simulations. One can note that for high the K-parameters the model approaches the *original* yield stress fluid

2.4 GOVERNING EQUATIONS

The rotational flows between two concentric cylinders are ruled by the governing equations obtained through mass and momentum balances in a control volume (in cylindrical

coordinates). Given the advective-diffusive nature of the governing equations, they are second-order partial differential equations, thus requiring two boundary conditions in each direction (θ, r, and z).

There are four variables (v_θ v_r, v_z, and p) and three momentum equations, which must be coupled with the mass conservation equation (also known as the continuity equation) in order to obtain the pressure field of the flow. The continuity equation and the momentum conservation equations, in all three cylindrical directions (θ, r, and z), are respectively as follows:

$$\frac{\partial \rho}{\partial t} + \frac{1}{r}\frac{\partial(\rho r v_r)}{\partial r} + \frac{1}{r}\frac{\partial(\rho v_\theta)}{\partial \theta} + \frac{\partial(\rho v_z)}{\partial z} = 0 \tag{2.18}$$

$$\begin{aligned}\frac{\partial(\rho v_\theta)}{\partial t} + \frac{\partial(\rho v_r v_\theta)}{\partial r} + \frac{1}{r}\frac{\partial(\rho v_\theta v_\theta)}{\partial \theta} + \frac{\rho v_r v_\theta}{r} + \frac{\partial(\rho v_z v_\theta)}{\partial z} \\ = -\left[\frac{1}{r}\frac{\partial(\tau_{\theta\theta})}{\partial \theta} + \frac{1}{r^2}\frac{\partial(r^2\tau_{r\theta})}{\partial r} + \frac{\partial(\tau_{z\theta})}{\partial z} + \frac{\tau_{\theta r} - \tau_{r\theta}}{r}\right] \\ - \frac{1}{r}\frac{\partial p}{\partial \theta} + \rho g_\theta\end{aligned} \tag{2.19}$$

$$\begin{aligned}\frac{\partial(\rho v_r)}{\partial t} + \frac{\partial(\rho v_r v_r)}{\partial r} + \frac{1}{r}\frac{\partial(\rho v_\theta v_r)}{\partial \theta} - \frac{\rho {v_\theta}^2}{r} + \frac{\partial(\rho v_z v_r)}{\partial z} \\ = -\left[\frac{1}{r}\frac{\partial(\tau_{\theta r})}{\partial \theta} + \frac{1}{r}\frac{\partial(r\tau_{rr})}{\partial r} + \frac{\partial(\tau_{zr})}{\partial z} - \frac{\tau_{\theta\theta}}{r}\right] - \frac{\partial p}{\partial r} + \rho g_r\end{aligned} \tag{2.20}$$

$$\begin{aligned}\frac{\partial(\rho v_z)}{\partial t} + \frac{\partial(\rho v_r v_z)}{\partial r} + \frac{1}{r}\frac{\partial(\rho v_\theta v_z)}{\partial \theta} + \frac{\partial(\rho v_z v_z)}{\partial z} \\ = -\left[\frac{1}{r}\frac{\partial(\tau_{\theta z})}{\partial \theta} + \frac{1}{r}\frac{\partial(r\tau_{rz})}{\partial r} + \frac{\partial(\tau_{zz})}{\partial z}\right] - \frac{\partial p}{\partial z} + \rho g_z\end{aligned} \tag{2.21}$$

For both Newtonian and non-Newtonian fluids ($\bar{\bar{\tau}} = \eta\bar{\bar{\dot{\gamma}}}$), the stress components are related with the shear rates components (BIRD, ARMSTRONG and HASSAGER, 1987) as follows:

$$\dot{\gamma}_{\theta\theta} = 2\left(\frac{1}{r}\frac{\partial v_\theta}{\partial \theta} + \frac{v_r}{r}\right) \tag{2.22}$$

$$\dot{\gamma}_{rr} = 2\frac{\partial v_r}{\partial r} \tag{2.23}$$

$$\dot{\gamma}_{zz} = 2\frac{\partial v_z}{\partial z} \tag{2.24}$$

$$\dot{\gamma}_{r\theta} = \dot{\gamma}_{\theta r} = r\frac{\partial}{\partial r}\left(\frac{v_\theta}{r}\right) + \frac{1}{r}\frac{\partial v_r}{\partial \theta} \tag{2.25}$$

$$\dot{\gamma}_{\theta z} = \dot{\gamma}_{z\theta} = \frac{1}{r}\frac{\partial v_z}{\partial \theta} + \frac{\partial v_\theta}{\partial z} \tag{2.26}$$

$$\dot{\gamma}_{zr} = \dot{\gamma}_{rz} = \frac{\partial v_r}{\partial z} + \frac{\partial v_z}{\partial r} \tag{2.27}$$

Stokes proposed that stress components for a Newtonian fluid flow could be described from:

$$\tau_{rr} = -p + 2\mu\frac{\partial v_r}{\partial r} \tag{2.28}$$

$$\tau_{\theta\theta} = -p + 2\mu\left(\frac{1}{r}\frac{\partial v_\theta}{\partial \theta} + \frac{v_r}{r}\right) \tag{2.29}$$

$$\tau_{zz} = -p + 2\mu\frac{\partial v_z}{\partial z} \tag{2.30}$$

$$\tau_{r\theta} = \tau_{\theta r} = \mu\left[r\frac{\partial}{\partial r}\left(\frac{v_\theta}{r}\right) + \frac{1}{r}\frac{\partial v_r}{\partial \theta}\right] \tag{2.31}$$

$$\tau_{\theta z} = \tau_{z\theta} = \mu\left[\frac{1}{r}\frac{\partial v_z}{\partial \theta} + \frac{\partial v_\theta}{\partial z}\right] \tag{2.32}$$

$$\tau_{zr} = \tau_{rz} = \mu\left[\frac{\partial v_r}{\partial z} + \frac{\partial v_z}{\partial r}\right] \tag{2.33}$$

Introducing the above Equations (2.28 to 2.33) into the equations from (2.19) to (2.21), and assuming an incompressible flow with constant viscosities, the so-called Navier-Stokes equations are retrieved:

$$\begin{aligned}\frac{\partial(\rho v_\theta)}{\partial t} + \frac{\partial(\rho v_r v_\theta)}{\partial r} + \frac{1}{r}\frac{\partial(\rho v_\theta v_\theta)}{\partial \theta} + \frac{\rho v_r v_\theta}{r} + \frac{\partial(\rho v_z v_\theta)}{\partial z} \\ = \mu\left[\frac{1}{r^2}\frac{\partial^2 v_\theta}{\partial \theta^2} + \frac{\partial}{\partial r}\left(\frac{1}{r}\frac{\partial}{\partial r}(r v_\theta)\right) + \frac{\partial^2 v_\theta}{\partial z^2} + \frac{2}{r^2}\frac{\partial v_r}{\partial \theta}\right] \\ - \frac{1}{r}\frac{\partial p}{\partial \theta} + \rho g_\theta\end{aligned} \tag{2.34}$$

$$\frac{\partial(\rho v_r)}{\partial t}+\frac{\partial(\rho v_r v_r)}{\partial r}+\frac{1}{r}\frac{\partial(\rho v_\theta v_r)}{\partial \theta}-\frac{\rho {v_\theta}^2}{r}+\frac{\partial(\rho v_z v_r)}{\partial z}$$
$$=\mu\left[\frac{1}{r^2}\frac{\partial^2 v_r}{\partial \theta^2}+\frac{\partial}{\partial r}\left(\frac{1}{r}\frac{\partial}{\partial r}(r v_r)\right)+\frac{\partial^2 v_r}{\partial z^2}-\frac{2}{r^2}\frac{\partial v_\theta}{\partial \theta}\right]-\frac{\partial p}{\partial r} \tag{2.35}$$
$$+\rho g_r$$

$$\frac{\partial(\rho v_z)}{\partial t}+\frac{\partial(\rho v_r v_z)}{\partial r}+\frac{1}{r}\frac{\partial(\rho v_\theta v_z)}{\partial \theta}+\frac{\partial(\rho v_z v_z)}{\partial z}$$
$$=\mu\left[\frac{1}{r^2}\frac{\partial^2 v_z}{\partial \theta^2}+\frac{1}{r}\frac{\partial}{\partial r}\left(r\frac{\partial v_z}{\partial r}\right)+\frac{\partial^2 v_z}{\partial z^2}\right]-\frac{\partial p}{\partial z}+\rho g_z \tag{2.36}$$

In the same way, regarding a fluid with variable viscosities, e.g. non-Newtonian fluid, the equations above are as follows:

$$\frac{\partial(\rho v_\theta)}{\partial t}+\frac{\partial(\rho v_r v_\theta)}{\partial r}+\frac{1}{r}\frac{\partial(\rho v_\theta v_\theta)}{\partial \theta}+\frac{\rho v_r v_\theta}{r}+\frac{\partial(\rho v_z v_\theta)}{\partial z}$$
$$=\left[\frac{2}{r^2}\frac{\partial}{\partial \theta}\left(\eta\frac{\partial v_\theta}{\partial \theta}\right)+\frac{1}{r^2}\frac{\partial}{\partial r}\left(\eta r^2\frac{\partial v_\theta}{\partial r}\right)+\frac{\partial}{\partial z}\left(\eta\frac{\partial v_\theta}{\partial z}\right)\right]$$
$$+\left[\frac{2}{r^2}\frac{\partial}{\partial \theta}(\eta v_r)+\frac{1}{r^2}\frac{\partial}{\partial r}\left(\eta r\frac{\partial v_r}{\partial \theta}\right)+\frac{\partial}{\partial z}\left(\frac{\eta}{r}\frac{\partial v_z}{\partial \theta}\right)\right.$$
$$\left.-\frac{1}{r^2}\frac{\partial}{\partial r}(\eta r v_\theta)\right]-\frac{1}{r}\frac{\partial p}{\partial \theta}+\rho g_\theta \tag{2.37}$$

$$\frac{\partial(\rho v_r)}{\partial t}+\frac{\partial(\rho v_r v_r)}{\partial r}+\frac{1}{r}\frac{\partial(\rho v_\theta v_r)}{\partial \theta}-\frac{\rho {v_\theta}^2}{r}+\frac{\partial(\rho v_z v_r)}{\partial z}$$
$$=\left[\frac{1}{r^2}\frac{\partial}{\partial \theta}\left(\eta\frac{\partial v_r}{\partial \theta}\right)+\frac{2}{r}\frac{\partial}{\partial r}\left(\eta r\frac{\partial v_r}{\partial r}\right)+\frac{\partial}{\partial z}\left(\eta\frac{\partial v_r}{\partial z}\right)\right]$$
$$+\left[\frac{1}{r}\frac{\partial}{\partial \theta}\left(\eta\frac{\partial v_\theta}{\partial r}\right)+\frac{\partial}{\partial z}\left(\eta\frac{\partial v_z}{\partial r}\right)-\frac{2\eta}{r^2}\frac{\partial v_\theta}{\partial \theta}-\frac{2\eta}{r^2}\frac{v_r}{r}\right.$$
$$\left.-\frac{1}{r^2}\frac{\partial(\eta v_\theta)}{\partial \theta}\right]-\frac{\partial p}{\partial r}+\rho g_r \tag{2.38}$$

$$\frac{\partial(\rho v_z)}{\partial t}+\frac{\partial(\rho v_r v_z)}{\partial r}+\frac{1}{r}\frac{\partial(\rho v_\theta v_z)}{\partial \theta}+\frac{\partial(\rho v_z v_z)}{\partial z}$$
$$=\left[\frac{1}{r^2}\frac{\partial}{\partial \theta}\left(\eta\frac{\partial v_z}{\partial \theta}\right)+\frac{1}{r}\frac{\partial}{\partial r}\left(\eta r\frac{\partial v_z}{\partial r}\right)+2\frac{\partial}{\partial z}\left(\eta\frac{\partial v_z}{\partial z}\right)\right] \tag{2.39}$$
$$+\left[\frac{1}{r}\frac{\partial}{\partial \theta}\left(\eta\frac{\partial v_\theta}{\partial z}\right)+\frac{1}{r}\frac{\partial}{\partial r}\left(\eta r\frac{\partial v_r}{\partial z}\right)\right]-\frac{\partial p}{\partial z}+\rho g_z$$

In all the above equations, the first term denotes the momentum temporal variation inside the control volume, whereas the other terms denote the momentum carried by advection through the control volume faces. The terms on the right side of the equations above stand for the momentum quantity transported by diffusion and the external forces acting on the flow, e.g. pressure gradient and gravitational force. For non-Newtonian fluids, the Newtonian viscosity μ should be shifted with the apparent viscosity η.

2.5 TAYLOR-COUETTE FLOW

As described in Chapter 1, the domain of a typical Taylor-Couette flow is shown in Figure 14, repeated here for convenience. The inner radius (R_{inn}) can also be denoted as kR, whereas k is the radius ratio. The fluid column height is denoted by h, whereas the cylinders' total height is denoted by H. In this case, the outer cylinder is held stationary while the inner one rotates independently with an imposed angular velocity ω. Also, the radius gap (δ), radius ratio (k) and aspect ratio (Γ) are the geometry parameters.

The dimensionless flow parameters are the rotational Reynolds number and Taylor number. The former is the ratio between inertial and viscous forces acting in the flow, whereas the latter relates the same forces taking the above geometrical parameters in consideration. Regarding the Newtonian fluids:

$$\mathrm{Re} = \frac{\rho(\omega R_{inn})\delta}{\mu} \tag{2.40}$$

$$\mathrm{Ta} = \left(\frac{\rho\omega}{\mu}\right)^2 R_{inn}\delta^3 = \left(\frac{1}{k} - 1\right)\mathrm{Re}^2 \tag{2.41}$$

whereas for Power-Law non-Newtonian fluids the Taylor number was applied as suggested by Sinevic, Kuboi and Nienow (1986), considering an effective viscosity determined from the theoretical shear rate ($\dot{\gamma}_C$), as follows:

$$\dot{\gamma}_C = \left(\frac{2\omega}{n}\right)\left[1 - k^{2/n}\right]^{-1} \tag{2.42}$$

FIGURE 14 - SCHEMATIC REPRESENTATION OF THE PHYSICAL DOMAIN.

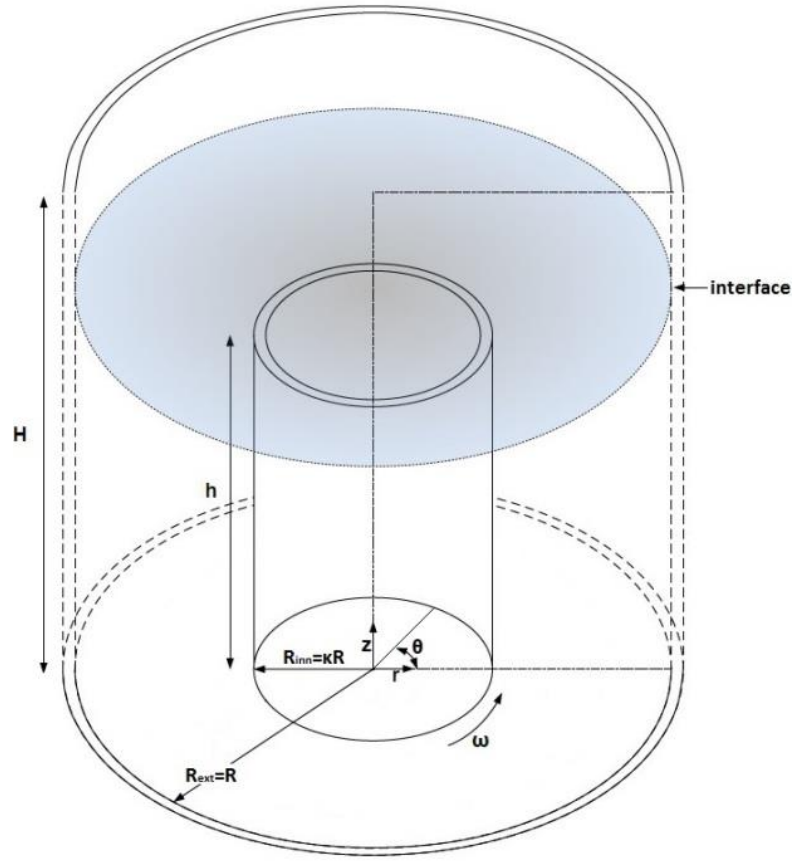

The flow is considered unstable when the viscous forces are not capable of inhibiting the disturbance caused by the inertial forces, which occurs when a critical value of the dimensionless number (either Reynolds or Taylor) is reached.

The following flow simplifying assumptions are adopted in the present work:

- Isothermal and incompressible flow;
- Natural convection effects were rejected as ($Gr / Re^2 \sim 10^{-2}$);
- The viscous dissipation was rejected as ($Ec / Re \sim 10^{-8}$);
- The gravitational force acts in the axial direction only;
- There is no meniscus on the free surface condition;
- The air-liquid interface is not considered as the air viscosity is much lower than that of liquid.

where Gr denotes the Grashof number (ratio of the buoyancy to the viscous force acting on a fluid) and Ec denotes the Eckert number (ratio between a flow's kinetic energy and the boundary layer enthalpy difference). The rejection of the natural convection and viscous dissipation were

based on the Fluid Dynamics and Heat Transfer literature (BIRD, STEWART, and LIGHTFOOT, 2006)

In order to emulate the behavior of a washing machine, the following boundary conditions are imposed

- At $z = 0 \rightarrow (v_\theta , v_r , v_z) = (0 , 0 , 0)$ for $R_{inn} \leq r \leq R_{out}$, bottom surface;
- At $z = H \rightarrow \left(\frac{\partial v_\theta}{\partial z} , \frac{\partial v_r}{\partial z}, v_z\right) = (0 , 0 , 0)$ for $R_{inn} \leq r \leq R_{out}$, if there is a free surface condition;
- At $z = H \rightarrow (v_\theta , v_r , v_z) = (0 , 0 , 0)$ for $R_{inn} \leq r \leq R_{out}$, if the surface is closed;
- For $r < R_{inn} \rightarrow (v_\theta , v_r , v_z) = (0 , 0 , 0)$ for $0 \leq z \leq H$, inside the inner cylinder;
- At $r = R_{inn} \rightarrow (v_\theta , v_r , v_z) = (\omega k R , 0 , 0)$ for $0 \leq z \leq H$;
- At $r = R_{out} \rightarrow (v_\theta , v_r , v_z) = (0 , 0 , 0)$ para $0 \leq z \leq H$;
- Neumann boundary conditions are applied for the pressure field on the surfaces;
- Cyclic boundary condition for $\theta = 0$ and $\theta = 2\pi$

Moreover, the second invariant of the shear rate tensor, needed for viscosity, is calculated as follows:

$$\begin{aligned} II_{\dot{\gamma}} &= \frac{1}{2}\left(tr\left(\bar{\bar{\dot{\gamma}}}\right)\right)^2 - tr\left(\bar{\bar{\dot{\gamma}}}^2\right) \\ &= \dot{\gamma}_{\theta\theta}\dot{\gamma}_{rr} + \dot{\gamma}_{\theta\theta}\dot{\gamma}_{zz} + \dot{\gamma}_{rr}\dot{\gamma}_{zz} - \dot{\gamma}_{\theta r}\dot{\gamma}_{r\theta} - \dot{\gamma}_{\theta z}\dot{\gamma}_{z\theta} - \dot{\gamma}_{rz}\dot{\gamma}_{zr} \end{aligned} \tag{2.43}$$

thus,

$$\begin{aligned} II_{\dot{\gamma}} = {} & 4\left(\frac{1}{r}\frac{\partial v_\theta}{\partial \theta} + \frac{v_r}{r}\right)\left(\frac{\partial v_r}{\partial r}\right) + 4\left(\frac{1}{r}\frac{\partial v_\theta}{\partial \theta} + \frac{v_r}{r}\right)\left(\frac{\partial v_z}{\partial z}\right) \\ & + 4\left(\frac{\partial v_r}{\partial r}\right)\left(\frac{\partial v_z}{\partial z}\right) - \left[r\frac{\partial}{\partial r}\left(\frac{v_\theta}{r}\right) + \frac{1}{r}\frac{\partial v_r}{\partial \theta}\right]^2 \\ & - \left(\frac{1}{r}\frac{\partial v_z}{\partial \theta} + \frac{\partial v_\theta}{\partial z}\right)^2 - \left(\frac{\partial v_r}{\partial z} + \frac{\partial v_z}{\partial r}\right)^2 \end{aligned} \tag{2.44}$$

Finally, it is possible to compute the magnitude of the tensor of a control volume inside the geometry through the equation above applied in the Equation (2.6).

Considering a laminar steady-state flow, where the cylinder height is sufficient to disregard the bottom and top boundary walls end-effects, the analytical solution for the tangential velocity is achieved close to the half-height of the cylinders, as shown in the top view of Figure 15. In this case, both axial and radial velocity components are considered negligible when compared to the tangential one. The derivation of the following equations is explained in Appendix III.

Considering a Newtonian fluid, the analytical solution for the tangential velocity is (WHITAKER, 1992), the solution yields:

$$v_\theta(r) = \frac{\omega k R}{1 - k^2}\left(\frac{r}{kR} - \frac{kR}{r}\right) \tag{2.45}$$

Moreover, for the Power-Law non-Newtonian fluid (BIRD, ARMSTRONG and HASSAGER, 1987):

$$\frac{v_\theta}{\omega r} = \frac{(R/r)^{2/n} - 1}{(1/k)^{2/n} - 1} \tag{2.46}$$

FIGURE 15 - REPRESENTATION OF A UNIDIMENSIONAL FLOW BETWEEN TWO CONCENTRIC CYLINDERS.

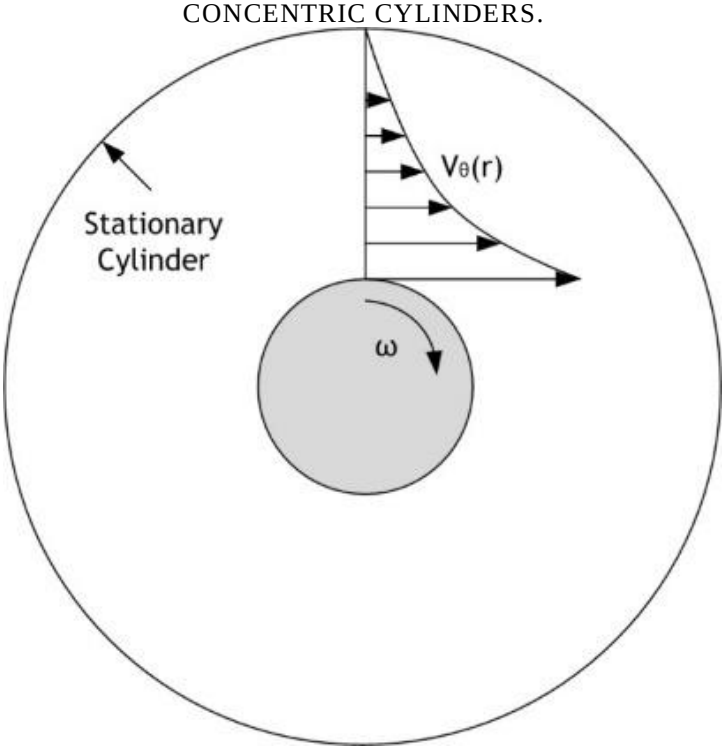

2.6 RHEOMETRY - COUETTE INVERSE PROBLEM

In general, rheometry is based on experimental techniques applied in the determination of the rheological properties of materials, which gives the relation (η) between deformation (shear rates $\bar{\bar{\dot{\gamma}}}$) and stresses ($\bar{\bar{\tau}}$) (JACOBSEN, 1974). The measurement of the fluid rheological properties, e.g., viscosity (by viscometry) and elastic modulus, relies on the physical parameters imposed to the fluid flow to find suitable tests conditions which allow the measurement of flow properties objectively and reproducibility (SCHRAMM, 1994). A deeper understanding of the rheology in the industry can be found in the work of Boger (2009).

An example of a wide-used rheometry technique is the so-called Couette inverse problem, which relies on the regression of the flow curve $\tau(\dot{\gamma})$ from the measurements of torque T (N·m) and angular velocity ω (rad/s) in a coaxial double cylinder rheometer, where τ is the shear stress (N·m^2) and $\dot{\gamma}$ is the shear rate (s^{-1}) (ANCEY, 2005). In the present study, one can note that the measurements of angular velocity and torque were held in the inner cylinder (agitator), while the outer cylinder (drum) remains stationary. The angular velocity variation over the gap can be described in terms of the shear stress and shear rate as follows (NGUYEN and BOGER, 1987):

$$\omega = \frac{1}{2}\int_{\tau_{out}}^{\tau_{inn}} \frac{\dot{\gamma}(\tau)}{\tau} d\tau = \int_{R_{out}}^{R_{inn}} \frac{\dot{\gamma}(r)}{r} dr \tag{2.47}$$

where for laminar steady-state flow,

$$\dot{\gamma} = r\frac{\partial\omega(r)}{\partial r} \tag{2.48}$$

In the cases where yield stress takes place within the gap, the upper limit of integration in Equation (2.47) must be replaced by the yield stress of the fluid (τ_0) and the plug radius (r_0). Therefore, solving the velocity profile, Equation (2.19), of a unidimensional tangential laminar steady-state flow between the gap, yields to (BARNES, HUTTON and WALTERS, 1989):

$$\frac{1}{r^2}\frac{\partial}{\partial r}(r^2\tau_{r\theta}) = 0 \tag{2.49}$$

which is reduced to

$$r^2\tau_{r\theta} = \text{constant} \tag{2.50}$$

where the shear stress and the inner cylinder radius can be related to a given radial position (r) as follows:

$$\tau_{r\theta} = \frac{R_{inn}^2}{r^2}\tau_{inn} \tag{2.51}$$

The equation above relates the shear stress to the radial position. Moreover, one can note that the shear stress measured in the inner cylinder can be obtained directly from the torque value, as follows (KRIEGER and MARON, 1952):

$$|\tau_{inn}| = \frac{T}{2\pi R_{inn}^2 H} \tag{2.52}$$

The solution of the Couette inverse problem, summarized by Equation (2.47), relies on the solution of a Volterra integral of the first kind (YEOW, KO, and TANG, 2000). Many authors proposed a practical way for solving Equation (2.47) by applying the existing NNF models in the equation, whose parameters are obtained by best-fitting to the experimental data (KELESSIDIS and MAGLIONE, 2008). The most-used fitting technique is the least square method.

For simplifying the mathematical analysis henceforth, the inverse of the radius ratio k (R_{inn}/R_{out}) will be represented as κ, which is R_{out}/R_{inn}. The following analysis is presented in accordance with the works of Kelessidis and Maglione (2006, 2008).

Considering that the fluid inside the geometry is a Newtonian one, and inserting the Equation (2.1) into the Equation (2.52) yields to:

$$|\tau_{inn}| = \frac{T}{2\pi R_{inn}^2 H} = \frac{2}{1-k^2}\mu\omega = \frac{2\kappa^2}{\kappa^2-1}\mu\omega \tag{2.53}$$

thus, the shear rate in the inner cylinder is obtained from:

$$|\dot{\gamma}_{inn}| = \frac{2}{1-k^2}\omega = \frac{2\kappa^2}{\kappa^2-1}\omega \tag{2.54}$$

When the gap between the cylinders is narrow, the above equations present a good approximation of the real values measured by the viscometer (JOYE, 2003). For this reason, commercial viscometers, also known as viscosimeters, frequently use the Newtonian fluids approximations for the shear rate (ESTELLÉ, LANOS, and PERROT, 2008). However, many fluids present a yield stress, thus requiring a wider gap between the cylinders in order to measure the yield stress and the true flow behavior of a non-Newtonian fluid (KELESSIDIS and MAGLIONE, 2006).

Starting from the Equation (2.52) one can note that the shear stress experienced by the non-Newtonian fluid between the cylinders is given by:

$$\tau = \frac{T}{2\pi r^2 H} \tag{2.55}$$

so, if one denotes:

$$y = \frac{r}{R_{inn}} \tag{2.56}$$

$$\tau = \frac{\tau_{inn}}{y^2} \tag{2.57}$$

it follows that from Equation (2.48):

$$\dot{\gamma} = r\frac{\partial\omega(r)}{\partial r} = f(\tau) = f\left(\frac{\tau_{inn}}{y^2}\right) = y\frac{d\omega}{dy} \tag{2.58}$$

which leads to

$$d\omega = f\left(\frac{\tau_{inn}}{y^2}\right)\frac{dy}{y} \tag{2.59}$$

Therefore, applying the following boundary conditions in two different notations (r and y) for a rotating inner cylinder and a statical outer cylinder. One can note that the imposed inner

cylinder tangential velocity (v_θ) is denoted as negative (counterclockwise) just for the sake of simplifying the mathematics, but it does not matter for physical interpretation.

$$\begin{aligned} &\text{at } r = R_{inn} \rightarrow \omega = -\Omega \\ &\text{at } r = R_{out} \rightarrow \omega = 0 \end{aligned} \tag{2.60}$$

$$\begin{aligned} &\text{at } y = {}^{R_{inn}}/_{R_{inn}} = 1 \rightarrow \omega = -\Omega \\ &\text{at } y = {}^{R_{out}}/_{R_{inn}} = \kappa \rightarrow \omega = 0 \end{aligned} \tag{2.61}$$

thus, leading Equation (2.59) to:

$$\Omega = \int_1^{\kappa} \left(\frac{1}{y}\right) f\left(\frac{\tau_{inn}}{y^2}\right) dy \tag{2.62}$$

The above equation denotes the relationship between the inner cylinder velocity and the shear stress within the Couette geometry viscometer. Some of the solutions for the Couette inverse problems found in the literature, concerning the most well-known yield stress non-Newtonian fluid models, are summarized in the next subsections.

Besides, one can obtain the value of the plug radius r_0 of a yield stress fluid, which is the region where the shear stress between the gap has the yield stress value (i.e. there is the presence of plug flow), by substituting these values into Equation (2.52):

$$r_0 = \sqrt{\frac{T}{2\pi H \tau_0}} \tag{2.63}$$

2.6.1 Casson Fluid

The Casson fluid was introduced previously in Equation (2.10) and its shear rate is represented as follows:

$$|\dot{\gamma}| = \frac{\left(\sqrt{\tau} - \sqrt{\tau_0}\right)^2}{\mu} \tag{2.64}$$

so, for a full shearing flow without plug existing between cylinders, Equation (2.62) becomes (KELESSIDIS and MAGLIONE, 2006):

$$\Omega = \int_1^{\kappa} \left(\frac{1}{y}\right) f\left(\frac{\tau_{inn}}{y^2}\right) dy = \int_1^{\kappa} \left(\frac{1}{y}\right) \frac{\left(\sqrt{\frac{\tau_{inn}}{y^2}} - \sqrt{\tau_0}\right)^2}{\mu} dy \tag{2.65}$$

which turns to,

$$\mu\Omega = \int_1^{\kappa} \left[\frac{\tau_{inn}}{y^3} - \frac{2}{y^2}\sqrt{\tau_{inn}}\sqrt{\tau_0} + \frac{\tau_0}{y}\right] dy \tag{2.66}$$

thus,

$$\mu\Omega = \tau_{inn} \int_1^{\kappa} \left(\frac{dy}{y^3}\right) - 2\sqrt{\tau_{inn}}\sqrt{\tau_0} \int_1^{\kappa} \left(\frac{dy}{y^2}\right) + \tau_0 \int_1^{\kappa} \frac{dy}{y} \tag{2.67}$$

solving separately the three integrals above yields

$$\Omega = \frac{1}{\mu}\left[\frac{\tau_{inn}}{2}\left(\frac{\kappa^2 - 1}{\kappa^2}\right) - 2\sqrt{\tau_{inn}}\sqrt{\tau_0}\left(\frac{\kappa - 1}{\kappa}\right) + \tau_0 \ln(\kappa)\right] \tag{2.68}$$

Thus, isolating the shear stress in the inner cylinder, one can achieve the following expression:

$$\tau_{inn} = \left[\sqrt{(\Omega\mu - \tau_0 \ln(\kappa))\frac{2\kappa^2}{\kappa^2 - 1} + \frac{4\kappa^2\tau_0}{(\kappa + 1)^2}} + \frac{2\kappa\tau_0}{\kappa + 1}\right]^2 \tag{2.69}$$

Hence, substituting the equation above into the Equation (2.10), the following expression for the shear rate in the inner cylinder is obtained:

$$|\dot{\gamma}|_{inn} = \frac{1}{\mu}\left[\sqrt{(\Omega\mu - \tau_0 \ln(\kappa))\frac{2\kappa^2}{\kappa^2 - 1} + \frac{4\kappa^2\tau_0}{(\kappa+1)^2}} + \sqrt{\tau_0}\left(\frac{\kappa - 1}{\kappa + 1}\right)\right]^2 \tag{2.70}$$

Moreover, combining the Equations (2.54) and (2.10), an equation for the shear stress experienced by the fluid in the inner cylinder for a Newtonian fluid is obtained.

$$\tau_{inn} = \left[\sqrt{\tau_0} + \sqrt{k\frac{2\kappa^2}{\kappa^2 - 1}\Omega}\right]^2 \tag{2.71}$$

One can note that Equation (2.54) has the same meaning of Equation (2.70), but denotes the behavior of a Newtonian fluid. It is important to mention that the equations above were obtained by the approach introduced by Kelessedis and Maglione (2006). Similarly, Joye (2003) achieved a similar expression for the flow of Casson fluids through a different approach.

2.6.2 Robertson-Stiff Fluid

Similarly, the same method used on Casson fluids is employed for the Robertson-Stiff fluid model in Equation (2.11) yielding to:

$$\tau_{inn} = \mu\left[\frac{2\kappa^{\frac{2}{n}}}{n\left(\kappa^{\frac{2}{n}} - 1\right)}(\Omega + \dot{\gamma}_0 \ln \kappa)\right]^n \tag{2.72}$$

Therefore, substituting the equation above into the Equation (2.11), the following equation for the shear rate in the inner cylinder is obtained for the Robertson-Stiff fluid similarly to the Casson fluid:

$$\dot{\gamma}_{inn} = \frac{2\Omega k^{\frac{2}{n}}}{n\left(\kappa^{\frac{2}{n}} - 1\right)} + \dot{\gamma}_0\left[\frac{2k^{\frac{2}{n}} \ln \kappa}{n\left(\kappa^{\frac{2}{n}} - 1\right)} - 1\right] \tag{2.73}$$

Finally, for a Newtonian fluid, combining the Equations (2.54) and (2.11), one can achieve:

$$\tau_{inn} = \mu\left[\dot{\gamma}_0 + \frac{2\kappa^2}{\kappa^2 - 1}\Omega\right]^n \tag{2.74}$$

2.6.3 Bingham Fluid

For a Bingham fluid, Equation (2.8), it is also possible to use the integration approach of Kelessidis and Maglione, by considering the same flow conditions (full shearing flow without plug).

$$\tau_{inn} = \frac{2\kappa^2\Omega\mu}{(\kappa^2 - 1)} + \frac{2\kappa^2\tau_0\ln(\kappa)}{(\kappa^2 - 1)} = \frac{2\kappa^2}{(\kappa^2 - 1)}(\Omega\mu + \tau_0\ln(\kappa)) \tag{2.75}$$

Substituting the equation above into the Equation (2.8), the following equation for the shear rate in the inner cylinder for the Bingham fluid is obtained after some simplifications:

$$\dot{\gamma}_{inn} = \frac{\tau_{inn} - \tau_0}{\mu} = \frac{\frac{2\kappa^2}{(\kappa^2 - 1)}(\Omega\mu + \tau_0\ln(\kappa)) - \tau_0}{\mu} \tag{2.76}$$

Similarly, for a Newtonian fluid, Equation (2.75) can be simplified into:

$$\tau_{inn} = \tau_0 + \mu\frac{2\kappa^2}{(\kappa^2 - 1)}\Omega \tag{2.77}$$

Alternatively, there is also the so-called Reiner-Riwlin equation, which relates the torque measured value in the cylinder surface with the imposed angular velocity.

$$T = \frac{4\pi H\tau_0}{\left(\frac{1}{R_{inn}^2} - \frac{1}{R_{out}^2}\right)}\ln(\kappa) + \frac{\mu 8\pi^2 H}{\left(\frac{1}{R_{inn}^2} - \frac{1}{R_{out}^2}\right)}\Omega \tag{2.78}$$

A more detailed explanation of this equation is found on Appendix III.3.

2.6.4 Herschel-Bulkey Fluid

The Herschel-Bulkley fluid was introduced previously in Equation (2.9) and, if its shear rate is isolated, it can be represented as follows:

$$|\dot{\gamma}| = \sqrt[n]{\frac{\tau-\tau_0}{m}} \tag{2.79}$$

So, by means of the Kellesidis and Maglione analysis, for a full shearing flow without plug existing between cylinders, Equation (2.62) yields (KELESSIDIS and MAGLIONE, 2008):

$$\Omega = \int_1^{\kappa} \left(\frac{1}{y}\right) f\left(\frac{\tau_{inn}}{y^2}\right) dy = \int_1^{\kappa} \left(\frac{1}{y}\right) \left(\frac{\tau_{inn} - \tau_0}{m}\right)^{\frac{1}{n}} dy \tag{2.80}$$

Letting that:

$$x = \frac{\tau_{inn}}{\tau_0 y^2} - 1 \tag{2.81}$$

$$y = \frac{\sqrt{\tau_{inn}/\tau_0}}{\sqrt{x+1}} - 1 \tag{2.82}$$

$$dy = -\frac{\sqrt{\tau_{inn}/\tau_0}}{2(x+1)^{3/2}} dx \tag{2.83}$$

Setting the new boundary conditions, which are the limits of the integration of the equation:

$$\begin{aligned} &\text{at } y = 1 \rightarrow x = \frac{\tau_{inn}}{\tau_0} - 1 \equiv \mathbb{A} \\ &\text{at } y = \kappa \rightarrow x = \frac{\tau_{inn}}{\tau_0 \kappa^2} - 1 \equiv \mathbb{B} \end{aligned} \tag{2.84}$$

Substituting the boundary conditions into the Equation (2.80) it becomes:

$$\Omega = \left(\frac{1}{2}\right)\left(\frac{\tau_{inn}}{m}\right)^{\frac{1}{n}} \int_{\mathbb{B}}^{\mathbb{A}} \frac{x^{\frac{1}{n}}}{(x+1)} dx \tag{2.85}$$

One can note that the equation above does not have an analytical solution, which can be only be achieved numerically through a series expansion. For the case where $-1 \leq x \leq 1$, which is true for values where $\tau_{inn} \leq 2\tau_0$, Equation (2.85) becomes:

$$\Omega = \left(\frac{1}{2}\right)\left(\frac{\tau_{inn}}{m}\right)^{\frac{1}{n}} \int_{\mathbb{B}}^{\mathbb{A}} x^{\frac{1}{n}}\left[1 - x + x^2 - x^3 + \cdots \pm x^j\right] dx \,; j = 0, \infty \tag{2.86}$$

Then, performing the integration above, one obtains:

$$\Omega = \left(\frac{1}{2}\right)\left(\frac{\tau_{inn}}{m}\right)^{\frac{1}{n}} \sum_{j=0}^{\infty} (-1)^j \left[\frac{\left(\frac{\tau_{inn}}{\tau_0} - 1\right)^{\frac{1}{n}+1+j} - \left(\frac{\tau_{inn}}{\tau_0 \kappa^2} - 1\right)^{\frac{1}{n}+1+j}}{\frac{1}{n} + 1 + j}\right] \tag{2.87}$$

Hence, for this condition, the true shear rate on the inner cylinder:

$$\dot{\gamma} = \left[\frac{\tau_{inn}}{m}\left[\frac{2\Omega}{\sum_{j=0}^{\infty}(-1)^j \left[\frac{\left(\frac{\tau_{inn}}{\tau_0} - 1\right)^{\frac{1}{n}+1+j} - \left(\frac{\tau_{inn}}{\tau_0 \kappa^2} - 1\right)^{\frac{1}{n}+1+j}}{\frac{1}{n} + 1 + j}\right]}\right]^n\right]^{\frac{1}{n}} \tag{2.88}$$

Now, for the case where $x \leq -1$and $x > 1$, which is true for shear stress values where $\tau_{inn} \geq \tau_0$, Equation (2.85) becomes

$$\Omega = \left(\frac{1}{2}\right)\left(\frac{\tau_{inn}}{m}\right)^{\frac{1}{n}} \int_{\mathbb{B}}^{\mathbb{A}} \frac{x^{\frac{1}{n}}}{(x+1)} dx = \left(\frac{\tau_{inn}}{m}\right)^{\frac{1}{n}} \int_{\mathbb{B}}^{\mathbb{A}} \frac{x^{\frac{1}{n}}/x}{(x+1)/x} dx$$
$$= \left(\frac{\tau_{inn}}{m}\right)^{\frac{1}{n}} \int_{\mathbb{B}}^{\mathbb{A}} \frac{x^{\frac{1}{n}-1}}{1+1/x} dx \tag{2.89}$$

The expansion of the term $\frac{1}{1+1/x}$ yields

$$\frac{1}{1+\frac{1}{x}} = 1 - \frac{1}{x} + \frac{1}{x^2} + \cdots + \frac{1}{x^j};\ j = 0, \infty \tag{2.90}$$

so

$$\Omega = \left(\frac{1}{2}\right)\left(\frac{\tau_{inn}}{m}\right)^{\frac{1}{n}} \int_{\mathbb{B}}^{\mathbb{A}} x^{\frac{1}{n}-1} \sum_{j=0}^{\infty} \left(\frac{-1}{x}\right)^j dx$$
$$= \left(\frac{\tau_{inn}}{m}\right)^{\frac{1}{n}} \int_{\mathbb{B}}^{\mathbb{A}} \sum_{j=0}^{\infty} (-1)^j\, x^{\left(-1-j+\frac{1}{n}\right)} dx \tag{2.91}$$

hence

$$\Omega = \left(\frac{1}{2}\right)\left(\frac{\tau_{inn}}{m}\right)^{\frac{1}{n}} \sum_{j=0}^{\infty} (-1)^j \left[\frac{\left(\frac{\tau_{inn}}{\tau_0} - 1\right)^{\frac{1}{n}-j} - \left(\frac{\tau_{inn}}{\tau_0 \kappa^2} - 1\right)^{\frac{1}{n}-j}}{\frac{1}{n} - j}\right] \tag{2.92}$$

Finally, the true shear rate for this case is calculated

$$\dot{\gamma} = \left[\frac{\tau_{inn}}{m}\left[\frac{2\Omega}{\sum_{j=0}^{\infty}(-1)^j\left[\frac{\left(\frac{\tau_{inn}}{\tau_0}-1\right)^{\frac{1}{n}-j}-\left(\frac{\tau_{inn}}{\tau_0\kappa^2}-1\right)^{\frac{1}{n}-j}}{\frac{1}{n}-j}\right]}\right]^n\right]^{\frac{1}{n}} \tag{2.93}$$

One can note that, differently from the other fluid models, the equations above for both cases depend also on the measured shear stress (torque) for different imposed angular velocities, and also on the gap value. Thus, the Herschel-Bulkley model parameters should be regressed through a method that minimizes the errors between the difference between computed shear stress value and the measured one. Kelessidis and Maglione (2008) suggested the mean square deviation (MSD) for limiting the range of the parameters and finding the best fitting values of n, m and τ_{inn}.

Alternatively, Heirman et al. (2008) proposed an integration approach similar to the Reiner-Riwlin equation to solve the Couette inverse problem for Herschel-Bulkley fluids,

$$T = \frac{4\pi H\tau_0}{\left(\frac{1}{R_{inn}^2}-\frac{1}{R_{out}^2}\right)}\ln\left(\frac{R_{out}}{R_{inn}}\right) + \frac{2^{2n+1}\pi^{n+1}Hm}{n^n\left(\frac{1}{R_{inn}^{2/n}}-\frac{1}{R_{out}^{2/n}}\right)^n}N^n \tag{2.94}$$

where N is the velocity of the inner cylinder in rps. A more detailed approach for the equation below is also depicted in Appendix III.3.

2.6.5 Experimental and Numerical Difficulties

The literature review showed some studies regarding the measurement errors associated with some experimental difficulties. The most common ones in a coaxial double cylinder Couette geometry are the end-effects, slip velocity (BARNES, 1995), and the viscous heating.

The end-effects are associated with the torque measurements in a coaxial Couette geometry by the contribution from the portion of the flow which is influenced by the solid bottom surface and the open air/fluid interface. As all the mentioned techniques simplify the

analysis to the $\tau_{r\theta}$ shear stress only, thus neglecting the effect of all other shear and normal stresses, an obvious way to minimize those effects is to design an apparatus with a sufficient height (SCHOWALTER, 1978). Also, when the bottom basis is rotating, there is a presence of a singularity at the corner between the bottom basis and the outer cylinder because of the difference of the velocity, which may lead to some numerical issues that must be removed (TAMANO, ITOH, et al., 2010).

In this work, both end-effects are present, and as the experimental rig is similar to a vertical axis washing machine, it is not practical to perform tests in a different apparatus. Thus, prior to the experimental tests, in order to minimize the torque gain caused by mechanical loss and air presence, some tests were performed without the presence of the fabric-water suspensions.

2.7 CHAPTER SUMMARY

The present theoretical description has been introduced with a brief review of the concepts of Newtonian and non-Newtonian fluids, as well as some empirical generalized models of Newtonian fluids. Then, a brief explanation concerning the Taylor-Couette flow was given, whereas the physical and mathematical models were presented. Finally, a brief review of the viscometry literature was quoted for some key non-Newtonian fluid models. In general, the raw experimental data obtained from the viscometer, i.e. the torque supplied to the fluid by the inner cylinder wall as a function of the angular velocity is converted into shear stress/shear rate data, which are used to correlate the rheological properties of the fluid. Despite many different methods can be found in the open literature, such as the Tikhonov regularization (YEOW, CHOON, et al., 2004) and the wavelet-vaguelette decomposition (ANCEY, 2005), the integration of the equation which relates the shear stress with the angular velocity was adopted in the present work as it returns the physical parameters of the model, while the other methods carry no physical background.

3 NUMERICAL METHODOLOGY

3.1 GENERAL VIEW

Even though flows of Newtonian and non-Newtonian fluids can be solved analytically in some restricted conditions (i.e., steady-state, and two-dimensional flows), in the present work, the mathematical model was solved numerically by means of CFD (Computational Fluid Dynamics) techniques due to the non-linear behavior of the governing equations and fluid rheology.

CFD techniques can solve, approximately, the governing equations for the advective and diffusive mass, momentum, and energy transport, thus making possible the prediction of the quantities carried by the flow (e.g., velocities, temperature, chemical composition, among others).

The choice of the numerical method is made considering the impact of some factors, such as computational cost, implementation complexity, and the accuracy of the results. The key numerical methods available for solving advective-diffusive problems are Finite-Difference Method (FDM) (MORINISHI, VASILYEV and OGI, 2004), Finite-Element Method (FEM), Boundary-Element Method (BEM) and Finite-Volume Method (FVM) (PATANKAR, 1980). The FVM was chosen to solve the Taylor-Couette problem in the present thesis due to its physical background based on the conservation of the transported quantities in each finite volume.

Therefore, the following numerical methodologies have been applied:

- Velocity-pressure coupling by the PRIME method (MALISKA, 1995);
- Staggered grid for the velocities control volumes (HARLOW and WELCH, 1965);
- Collocated grid for the pressure field (PATANKAR, 1980);
- Non-uniform cylindrical grid at r and z-axes adapted from Wood (1996);
- Power-Law interpolation scheme (PATANKAR, 1980);
- Biconjugate gradient stabilized method (BiCGSTAB) to solve the linear system (VAN DER VORST, 1992);
- TDMA (Tridiagonal Matrix Algorithm, also known as Thomas Algorithm) as the preconditioner for the BiCGSTAB method. The line-by-line method (PATANKAR, 1980) is applied for the radial and axial axes, while on θ axis,

due to its cyclic boundary condition, required the CTDMA (Cyclic Tridiagonal Matrix Algorithm) method is used (AHLBERG, NILSON and WALSH, 1967);

- No-slip boundary conditions applied when the surface velocity is zero (i.e., Dirichlet boundary conditions) (CHENG and CHENG, 2005);
- Neumann boundary conditions applied for the pressure field in all directions (CHENG and CHENG, 2005).

3.2 DISCRETIZATION OF THE GOVERNING EQUATIONS

The FMV consists in integrating the differential equations in their conservative forms, in each of the elementary control volumes of the domain. For the generalized advective-diffusive transport equation concerning a generic variable $\phi=\{v_\theta,v_r,v_z\}$ and a general diffusivity (Γ) in polar cylindrical coordinates, the following expression was adopted:

$$\frac{\partial(\rho\phi)}{\partial t}+\frac{1}{r}\frac{\partial(\rho v_\theta\phi)}{\partial\theta}+\frac{\partial(\rho v_r\phi)}{\partial r}+\frac{\partial(\rho v_z\phi)}{\partial z} = \left[\frac{1}{r^2}\frac{\partial}{\partial\theta}\left(\Gamma\frac{\partial\phi}{\partial\theta}\right)+\frac{1}{r}\frac{\partial}{\partial r}\left(\Gamma r\frac{\partial\phi}{\partial r}\right)+\frac{\partial}{\partial z}\left(\Gamma\frac{\partial\phi}{\partial z}\right)\right]+S \tag{3.1}$$

where the terms on the left-hand side of the equation above correspond to the temporal variation of ϕ inside the control volume and the advective fluxes that carries ϕ through the control volume boundaries, while the terms on the right-hand side of the equation correspond to the assessment of the diffusive fluxes and the source term (S), respectively.

Thus, integrating the Equation (3.1) over the control volume of finite dimensions, and then applying the divergence theorem, one can obtain:

$$\int_\forall \frac{\partial(\rho\phi)}{\partial t}d\forall+\int_A(\rho\vec{v}\phi).\hat{n}dA = \int_A\left(\Gamma^\phi\vec{\nabla}\phi\right).\hat{n}dA+\int_\forall S^\phi d\forall \tag{3.2}$$

So, defining the advective flux as $\vec{J} = (\rho\vec{v}\phi)-\left(\Gamma^\phi\vec{\nabla}\phi\right)$, the Equation (3.2) can be rewritten as:

$$\int_\forall \frac{\partial}{\partial t}(\rho\phi)d\forall+\int_A\vec{J}.\hat{n}dA = \int_\forall S^\phi d\forall \tag{3.3}$$

Figure 16 demonstrates the control volumes in cylindrical coordinates in (a) two dimensions and (b) three dimensions. Whereas the discretized control volume represents the central nodal point P, the points E, W, N, S, T, and B represent the points of the neighbor control volumes immediately at east, west, north, south, top, and bottom, respectively. One can note that the points e, w, n, s, t, and b represent the control surfaces to the east, west, north, south, top, and bottom, respectively. $\Delta\theta$, Δr, and Δz represent the control volume dimensions, while $\delta\theta_e$, $\delta\theta_w$, δr_n, δr_s, δz_t and δz_b symbolize the distances from the nodal point P to the respective points of the neighborhood.

Considering an incompressible flow, with a first-order implicit temporal approximation, the discretized Equation (3.3) is as follows:

$$\rho(\phi - \phi^0)\frac{r\Delta r\Delta\theta\Delta z}{\Delta t} + (J_e - J_w)\Delta r\Delta z + (J_n - J_s)r\Delta\theta\Delta z + (J_t - J_b)r\Delta r\Delta\theta = S_P^{\phi} r\Delta r\Delta\theta\Delta z \tag{3.4}$$

Similarly, the continuity equation can be expressed in terms of a flux integral as:

$$\int_{\forall}\frac{\partial}{\partial t}(\rho\phi)d\forall + \int_A(\rho\vec{v}).\hat{n}dA = 0 \tag{3.5}$$

So, the discretization of the Equation (3.5) over the control volume yields:

$$(\rho - \rho^0)\frac{r\Delta r\Delta\theta\Delta z}{\Delta t} + [(\rho v_\theta)_e - (\rho v_\theta)_w]\Delta r\Delta z + [(\rho r v_r)_n - (\rho r v_r)_s]\Delta\theta\Delta z + [(\rho v_z)_t - (\rho v_z)_b]r\Delta r\Delta\theta = 0 \tag{3.6}$$

FIGURE 16 - DISCRETIZED CONTROL VOLUME.

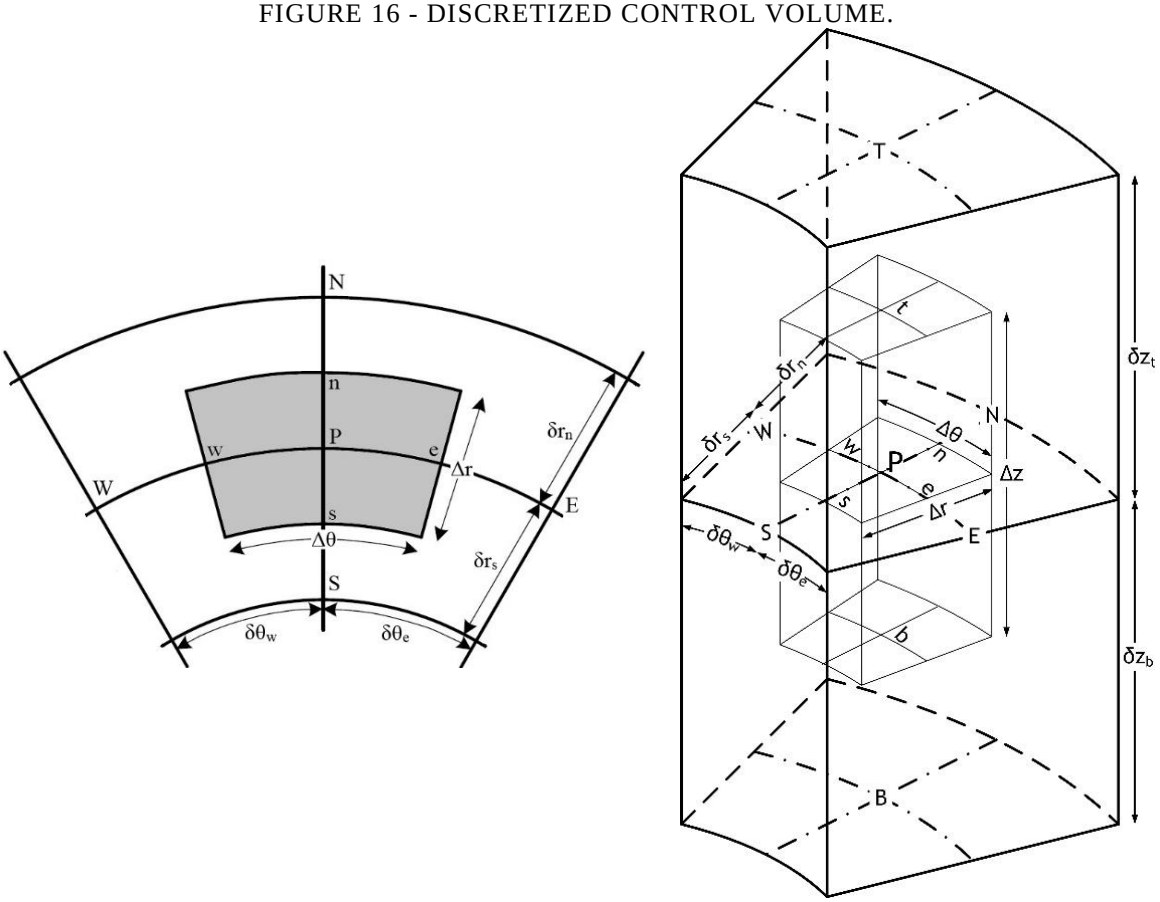

(A) (B)

(A) TWO-DIMENSIONAL AND (B) THREE-DIMENSIONAL.

Multiplying Equation (3.6) by ϕ_P, and then subtracting it from the Equation (3.4), the following expression is obtained for an incompressible fluid:

$$\begin{aligned}\rho(\phi-\phi^0)\frac{r\Delta r\Delta\theta\Delta z}{\Delta t}&+\left[\left(J_e-\rho v_{\theta_e}\phi_P\right)-\left(J_w-\rho v_{\theta_w}\phi_P\right)\right]\Delta r\Delta z\\&+\left[(J_n-\rho(rv_r)_n\phi_P)-(J_s-\rho(rv_r)_s\phi_P)\right]\Delta\theta\Delta z\\&+\left[\left(J_t-\rho v_{z_t}\phi_P\right)-\left(J_b-\rho v_{z_b}\phi_P\right)\right]r\Delta r\Delta\theta=S_P^{\phi}\Delta V\end{aligned}\tag{3.7}$$

where,

$$\begin{cases} \left(J_e - \rho v_{\theta_e}\phi_P\right)\Delta r\Delta z = A_e(\phi_P - \phi_E) \\ \left(J_w - \rho v_{\theta_w}\phi_P\right)\Delta r\Delta z = -A_w(\phi_P - \phi_W) \\ (J_n - \rho(rv_r)_n\phi_P)\Delta\theta\Delta z = A_n(\phi_P - \phi_N) \\ (J_s - \rho(rv_r)_s\phi_P)\Delta\theta\Delta z = -A_s(\phi_P - \phi_S) \\ \left(J_t - \rho v_{z_t}\phi_P\right)r\Delta r\Delta\theta = A_t(\phi_P - \phi_T) \\ \left(J_b - \rho v_{z_b}\phi_P\right)r\Delta r\Delta\theta = -A_b(\phi_P - \phi_B) \end{cases} \tag{3.8}$$

Hence, the following heptadiagonal system of algebraic equation is obtained:

$$A_p\phi_P = A_e\phi_E + A_w\phi_W + A_n\phi_N + A_s\phi_S + A_t\phi_T + A_b\phi_B + B \tag{3.9}$$

where,

$$\begin{cases} A_p = A_e + A_w + A_n + A_s + A_t + A_b - S_p^{\phi}\Delta V \\ A_e = D_e\mathcal{J}(Pe) + \|-F_e, 0\| \\ A_w = D_w\mathcal{J}(Pe) + \|-F_w, 0\| \\ A_n = D_n\mathcal{J}(Pe) + \|F_n, 0\| \\ A_s = D_s\mathcal{J}(Pe) + \|-F_s, 0\| \\ A_t = D_t\mathcal{J}(Pe) + \|F_t, 0\| \\ A_b = D_b\mathcal{J}(Pe) + \|-F_b, 0\| \\ B = A_p^0\phi_P^0\Delta V + S_\varsigma^0\Delta V \end{cases} \tag{3.10}$$

where $\mathcal{J}$ denote the interpolation function on the control volume surfaces, which depends only on the Péclèt local number based on the control volume size ($Pe = F/D$) and the symbol $\|\quad\|$ denotes the highest number inside the argument.

The source term was linearized so that $S_P^{\phi} = S_\varsigma^0 + S_p^{\phi}\phi_P$. Therefore, the advective flow rate (F) and the diffusivity flow rate (D), can be obtained by the following expressions:

$$\begin{cases} F_e = \rho v_{\theta_e}\Delta r\Delta z \\ F_w = \rho v_{\theta_w}\Delta r\Delta z \\ F_n = \rho(rv_r)_n\Delta\theta\Delta z \\ F_s = \rho(rv_r)_s\Delta\theta\Delta z \\ F_t = \rho v_{z_t}r\Delta r\Delta\theta \\ F_b = \rho v_{z_b}r\Delta r\Delta\theta \end{cases} \tag{3.11}$$

θ-axis	r-axis	z-axis
$\begin{cases} D_e = \frac{\Gamma}{r}\frac{\Delta r \Delta z}{\delta\theta_e} \\ D_w = \frac{\Gamma}{r}\frac{\Delta r \Delta z}{\delta\theta_w} \\ D_n = \Gamma r \frac{\Delta\theta\Delta z}{\delta r_n} \\ D_s = \Gamma r \frac{\Delta\theta\Delta z}{\delta r_s} \\ D_t = \Gamma \frac{r\Delta r\Delta\theta}{\delta z_t} \\ D_b = \Gamma \frac{r\Delta r\Delta\theta}{\delta z_b} \end{cases}$	$\begin{cases} D_e = \frac{\Gamma}{r}\frac{\Delta r \Delta z}{\delta\theta_e} \\ D_w = \frac{\Gamma}{r}\frac{\Delta r \Delta z}{\delta\theta_w} \\ D_n = \Gamma r \frac{\Delta\theta\Delta z}{\delta r_n} \\ D_s = \Gamma r \frac{\Delta\theta\Delta z}{\delta r_s} \\ D_t = \Gamma \frac{r\Delta r\Delta\theta}{\delta z_t} \\ D_b = \Gamma \frac{r\Delta r\Delta\theta}{\delta z_b} \end{cases}$	$\begin{cases} D_e = \frac{\Gamma}{r}\frac{\Delta r \Delta z}{\delta\theta_e} \\ D_w = \frac{\Gamma}{r}\frac{\Delta r \Delta z}{\delta\theta_w} \\ D_n = \Gamma r_n \frac{\Delta\theta\Delta z}{\delta r_n} \\ D_s = \Gamma r_s \frac{\Delta\theta\Delta z}{\delta r_s} \\ D_t = \Gamma \frac{r\Delta r\Delta\theta}{\delta z_t} \\ D_b = \Gamma \frac{r\Delta r\Delta\theta}{\delta z_b} \end{cases}$

(3.12)

Table 6 shows some of the interpolation functions used in the literature (PATANKAR, 1980).

TABLE 6 - $\mathcal{J}$(PE) FUNCTION FOR SOME INTERPOLATION SCHEMES.

Interpolation function	$\boldsymbol{\mathcal{J}(\mathrm{Pe} = \mathrm{F}/\mathrm{D})}$
Up-Wind scheme	1
Hybrid scheme	$\left\|0, \left(1 - \frac{1}{2}\lvert \mathrm{Pe} \rvert\right)\right\|$
Power-Law scheme	$\left\|0, \left(1 - \frac{1}{10}\lvert \mathrm{Pe} \rvert\right)^5\right\|$

SOURCE: PATANKAR (1980).

Accordingly, the heptadiagonal linear system can be represented in a compact form, as follows:

$$A_p\phi_P - \sum A_{nb}\phi_{NB} = B \tag{3.13}$$

where $A_{nb}\phi_{NB}$ stands for the products of the neighborhood coefficients with their respective variables. The above linear system is solved by means of the Biconjugate gradient stabilized method (BiCGSTAB) together with the Thomas Algorithm (TDMA - Tridiagonal Matrix Algorithm) as a preconditioner. Both TDMA and BiCGSTAB are explained in detail in Appendixes I and II, respectively. The TDMA is applied iteratively by means of a line-by-line

procedure in the radial and the axial axis (r and z), while in the tangential axis (θ) the cyclic nature of the problem is considered by means of an algorithm called CTDMA.

3.3 DISCRETIZED EQUATIONS IN THE STAGGERED GRID

A staggered grid is applied for the velocity computation (HARLOW and WELCH, 1965) to avoid non-physical behaviors of the pressure gradients (VERSTEEG and MALALASEKERA, 2007). The pressure field is evaluated at the central points, while the velocities are evaluated at the control volume surfaces (PATANKAR, 1980). Consequently, the pressure field remains properly coupled with the velocity fields.

Figure 17 symbolizes a two-dimensional mesh with the staggered grid, where the i and j indices represent the control volume positions, while I and J stand for the control volume surfaces. In a three-dimensional mesh, the indices k and K are also used to represent, respectively, the control volume position and points on the vertical axis (z). One can note that the velocity control volumes are shifted: the tangential one (green) is shifted clockwise and centered on the east face of the pressure control volume. In the same way, the radial velocity control volume (red) is shifted to the north, while the axial one is shifted to the top direction, despite not being depicted in the figure.

As the points for pressure integration coincide with the velocities faces of the control volumes in the staggered grid, the pressure gradients can be discretized as follows:

$$\frac{1}{r}\frac{\partial p}{\partial \theta} = \frac{1}{r}\frac{p_E - p_P}{\Delta\theta_{v_\theta}} \tag{3.14}$$

$$\frac{\partial p}{\partial r} = \frac{p_N - p_P}{\Delta r_{v_r}} \tag{3.15}$$

$$\frac{\partial p}{\partial z} = \frac{p_T - p_P}{\Delta z_{v_z}} \tag{3.16}$$

FIGURE 17 - STAGGERED TWO-DIMENSIONAL MESH IN POLAR CYLINDRICAL COORDINATES.

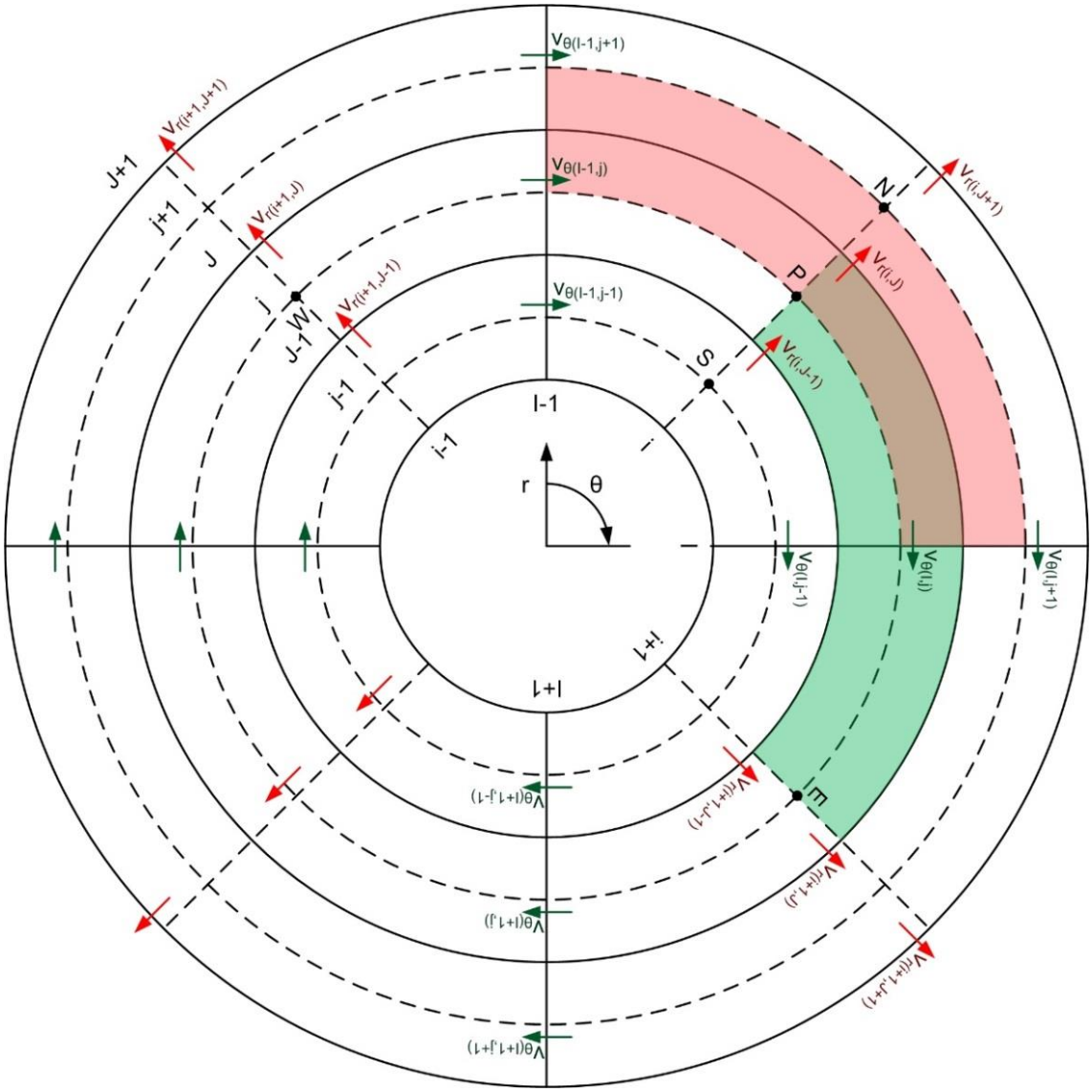

where $\Delta\theta_{v_\theta}$, Δr_{v_r} and Δz_{v_z} represent the control volumes dimensions in their respective directions.

Thus, the momentum conservation equations (represented in a general form by Equation 3.9) are integrated, so that the discretized equations are as follows:

$$A_{I,j,k} v_{\theta_{I,j,k}} = \sum A_{nb} v_{\theta_{nb}} + \frac{1}{r_j} \frac{\left(p_{i,j,k} - p_{i+1,j,k}\right)}{\Delta\theta_{v_\theta}} \Delta V_{v_\theta} + \overline{B}_{v_\theta} \Delta V_{v_\theta} \qquad (3.17)$$

$$A_{i,J,k} v_{r_{i,J,k}} = \sum A_{nb} v_{r_{nb}} + \frac{\left(p_{i,j,k} - p_{i,j+1,k}\right)}{\Delta r_{v_r}} \Delta V_{v_r} + \overline{B}_{v_r} \Delta V_{v_r} \qquad (3.18)$$

$$A_{i,j,K} v_{z_{i,j,K}} = \sum A_{nb} v_{z_{nb}} + \frac{\left(p_{i,j,k} - p_{i,j,k+1}\right)}{\Delta z_{v_z}} \Delta V_{v_z} + \overline{B}_{v_z} \Delta V_{v_z} \qquad (3.19)$$

where $\overline{B}$ denotes the source term without the pressure differential term and ΔV stands for the present control volume.

Moreover, the advective and diffusive fluxes, for all control volumes in the staggered grid, is necessary to evaluate the coefficients (A) of the pressure linear system. Therefore, the dimensions of the control volumes in all directions are defined, as well as the pressure control volumes, are shown in Table 7.

TABLE 7 - CONTROL VOLUMES DIMENSIONS: STAGGERED GRID (VELOCITIES) AND CO-LOCATED (PRESSURE).

v_θ	v_r	v_z	p
$\Delta\theta = \theta_{i+1} - \theta_i$ $\delta\theta_e = \theta_{I+1} - \theta_I$ $\delta\theta_w = \theta_I - \theta_{I-1}$ $\Delta r = r_J - r_{J-1}$ $\delta r_n = r_{j+1} - r_j$ $\delta r_s = r_j - r_{j-1}$ $\Delta z = z_K - z_{K-1}$ $\delta z_t = z_{k+1} - z_k$ $\delta z_b = z_k - z_{k-1}$	$\Delta\theta = \theta_I - \theta_{I-1}$ $\delta\theta_e = \theta_{i+1} - \theta_i$ $\delta\theta_w = \theta_i - \theta_{i-1}$ $\Delta r = r_{j+1} - r_j$ $\delta r_n = r_{J+1} - r_J$ $\delta r_s = r_J - r_{J-1}$ $\Delta z = z_K - z_{K-1}$ $\delta z_t = z_{k+1} - z_k$ $\delta z_b = z_k - z_{k-1}$	$\Delta\theta = \theta_I - \theta_{I-1}$ $\delta\theta_e = \theta_{i+1} - \theta_i$ $\delta\theta_w = \theta_i - \theta_{i-1}$ $\Delta r = r_J - r_{J-1}$ $\delta r_n = r_{j+1} - r_j$ $\delta r_s = r_j - r_{j-1}$ $\Delta z = z_{k+1} - z_k$ $\delta z_t = z_{K+1} - z_K$ $\delta z_b = z_K - z_{K-1}$	$\Delta\theta = \theta_I - \theta_{I-1}$ $\delta\theta_e = \theta_{i+1} - \theta_i$ $\delta\theta_w = \theta_i - \theta_{i-1}$ $\Delta r = r_J - r_{J-1}$ $\delta r_n = r_{j+1} - r_j$ $\delta r_s = r_j - r_{j-1}$ $\Delta z = z_K - z_{K-1}$ $\delta z_t = z_{k+1} - z_k$ $\delta z_b = z_k - z_{k-1}$

The coefficients of the heptadiagonal set of equations are evaluated in a different way for flows of Newtonian and non-Newtonian fluids as follows:

3.3.1 Newtonian Fluid

Considering a flow of Newtonian fluid, the advective (F) and diffusive (D) fluxes of the discretized terms of the Navier-Stokes equations can be evaluated as follows:

$$\begin{cases} F_e = \rho v_{\theta_e} \Delta r \Delta z \\ F_w = \rho v_{\theta_w} \Delta r \Delta z \\ F_n = \rho r_n v_{r_n} \Delta\theta \Delta z \\ F_s = \rho r_s v_{r_s} \Delta\theta \Delta z \\ F_t = \rho v_{z_t} r \Delta\theta \Delta r \\ F_b = \rho v_{z_t} r \Delta\theta \Delta r \end{cases} \qquad (3.20)$$

$$\begin{cases} D_e = \frac{\mu}{r}\frac{\Delta r \Delta z}{\delta\theta_e} \\ D_w = \frac{\mu}{r}\frac{\Delta r \Delta z}{\delta\theta_w} \\ D_n = \mu\frac{r\Delta\theta\Delta z}{\delta r_n}\left(\frac{r}{r_n}\right) \\ D_s = \mu\frac{r\Delta\theta\Delta z}{\delta r_s}\left(\frac{r}{r_s}\right) \\ D_t = \mu\frac{r\Delta\theta\Delta r}{\delta z_t} \\ D_b = \mu\frac{r\Delta\theta\Delta r}{\delta z_b} r \end{cases} \tag{3.21}$$

Also, the source terms (B), without the pressure gradients, and the $S_p^{\phi}\Delta V$ terms can be evaluated as follows:

- Tangential velocity component (v_θ):

$$\begin{gathered} S_p^{\phi}\Delta V = \rho\frac{r\Delta\theta\Delta r\Delta z}{\Delta t} + \rho v_r \phi_P \Delta r\Delta\theta\Delta z \\ B = \rho\phi_P^0\frac{r\Delta\theta\Delta r\Delta z}{\Delta t} + \frac{2\mu}{r}\left[v_{r_e} - v_{r_w}\right]\Delta r\Delta z + \rho g_\theta r\Delta r\Delta\theta\Delta z \end{gathered} \tag{3.22}$$

- Radial velocity component (v_r):

$$\begin{gathered} S_p^{\phi}\Delta V = \rho\frac{r\Delta\theta\Delta r\Delta z}{\Delta t} \\ B = \rho\phi_P^0\frac{r\Delta\theta\Delta r\Delta z}{\Delta t} + \rho {v_\theta}^2\Delta r\Delta\theta\Delta z - \frac{2\mu}{r}\left[v_{\theta_e} - v_{\theta_w}\right]\Delta r\Delta z \\ + \rho g_r r\Delta r\Delta\theta\Delta z \end{gathered} \tag{3.23}$$

- Axial velocity component (v_z):

$$\begin{gathered} S_p^{\phi}\Delta V = \rho\frac{r\Delta\theta\Delta r\Delta z}{\Delta t} \\ B = \rho\phi_P^0\frac{r\Delta\theta\Delta r\Delta z}{\Delta t} + \rho g_z r\Delta r\Delta\theta\Delta z \end{gathered} \tag{3.24}$$

3.3.2 Non-Newtonian Fluid

In the case of a flow of non-Newtonian fluid, the apparent viscosity at each control volume is of great importance as the viscosity is dependent on the shear rate. Thereafter, in all iterations, both the shear rate and apparent viscosity are evaluated for all control volumes. Therefore, the advective (F) and diffusive (D) terms of the discretized Navier-Stokes equations can be evaluated as follows:

$$\begin{cases} F_e = \rho v_{\theta_e} \Delta r \Delta z \\ F_w = \rho v_{\theta_w} \Delta r \Delta z \\ F_n = \rho (r v_r)_n \Delta\theta \Delta z \\ F_s = \rho (r v_r)_s \Delta\theta \Delta z \\ F_t = \rho v_{z_t} r \Delta r \Delta\theta \\ F_b = \rho v_{z_b} r \Delta r \Delta\theta \end{cases} \tag{3.25}$$

θ-axis	r-axis	z-axis
$\begin{cases} D_e = \frac{2}{r}\eta_e \frac{\Delta r \Delta z}{\delta\theta_e} \\ D_w = \frac{2}{r}\eta_w \frac{\Delta r \Delta z}{\delta\theta_w} \\ D_n = \frac{r_n^2}{r}\eta_n \frac{\Delta\theta \Delta z}{\delta r_n} \\ D_s = \frac{r_s^2}{r}\eta_s \frac{\Delta\theta \Delta z}{\delta r_s} \\ D_t = \eta_t \frac{r \Delta r \Delta\theta}{\delta z_t} \\ D_b = \eta_b \frac{r \Delta r \Delta\theta}{\delta z_b} \end{cases}$	$\begin{cases} D_e = \frac{1}{r}\eta_e \frac{\Delta r \Delta z}{\delta\theta_e} \\ D_w = \frac{1}{r}\eta_w \frac{\Delta r \Delta z}{\delta\theta_w} \\ D_n = 2 r_n \eta_n \frac{\Delta\theta \Delta z}{\delta r_n} \\ D_s = 2 r_s \eta_s \frac{\Delta\theta \Delta z}{\delta r_s} \\ D_t = \eta_t \frac{r \Delta r \Delta\theta}{\delta z_t} \\ D_b = \eta_b \frac{r \Delta r \Delta\theta}{\delta z_b} \end{cases}$	$\begin{cases} D_e = \frac{1}{r}\eta_e \frac{\Delta r \Delta z}{\delta\theta_e} \\ D_w = \frac{1}{r}\eta_w \frac{\Delta r \Delta z}{\delta\theta_w} \\ D_n = r_n \eta_n \frac{\Delta\theta \Delta z}{\delta r_n} \\ D_s = r_s \eta_s \frac{\Delta\theta \Delta z}{\delta r_s} \\ D_t = 2\eta_t \frac{r \Delta r \Delta\theta}{\delta z_t} \\ D_b = 2\eta_b \frac{r \Delta r \Delta\theta}{\delta z_b} \end{cases}$

(3.26)

Similarly, the source terms (B), without the pressure gradients, and the $S_p^\phi \Delta V$ terms are evaluated as follows.

- Tangential velocity component (v_θ):

$$S_p^\phi \Delta V = \rho \frac{r \Delta\theta \Delta r \Delta z}{\Delta t} + \rho v_r \phi_P \Delta r \Delta\theta \Delta z \tag{3.27}$$

$$B = \rho\phi_P^0 \frac{r\Delta\theta\Delta r\Delta z}{\Delta t} + \frac{2}{r}\left[\eta_e v_{r_e} - \eta_w v_{r_w}\right]\Delta r\Delta z + \frac{1}{r}\left[\eta_n r_n \left(\frac{v_{r_e} - v_{r_w}}{\Delta\theta}\right)_n - \eta_s r_s \left(\frac{v_{r_e} - v_{r_w}}{\Delta\theta}\right)_s\right]\Delta\theta\Delta z + \left[\eta_t \left(\frac{v_{z_e} - v_{z_w}}{\Delta\theta}\right)_t - \eta_b \left(\frac{v_{z_e} - v_{z_w}}{\Delta\theta}\right)_b\right]\Delta\theta\Delta r - \frac{1}{r}\left[(\eta r\phi)_n - (\eta r\phi)_s\right]\Delta\theta\Delta z + \rho g_\theta r\Delta r\Delta\theta\Delta z$$

- Radial velocity component (v_r):

$$S_p^\phi \Delta V = \rho \frac{r\Delta\theta\Delta r\Delta z}{\Delta t} + \frac{2\eta}{r}\phi_P \Delta\theta\Delta r\Delta z$$

$$B = \rho\phi_P^0 \frac{r\Delta\theta\Delta r\Delta z}{\Delta t} + \left[\eta_e \left(\frac{v_{\theta_n} - v_{\theta_s}}{\Delta r}\right)_e - \eta_s \left(\frac{v_{\theta_n} - v_{\theta_s}}{\Delta r}\right)_w\right]\Delta r\Delta z + \left[\eta_t \left(\frac{v_{z_n} - v_{z_s}}{\Delta r}\right)_t - \eta_b \left(\frac{v_{z_n} - v_{z_s}}{\Delta r}\right)_b\right] r\Delta\theta\Delta r + \rho {v_\theta}^2 \Delta r\Delta\theta\Delta z - \frac{2\eta}{r}\left[v_{\theta_e} - v_{\theta_w}\right]\Delta r\Delta z - \frac{1}{r}\left[(\eta v_\theta)_e - (\eta v_\theta)_w\right]\Delta r\Delta z + \rho g_r r\Delta r\Delta\theta\Delta z \tag{3.28}$$

- Axial velocity component (v_z)

$$S_p^\phi \Delta V = \rho \frac{r\Delta\theta\Delta r\Delta z}{\Delta t}$$

$$B = \rho\phi_P^0 \frac{r\Delta\theta\Delta r\Delta z}{\Delta t} + \left[\eta_e \left(\frac{v_{\theta_t} - v_{\theta_b}}{\Delta z}\right)_e - \eta_w \left(\frac{v_{\theta_t} - v_{\theta_b}}{\Delta z}\right)_w\right]\Delta r\Delta z + \left[\eta_n r_n \left(\frac{v_{r_t} - v_{r_b}}{\Delta z}\right)_n - \eta_s r_s \left(\frac{v_{r_t} - v_{r_b}}{\Delta z}\right)_s\right]\Delta\theta\Delta z + \rho g_z r\Delta r\Delta\theta\Delta z \tag{3.29}$$

3.4 PRIME METHOD

The PRIME method (PRessure Implicit Momentum Explicit), introduced by Maliska and Raithby (1984), is applied to solve the pressure-velocity coupling. According to this method, the pressure field is computed implicitly, while the velocity components (v_θ, v_r, and v_z) are

computed explicitly so that there is only one linear system (pressure) that must be solved. The velocities correction and the pressure computation are realized in one step, whereas the pressure field is used to correct iteratively the velocities on the next step.

The method consists of introducing the transport equations, written in explicit form for the velocity components, into the mass conservation, thus obtaining a Poisson-like implicit equation to calculate the pressure field.

To apply the method, it is necessary to compute, beforehand, the pseudo-velocities from the discretized governing equations, as follows:

$$\widehat{v_{\theta_P}} = \frac{A_{nb} v_{\theta_{NB}}}{A_P} \tag{3.30}$$

$$\widehat{v_{r_P}} = \frac{A_{nb} v_{r_{NB}}}{A_P} \tag{3.31}$$

$$\widehat{v_{z_P}} = \frac{A_{nb} v_{z_{NB}}}{A_P} \tag{3.32}$$

Next, the pseudo-velocities $\widehat{v_{\theta_P}}$, $\widehat{v_{r_P}}$, and $\widehat{v_{z_P}}$, which compute all the terms from the conservation equations but the pressure ones, are used for the computation of v_θ, v_r, and v_z velocity components, which are stored on the faces of the pressure control volumes, as follows:

$$v_{\theta_e} = v_{\theta_{I,j,k}} = \widehat{v_{\theta_e}} - \bar{d}_e (p_E - p_P) \tag{3.33}$$

$$v_{\theta_w} = v_{\theta_{I-1,j,k}} = \widehat{v_{\theta_w}} - \bar{d}_e (p_P - p_W) \tag{3.34}$$

$$v_{r_n} = v_{r_{i,J,k}} = \widehat{v_{r_n}} - \bar{d}_n (p_N - p_P) \tag{3.35}$$

$$v_{r_s} = v_{r_{i,J-1,k}} = \widehat{v_{r_s}} - \bar{d}_s (p_P - p_S) \tag{3.36}$$

$$v_{z_t} = v_{z_{i,j,K}} = \widehat{v_{z_t}} - \bar{d}_t (p_T - p_P) \tag{3.37}$$

$$v_{z_b} = v_{r_{i,j,K-1}} = \widehat{v_{z_b}} - \bar{d}_b (p_P - p_B) \tag{3.38}$$

where the $\bar{d}$ terms are as follows:

$$\bar{d}_e = \frac{\Delta r \Delta z}{A_{p_{I,j,k}}} \tag{3.39}$$

$$\bar{d}_w = \frac{\Delta r \Delta z}{A_{p_{I-1,j,k}}} \tag{3.40}$$

$$\bar{d}_n = \frac{r_J \Delta\theta \Delta z}{A_{p_{i,J,k}}} \tag{3.41}$$

$$\bar{d}_s = \frac{r_{J-1} \Delta\theta \Delta z}{A_{p_{i,J-1,k}}} \tag{3.42}$$

$$\bar{d}_t = \frac{r_j \Delta\theta \Delta r}{A_{p_{i,j,K}}} \tag{3.43}$$

$$\bar{d}_b = \frac{r_j \Delta\theta \Delta r}{A_{p_{i,j,K-1}}} \tag{3.44}$$

Previously, the coefficients of the linear system, A_p, have been calculated for each velocity component. So, substituting Equations (3.33) to (3.38) into the discretized continuity Equation (3.6) yields:

$$\begin{aligned} \rho\left[\widehat{v_\theta}_e - \bar{d}_e(p_E - p_P) - \widehat{v_\theta}_w - \bar{d}_w(p_P - p_W)\right]\Delta r \Delta z \\ + \frac{\rho}{r}\left[r_n \widehat{v}_{r_n} - r_n \bar{d}_n (p_N - p_P) - r_s \widehat{v}_{r_s}\right. \\ \left. - r_s \bar{d}_s (p_P - p_S)\right] r \Delta\theta \Delta z \\ + \rho\left[\widehat{v}_{z_t} - \bar{d}_t(p_T - p_P) - \widehat{v}_{z_b}\right. \\ \left. - \bar{d}_b(p_P - p_B)\right] r \Delta r \Delta\theta = 0 \end{aligned} \tag{3.45}$$

So, one can obtain the heptadiagonal linear system for pressure calculation by rearranging the equation above:

$$A_p p_P = A_e p_E + A_w p_W + A_n p_N + A_s p_S + A_t p_T + A_b p_B + B \tag{3.46}$$

where,

$$\begin{cases} A_p = A_e + A_w + A_n + A_s + A_t + A_b \\ A_e = \rho \bar{d}_e \Delta r \Delta z \\ A_w = \rho \bar{d}_w \Delta r \Delta z \\ A_n = \rho \left(\frac{r_n}{r}\right) \bar{d}_n r \Delta\theta \Delta z \\ A_s = \rho \left(\frac{r_s}{r}\right) \bar{d}_s r \Delta\theta \Delta z \\ A_t = \rho \bar{d}_t r \Delta\theta \Delta r \\ A_b = \rho \bar{d}_b r \Delta\theta \Delta r \end{cases} \tag{3.47}$$

and

$$B = \rho \left[\left(\widehat{v_\theta}_w - \widehat{v_\theta}_e\right) \Delta r \Delta z + \left(\left(\frac{r_s}{r}\right) \widehat{v}_{r_s} - \left(\frac{r_n}{r}\right) \widehat{v}_{r_n} \right) r \Delta\theta \Delta z + \left(\widehat{v}_{z_b} - \widehat{v}_{z_t}\right) \right] r \Delta\theta \Delta r \Delta z \tag{3.48}$$

Equation (3.46) is then solved by means of the Biconjugate gradient stabilized method (BiCGSTAB) together with the TDMA algorithm, applied line-by-line, as a preconditioner.

The PRIME algorithm follows the steps below (MALISKA, 1995):

1. Estimate the velocity (v_θ, v_r, and v_z) and pressure (p) fields;
2. Compute the momentum equations coefficients;
3. Compute the pseudo-velocities on the surfaces of the pressure control volumes;
4. Solve the linear system and compute the pressure field, from Equation (3.46);
5. Correct the velocity components;
6. Go back to step 2 until convergence is achieved.

3.5 COMPUTATIONAL MESH

The discretization employed here uses a non-uniform cylindrical mesh with a co-located arrangement for the pressure control volumes, and a staggered one for the velocities. In the discretized domain, it was decided to place points on its physical boundaries. Moreover, the non-uniform mesh has a high-concentration of points near the boundaries for the radial and axial axes. For the θ axis, the non-uniform arrangement is used only for non-steady state flows. This kind of arrangement favors a faster convergence as the pressure and velocities gradients are more intense near the physical boundaries.

The non-uniform mesh was generated algebraically from the equation proposed by Wood (1996) in radial and axial directions:

$$\varepsilon = \frac{\varepsilon^*(\varsigma + 1) - (\varsigma - 1)}{2(\delta^* + 1)} \tag{3.49}$$

where

$$\varepsilon^* = \left(\frac{\varsigma + 1}{\varsigma - 1}\right)^{\frac{2q-Q-1}{Q-1}} \tag{3.50}$$

where ε denotes control volume surface position, q the volume index, Q the number of control volumes along the coordinate direction and ς is a concentration factor.

3.6 CONVERGENCE CRITERIA

In the present work, both the mass convergence and the momentum convergence are monitored to advance the simulation to the next time step. If both mass and momentum (3 directions) conservation residues, for all the control volumes, converge to a value below the convergence (tolerance), the simulation proceeds to the next time step.

The following equations demonstrate how the residues are evaluated. For the mass conservation:

$$\mathrm{ERR}_{\mathrm{mass}} = 1 - \frac{\sum \mathrm{F}_{\mathrm{in}}}{\sum \mathrm{F}_{\mathrm{out}}} \tag{3.51}$$

One can note that, as the fluid is considered incompressible, the residue is a simple ratio between the sum of the mass fluxes that enter the control volume and the sum of the mass fluxes that exit the control volume. Similarly, the momentum residues are as follows:

$$\mathrm{ERR}_{\mathrm{momentum}} = 1 - \frac{\mathrm{A_p}\phi_{\mathrm{P}}}{\mathrm{B} + \sum \mathrm{A_{nb}}\phi_{\mathrm{NB}}} \tag{3.52}$$

The error between the evaluated velocity field and the one from the prior iteration are monitored in all iterations, as well as the residue from the linear system solution through the norm of the BiCGSTAB residue.

Furthermore, the discrepancies between (experimental and numerical) values obtained from the open literature, and numerical residues of the present work were quantified through the RMS deviation (Root Mean Square) as follows:

$$\mathrm{RMS} = \sqrt{\frac{\sum_{i=1}^{n}\left(\phi_j - \phi_i\right)^2}{n - p}} \tag{3.53}$$

where ϕ is the generic variable, and ϕ_j is the reference value of the generic variable either measured by experiments or found in the open literature. Also, n is the total number of points, and p represents the degree of freedom of model (e.g., 2 for Power-Law model and 3 for Herschel-Bulkley model).

A simple statistical indicator is the SSE (sum of square errors), which is computed from:

$$\mathrm{SSE} = \sum_{i=1}^{n}\left(\phi_j - \phi_i\right)^2 \tag{3.54}$$

So, both the RMS and SSE are used to compare the numerical results with the experimental measurements. Also, it can be used to evaluate the best-fitting parameters for fluid model regressions.

3.7 CHAPTER SUMMARY

The algorithm employed for both Newtonian and non-Newtonian fluids is summarized in Figures 18 and 19. Because the PRIME method treats the pressure field implicitly, it can solve the linear system for each control volume in all iterations. The numerical simulations are detailed in Chapter 5, while the BiCGSTAB and TDMA solvers algorithms are presented in the appendixes.

FIGURE 18 - NEWTONIAN FLUID FLOW SOLVER.

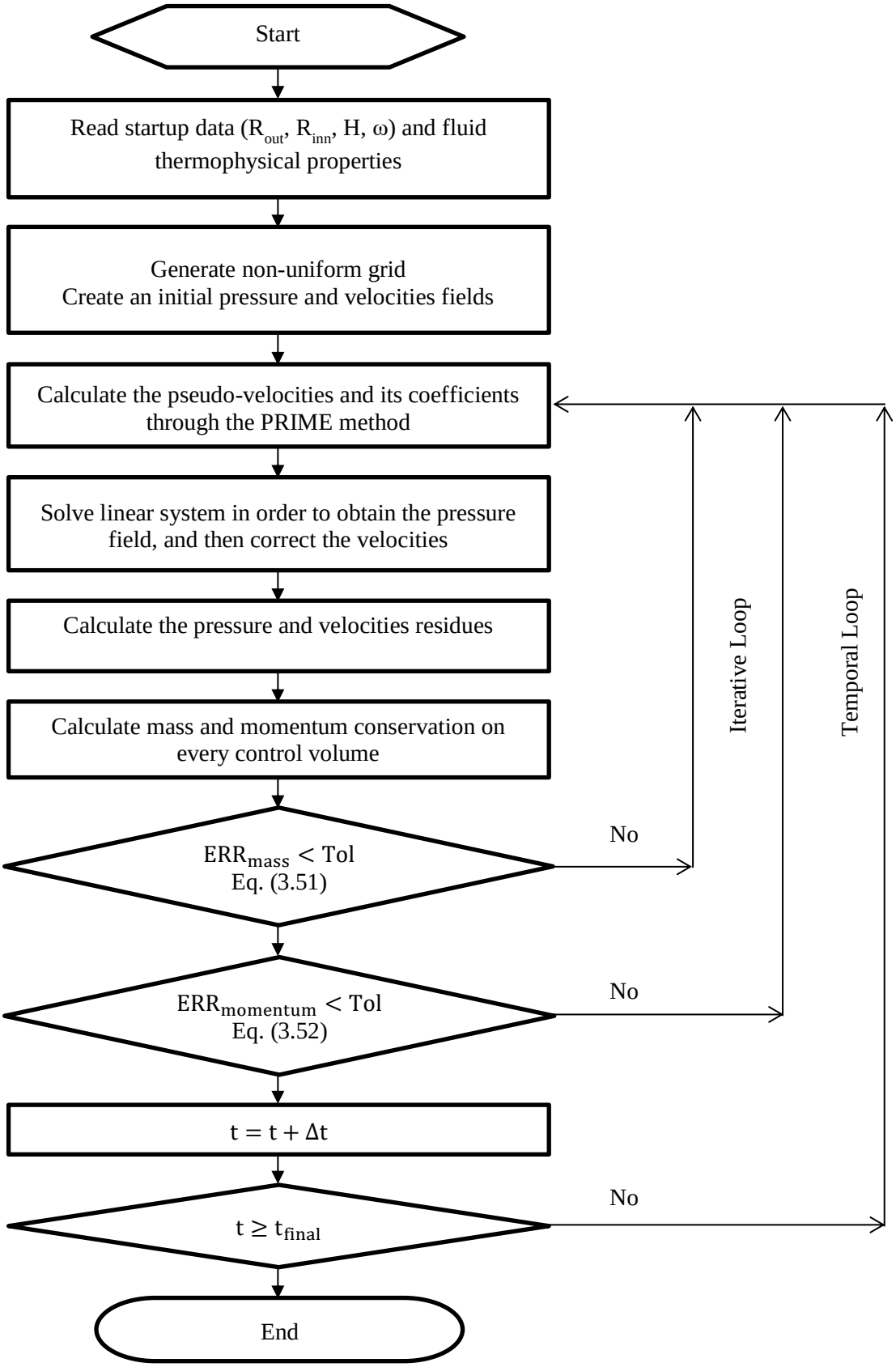

FIGURE 19 - NON-NEWTONIAN FLUID FLOW SOLVER.

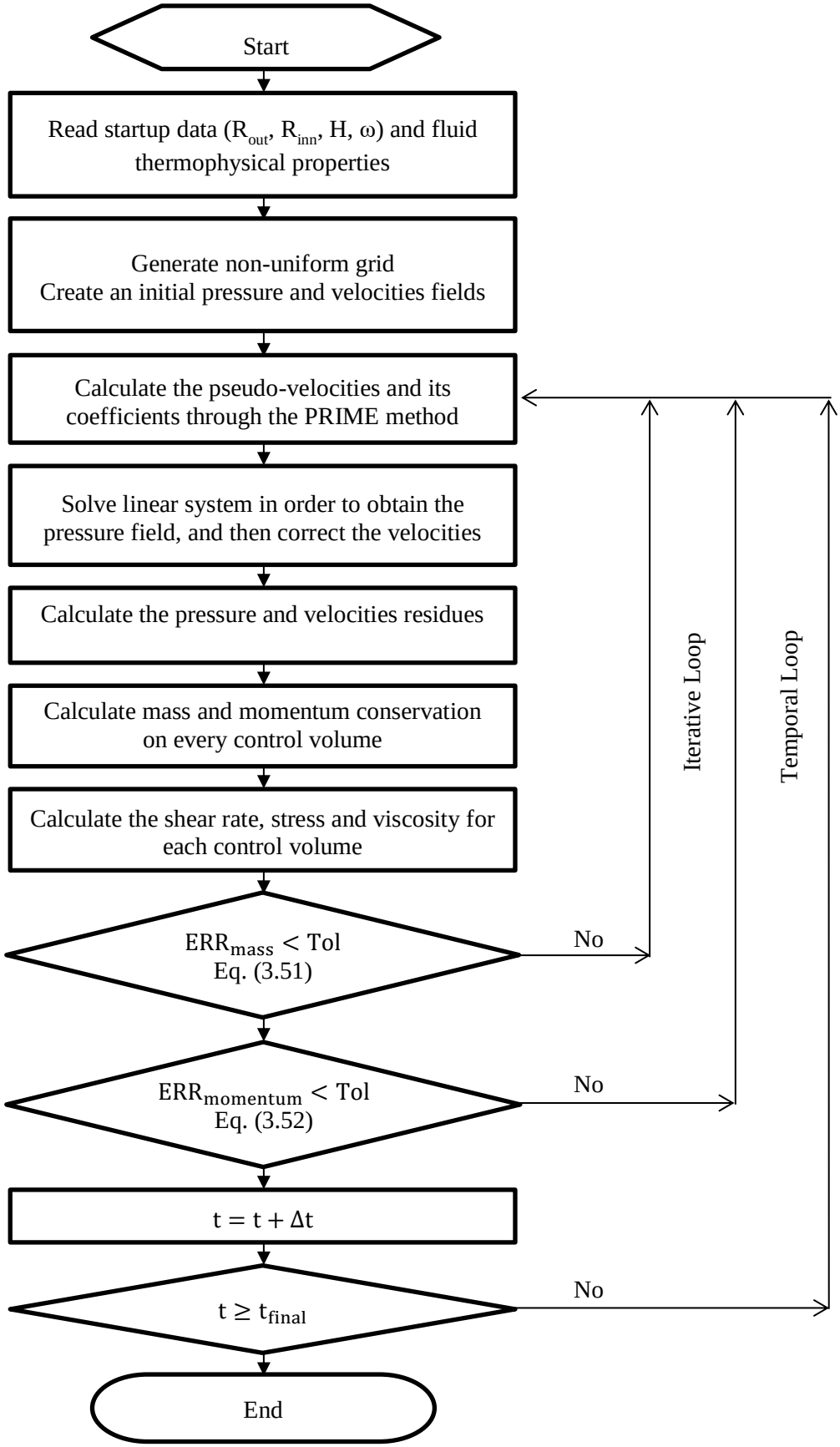

4 EXPERIMENTAL WORK

Experimental tests were carried out, in the LTT – UFPR, to obtain a reliable database of torque and angular velocity, which is used to calculate rheological parameters of the fabric-water suspensions through data regression. This chapter presents a description of the experimental facility and its equipment (i.e., servo-motor, servo-drive, test rig, data acquisition, control system and closed-loop water supply). Moreover, the test plan, that was designed according to the rheometry model (Couette inverse problem), shown in Chapter 2, is also detailed. The results for both steady-state and periodic tests are presented and discussed.

4.1 TEST RIG

A purpose-built experimental facility was constructed for this thesis work. The experimental apparatus is comprised of a tank, a basket, an inner rotating cylinder, and a metallic structure. The cylindrical structure is presented in Figure 20, while the schematic view of the test apparatus is presented in Figure 21. At first, the plastic inner cylinder had a smooth surface with a radius of 73 mm, while the aluminum outer cylinder has a radius of 269 mm. Consequently, the radius ratio, $k = R_{inn}/R_{out}$, was approximately 0.27, which is considered a wide-gap geometry for the sake of rheometry and large enough to measure the viscosity of large particles (BARNES, 2000).

FIGURE 20 - TOP VIEW OF THE TAYLOR-COUETTE RHEOMETER.

FIGURE 21 - SCHEMATIC VIEW OF THE TEST APPARATUS.

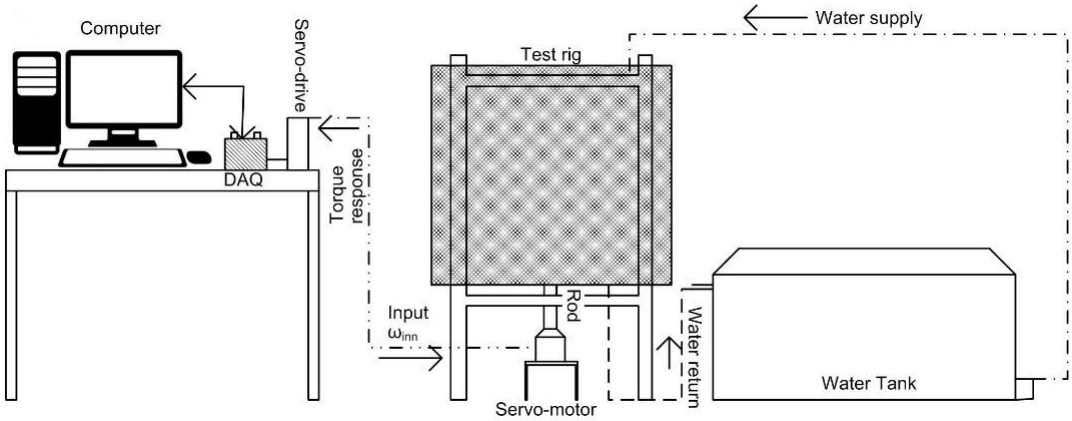

The servo-motor is coupled to a rod to drive the inner cylinder, while the rotation is controlled by the servo-drive, whose acquisition system records the torque values transmitted from the cylinder.

Additionally, the water used in the experimental tests is pumped from a 310-L tank, which forms a closed loop, as depicted in Figure 21. To avoid backflow caused by the residual water in the hose, a ball valve was installed in the discharge line between the basket and tank. After the test, the water is pumped back to the water tank through an additional pump. The metallic structure was made of structural steel and fixed to the floor. Also, elastomeric components were used to fix the tank to the structure so as to prevent vibrations.

Figure 22 represents the rheometer internal section. A scale was used to calibrate the water volume inside the basket through a visual inspection. Figure 23 depicts the calibration curve between the water column height (h) and the volume of water within the gap between the two cylinders. One can note that the symbols indicate the water volume while the line refers to the theoretical volume between the gap $(h\pi R_{out}^2 - h\pi R_{inn}^2)$.

FIGURE 22 - WATER COLUMN INSIDE THE GAP.

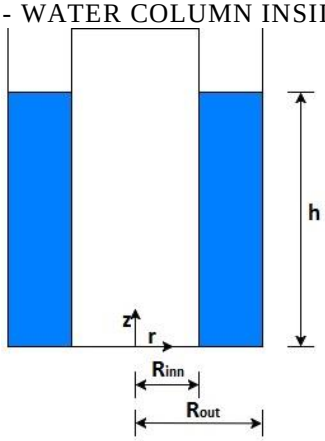

FIGURE 23 - WATER VOLUME CALIBRATION.

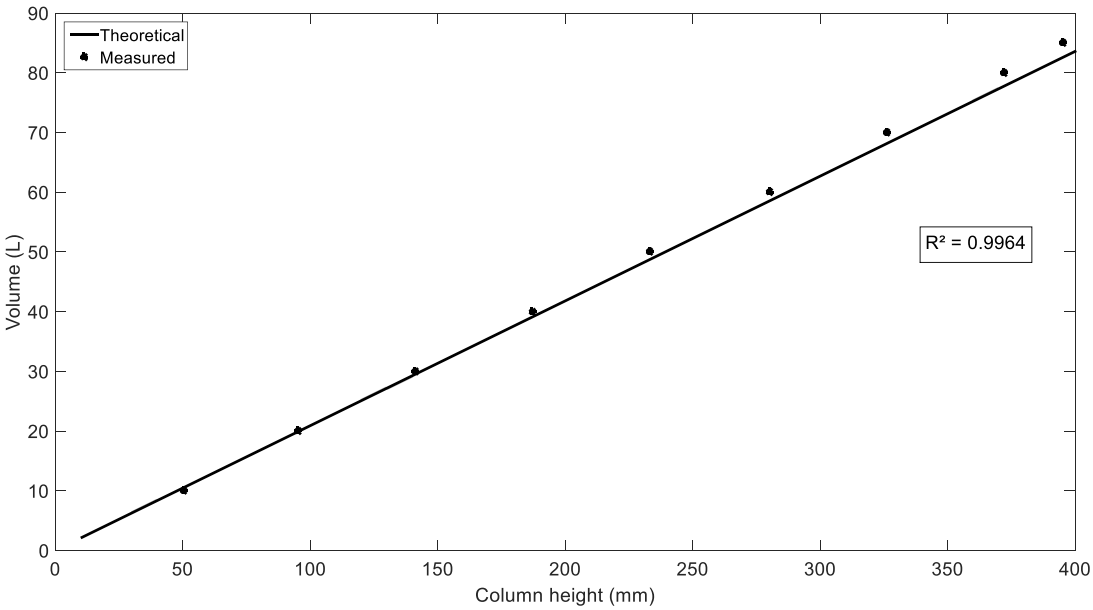

The torque required to drive the inner cylinder is provided by a servo-motor (Delta Electronics, model ECMA-E21320ES), which may be controlled through rotation, torque, angular position by combining two parameters. Table 8 presents the technical specifications of the equipment.

TABLE 8 - SPECIFICATIONS OF THE SERVO-MOTOR.

Power	2.0 kW
Maximum velocity	2000 rpm
Torque	9.55 N·m
Voltage	110 V
Electric current	11.0 A
Rotor inertia	$14.59 \cdot 10^{-4}$ kg·m²

The servo-motor control is handled through a servo-drive (Delta Electronics, model ASDA-B2-2023-B), which is powered by Triphase 220V. The servo-drive was programmed through the velocity control mode, setting the angular velocity of the inner cylinder transmitted to the fluid in each time instant (10^{-3} s). Also, the servo-drive when operated on speed control mode has a speed fluctuation rate of 0.01% or less at load fluctuation 0 to 100%, 0.01% or less at power fluctuation ±10%, and 0.01% or less at ambient temperature fluctuation 0°C to 50°C. The control is performed through the LabVIEW software, from National Instruments.

A data acquisition system (DAQ) from National Instruments (model cDAQ-9174 with 4 series modules) is connected to the servo-drive to convert the output electric signal into the rotation, torque, and angular position values. The modules NI 9215 for analogical inputs and the NI 9263 for analogical outputs, described in Table 9, were used.

TABLE 9 - DAQ MODULES.

Model	NI 9215	NI 9263
Channels	4	4
Resolution	16 bits	16 bits
Maximum voltage	10 V	10 V
Voltage maximum range	± 10 V	± 10 V

The angular velocity profile, which represents the inner cylinder behavior in time scale, is depicted in Figure 24. One can note that this behavior is similar to the agitation profile in a top-load vertical axis washing machine Firstly, an abrupt acceleration takes place, later the cylinder maintains the maximum velocity for a short period of time. So, the velocity decreases until the cylinder stops (i.e., time off). The same operation is repeated with the opposite direction.

FIGURE 24 - ANGULAR VELOCITY PROFILE.

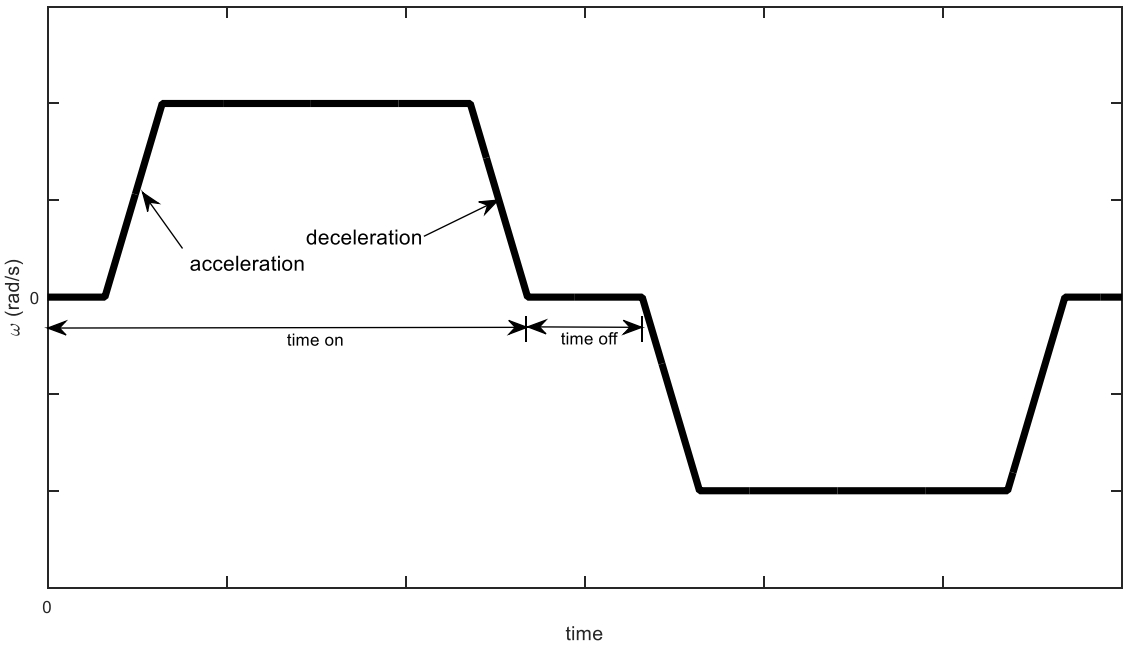

4.2 TESTES PLANNING

The experimental plan was designed considering three main variables: (a) fabric material, (b) fabric amount, and (c) angular velocity (ω). Two different tests were regimes proposed: (a) steady-state flow and (b) periodic flow. The raw data from the former was applied to obtain the non-Newtonian model parameters according to the rheometry techniques described in Chapter 2. In all tests, a water volume of 64 liters was established (which equals to 310 mm of the water column height).

4.2.1 Steady-state Tests

It has been mentioned in Chapter 2 that the measurement of rheological properties of suspensions, composed of large components (e.g., fabrics) in the disperse phase, may experience the undesirable wall-slip effects, which are observed when smooth walls, low shear rates, and large suspensions take place. Such an effect can be mitigated by roughening the cylinder walls or using the vane geometry assuming that the fluid is trapped between the blades, thus acting as a solid cylinder (BARNES and NGUYEN, 2001).

On that purpose, a rugged plastic inner cylinder surface, composed of small blades, was used to cover the inner cylinder surface with a radius of 76 mm, while the aluminum outer cylinder has a radius of 269 mm. This structure is depicted in Figure 25. Also, the inner surface has a four-bladed structure with 34 mm length, so that $k = R_{inn}/R_{out}$ is approximately 0.4. Experiments were carried out with different fabric-water suspensions, as follows: (i) 1.25 kg and 2.50 kg of 400 cm² (20 x 20 cm) cotton fabrics, (ii) 1.25 and 2.50 kg of 400 cm² semi-synthetic fabrics and (iii) 1.25 and 2.50 kg mix of 400 cm² cotton, and semi-synthetic fabrics. All the tests were carried out with a 310-mm column of fluid (fabric and water), thus the cylinders aspect ratio was $\Gamma = 1.96$. This structure is also represented in Figure 26, where one can see the inner cylinder surface with four-blade vane geometry from (a) front view and (b) top view.

FIGURE 25 - SCHEMATIC VIEW OF THE FOUR-BLADE VANE-GEOMETRY.

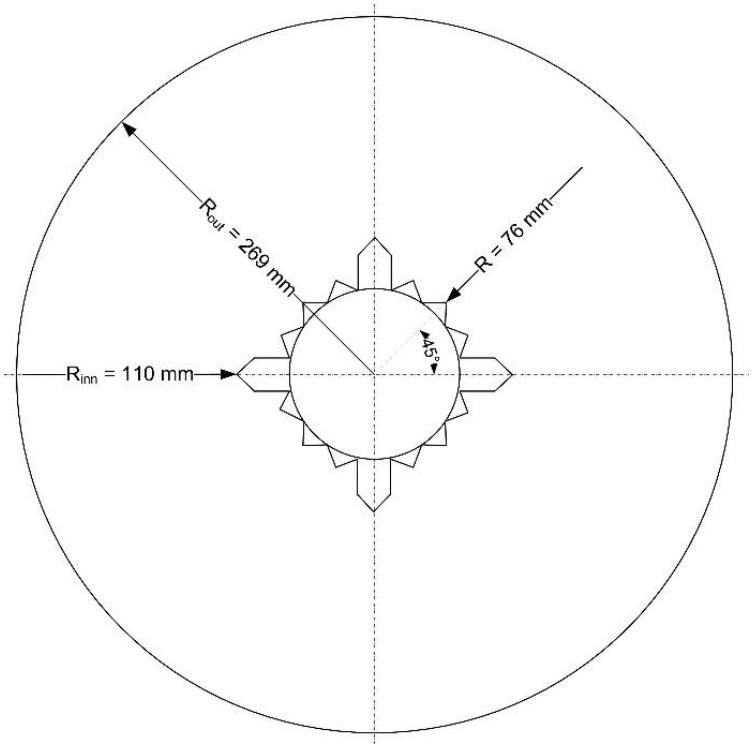

FIGURE 26 - RUGGED INNER CYLINDER SURFACE WITH FOUR-BLADE VANE GEOMETRY.

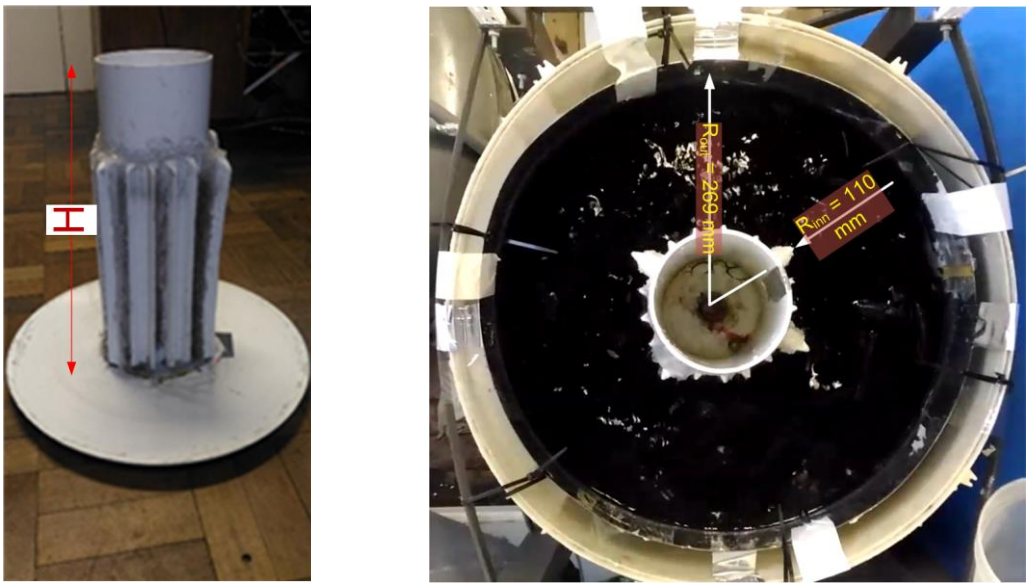

(A) (B)

(A) FRONT VIEW AND (B) TOP VIEW.

Ten pieces of cotton fabric have a mass of 93.94 g, so 134 pieces have 1.259 kg, and 268 pieces 2.517 kg. On the other hand, ten pieces of semi-synthetic fabric have a mass of 41.70 g, 300 pieces 1.251 kg, and 600 pieces of fabric have 2.502 kg. Considering the mixtures with different fabrics, the mixed fabric-water suspension is produced, so that the two different fabric

types have nearly the same mass. Thus, 150 pieces of semi-synthetic fabric and 66 pieces of cotton fabric totalize 1.246 kg, whereas 300 pieces of semi-synthetic fabric and 132 pieces of cotton fabric totalize 2.491 kg of mass.

For the steady-state flow, two main parameters were varied: (i) the angular velocities in the clockwise direction – 5, 10, 20, 30, 40, 50, 60, 70, 80, 90, 100, 110 and 120 rpm; and (ii) 6 fabric-water suspension characteristics. Therefore, 78 different tests were carried out, each one repeated 3 times, thus totalizing 234 tests. The steady-state tests plan is summarized in Table 10.

TABLE 10 - STEADY-STATE TESTS PLANNING.

Test	ω (rpm)	Fabric	Mass (kg)	Test	ω (rpm)	Fabric	Mass (kg)	Test	ω (rpm)	Fabric	Mass (kg)
1	5	Cotton	1.25	**27**	5	S.S.	1.25	**53**	5	Mixed	1.25
2	10	Cotton	1.25	**28**	10	S.S.	1.25	**54**	10	Mixed	1.25
3	20	Cotton	1.25	**29**	20	S.S.	1.25	**55**	20	Mixed	1.25
4	30	Cotton	1.25	**30**	30	S.S.	1.25	**56**	30	Mixed	1.25
5	40	Cotton	1.25	**31**	40	S.S.	1.25	**57**	40	Mixed	1.25
6	50	Cotton	1.25	**32**	50	S.S.	1.25	**58**	50	Mixed	1.25
7	60	Cotton	1.25	**33**	60	S.S.	1.25	**59**	60	Mixed	1.25
8	70	Cotton	1.25	**34**	70	S.S.	1.25	**60**	70	Mixed	1.25
9	80	Cotton	1.25	**35**	80	S.S.	1.25	**61**	80	Mixed	1.25
10	90	Cotton	1.25	**36**	90	S.S.	1.25	**62**	90	Mixed	1.25
11	100	Cotton	1.25	**37**	100	S.S.	1.25	**63**	100	Mixed	1.25
12	110	Cotton	1.25	**38**	110	S.S.	1.25	**64**	110	Mixed	1.25
13	120	Cotton	1.25	**39**	120	S.S.	1.25	**65**	120	Mixed	1.25
14	5	Cotton	2.50	**40**	5	S.S.	2.50	**66**	5	Mixed	2.50
15	10	Cotton	2.50	**41**	10	S.S.	2.50	**67**	10	Mixed	2.50
16	20	Cotton	2.50	**42**	20	S.S.	2.50	**68**	20	Mixed	2.50
17	30	Cotton	2.50	**43**	30	S.S.	2.50	**69**	30	Mixed	2.50
18	40	Cotton	2.50	**44**	40	S.S.	2.50	**70**	40	Mixed	2.50
19	50	Cotton	2.50	**45**	50	S.S.	2.50	**71**	50	Mixed	2.50
20	60	Cotton	2.50	**46**	60	S.S.	2.50	**72**	60	Mixed	2.50
21	70	Cotton	2.50	**47**	70	S.S.	2.50	**73**	70	Mixed	2.50
22	80	Cotton	2.50	**48**	80	S.S.	2.50	**74**	80	Mixed	2.50
23	90	Cotton	2.50	**49**	90	S.S.	2.50	**75**	90	Mixed	2.50
24	100	Cotton	2.50	**50**	100	S.S.	2.50	**76**	100	Mixed	2.50
25	110	Cotton	2.50	**51**	110	S.S.	2.50	**77**	110	Mixed	2.50
26	120	Cotton	2.50	**52**	120	S.S.	2.50	**78**	120	Mixed	2.50

All tests lasted for ten minutes, where the first two minutes had a constant acceleration of the inner cylinder until the maximum velocity was reached. The following steady-state criterion was applied: a time span was selected and the average torque in the interval was considered. If the tendency of the torque values tends to a horizontal line within the uncertainty thresholds it is considered that the steady-state was achieved, as depicted in Figure 27. This methodology considers that the fabric-water suspension does not exhibit a thixotropic behavior.

FIGURE 27 - ILLUSTRATION OF THE STEADY-STATE CRITERION.

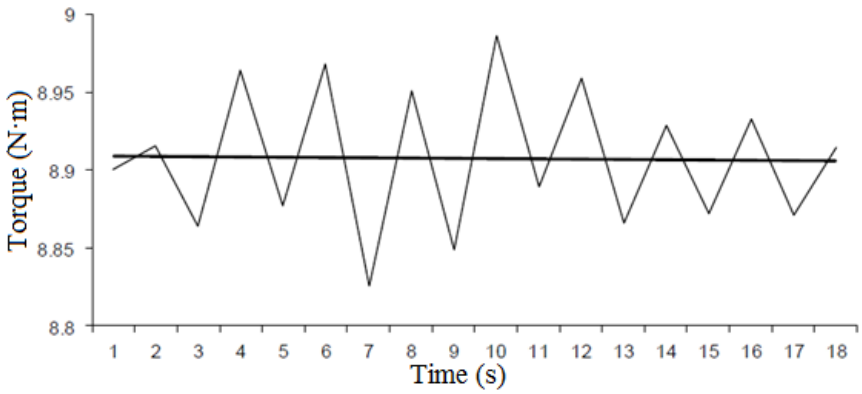

Also, the regression provides the average power supplied to the suspension:

$$\dot{W} = \frac{\pi \overline{T} \omega}{30} \tag{4.1}$$

where ω is the inner cylinder velocity (rpm) and $\overline{T}$ is the average torque (N.m) calculated from:

$$\overline{T} = \int T dt \tag{4.2}$$

In addition, to prove that in a vane-geometry the fluid is trapped between the vane blade thus acting like a solid cylinder, additional tests were carried out with longer four-blades with 45.5 mm each blade, thus $k = R_{inn}/R_{out}$ is approximately 0.44 and $\Gamma = 2.10$. At this time, the experiments were carried with the mixed fabrics only, while the water column is still the same (310 mm).

Additional tests were carried out with no liquid in the cylinder gap. The average torque values of this tests are subtracted from the tests with the fabric-water suspension in order to obtain the torque transmitted to the suspension only. Thus, the torque transmitted to the

suspension is calculated from: $\overline{T}_{net} = \overline{T}_{loaded} - \overline{T}_{unloaded}$. These tests are depicted in section 4.3.

Figure 28 (a) depicts the torque response for a 10-minute test. One can note that the signal noise muddles the analysis and the visual aspect of the graphs (OPPENHEIM, SCHAFER and BUCK, 1999). The moving average filter is a simple method for smoothing noisy data with the size of a window (ws) of 600 milliseconds is depicted in Figure 30 (b) where the response y(n) was the filter is computed through the following expression:

$$y(n) = \frac{1}{ws}(x(n) + (x(n-1) + \cdots + (x(n-(ws-1))) \tag{4.3}$$

Since the moving average filter with a sufficient windows size resulted in a reasonably smooth signal, it was applied henceforth in this work.

FIGURE 28 - EXAMPLE OF TORQUE RESPONSE.

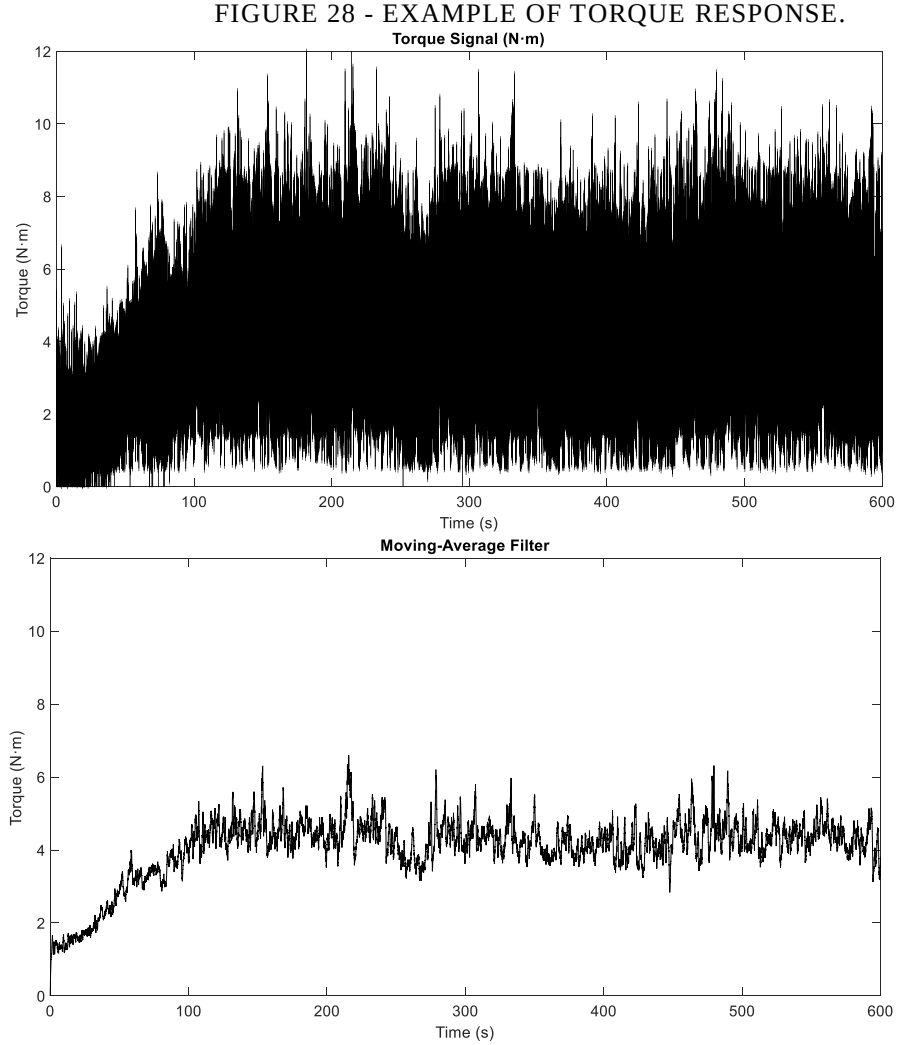

(A)

(B)

(A) RAW DATA, (B) MOVING AVERAGE FILTER.

4.2.2 Periodic Tests

Four different tests were carried out concerning periodic conditions. Figure 29 shows the angular velocity sweep over time, while Figure 30 shows the angular acceleration for the different tests. One can see that all the tests have swift acceleration and deceleration steps, where the difference between them is the maximum velocity. Tests 1 and 2 cycles last three seconds, while Tests 3 and 4 last six seconds. Also, Tests 1 and 3 have a maximum velocity of 40 rpm, while 80 rpm is designed for Tests 2 and 4.

Similarly, the water column is maintained in 310 mm (64 Liters of water) and the mixed fabric-water suspensions were used as working fluid. All tests were conducted with the four-bladed inner cylinder, with and without the smooth bottom basis rotating with the inner cylinder.

The input parameters for the periodic tests are (i) agitation profile, (ii) amount: 1.25 kg and 2.50 kg, and (iii) with and without the rotating bottom basis. In total, 16 periodic tests were carried out, each one repeated 5 times.

FIGURE 29 - ANGULAR VELOCITY FOR DIFFERENT PERIODIC TESTS.

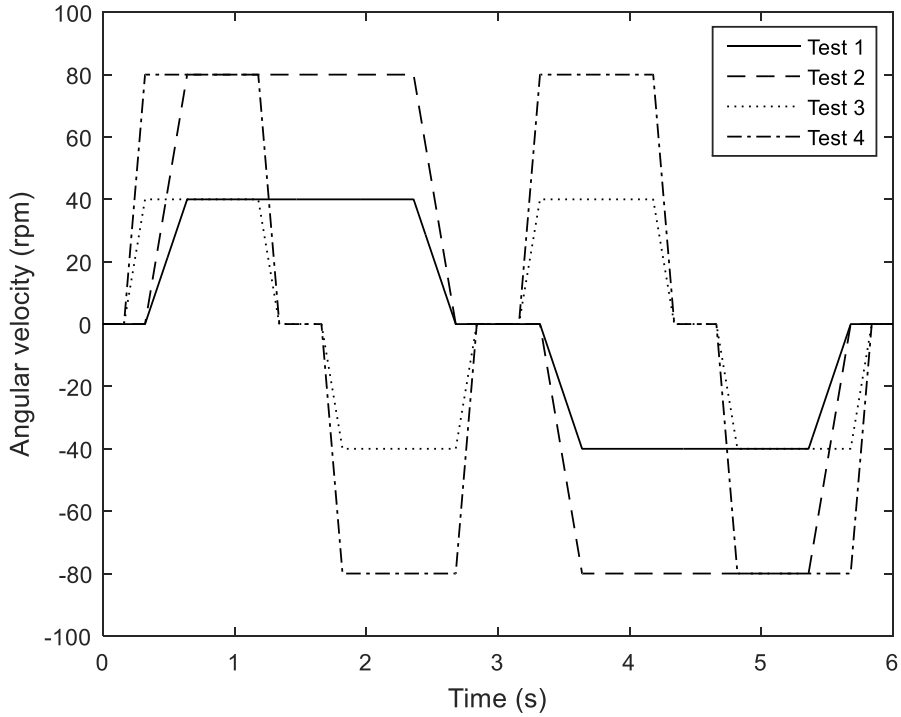

FIGURE 30 - ANGULAR ACCELERATION FOR DIFFERENT PERIODIC TESTS.

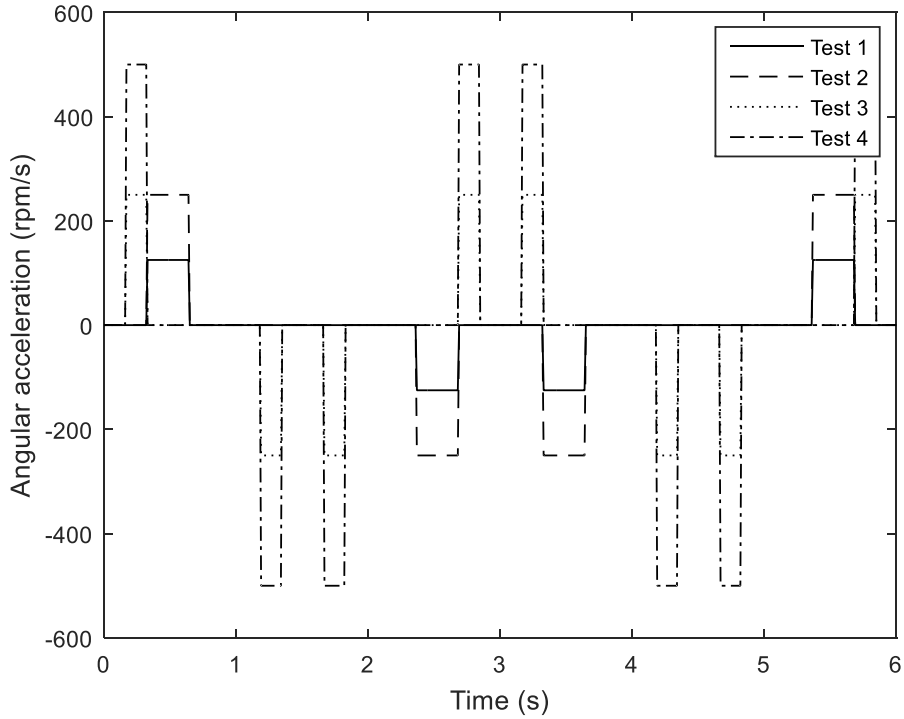

4.3 EXPERIMENTAL RESULTS

4.3.1 Raw Data - Steady-State Results

Before performing the regression of the raw data for different non-Newtonian fluid models, all the measured torque values (T) for various angular velocities (ω) is presented for all runs. The raw data regression itself relies on the solution of the inverse Couette problem, thus obtaining the curve $\tau(\dot{\gamma})$ from the measurements of torque T (N·m) and angular velocity ω (rad/s) in a coaxial cylinder rheometer, as explained in section 2.6 (Chapter 2).

Tables 11 and 12 present the raw data considering three repetitions for each test for the two different cotton fabric-water suspensions. One can note the unloaded columns in the tables, which represent the torque value obtained when there was only air within the cylinders gap. The average value of the three runs, deducting the unloaded value, provides the torque transmitted from the inner cylinder to the liquid. As $\mu_T^2 = \mu_m^2 + \mu_P^2$, where μ_m is the uncertainty of the measurement instruments, whereas μ_P of the process itself, being p $\mu_P >> \mu_m$, then $\mu_T = \mu_P$ (2σ for 95% of confidence bounds).

TABLE 11 - EXPERIMENTAL TORQUE FOR 1.25 KG OF COTTON FABRIC-WATER SUSPENSIONS.

	Torque (N·m) values for cotton fabric-water suspensions					
	1.251 kg of cotton fabrics					
ω_{inn} (rpm)	Run 1	Run 2	Run 3	**Loaded**	Unloaded	**Net**
5	1.12	1.09	1.10	**1.104 ± 0.030**	0.973 ± 0.053	**0.131**
10	1.16	1.13	1.13	**1.139 ± 0.029**	0.971 ± 0.004	**0.168**
20	1.27	1.30	1.30	**1.291 ± 0.042**	1.072 ± 0.006	**0.218**
30	1.74	1.67	1.62	**1.675 ± 0.116**	1.144 ± 0.024	**0.530**
40	2.37	2.14	2.40	**2.303 ± 0.284**	1.207 ± 0.025	**1.096**
50	3.14	3.21	3.23	**3.196 ± 0.095**	1.260 ± 0.011	**1.936**
60	3.47	3.47	3.48	**3.474 ± 0.016**	1.320 ± 0.041	**2.154**
70	3.64	3.65	3.67	**3.652 ± 0.038**	1.329 ± 0.045	**2.323**
80	3.87	3.90	3.87	**3.879 ± 0.035**	1.346 ± 0.017	**2.533**
90	4.16	4.11	4.06	**4.108 ± 0.106**	1.391 ± 0.031	**2.717**
100	4.46	4.48	4.41	**4.454 ± 0.072**	1.416 ± 0.015	**3.037**
110	4.63	4.75	4.70	**4.697 ± 0.120**	1.474 ± 0.039	**3.223**
120	5.02	5.04	4.98	**5.013 ± 0.068**	1.481 ± 0.048	**3.532**

TABLE 12 - EXPERIMENTAL TORQUE FOR 2.50 KG OF COTTON FABRIC-WATER SUSPENSIONS.

	Torque (N·m) values for cotton fabric-water suspensions					
	2.502 kg of cotton fabrics					
ω_{inn} (rpm)	Run 1	Run 2	Run 3	**Loaded**	Unloaded	**Net**
5	1.23	1.23	1.23	**1.229 ± 0.008**	0.973 ± 0.053	**0.256**
10	1.59	1.45	1.44	**1.493 ± 0.167**	0.971 ± 0.004	**0.522**
20	2.56	2.45	2.26	**2.425 ± 0.302**	1.072 ± 0.006	**1.352**
30	2.41	2.55	2.79	**2.586 ± 0.384**	1.144 ± 0.024	**1.442**
40	2.79	2.61	2.79	**2.730 ± 0.213**	1.207 ± 0.025	**1.523**
50	3.40	2.73		**3.064 ± 0.941**	1.260 ± 0.011	**1.805**
60	4.75	4.77	4.57	**4.695 ± 0.219**	1.320 ± 0.041	**3.375**
70	5.26	5.47	4.73	**5.152 ± 0.762**	1.329 ± 0.045	**3.822**
80	6.84	6.42	6.02	**6.427 ± 0.819**	1.346 ± 0.017	**5.082**
90	6.87	6.93	6.86	**6.885 ± 0.074**	1.391 ± 0.031	**5.495**
100	6.88	7.64	7.32	**7.278 ± 0.758**	1.416 ± 0.015	**5.862**
110	7.61	7.55	7.45	**7.535 ± 0.161**	1.474 ± 0.039	**6.061**
120	7.37	7.65	7.72	**7.580 ± 0.379**	1.481 ± 0.048	**6.100**

Figure 31 plots the torques for each suspension of cotton fabric-water suspension. The solid line represents the average torque (spline), whereas the symbols indicate the measurement from each of the 3 runs. One can notice that, as expected, the torque values are higher the higher the quantity of fabric and that the two different fluids exhibit different sort of behaviors. On the one hand, the suspension with 1.25 kg of cotton shows a swifter torque growth from 5 to 50 rpm, after that it tends to a nearly linear behavior. On the other hand, the suspension with 2.50 kg of cotton has a slow torque growth until 50-rpm is reached. Afterward, an asymptotic torque growth can be observed.

Likewise, Tables 13 and 14 summarize the raw data for torque values concerning the tests for different suspensions of semi-synthetic fabric (1.25 and 2.50 kg). Similarly, the unloaded column is also provided.

FIGURE 31 - AVERAGE TORQUE FOR TWO DIFFERENT COTTON FABRIC-WATER SUSPENSIONS.

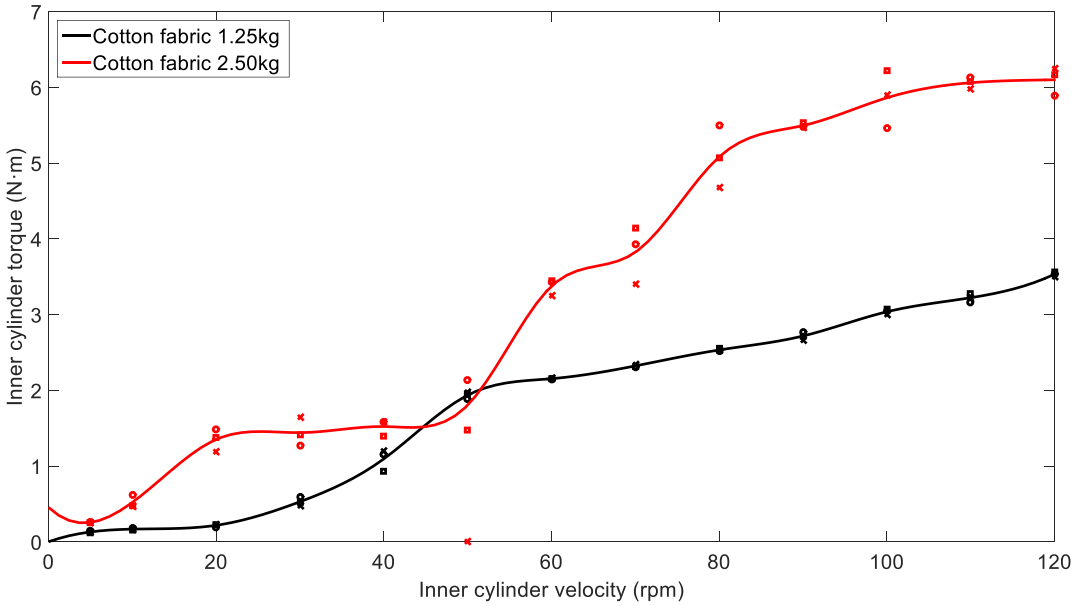

TABLE 13 - TORQUE MEASUREMENTS FOR 1.25 KG OF SEMI-SYNTHETIC FABRIC-WATER SUSPENSIONS.

	Torque (N·m) values for semi-synthetic fabric-water suspensions					
	1.251 kg of semi-synthetic fabrics					
ω_{inn} (rpm)	Run 1	Run 2	Run 3	**Loaded**	Unloaded	**Net**
5	1.06	1.09	1.12	**1.090 ± 0.057**	0.973 ± 0.053	**0.118**
10	1.12	1.11	1.10	**1.111 ± 0.022**	0.971 ± 0.004	**0.140**
20	1.28	1.35	1.25	**1.293 ± 0.103**	1.072 ± 0.006	**0.220**
30	1.46	1.50	1.39	**1.449 ± 0.101**	1.144 ± 0.024	**0.304**
40	1.77	1.54	1.54	**1.618 ± 0.263**	1.207 ± 0.025	**0.411**
50	1.93	1.90	1.99	**1.940 ± 0.098**	1.260 ± 0.011	**0.680**
60	2.52	2.45	2.52	**2.497 ± 0.081**	1.320 ± 0.041	**1.178**
70	2.48	2.77	2.70	**2.651 ± 0.301**	1.329 ± 0.045	**1.321**
80	2.95	2.93	2.85	**2.910 ± 0.104**	1.346 ± 0.017	**1.564**
90	3.56	3.54	3.43	**3.508 ± 0.132**	1.391 ± 0.031	**2.118**
100	3.66	3.61	3.94	**3.738 ± 0.356**	1.416 ± 0.015	**2.322**
110	4.23	3.99	4.35	**4.192 ± 0.373**	1.474 ± 0.039	**2.718**
120	4.21	4.65	4.65	**4.502 ± 0.511**	1.481 ± 0.048	**3.022**

Figure 32 plots the average torque for each semi-synthetic suspension represented by the solid lines. The symbols refer to the 3 runs. Again, one can notice that the torques are higher the higher the quantity of fabric. The suspension with 1.25 kg of semi-synthetic fabric shows a

slow torque growth from 5 to 40 rpm, after that it tends to a higher almost linear growth. On the other hand, the suspension with 2.50 kg, albeit showing an analogous behavior to the lighter suspension for higher velocities, with a plato between 10 and 40 rpm, presents a different behavior for low velocities.

TABLE 14 - TORQUE MEASUREMENTS FOR 2.50 KG OF SEMI-SYNTHETIC FABRIC-WATER SUSPENSIONS.

	Torque (N·m) values for semi-synthetic fabric-water suspensions					
	2.502 kg of semi-synthetic fabrics					
ω_{inn} (rpm)	Run 1	Run 2	Run 3	**Loaded**	Unloaded	**Net**
5	1.88	1.84	1.52	**1.745 ± 0.393**	0.973 ± 0.053	**0.772**
10	2.09	2.15	2.18	**2.140 ± 0.092**	0.971 ± 0.004	**1.169**
20	2.31	2.32	2.37	**2.333 ± 0.060**	1.072 ± 0.006	**1.262**
30	2.11	2.29	2.95	**2.450 ± 0.886**	1.144 ± 0.024	**1.306**
40	2.87	2.59	2.18	**2.547 ± 0.688**	1.207 ± 0.025	**1.340**
50	3.19	2.77	3.46	**3.137 ± 0.697**	1.260 ± 0.011	**1.877**
60	3.26	3.27	3.62	**3.386 ± 0.413**	1.320 ± 0.041	**2.066**
70	3.75	3.93	4.03	**3.902 ± 0.291**	1.329 ± 0.045	**2.573**
80	4.61	4.40	4.33	**4.447 ± 0.294**	1.346 ± 0.017	**3.102**
90	4.83	5.22	4.51	**4.855 ± 0.711**	1.391 ± 0.031	**3.465**
100	5.52	5.14	5.55	**5.405 ± 0.457**	1.416 ± 0.015	**3.989**
110	5.81	5.64	5.88	**5.778 ± 0.245**	1.474 ± 0.039	**4.304**
120	6.25	6.11	6.46	**6.272 ± 0.349**	1.481 ± 0.048	**4.791**

FIGURE 32 - AVERAGE TORQUE FOR TWO DIFFERENT SEMI-SYNTHETIC FABRIC-WATER SUSPENSIONS.

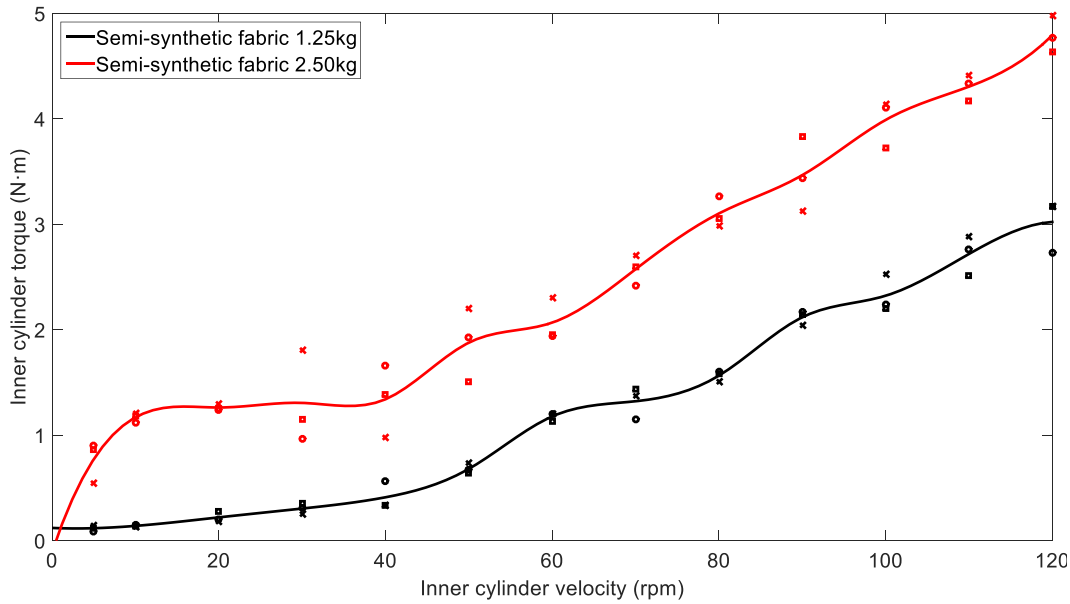

Tables 15 and 16 summarizes the raw data for the two different mixed cotton and semi-synthetic suspensions. Likewise, the torque transmitted only to the suspension is depicted in the last column.

TABLE 15 - TORQUE MEASUREMENTS FOR 1.25 KG OF MIXED FABRIC-WATER SUSPENSIONS.

	Torque (N·m) values for mixed fabric-water suspensions					
	1.251 kg of mixed fabrics					
ω_{inn} (rpm)	Run 1	Run 2	Run 3	**Loaded**	Unloaded	**Net**
5	1.21	1.20	1.16	**1.190 ± 0.055**	0.973 ± 0.053	**0.217**
10	1.21	1.25	1.23	**1.232 ± 0.037**	0.971 ± 0.004	**0.261**
20	1.42	1.45	1.44	**1.439 ± 0.033**	1.072 ± 0.006	**0.367**
30	1.65	1.68	1.51	**1.614 ± 0.176**	1.144 ± 0.024	**0.470**
40	2.03	1.93	1.70	**1.886 ± 0.329**	1.207 ± 0.025	**0.679**
50	2.53	2.26	2.43	**2.407 ± 0.276**	1.260 ± 0.011	**1.147**
60	2.86	2.93	2.98	**2.922 ± 0.120**	1.320 ± 0.041	**1.602**
70	3.05	3.15	3.22	**3.142 ± 0.174**	1.329 ± 0.045	**1.813**
80	3.64	3.28	3.38	**3.434 ± 0.372**	1.346 ± 0.017	**2.088**
90	3.83	3.77	3.89	**3.831 ± 0.121**	1.391 ± 0.031	**2.441**
100	4.33	4.12	4.20	**4.216 ± 0.217**	1.416 ± 0.015	**2.800**
110	4.36	4.44	4.42	**4.408 ± 0.078**	1.474 ± 0.039	**2.934**
120	4.87	4.94	4.76	**4.860 ± 0.181**	1.481 ± 0.048	**3.380**

Figure 33 plots the torque for each suspension, represented by the full lines, while the symbols refer to the different runs. One can note that the behavior of those suspensions holds some characteristics from the two different fabrics. In this case, with growth following an exponential behavior.

TABLE 16 - TORQUE MEASUREMENTS FOR 2.50 KG OF MIXED FABRIC-WATER SUSPENSIONS.

	Torque (N·m) values for mixed fabric-water suspensions					
	2.502 kg of mixed fabrics					
ω_{inn} (rpm)	Run 1	Run 2	Run 3	**Loaded**	Unloaded	**Net**
10	1.35	1.36	1.26	**1.324 ± 0.114**	0.973 ± 0.053	**0.353**
20	2.29	1.66	1.71	**1.886 ± 0.703**	0.971 ± 0.004	**0.813**
30	1.90	2.03	2.20	**2.043 ± 0.297**	1.072 ± 0.006	**0.899**
40		2.53	2.63	**2.581 ± 0.137**	1.144 ± 0.024	**1.374**
50	3.08	2.43	3.27	**2.926 ± 0.874**	1.207 ± 0.025	**1.666**
60	3.73	3.36	3.55	**3.548 ± 0.373**	1.260 ± 0.011	**2.228**
70	3.98	4.30	3.81	**4.031 ± 0.495**	1.320 ± 0.041	**2.702**
80	4.83	4.82	4.45	**4.697 ± 0.434**	1.329 ± 0.045	**3.352**
90	5.61	4.84	5.31	**5.252 ± 0.781**	1.346 ± 0.017	**3.862**
100	6.09	5.78	5.95	**5.943 ± 0.312**	1.391 ± 0.031	**4.526**
110	6.53	6.21	5.98	**6.240 ± 0.548**	1.416 ± 0.015	**4.766**
120	6.75	6.42	6.43	**6.534 ± 0.379**	1.474 ± 0.039	**5.054**

FIGURE 33 - AVERAGE TORQUE FOR TWO DIFFERENT MIXED FABRIC-WATER SUSPENSIONS.

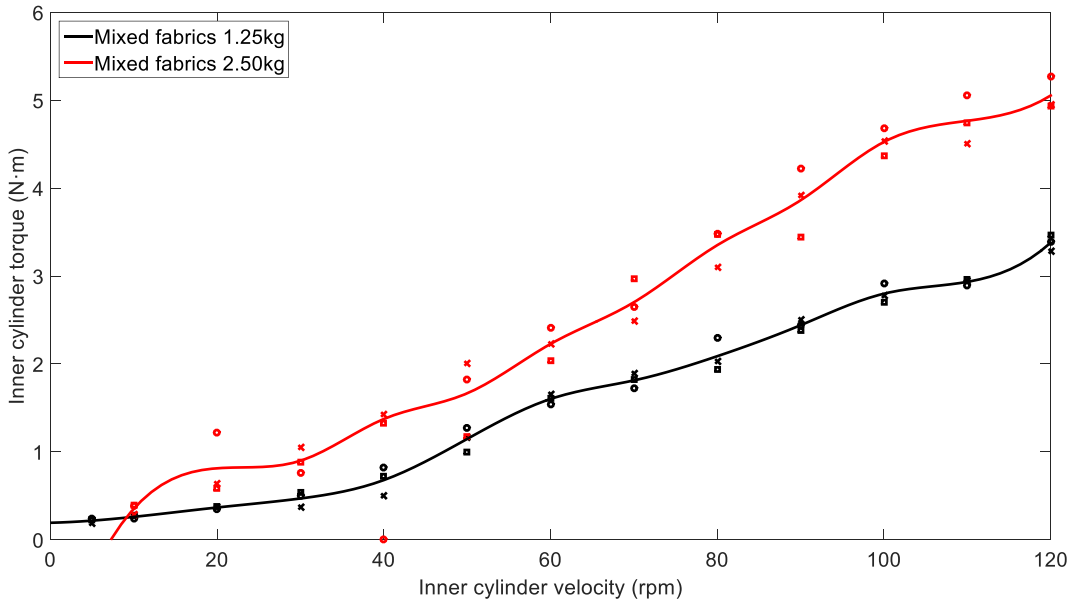

4.3.2 Data Regression – Short Blade Vane

The experimental raw data organized in the tables above have been analyzed to figure out which yield stress fluid model best fitted the data (Bingham fluid, Casson Fluid, Robertson-Stiff fluid, and Herschel-Bulkley model). Similarly, the Kelessidis and Maglione (2006 and 2008) approach, where both Newtonian shear rate and true shear rate are compared in order to evaluate whether the Newtonian approach applicable for narrow-gap geometry is accurate or not, is used in this work. Such a procedure has been applied for all different suspensions.

Furthermore, to evaluate the assumption that for vane-in-cup geometries the fluid is trapped between the vane blades acting as a solid cylinder, additional tests for mixed fabric-water suspensions were carried out with longer blades. In this case, similar results are expected for the two different four-blade lengths.

It is important to mention that for the Newtonian shear rate for each angular velocity (in rad/s) is calculated from Equation (2.54). Then, then non-linear regression is performed by statistical techniques (*least square fitting*), with 95% of confidence bounds, in order to determine the appropriate rheological parameters for each non-Newtonian fluid model. All non-linear regressions are evaluated through three statistical indicators, R^2 (coefficient of determination), SSE (sum of square errors) and RMS (root mean square).

Finally, the plots comparing the differences between the Newtonian and true shear rates, also known as rheogram, show the shear stresses in the surface of the inner cylinder (τ_{inn}) plotted as a function of different shear rates.

4.3.2.1 Bingham Fluid

Data fitting to the Bingham fluid model is not very accurate, despite showing relatively good statistical indicators (R^2, SSE, and RMS) for all the fluids. Table 17 shows the yield stress (τ_0) and dynamic viscosities (μ) calculated by the least square fitting, for all the six different fluid suspensions and the two different data verification approaches wide gap (true) and narrow gap (Newtonian). The Bingham fluid model describes a Newtonian fluid behavior with the presence of a yield stress, below which there is no deformation of the fluid flow. For that reason, the values obtained for both Newtonian and true shear rate approaches are quite the same for all the fluids but the semi-synthetic fabric (2.50 kg) and water suspension (Figures 34 - 36). The best-fitted parameters were calculated by regression of Equation (2.75) for true shear rates and Equation (2.77) for Newtonian shear rates. A data-fitting was also computed for the Reiner-Riwlin Equation (2.78), also depicted in Table 16.

One can note that the fluid suspension with semi-synthetic fabric (2.50 kg) is the only one which presents a significant yield stress (τ_0) value. In all cases, the nature of the Bingham model does not follow the trend of the data. Figure 34 shows the rheogram for cotton fabric-water suspensions, Figure 35 for 1.25 kg semi-synthetic fabric-water suspension, Figure 36 for semi-synthetic fabric-water suspensions, and finally, Figure 36 for mixed fabric-water suspensions. One can also note, that the true and Newtonian shear rates are coincident as the calculated parameters of the model are quite the same, but for the 2.50 kg of semi-synthetic fabric-water fluid, which presents a higher yield stress because of the fabric agglomeration near the inner cylinder.

TABLE 17 - BINGHAM MODEL RHEOLOGICAL PARAMETERS FOR NEWTONIAN (NARROW GAP) AND TRUE (WIDE GAP) SHEAR RATES, AND EQUATION (2.78) (95% CONFIDENCE BOUNDS).

Fluid suspension - Shear rate approach	τ_0 (Pa)	μ (Pa·s)	R^2	SSE	RMS
Cotton (1.25kg) - True	$2.2\ 10^{-14}$	5.16 ± 0.35	0.963	1238	10.16
Cotton (1.25kg) - Newt.	$2.4\ 10^{-14}$	5.16 ± 0.35	0.963	1238	10.16
Cotton (1.25kg) - (2.78)	$2.4\ 10^{-14}$	5.16	0.963	1238	10.16
Cotton (2.50kg) - True	$4.3\ 10^{-14}$	9.32 ± 0.67	0.957	4687	19.76
Cotton (2.50kg) - Newt.	$2.2\ 10^{-14}$	9.32 ± 0.67	0.957	4687	19.76
Cotton (2.50kg) - (2.78)	$2.2\ 10^{-14}$	9.32	0.957	4687	19.76
S.S. (1.25kg) - True	$2.2\ 10^{-14}$	3.74 ± 0.41	0.926	1710	11.94
S.S. (1.25kg) - Newt.	$2.2\ 10^{-14}$	3.74 ± 0.41	0.926	1710	11.94
S.S. (1.25kg) - (2.78)	$2.2\ 10^{-14}$	3.74	0.926	1710	11.94
S.S. (2.50kg) - True	7.61 ± 6.34	5.81 ± 0.77	0.958	1502	11.68
S.S. (2.50kg) - Newt.	16.45 ± 13.7	5.81 ± 0.77	0.961	1502	11.68
S.S. (2.50kg) - (2.78)	16.45 ± 13.7	5.81	0.961	1502	11.68
Mixed (1.25kg) - True	$2.4\ 10^{-14}$	4.49 ± 0.26	0.974	691.8	7.59
Mixed (1.25kg) - Newt.	$2.2\ 10^{-14}$	4.49 ± 0.26	0.974	691.8	7.59
Mixed (1.25kg) - (2.78)	$2.2\ 10^{-14}$	4.49	0.974	691.8	7.59
Mixed (2.50kg) - True	$2.5\ 10^{-14}$	7.04 ± 0.36	0.977	1233	10.59
Mixed (2.50kg) - Newt.	$2.2\ 10^{-14}$	7.04 ± 0.36	0.977	1233	10.59
Mixed (2.50kg) - (2.78)	$2.2\ 10^{-14}$	7.04	0.977	1233	10.59

FIGURE 34 - RHEOGRAM FOR COTTON FABRIC-WATER SUSPENSION WITH BINGHAM MODEL.

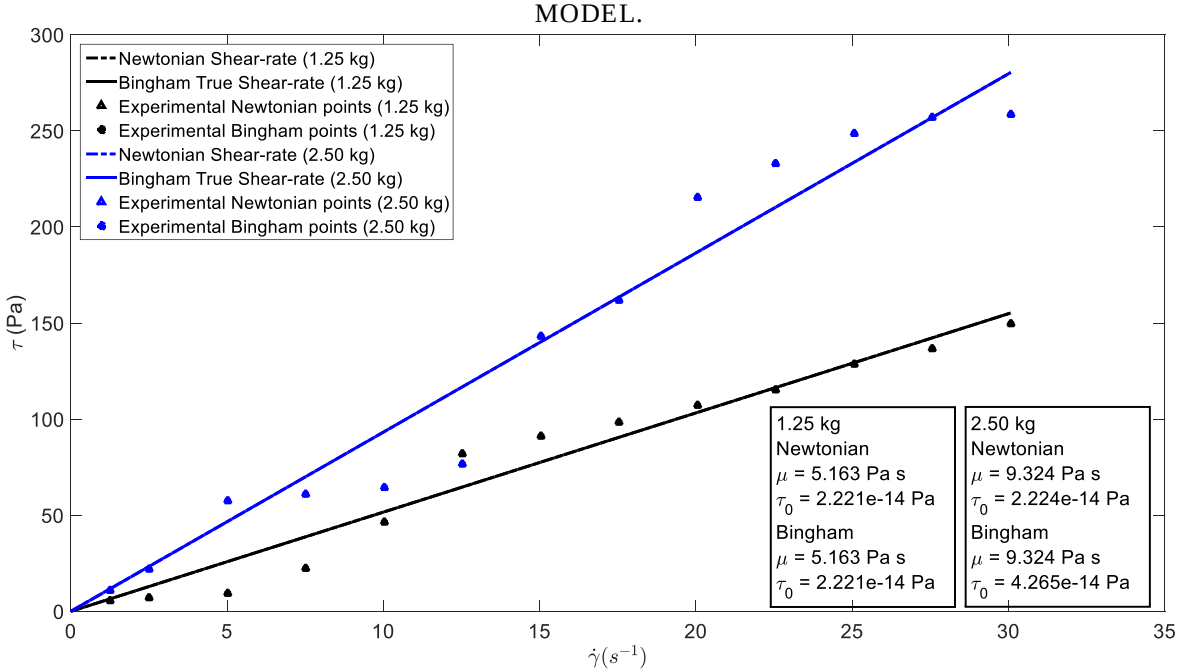

FIGURE 35 - RHEOGRAM FOR SEMI-SYNTHETIC FABRIC-WATER SUSPENSION WITH BINGHAM MODEL.

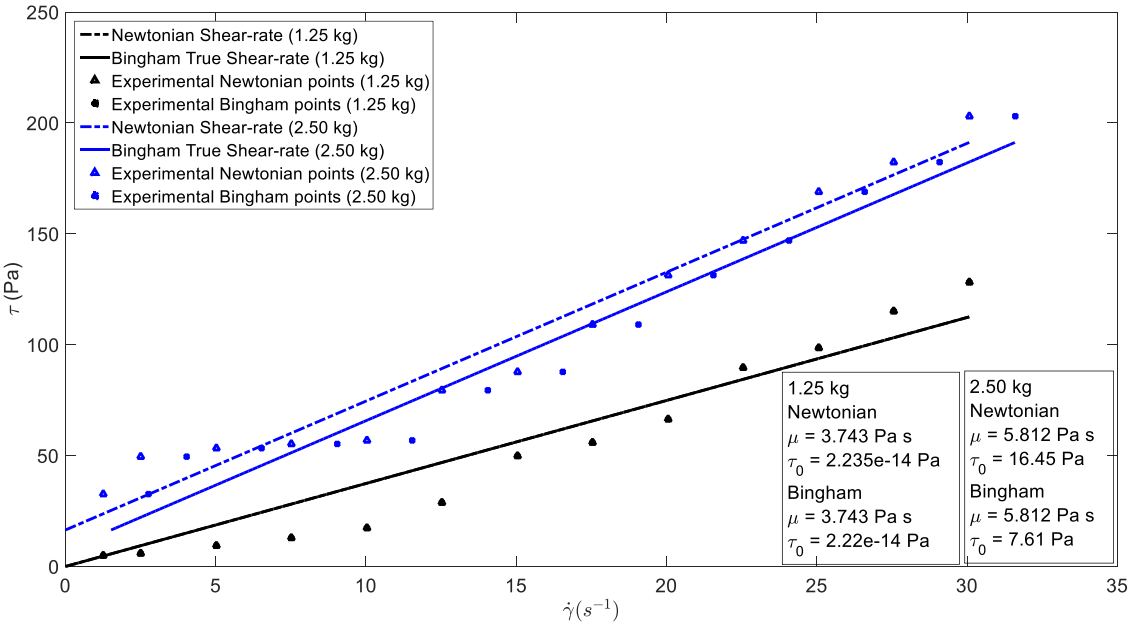

FIGURE 36 - RHEOGRAM FOR MIXED FABRIC-WATER SUSPENSION WITH BINGHAM MODEL.

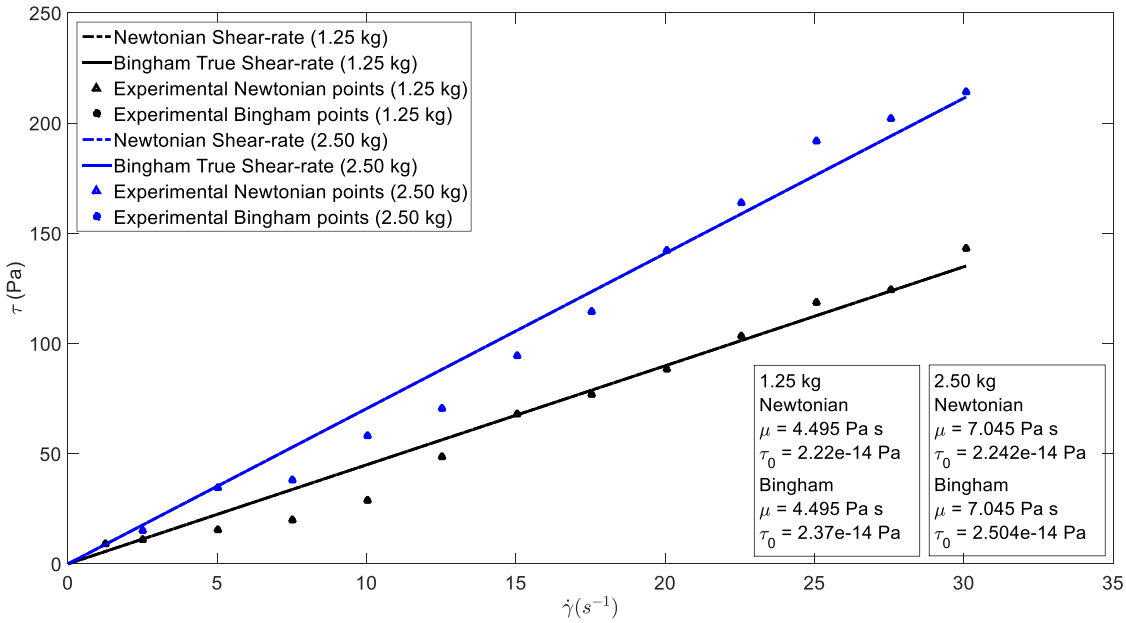

4.3.2.2 Casson Fluid

Likely to the Bingham fluid, data fitting to Casson fluid model is not very accurate, despite showing good statistical indicators. Table 18 shows the yield stress (τ_0) and dynamic viscosities (μ) best-fitted for the six different fluid suspensions through the two different shear rate approaches (true and Newtonian). The Casson fluid is widely used to model the flow

behavior of chocolate and bloodstreams (JOYE, 2003), which are shear-thinning fluids, but it could not describe in a good way the behavior of the suspensions of this work. Similar to the Bingham fluid, the values obtained for both Newtonian and true shear rate approaches are almost the same for all the fluids but the semi-synthetic fabric (2.50 kg) and water suspension. The fitted parameters were calculated by regression of Equation (2.69) for true shear rates and Equation (2.71) for Newtonian shear rates.

One can note that the fluid suspension with semi-synthetic fabric (2.50 kg) is the only one that presents a significant yield stress value too. In all cases, the nature of the Casson model cannot follow the experimental curves because of its 2 parameters are not sufficient to fit the experimental points.

Finally, Figure 37 shows the rheogram of cotton fabric-water suspensions, Figure 38 for semi-synthetic fabric-water suspensions and Figure 39 for mixed fabric-water suspensions. Again, the true and Newtonian shear rates are coincident for almost all curves.

TABLE 18 - CASSON MODEL RHEOLOGICAL PARAMETERS FOR NEWTONIAN AND TRUE SHEAR RATES (WITH 95% CONFIDENCE BOUNDS).

Shear rate approach	τ_0 (Pa)	μ (Pa·s)	R^2	SSE	RMS
Cotton (1.25kg) - True	$4.7\ 10^{-07} \pm 1.7\ 10^{-03}$	5.15 ± 1.77	0.963	1239	10.61
Cotton (1.25kg) - Newt.	$9.5\ 10^{-07} \pm 3.5\ 10^{-03}$	5.15 ± 1.77	0.963	1239	10.61
Cotton (2.50kg) - True	$8.1\ 10^{-07} \pm 3.3\ 10^{-03}$	9.27 ± 3.45	0.956	4700	20.67
Cotton (2.50kg) - Newt.	$7.0\ 10^{-07} \pm 4.3\ 10^{-03}$	9.27 ± 3.45	0.956	4699	20.67
S.S. (1.25kg) - True	$2.2\ 10^{-14}$	3.74 ± 0.41	0.926	1710	11.94
S.S. (1.25kg) - Newt.	$2.2\ 10^{-14}$	3.74 ± 0.41	0.926	1710	11.94
S.S. (2.50kg) - True	1.11 ± 2.75	5.05 ± 1.83	0.949	1993	13.46
S.S. (2.50kg) - Newt.	2.28 ± 5.38	5.04 ± 1.79	0.949	1983	13.43
Mixed (1.25kg) - True	$9.4\ 10^{-07} \pm 2.0\ 10^{-03}$	4.43 ± 1.34	0.974	711	8.04
Mixed (1.25kg) - Newt.	$6.6\ 10^{-07} \pm 2.4\ 10^{-03}$	4.43 ± 1.34	0.974	710	8.03
Mixed (2.50kg) - True	$9.7\ 10^{-07} \pm 2.4\ 10^{-03}$	6.96 ± 1.99	0.974	1267	11.25
Mixed (2.50kg) - Newt.	$7.1\ 10^{-07} \pm 2.9\ 10^{-03}$	6.96 ± 1.99	0.974	1265	11.25

FIGURE 37 - RHEOGRAM FOR COTTON FABRIC-WATER SUSPENSION WITH CASSON MODEL.

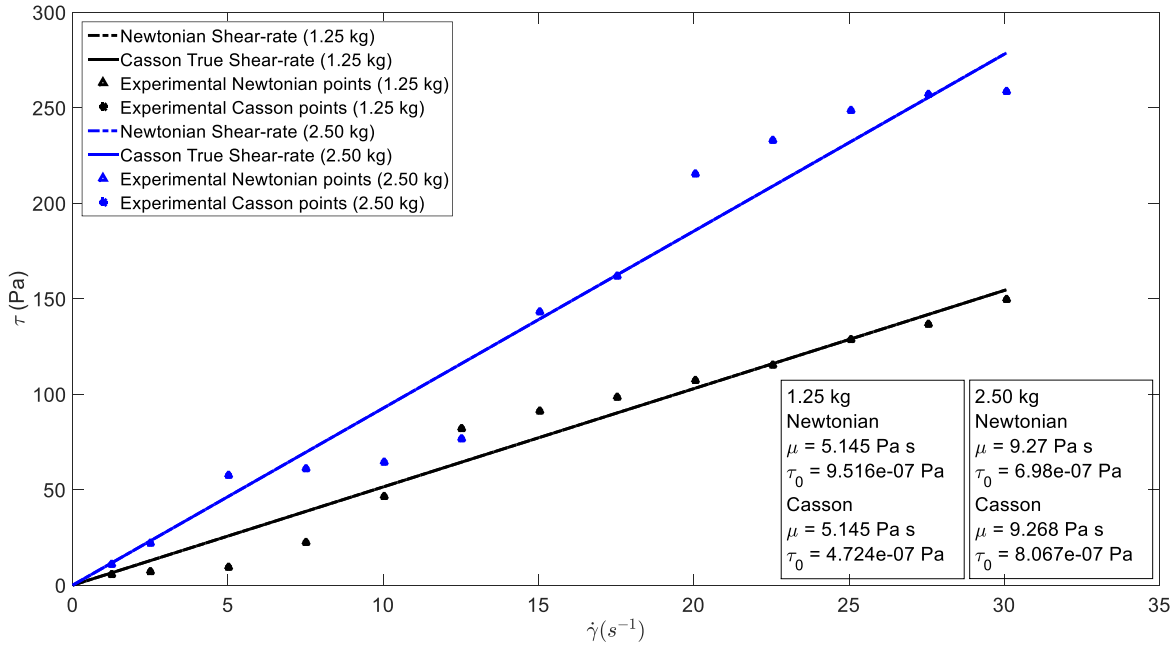

FIGURE 38 - RHEOGRAM FOR SEMI-SYNTHETIC FABRIC-WATER SUSPENSION WITH CASSON MODEL.

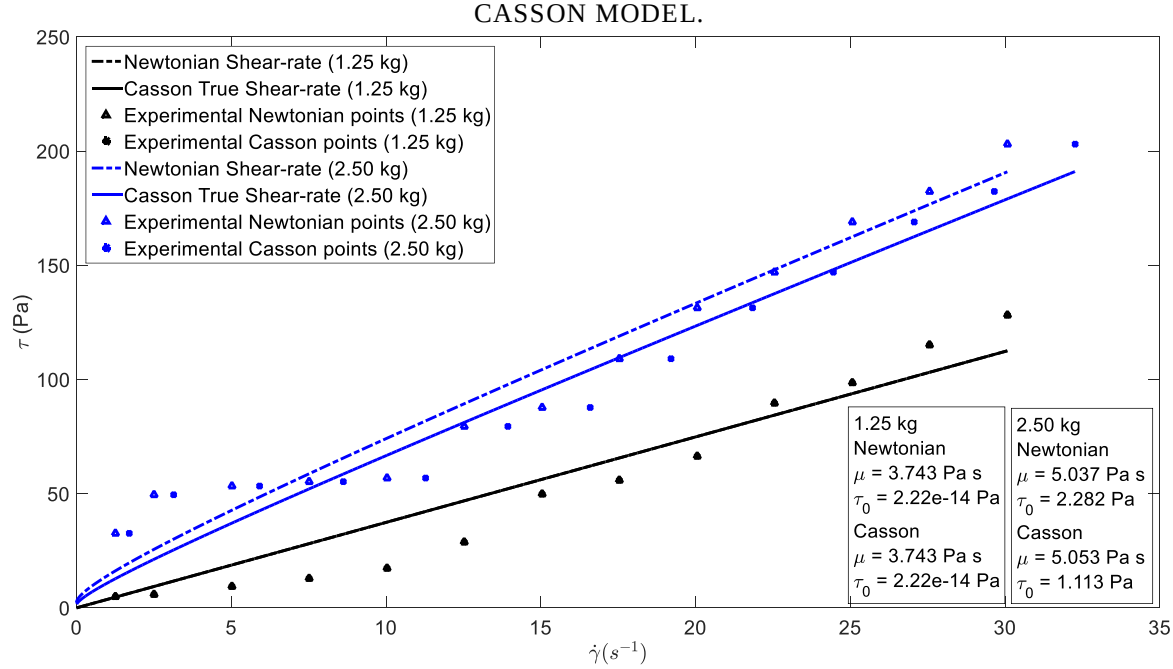

FIGURE 39 - RHEOGRAM FOR MIXED FABRIC-WATER SUSPENSION WITH CASSON MODEL.

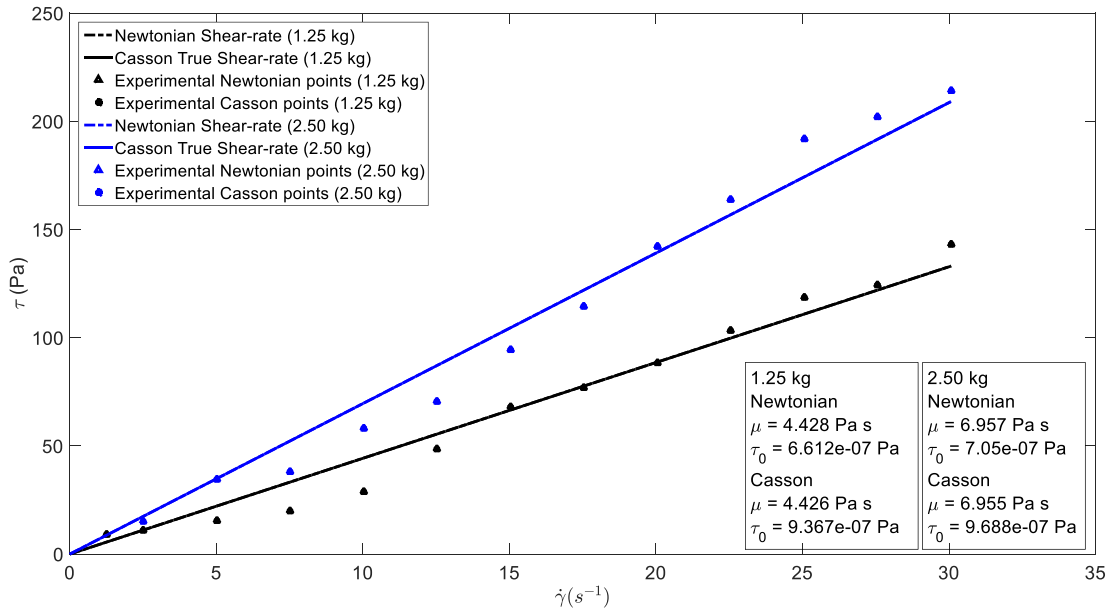

4.3.2.3 Robertson-Stiff Fluid

In contrast to the Bingham and Casson fluids models, the Robertson-Stiff one, which is a three-parameter model, describes the fluid flows a little better. The Robertson-Stiff model has been used in the open literature to describe the behavior of bentonite suspensions, drilling fluids, cement slurries and maize flour samples (shear-thickening). Table 18 depicts the values of the best-fitted consistency index (m), the index behavior (n) and the shear rate correction factor ($\dot{\gamma}_0$) for all fluids, as well as the statistical indicators. One can see that the model can best describe the rheological behavior of the semi-synthetic and the mixed fabric-water suspension fluids, albeit the behavior of the cotton fabric-water fluid suspensions is not well represented. The reason is explained by the absence of the shear rate correction factor for such a model.

In this case, one can note the differences between the true and Newtonian shear rate, with good results for cotton and mixed fabric-water fluid suspensions, but much better for the fluid with 2.50 kg of semi-synthetic fabrics. The best-fitted parameters were calculated by regression of Equation (2.72) for true shear rates and Equation (2.74) for Newtonian shear rates.

TABLE 19 - ROBERTSON-STIFF MODEL RHEOLOGICAL PARAMETERS FOR NEWTONIAN AND TRUE SHEAR RATES (WITH 95% CONFIDENCE BOUNDS).

Shear rate approach	$\dot{\gamma}_0$ (s^{-1})	m ($Pa \cdot s^n$)	n	R^2	SSE	RMS
Cotton (1.25kg) - True	2.22 10^{-14}	5.15 ± 2.70	1.00 ± 0.21	0.963	1238	10.61
Cotton (1.25kg) - Newt.	6.31 10^{-04}	3.88 ± 7.41	1.09 ± 0.52	0.959	1346	11.60
Cotton (2.50kg) - True	2.22 10^{-14}	7.85 ± 4.53	1.07 ± 0.23	0.958	4490	20.20
Cotton (2.50kg) - Newt.	2.28 10^{-05}	7.30 ± 13.8	1.08 ± 0.52	0.958	4493	21.20
S.S. (1.25kg) - True	0.21 ± 2.50	0.81 ± 1.30	1.61 ± 0.50	0.992	179.3	4.23
S.S. (1.25kg) - Newt.	0.45 ± 5.4	0.53 ± 1.04	1.61 ± 0.50	0.992	179.3	4.23
S.S. (2.50kg) - True	16.54 ± 26	0.0026	3.05 ± 3.21	0.989	432.9	6.94
S.S. (2.50kg) - Newt.	7.27 ± 18	0.50 ± 2.75	1.67 ± 1.32	0.957	1675	12.94
Mixed (1.25kg) - True	0.34 ± 1.90	2.15 ± 2.36	1.28 ± 0.35	0.990	259.4	5.09
Mixed (1.25kg) - Newt.	0.73 ± 4.11	1.78 ± 2.38	1.28 ± 0.35	0.990	259.4	5.09
Mixed (2.50kg) - True	0.29 ± 2.10	3.75 ± 4.3	1.24 ± 0.37	0.992	457.3	7.13
Mixed (2.50kg) - Newt.	0.62 ± 4.54	3.18 ± 4.44	1.24 ± 0.37	0.992	457.3	7.13

Casson and Bingham fluid could not describe well the non-Newtonian behavior of the fluid suspensions. Conversely, in all cases but the cotton fabric-water fluid suspensions, the Robertson-Stiff model follows to the curvatures of the rheological behavior of the fluids.

For the Robertson-Stiff fluid mode, Figure 40 shows the rheogram of cotton fabric-water suspensions, Figure 41 for semi-synthetic fabric-water suspensions and Figure 42 for mixed fabric-water suspensions.

FIGURE 40 - RHEOGRAM FOR COTTON FABRIC-WATER SUSPENSION WITH ROBERTSON-STIFF MODEL.

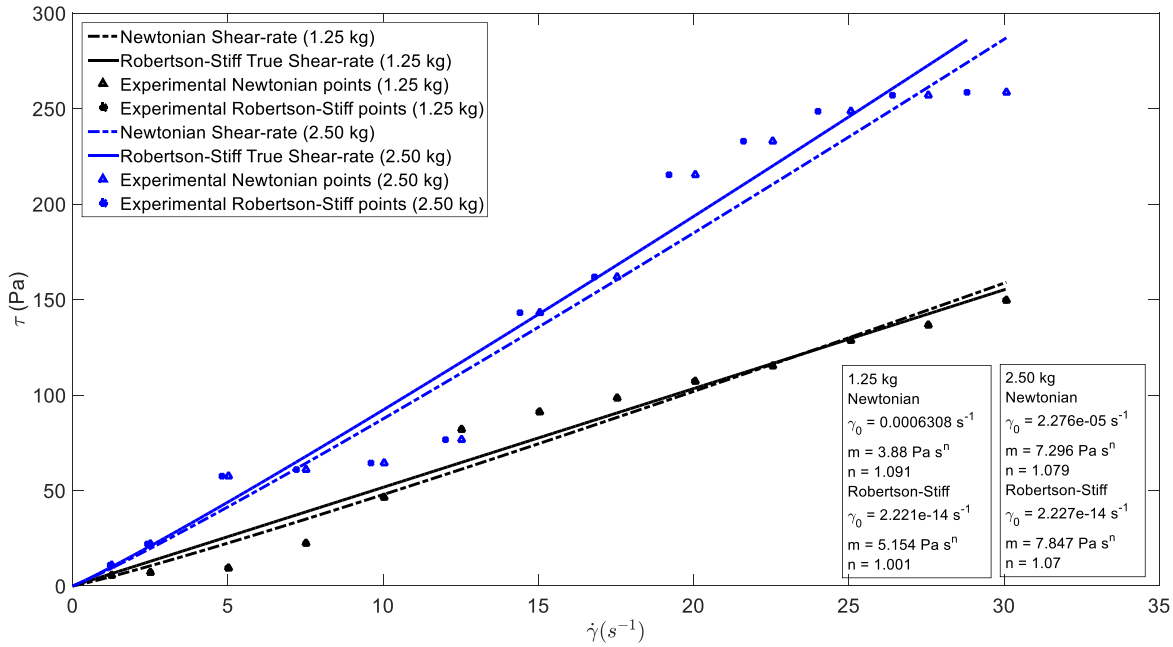

FIGURE 41 - RHEOGRAM FOR SEMI-SYNTHETIC FABRIC-WATER SUSPENSION WITH ROBERTSON-STIFF MODEL.

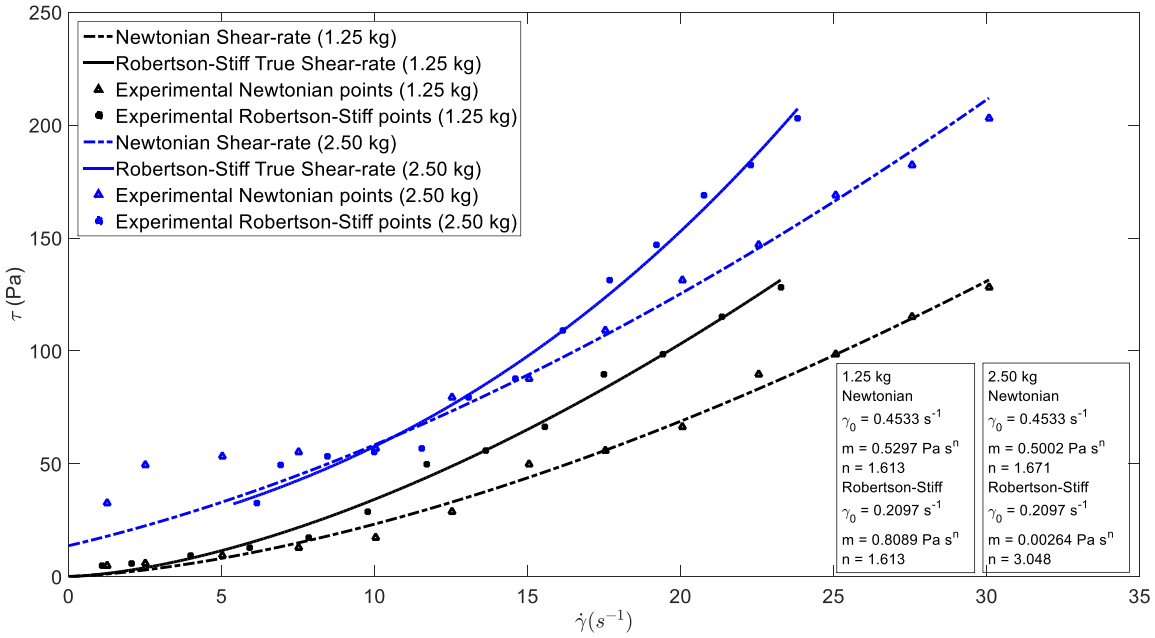

FIGURE 42 - RHEOGRAM FOR MIXED FABRIC-WATER SUSPENSION WITH ROBERTSON-STIFF MODEL.

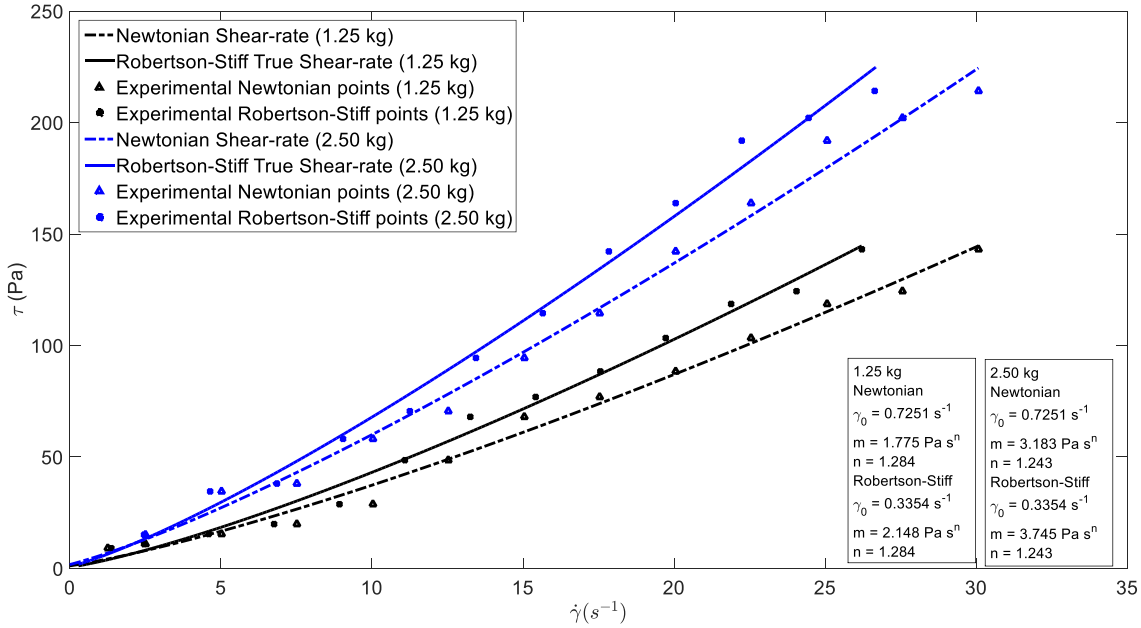

4.3.2.4 Herschel-Bulkley Fluid

Similarly, the Herschel-Bulkley model, which is also a three-parameter model that combines the Power-Law and Bingham model, describe the suspensions better than the Bingham and Casson models. One should note that the Herschel-Bulkley model is not a wide-spread model due to the difficulty in finding an analytical solution to perform the parameter

regression model, although it has been used to describe the behavior of cement slurries (HEIRMAN, VANDEWALLE, *et al.*, 2008). Table 19 depicts the values of the best-fitted consistency index (m), the index behavior (n) and the yield stress (τ_0) for all suspensions, as well as the statistical indicators.

In this case, one can note the differences between the true and Newtonian shear rate, which more notable for all suspensions. The best-fitted parameters were calculated by regression of Equation (2.92) for True shear rates. As there is no analytical solution for this fluid, a one-hundred terms series was applied to minimize the errors between the numerical and experimental shear stress (RMS), then obtaining the best-fitted parameters for the model. Figure 43 describes the rheogram for cotton fabric-water suspensions. For the 1.25 kg one, a near Newtonian behavior is observed (n is almost 1), but the true shear rate approach indicates a higher yield stress value for the fluid. Also, for the 2.50 kg suspension more shear-thickening behavior is observed, but also the true shear rate approach indicates a higher yield stress value for the fluid again.

TABLE 20 - HERSCHEL-BULKLEY MODEL RHEOLOGICAL PARAMETERS FOR NEWTONIAN AND TRUE SHEAR RATES, AND EQUATION (2.103) (WITH 95% CONFIDENCE BOUNDS).

Shear rate approach	τ_0 (Pa)	m (Pa·s^n)	n	R^2	SSE	RMS
Cotton (1.25kg) - True	0.48 ± 0.05	4.94 ± 3.62	1.02 ± 0.30	0.957	8.37	0.91
Cotton (1.25kg) - Newt.	3.49 10^{-14}	5.15 ± 3.39	1.00 ± 0.21	0.963	1238	10.61
Cotton (1.25kg) - 2.94	4.35 10^{-13}	5.15	1.00 ± 0.21	0.963	0.69	0.25
Cotton (2.50kg) - True	0.88 ± 20.6	6.10 ±10.2	1.17 ± 0.60	0.960	7.83	0.88
Cotton (2.50kg) - Newt.	4.84 10^{-14}	7.13 ± 12.0	1.09 ± 0.48	0.958	4500	21.21
Cotton (2.50kg) - 2.94	6.80 10^{-13}	7.85	1.07 ± 0.23	0.958	2.50	0.48
S.S. (1.25kg) - True	0.41 ± 2.82	0.88 ± 0.83	1.59 ± 0.32	0.987	2.60	0.51
S.S. (1.25kg) - Newt.	1.80 ± 6.24	0.51 ± 0.45	1.63 ± 0.26	0.993	173	4.16
S.S. (1.25kg) - 2.94	0.83	0.79	1.63 ± 0.26	0.993	0.10	0.10
S.S. (2.50kg) - True	2.81 ± 0.02	6.27 ± 2.96	1.00 ± 0.19	0.966	6.65	0.82
S.S. (2.50kg) - Newt.	38.16 ± 9.1	0.69 ± 0.68	1.62 ± 0.29	0.991	365	6.04
S.S. (2.50kg) - 2.94	17.65	1.06	1.61 ± 0.29	0.990	0.20	0.14
Mixed (1.25kg) - True	0.75 ± 5.28	2.28 ± 2.30	1.27 ± 0.37	0.988	2.41	0.49
Mixed (1.25kg) - Newt.	2.75 ± 9.2	1.79 ± 1.54	1.29 ± 0.25	0.991	253	5.03
Mixed (1.25kg) - 2.94	1.27	2.16	1.29 ± 0.25	0.990	0.14	0.12
Mixed (2.50kg) - True	1.23 ± 12.2	3.77 ± 4.14	1.25 ± 0.38	0.992	1.26	0.37
Mixed (2.50kg) - Newt.	3.62 ± 18.7	3.23 ± 3.13	1.24 ± 0.27	0.992	454	7.10
Mixed (2.50kg) - 2.94	1.67	3.79	1.24 ± 0.27	0.992	0.25	0.17

FIGURE 43 - RHEOGRAM FOR COTTON FABRIC-WATER SUSPENSION WITH HERSCHEL-BULKLEY MODEL.

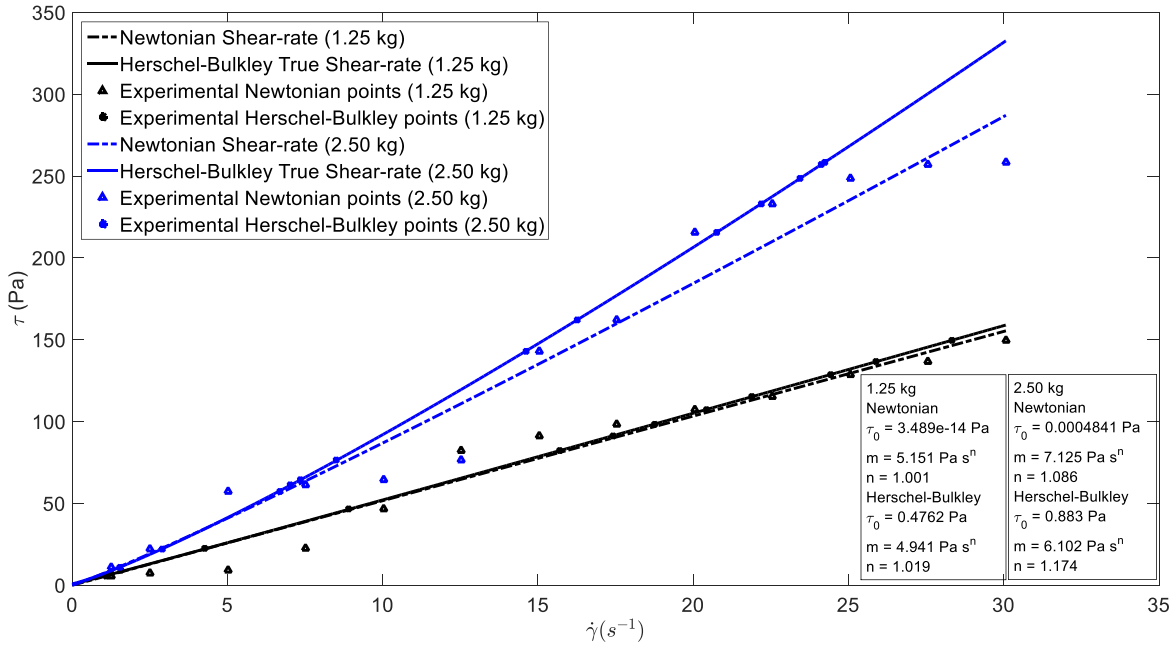

Figures 44 describes the rheogram of 1.25 kg and 2.50 semi-synthetic fabric-water suspension, respectively. While the lighter suspension presents a more shear-thickening behavior, the heavier suspension presents a more Newtonian-like behavior with a more viscous suspension with a higher yield stress value. It might happen because for achieving such mass of semi-synthetic fabric bulks a higher quantity of fabric tissues is needed thus saturating the fluid suspension if compared to the cotton fabric-water suspensions case.

Again, the rheogram of 1.25 and 2.50 kg of mixed fabric-water of cotton and semi-synthetic are depicted in Figure 45. As expected, a mixed behavior of the two fluids is observed as well. For the lighter suspension, an index value (n) of 1.27, which is higher than the cotton one and smaller than the semi-synthetic one, is observed. The same is observed for the yield stress (τ_0) and consistency index (m). On the other hand, the heavier fluid also shows a more shear-thickening behavior, contrary to the semi-synthetic fabric-water fluid suspension, thus also mixing the behaviors of the two fabrics types suspensions.

FIGURE 44 - RHEOGRAM FOR SEMI-SYNTHETIC FABRIC-WATER SUSPENSION WITH HERSCHEL-BULKLEY MODEL.

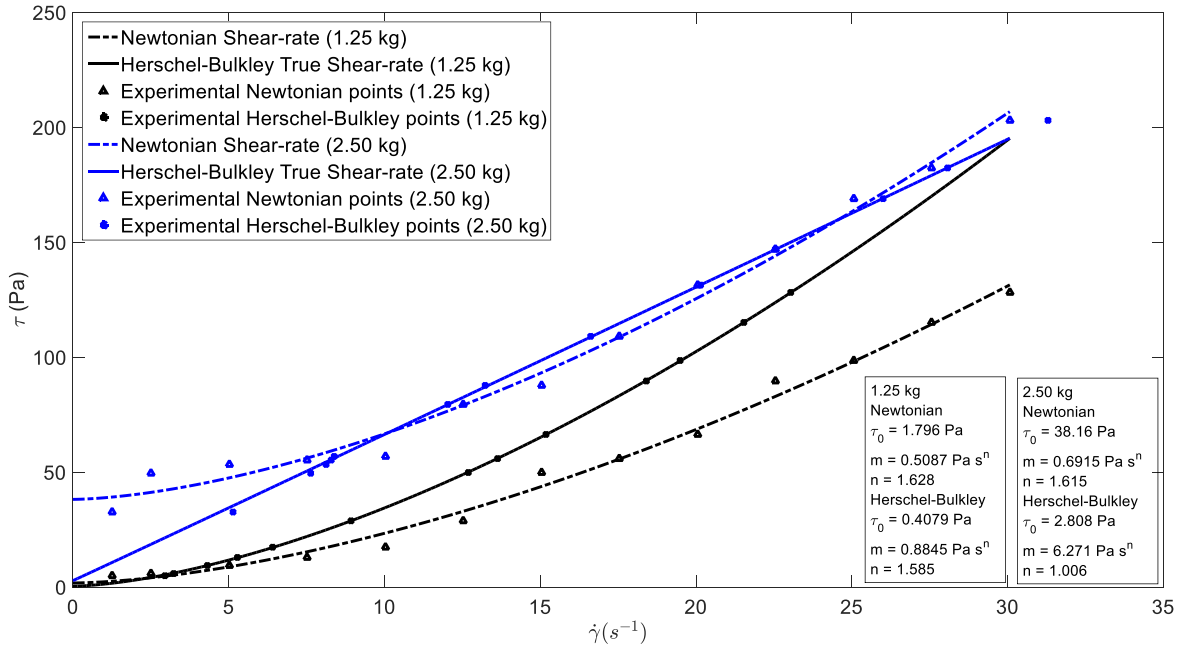

FIGURE 45 - RHEOGRAM FOR MIXED FABRIC-WATER SUSPENSION WITH HERSCHEL-BULKLEY MODEL.

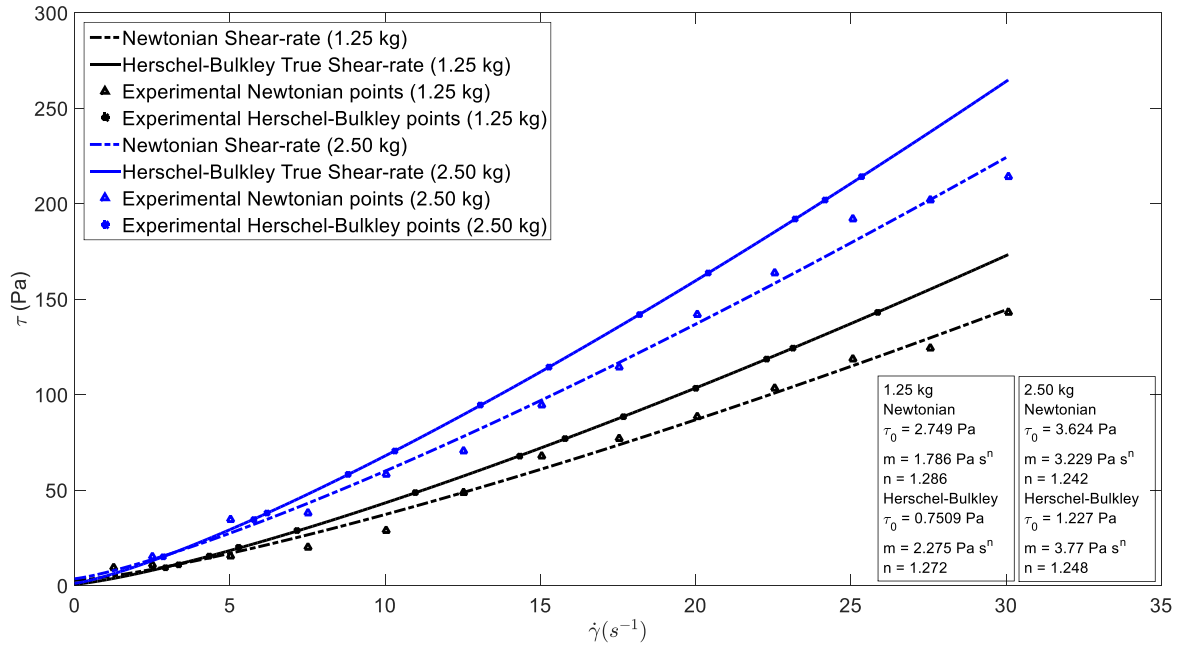

4.3.3 Comparison

The different flows have been analyzed by regression of the parameters for four different yield stress NNF models. In all the following figures, the different fluid models are plotted together in order to find out the one that best represents the fluid behavior, taking into account the shear stress value in the inner cylinder surface.

Figure 46 represents the flow behavior for the 1.25 kg of cotton fabric-water suspension, which presents a nearly Newtonian fluid behavior because almost no curvature is observed. In this case, both Robertson-Stiff and Herschel-Bulkley fluid models cover the experimental points in a better way than the Bingham and Casson fluids.

Figure 47 depicts the flow behavior of the 2.50 kg of cotton fabric-water suspension, which presents a more shear-thickening behavior than the lighter fluid. Because of the nature of the models, again both Robertson-Stiff and Herschel-Bulkley fluid models follow the experimental points better than the others.

FIGURE 46 - COMPARISON OF DIFFERENT FLUID MODELS REGRESSIONS FOR A 1.25 KG OF COTTON FABRIC-WATER SUSPENSION.

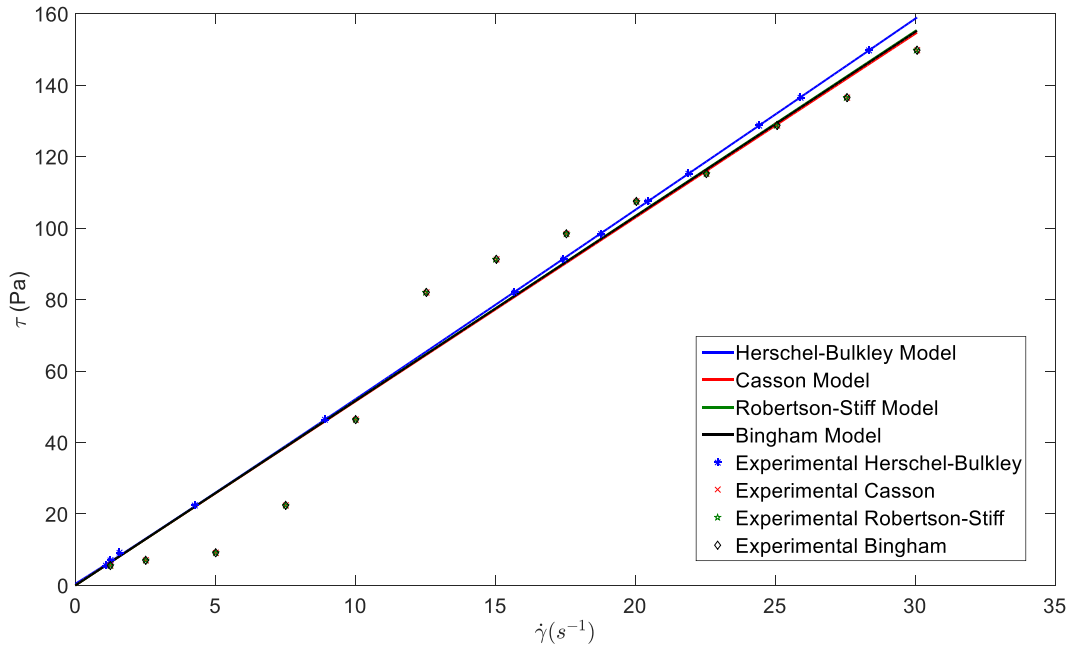

Considering the semi-synthetic fabric-water fluid flows, Figures 48 and 49 show the flow behavior of the 1.25 kg and 2.50 kg of fabric-water suspension, respectively. For those cases, the differences between the models, where Casson and Bingham models fail in representing the experimental points in lower velocities.

FIGURE 47 - COMPARISON OF DIFFERENT FLUID MODELS REGRESSIONS FOR A 2.50 KG OF COTTON FABRIC-WATER SUSPENSION.

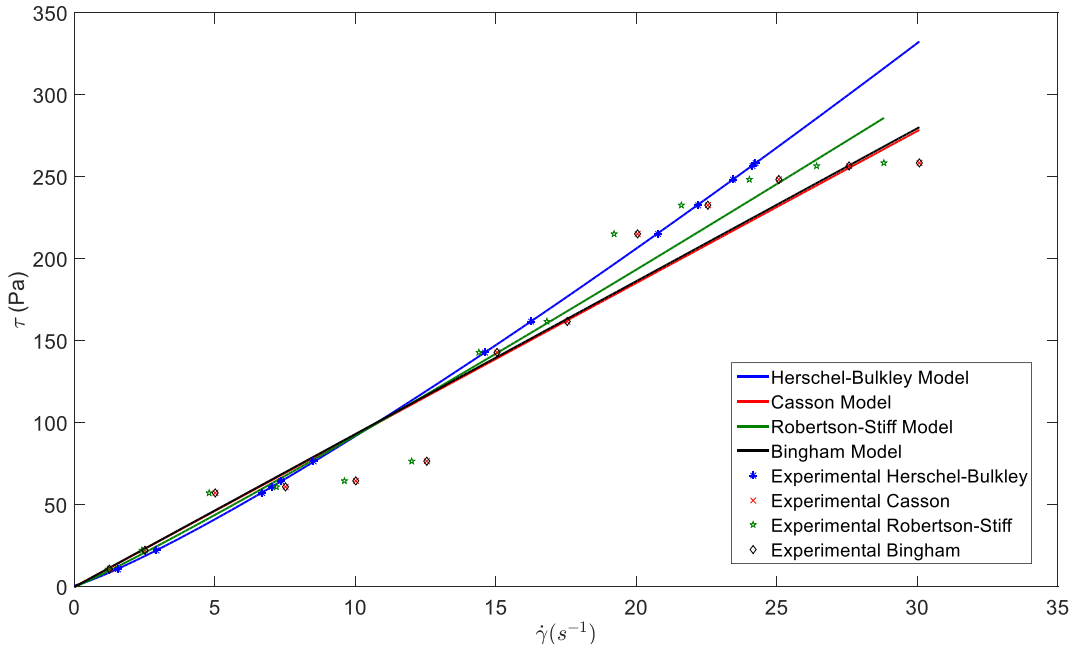

FIGURE 48 - COMPARISON OF DIFFERENT FLUID MODELS REGRESSIONS FOR A 1.25KG OF SEMI-SYNTHETIC FABRIC-WATER SUSPENSION.

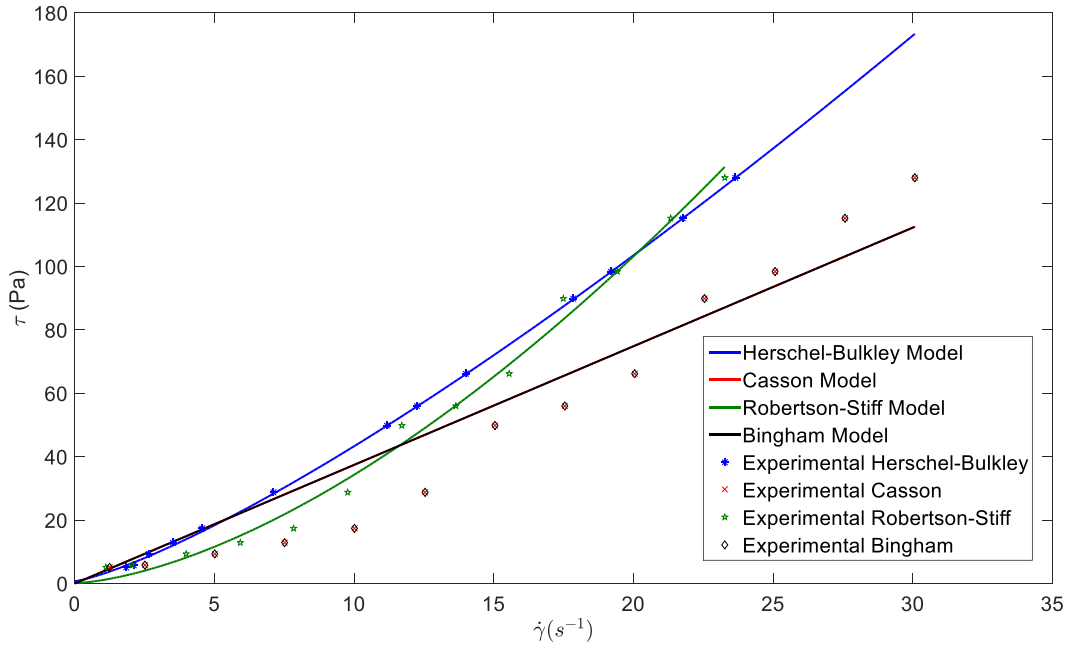

FIGURE 49 - COMPARISON OF DIFFERENT FLUID MODELS REGRESSIONS FOR A 2.50KG OF SEMI-SYNTHETIC FABRIC-WATER SUSPENSION.

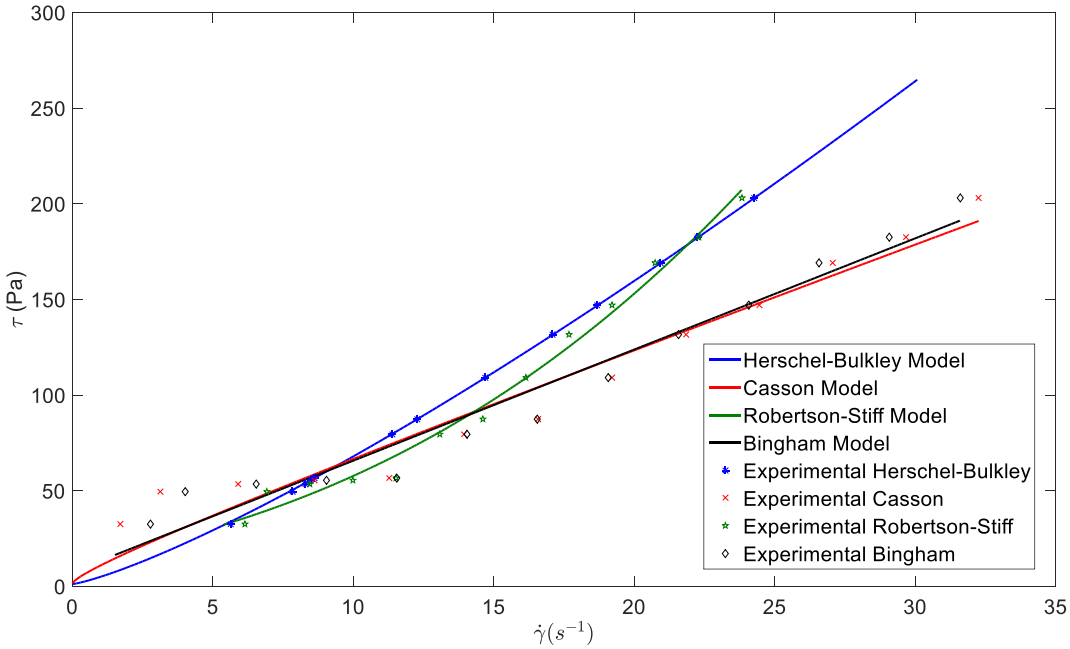

Figure 50 shows the flow behavior for the 1.25 kg of mixed fabric-water and water suspension, which presents a very shear-thickening behavior, where Bingham and Casson fluids fail in following the flow behavior, while the other fluids represent the curves properly.

FIGURE 50 - COMPARISON OF DIFFERENT FLUID MODELS REGRESSIONS FOR A 1.25KG OF MIXED FABRIC-WATER SUSPENSION.

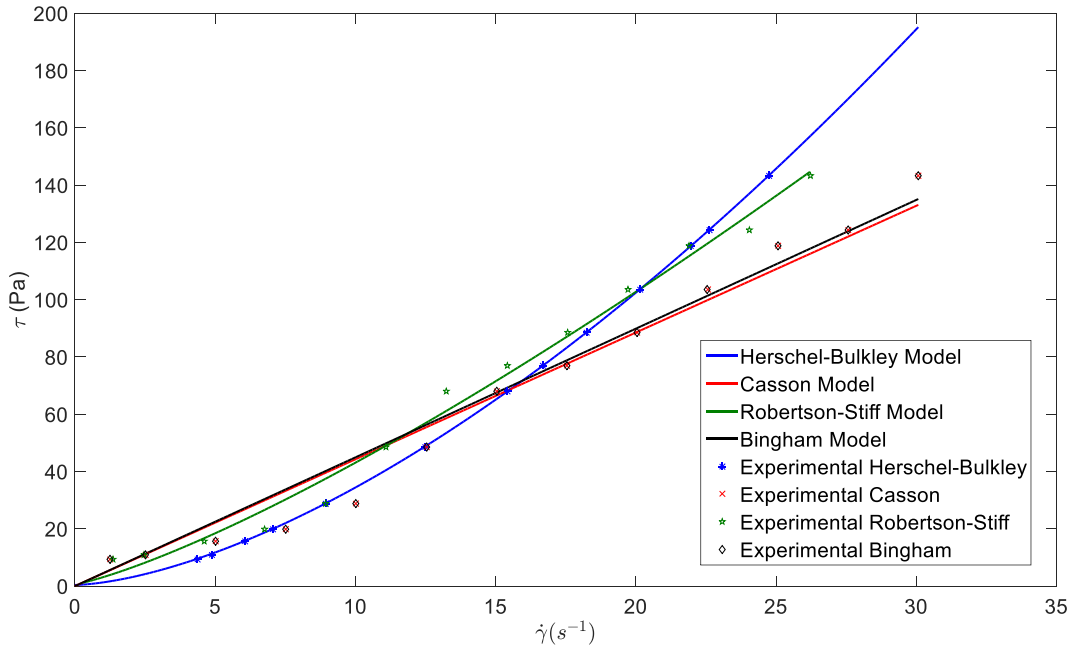

Finally, Figure 51 represents the flow behavior for the 2.50 kg of mixed fabric-water suspension. This fluid, when compared to the lighter one with the same fabric types, shows a more similar Newtonian fluid model behavior. Again, the Herschel-Bulkley showed a better approximation of the experimental curve.

FIGURE 51 - COMPARISON OF DIFFERENT FLUID MODELS REGRESSIONS FOR A 2.50 KG OF MIXED FABRIC-WATER SUSPENSION.

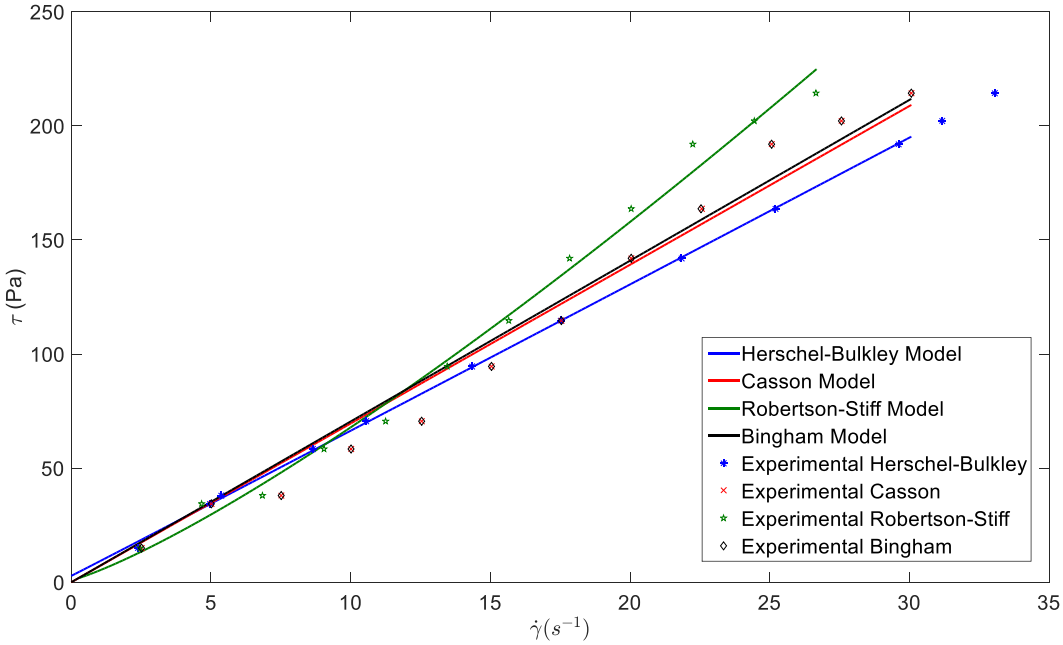

Observing the figures above, the following remarks can be summarized:

- All the fluids present a shear-thickening behavior, which is in general more perceptible for the heavier ones;
- The yield stress values are also higher for the heavier suspensions using a single fabric type;
- The Robertson-Stiff and Herschel-Bulkley fluid models represent the experimental points better than the others;
- The mixed fabric-water fluid suspensions combine the different behaviors of the cotton and semi-synthetic fabrics.

A possible explanation for the shear-thickening behavior is that the greater the imposed velocity by the inner cylinder, the higher the agglomerated of fabric tissues near the inner cylinder surface, which tends to elevate the viscosity near the cylinder. The yield stress growth

is clear as the higher the concentration of suspended fabrics the harder is to deflagrate the fluid flow.

Comparing the cotton and semi-synthetic fabric-water suspensions, it has been noticed that the cotton ones present a more Newtonian-like behavior. Leaving aside the physical stretching behavior of the cotton fabric and the more rigid behavior of the semi-synthetic fabric-water suspension, one possible explanation for the different regimes is that much more fabric tissues of semi-synthetic are needed to achieve the same mass value of the cotton tissues fabrics, thus resulting in a more concentrated suspension, which tends to increase the agglomeration of the tissue fabrics and elevating the viscosities values for this fluid suspensions.

4.3.4 Data Reduction – Long Blade Vane

Tables 21 and 22 present the Torque measurements values considering the three repetitions for each test for the two different bulks of mixed fabric-water suspensions. In this case, tests were carried out with longer four-blades with 45.5 mm, thus $k = R_{inn}/R_{out}$ is approximately 0.44, while the water column is the same (310 mm).

Tests concerning other fabric-water suspensions have not been carried out because the main purpose is to show that the vane-geometry is adequate to avoid the presence of wall slip velocity on the inner cylinder.

Figure 52 shows of the average values for each suspension (mixed fabrics), represented by the solid lines, where the symbols refer to the different runs for each test condition with the longer blades vane-geometry. One can note that the behavior of the fluid flows when compared to the shorter blade vane-geometry is roughly similar with higher torque values observed.

TABLE 21 - TORQUE MEASUREMENTS FOR 1.25 KG OF MIXED FABRIC-WATER SUSPENSIONS (LONG-BLADE GEOMETRY).

	Torque (N.m) values for mixed fabric-water suspensions					
	1.251 kg of mixed fabrics					
ω_{inn} (rpm)	Run 1	Run 2	Run 3	**Loaded**	Unloaded	**Net**
5	1.34	1.15	1.10	**1.199 ± 0.257**	0.973 ± 0.053	**0.226**
10	1.34	1.26	1.29	**1.298 ± 0.077**	0.971 ± 0.004	**0.327**
20	1.65	1.68	1.60	**1.642 ± 0.083**	1.072 ± 0.006	**0.569**
30	1.84	1.77	1.79	**1.799 ± 0.064**	1.144 ± 0.024	**0.655**
40	2.08	2.60	2.85	**2.509 ± 0.782**	1.207 ± 0.025	**1.302**
50	2.86	3.08	3.14	**3.029 ± 0.292**	1.260 ± 0.011	**1.769**
60	3.42	3.38	3.41	**3.404 ± 0.043**	1.320 ± 0.041	**2.084**
70	3.60	3.49	3.70	**3.599 ± 0.209**	1.329 ± 0.045	**2.269**
80	3.82	4.08	3.85	**3.916 ± 0.282**	1.346 ± 0.017	**2.570**
90	4.48	4.43	4.36	**4.426 ± 0.120**	1.391 ± 0.031	**3.035**
100	4.81	4.71	4.86	**4.792 ± 0.153**	1.416 ± 0.015	**3.376**
110	4.97	5.03	4.59	**4.862 ± 0.474**	1.474 ± 0.039	**3.388**
120	5.24	5.07	5.37	**5.225 ± 0.300**	1.481 ± 0.048	**3.745**

TABLE 22 - TORQUE MEASUREMENTS FOR 2.50 KG OF MIXED FABRIC-WATER SUSPENSIONS (LONG-BLADE GEOMETRY).

	Torque (N.m) values for mixed fabric-water suspensions					
	2.502 kg of mixed fabrics					
ω_{inn} (rpm)	Run 1	Run 2	Run 3	**Loaded**	Unloaded	**Net**
5	2.07	2.03	2.07	**2.055 ± 0.047**	0.973 ± 0.053	**1.083**
10	2.15	2.13	2.35	**2.210 ± 0.239**	0.971 ± 0.004	**1.239**
20	2.52	2.75	2.56	**2.608 ± 0.249**	1.072 ± 0.006	**1.535**
30	2.85	2.77	2.76	**2.793 ± 0.091**	1.144 ± 0.024	**1.648**
40	3.25	3.15	3.27	**3.223 ± 0.135**	1.207 ± 0.025	**2.016**
50	3.94	3.92	3.29	**3.717 ± 0.736**	1.260 ± 0.011	**2.458**
60	4.03	4.31	4.04	**4.126 ± 0.316**	1.320 ± 0.041	**2.806**
70	4.35	5.16	4.52	**4.678 ± 0.858**	1.329 ± 0.045	**3.349**
80	5.39	5.56	5.50	**5.483 ± 0.169**	1.346 ± 0.017	**4.137**
90	6.28	5.96	6.00	**6.081 ± 0.349**	1.391 ± 0.031	**4.691**
100	6.83	6.73	6.53	**6.696 ± 0.301**	1.416 ± 0.015	**5.280**
110	6.74	7.02	7.09	**6.952 ± 0.372**	1.474 ± 0.039	**5.478**
120	7.26	7.15	6.63	**7.012 ± 0.676**	1.481 ± 0.048	**5.531**

FIGURE 52 - EXPERIMENTAL AVERAGE TORQUE VALUES FOR TWO DIFFERENT MIXED FABRIC-WATER SUSPENSIONS BULKS STEADY-STATE FLOWS (LONG-BLADED GEOMETRY).

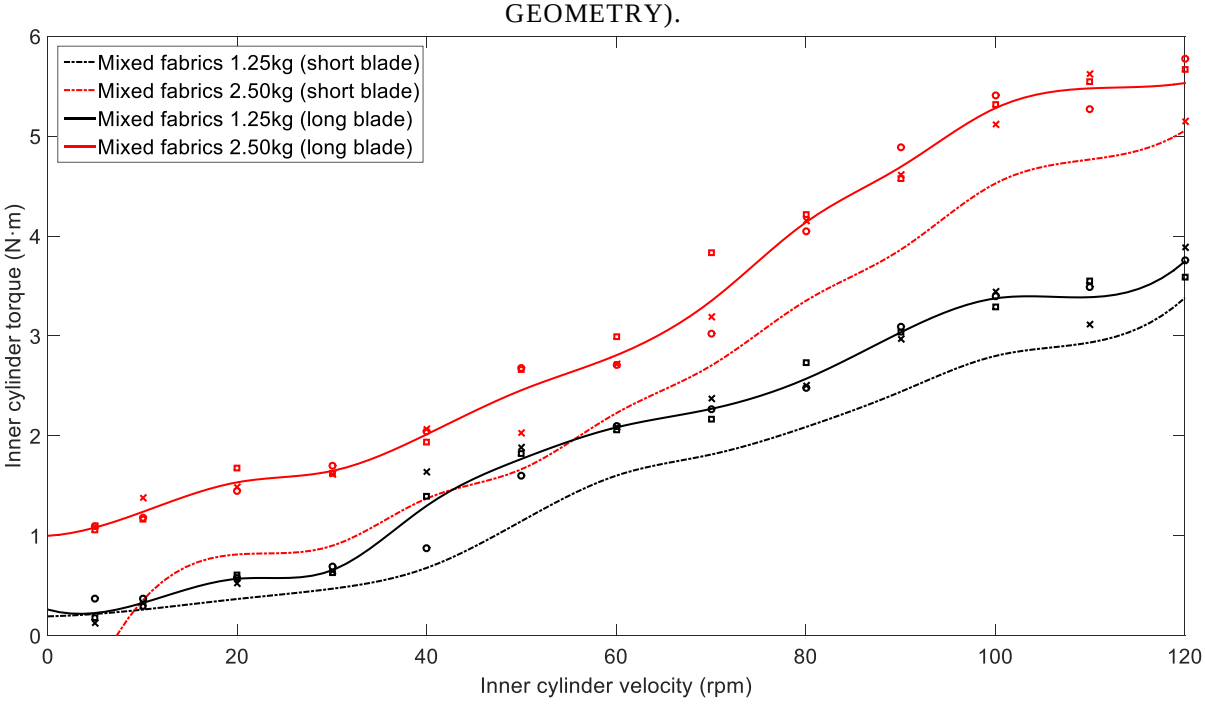

Figure 53 shows the difference between the rheograms for different blade length vane-geometries for a 1.25 kg of mixed fabric-water suspension. In this case, both geometries present similar yield stress and flow index value, and the difference between both curves is due to the difference of the Power-Law index (n), which is 1.27 for the shorter blades and 1.15 for the longer blades.

Figure 54 shows the difference between the rheograms of different blade length vane-geometries for a 2.50 kg of mixed fabric-water suspension. In this case, probably because of the longer length of the blades, the yield stress values are higher in this geometry, but both flow index values (m) and Power-Law index values (n) are much closer (1.25 and 1.17), which can be observed in the closest approximation of the curves.

Despite some difference between the curves, one can see the convergence of the values obtained for different vane-geometries dimensions for the same fluids. This denotes that both succeed to avoid the slip velocity and prove the assumption that the fluid is trapped between the vane blade acting like a solid cylinder.

FIGURE 53 - RHEOGRAM COMPARISON FOR DIFFERENT BLADE LENGTH VANE-GEOMETRIES FOR A 1.25KG OF MIXED FABRIC-WATER SUSPENSION.

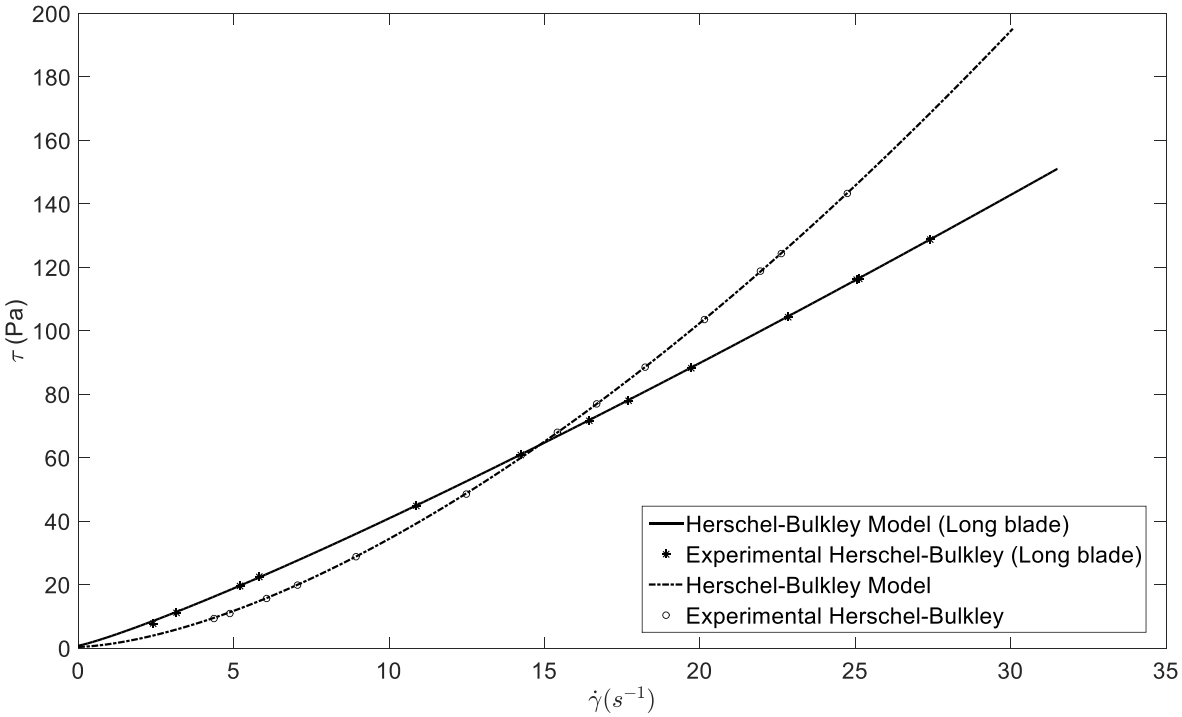

FIGURE 54 - RHEOGRAM COMPARISON FOR DIFFERENT BLADE LENGTH VANE-GEOMETRIES FOR A 2.50KG OF MIXED FABRIC-WATER SUSPENSION.

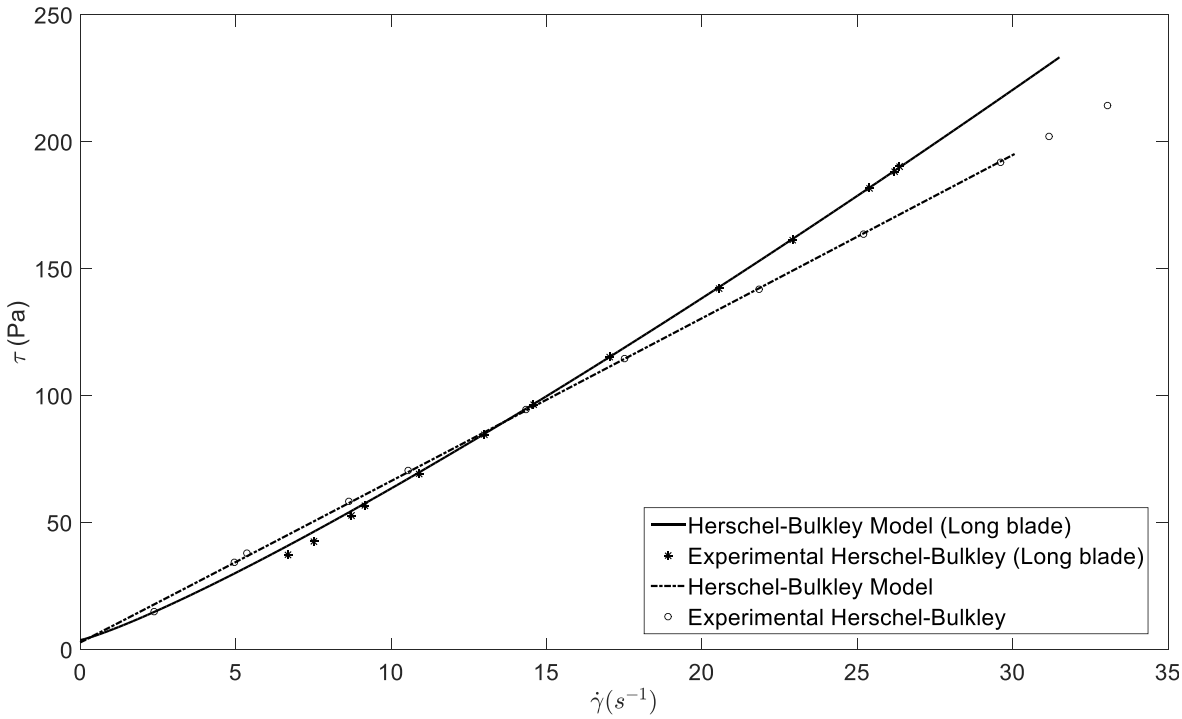

4.3.5 Periodic Flow

Based on Figures 29 and 30, four different periodic tests were performed. Tests 1 and 2 have the following cycle step: acceleration and deceleration times of 0.32 s each, time in constant maximum or minimum velocity of 1.72 s, and time-off of 0.64 s. For Tests 3 and 4, all the times above are cutted to half. The tests were conducted with the four-bladed inner cylinder with 34 mm of blade length, with and without the smooth bottom basis rotating with the inner cylinder. For all test conditions, five repetitions were performed.

4.3.5.1 Static Bottom Basis Flow

The results for the Test 1 are presented below. Figure 55 shows the five runs for 1.25 kg of mixed fabric-water suspension, while Figure 56 shows the results for 2.50 kg of mixed fabric-water suspension.

FIGURE 55 - EXPERIMENTAL TORQUE DATA OF THE 1.25 KG OF MIXED FABRIC-WATER SUSPENSION IN PERIODIC TEST 1.

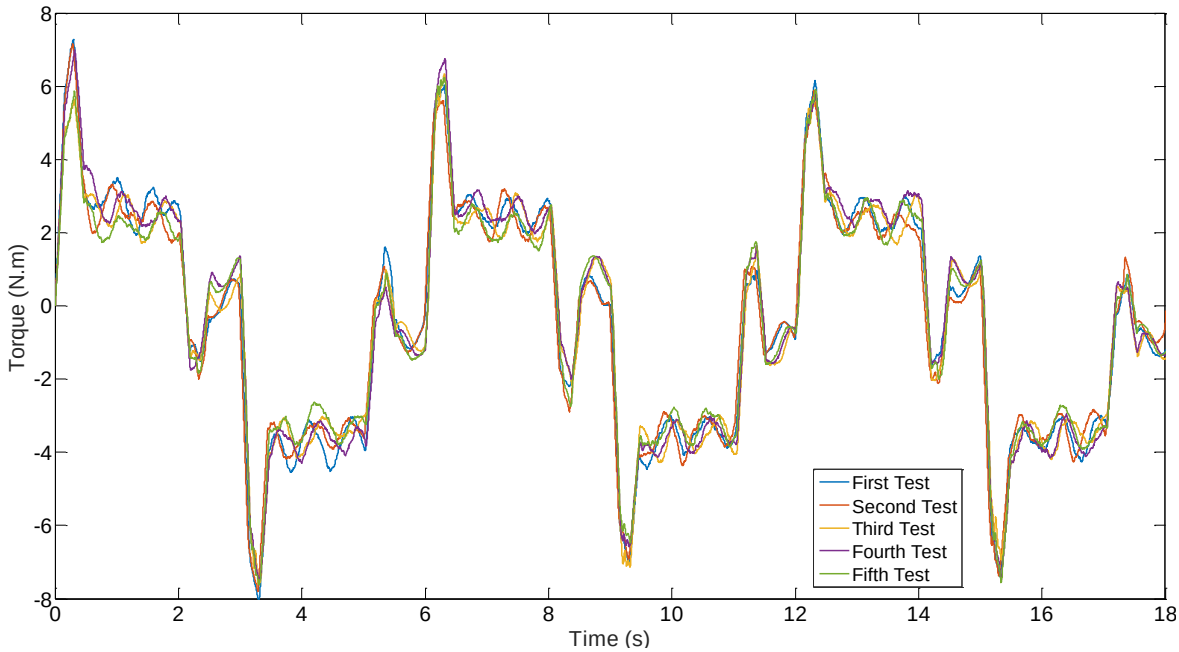

FIGURE 56 - EXPERIMENTAL TORQUE DATA OF THE 2.50 KG OF MIXED FABRIC-WATER SUSPENSION IN PERIODIC TEST 1.

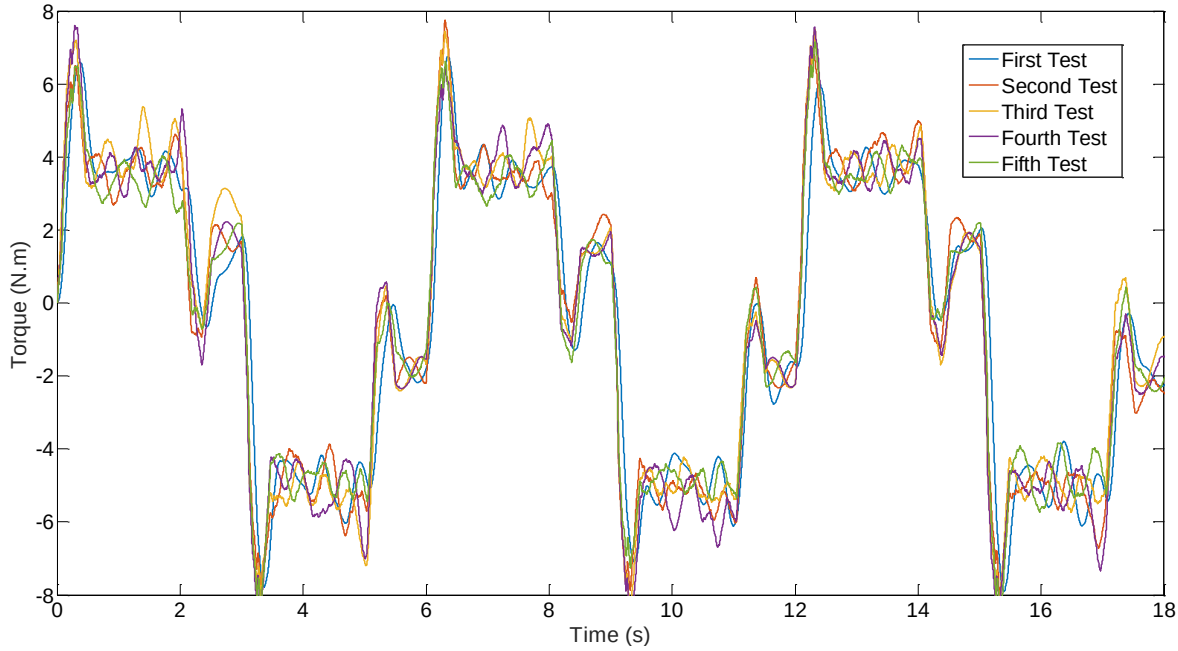

Figure 57 shows comparisons between the average torque of the two conditions above. One can note that all the tests present higher peaks every time a swift acceleration and deceleration takes place. In times when constant or null velocities takes place, the torque response tends to a more linear behavior. As expected, the torque response values are higher the heavier is the suspension.

FIGURE 57 - EXPERIMENTAL AVERAGE TORQUE DATA FOR TWO DIFFERENT BULKS OF MIXED FABRIC-WATER SUSPENSIONS IN PERIODIC TEST 1.,

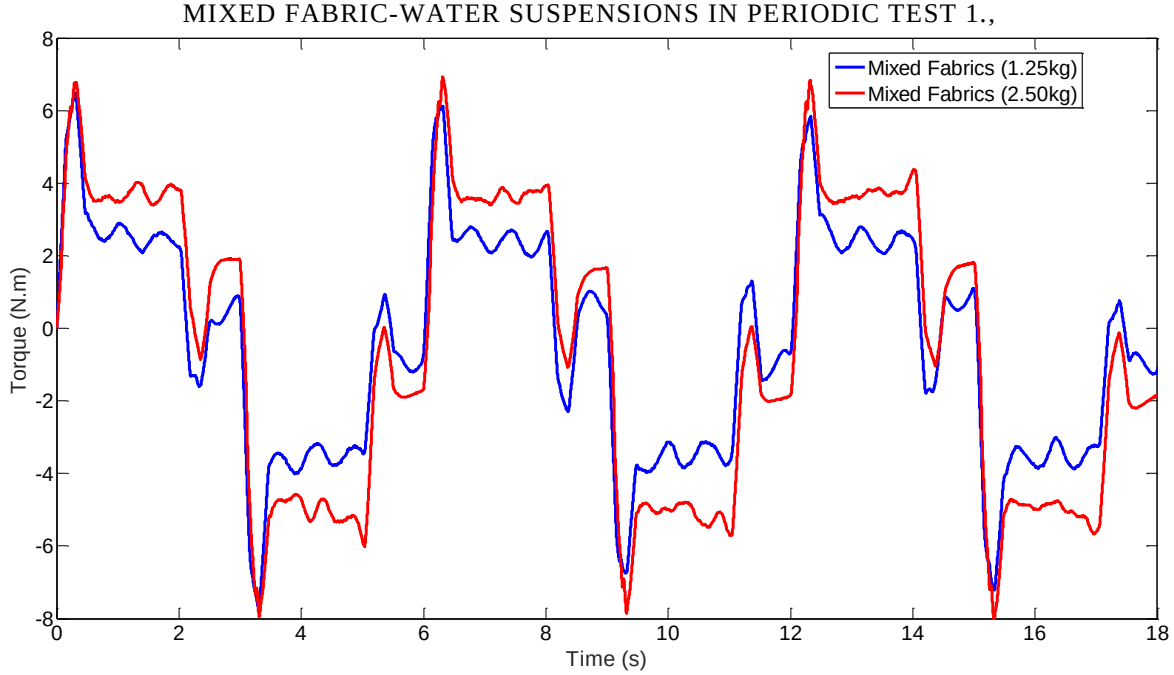

Figure 58 shows the average velocities of all runs on time. It is observed that a good response, between the imposed and the measured velocities, was achieved for all tests.

FIGURE 58 - EXPERIMENTAL AVERAGE VELOCITY DATA FOR TWO DIFFERENT BULKS OF MIXED FABRIC-WATER SUSPENSIONS IN PERIODIC TEST 1.

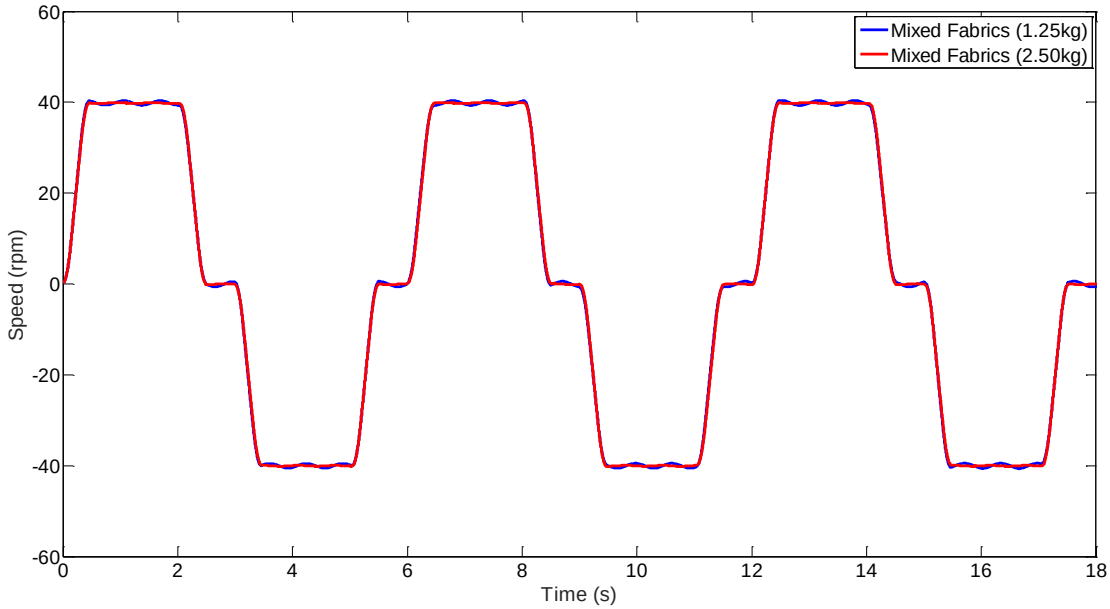

Similarly, the results for Test 2 are presented in Figure 59. Which depicts comparisons between the average values of the torque for two conditions. As expected, when compared to Test 1, the torque responses are higher not only because the maximum velocity is higher, but also the acceleration and deceleration values are higher as well.

FIGURE 59 - EXPERIMENTAL AVERAGE TORQUE DATA FOR TWO DIFFERENT BULKS OF MIXED FABRIC-WATER SUSPENSIONS IN PERIODIC TEST 2.

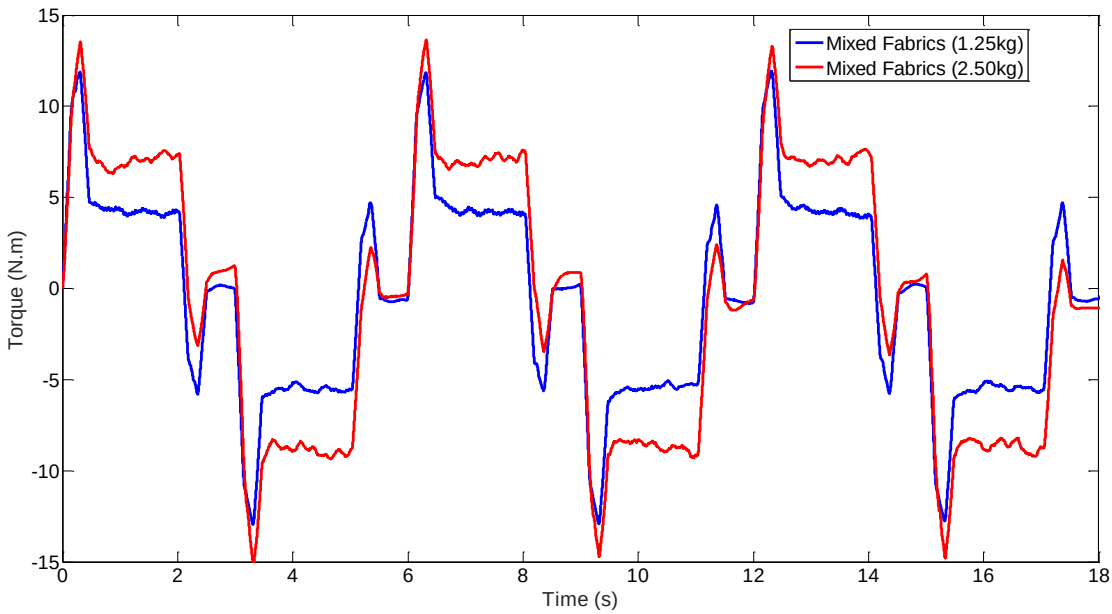

Figure 60 shows the average velocities of all tries along with time for Test 2 tries. One can notice that a quite good response and similarity between the tests are observed.

FIGURE 60 - EXPERIMENTAL AVERAGE VELOCITY DATA FOR TWO DIFFERENT BULKS OF MIXED FABRIC-WATER SUSPENSIONS IN PERIODIC TEST 2.

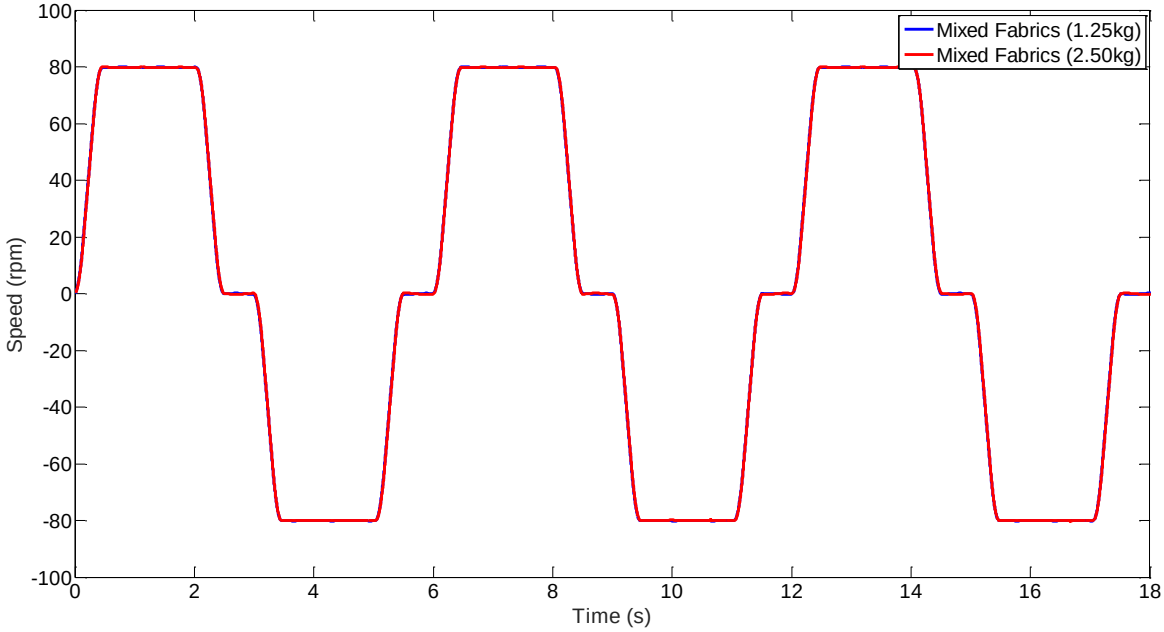

Figure 61 shows comparisons between the average values of the two conditions. As Test 3 period is shorter, thus acceleration and deceleration periods are faster, the peaks of torque values have a higher magnitude in comparison with Test 1.

FIGURE 61 - EXPERIMENTAL AVERAGE TORQUE DATA FOR TWO DIFFERENT BULKS OF MIXED FABRIC-WATER SUSPENSIONS IN PERIODIC TEST 3.

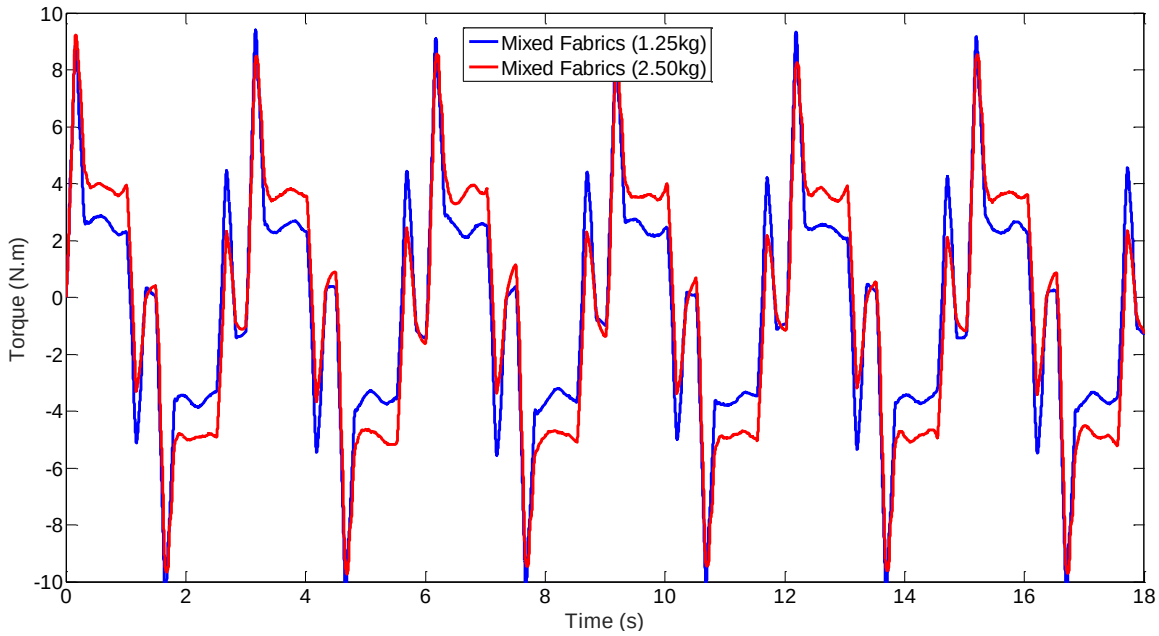

Figure 62 shows the average velocities of all tries along with time for Test 3 tries, showing a good velocity response even for faster acceleration and deceleration periods.

FIGURE 62 - EXPERIMENTAL AVERAGE VELOCITY DATA FOR TWO DIFFERENT BULKS OF MIXED FABRIC-WATER SUSPENSIONS IN PERIODIC TEST 3.

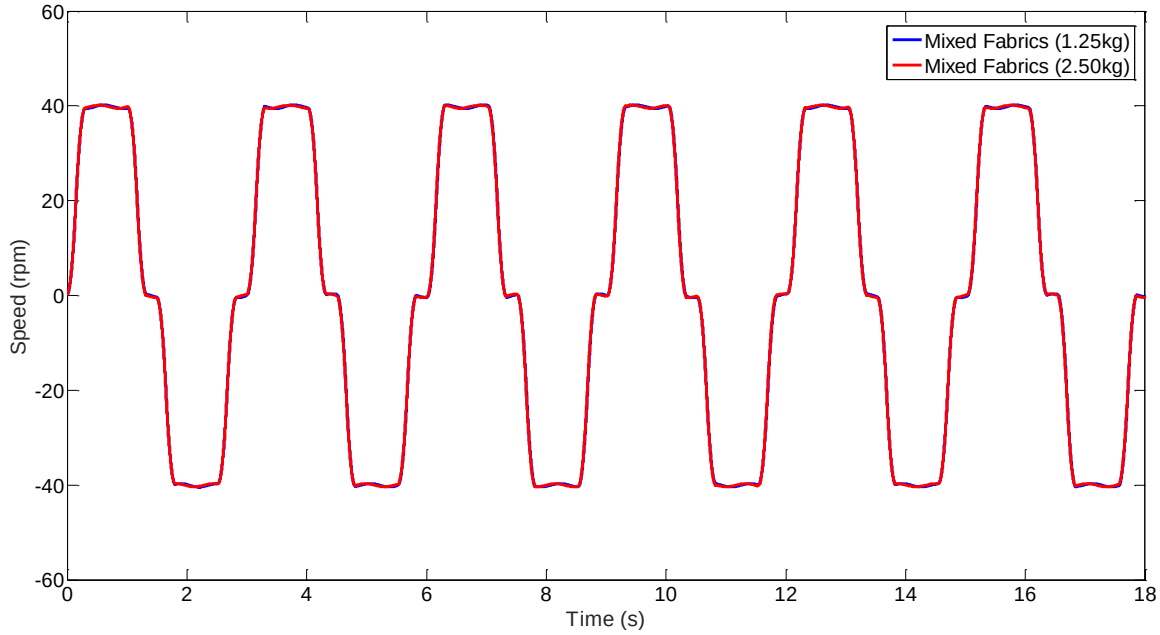

Similar to Figure 61, Figure 63 shows comparisons between the average values of the two conditions. Again, it presents higher peaks of torque magnitude in reason of the maximum velocity and the shorter periods of acceleration and deceleration.

FIGURE 63 - EXPERIMENTAL AVERAGE TORQUE DATA FOR TWO DIFFERENT BULKS OF MIXED FABRIC-WATER SUSPENSIONS IN PERIODIC TEST 4

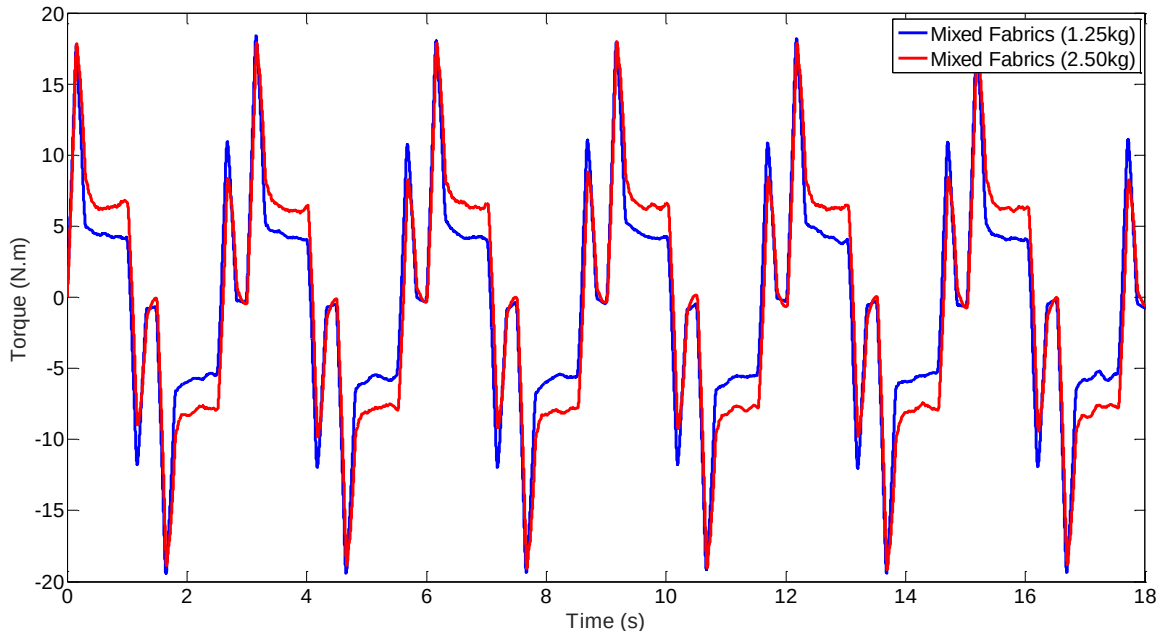

Figure 64 shows the average velocities of all tries along with time for Test 4 runs.

FIGURE 64 - EXPERIMENTAL AVERAGE VELOCITY DATA FOR TWO DIFFERENT BULKS OF MIXED FABRIC-WATER SUSPENSIONS IN PERIODIC TEST 4.

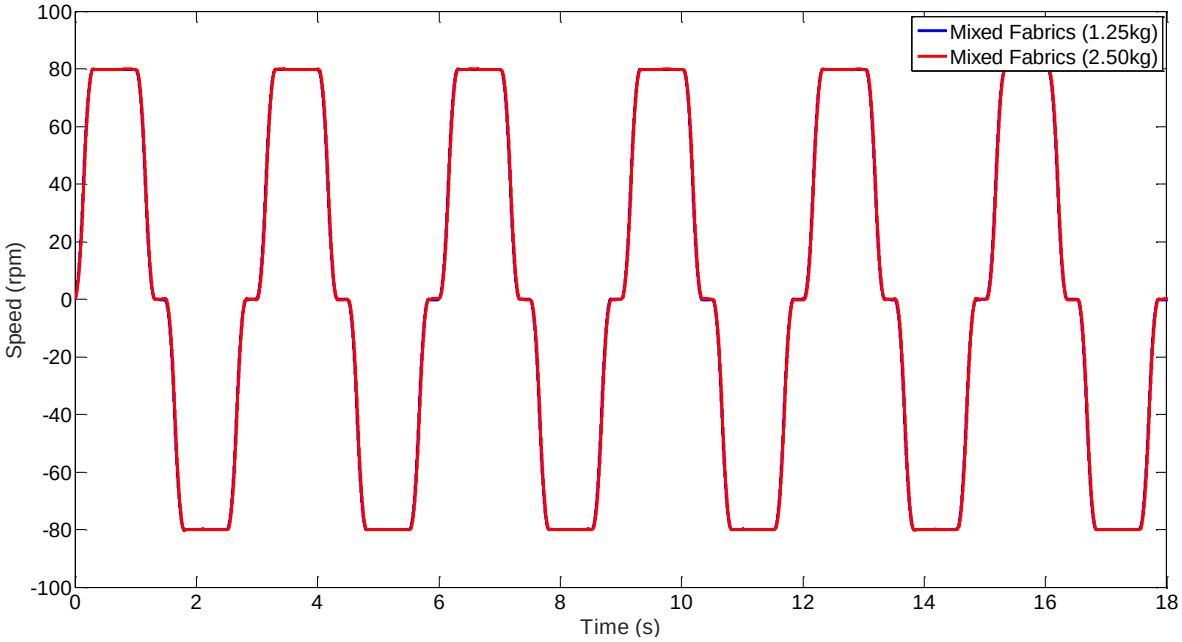

4.3.5.2 Rotating Bottom Basis Flow

As mentioned before, additional tests with the bottom rotating with the inner cylinder at the same speed were carried out to emulate the conditions found in a household vertical-axis top-load washing machine. Thus, the total torque, comprised of the torque to drive the inner cylinder plus the bottom basis, and the torque transmitted to the fluid were measured. In this case, the figures showing the angular velocities over time are not presented, as they look like almost the same due to the good velocity control.

The results for the Test 1 are presented below. Figure 65 shows the results of the five tries for the 1.25 kg of mixed fabric-water suspension, while Figure 66 shows the results for 2.50 kg of mixed fabric-water suspension. Figure 67 shows comparisons between the average values of the two figures above. One can note that, when compared to Figure 82, all the tests present higher peaks every time a swift acceleration and deceleration takes place. As one could have expected, with the basis contribution addition, the torque values response is also higher.

FIGURE 65 - EXPERIMENTAL TORQUE DATA OF 1.25 KG OF MIXED FABRIC-WATER SUSPENSION IN PERIODIC TEST 1 (WITH ROTATING BASIS).

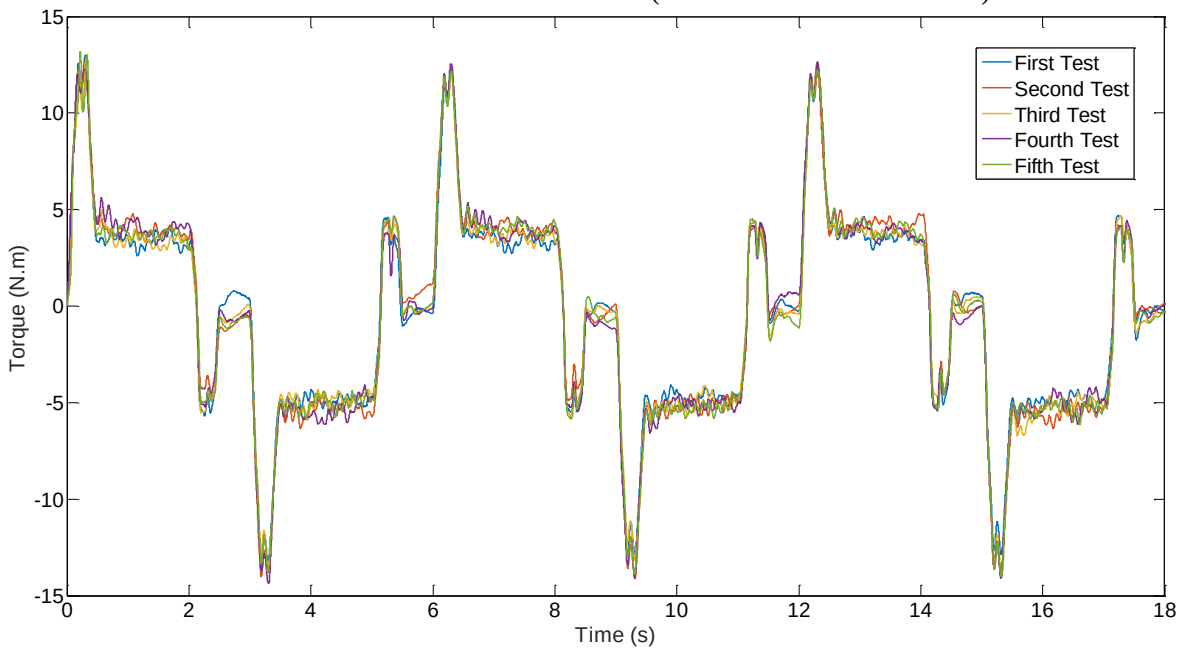

FIGURE 66 - EXPERIMENTAL TORQUE DATA OF 2.50 KG OF MIXED FABRIC-WATER SUSPENSION IN PERIODIC TEST 1 (WITH ROTATING BASIS).

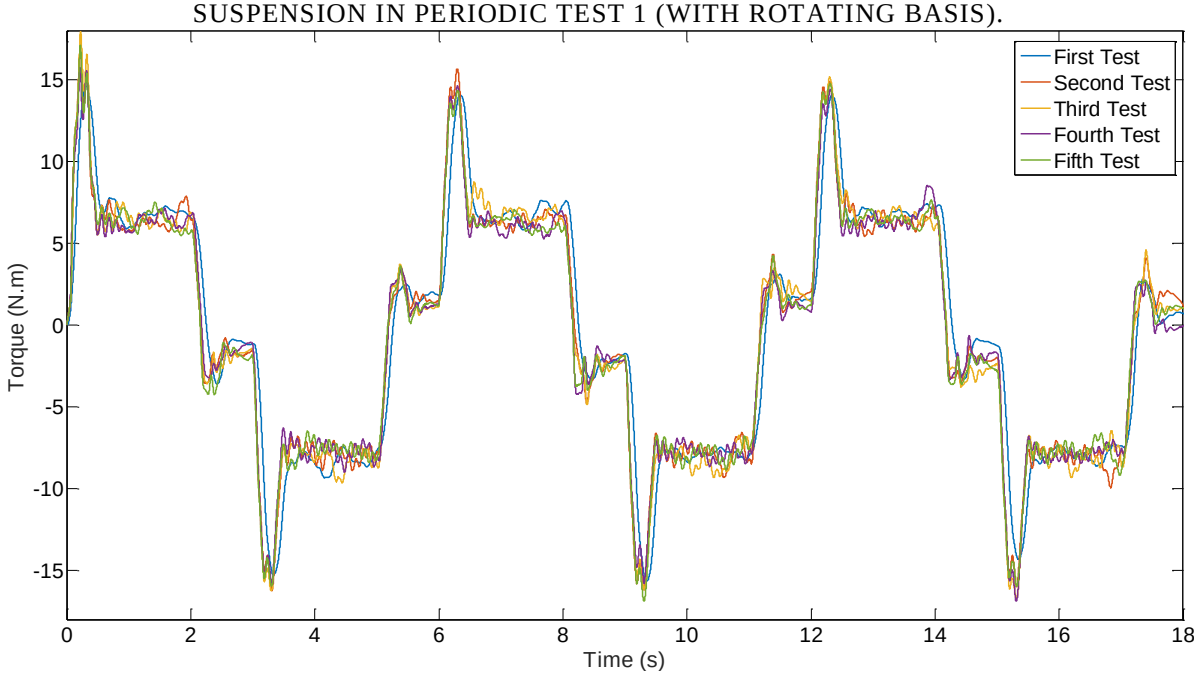

FIGURE 67 - EXPERIMENTAL AVERAGE TORQUE DATA FOR TWO DIFFERENT BULKS OF MIXED FABRIC-WATER SUSPENSIONS IN PERIODIC TEST 1 (WITH ROTATING BASIS).

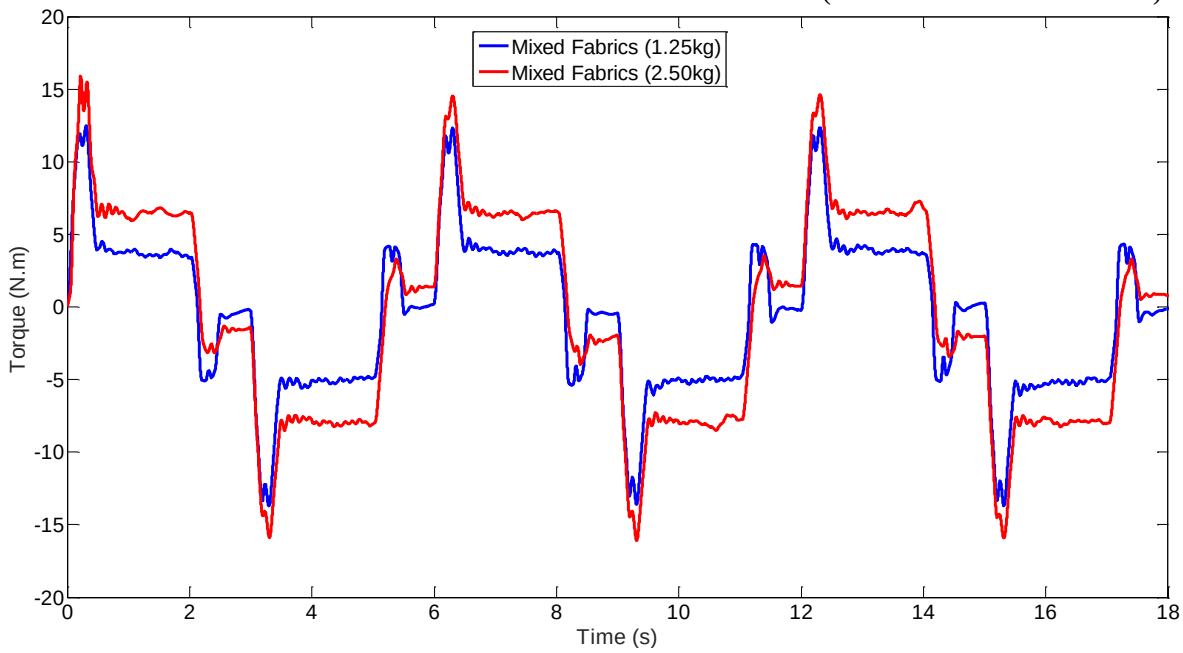

Figure 68 shows comparisons between the average values of the two conditions (1.25 and 2.50 kg of fabric) for Test 2. Again, when compared to Figure 57, all the torque responses are higher, similar to Figure 67. It also should be mentioned that the torque value signal has more noise than before.

FIGURE 68 - EXPERIMENTAL AVERAGE TORQUE DATA FOR TWO DIFFERENT BULKS OF MIXED FABRIC-WATER SUSPENSIONS IN PERIODIC TEST 2 (WITH ROTATING BASIS).

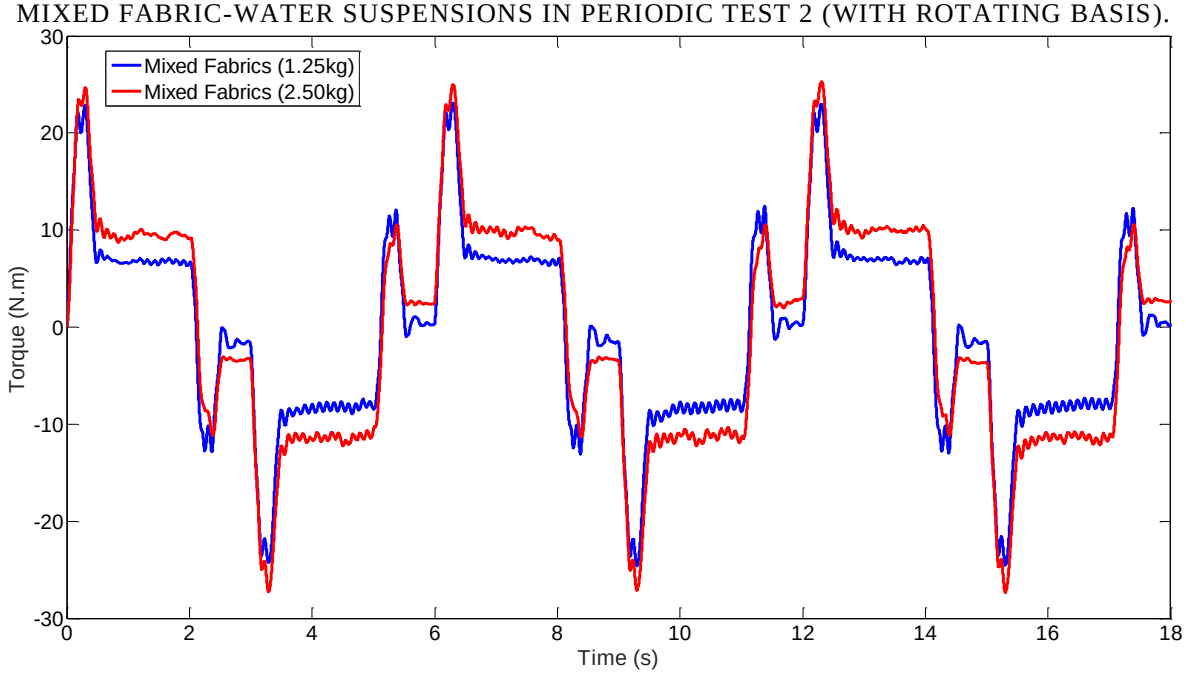

Like the other tests, Figure 69 shows comparisons between the average values of the two conditions (1.25 and 2.50 kg of fabric) for Test 3, which torque values are higher than the ones observed in Figure 61.

FIGURE 69 - EXPERIMENTAL AVERAGE TORQUE DATA FOR TWO DIFFERENT BULKS OF MIXED FABRIC-WATER SUSPENSIONS IN PERIODIC TEST 3 (WITH ROTATING BASIS).

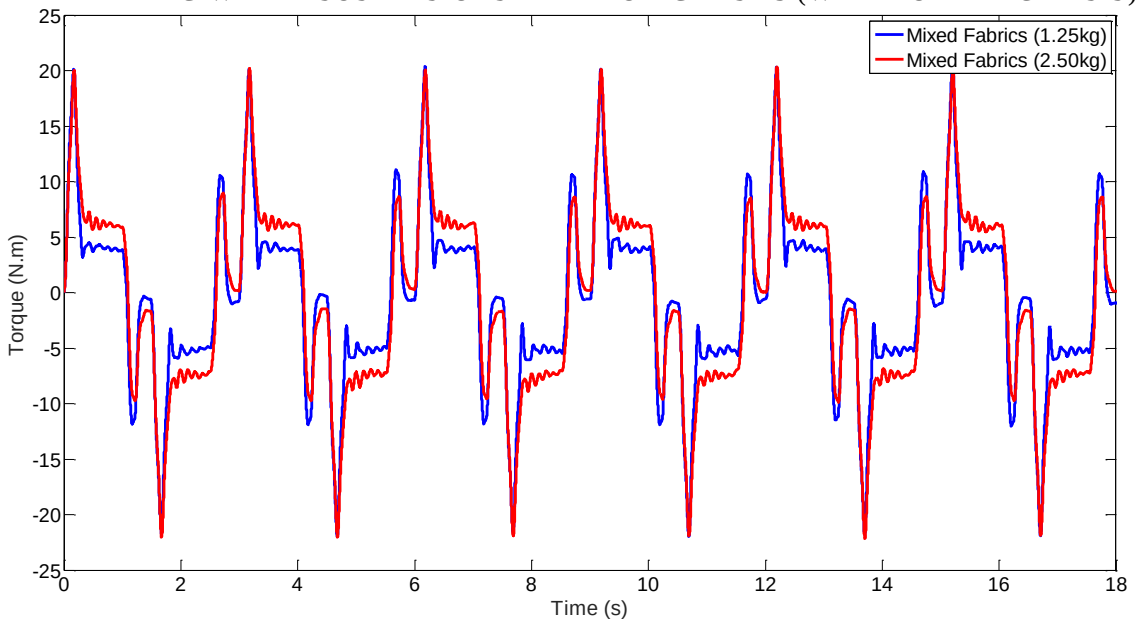

In conclusion, Figure 68 shows comparisons between the average values of the two conditions (1.25 and 2.50 kg of fabric) for Test 4. One can observe that the heavier fluid presents higher torque values, despite the peak points is similar for both fluids.

FIGURE 70 - EXPERIMENTAL AVERAGE TORQUE DATA FOR TWO DIFFERENT BULKS OF MIXED FABRIC-WATER SUSPENSIONS IN PERIODIC TEST 4 (WITH ROTATING BASIS).

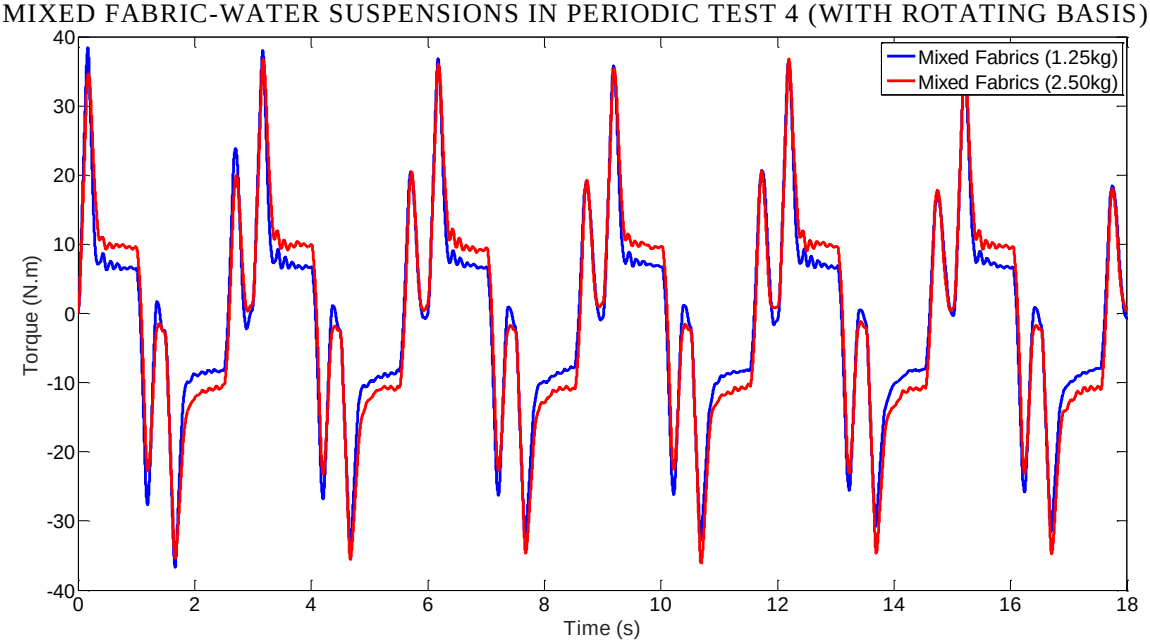

4.4 CHAPTER SUMMARY

This chapter presented test rig used to measure the torque transmitted from the rotating inner cylinder surface to the fluid through a controlled angular velocity imposed to the inner cylinder. The geometry of the apparatus consists in a coaxial double cylinder viscometer. In addition, a plan of tests was designed considering three main parameters: (a) fabric type, (b) amount of fabric and (c) angular velocity (ω_{inn}). Two different regimes were proposed: (a) steady-state flow and (b) periodic flow.

At first, the steady-state tests have been carried out and their results were used for the regression of the rheological behavior of the fluid through a method called Couette inverse problem. It consists of obtaining the curve of shear stress in function of the shear rate values from measured torques for different angular velocities. In this work, four different NNF models with yield stress were investigated to find out which model is more suitable to describe the rheological behavior of the fabric-water suspensions. It was observed that the Herschel-Bulkley was the best fitting NNF model among all the options so that its parameters are used for modeling the numerical simulations of water-fabric suspensions flows henceforth. Also, different flow behaviors were discussed when the fabric types and the fabric amounts were changed, as well as the comparison between two different ways to obtain the shear rate values (true and Newtonian approaches). While the Newtonian approach is mostly used for narrow gap geometries, the so-called “true” approach is a more suitable way to describe the rheological behavior of a fluid flow in a wide-gap geometry, which is the here.

Finally, periodic tests with the mixed fabric-water suspensions (cotton and semi-synthetic) were carried out for two different geometry conditions: (i) non-rotating bottom basis and (ii) rotating bottom basis. The latter one was performed in order to emulate the conditions found in a real washing machine.

The results obtained in this Chapter were used as boundary conditions for fluid modeling in numerical experimentation in Chapter 5.

5 NUMERICAL SIMULATIONS

This chapter presents the implementation of the numerical methodology, presented in Chapter 3, by means of numerical carried out by means of a finite-volume-based code. Numerical results are verified against the experimental measurements presented in Chapter 4. For that reason, the NNF is modeled considering the regressed parameters for the Herschel-Bulkley fluid model. Furthermore, not only steady-state simulations are on the matter of this Chapter, but also periodic fluid flows.

5.1 CODE VERIFICATION AND NUMERICAL EXPERIMENTATION

Code verification and numerical experimentation by means of a homemade finite-volume-based code using CFD techniques are presented. The simulation results have been verified against analytical solutions for laminar steady-state simulations and numerical-experimental database obtained in the open literature.

5.1.1 Two-dimensional Results Verification

A two-dimensional laminar steady-state simulation using glycerin as the Newtonian fluid ($\rho = 1261.3\,\mathrm{kg/m^3}$ and $\mu = 1.412\ \mathrm{Pa \cdot s}$) was held and its results were compared to the analytical solution (Equation 2.46). The geometric parameters utilized in this simulation were: $R_{inn} = 0.075$ m and $R_{out} = 0.265$ m, which indicates that both radius ratio and gap are respectively $k = 0.283$ and $\delta = 0.19$ m. The angular inner cylinder speed was $\omega = \pi\,\mathrm{rad/s}$, while the outer cylinder remained static. Those geometrical parameters and input parameter lead to the following dimensionless numbers: $\mathrm{Re} = 48.4$ and $\mathrm{Ta} = 5932$. The convergence criterion used in this simulation was 10^{-10} for both mass and momentum residues (Equations 3.51 and 3.52).

Figure 71 shows a comparison between the numerical results for the tangential velocity component and the analytical solution along the radial direction (n_θ and n_r = 15). In the dimensionless scale, the zero value indicates the inner cylinder while the unitary value indicates the outer cylinder. The maximum velocity is obtained along the inner cylinder surface (ωR_{inn}). One can observe that there is a good matching between the solutions. Figure 72 shows the tangential velocity component behavior along the tangential direction in the middle of the radial

gap. For a steady-state simulation, it is expected that the velocity maintains a constant value, which can be observed in the figure.

FIGURE 71 - TWO-DIMENSIONAL VALIDATION: TANGENTIAL VELOCITY COMPONENT (V_Θ) PROFILE IN RADIAL DIRECTION (R).

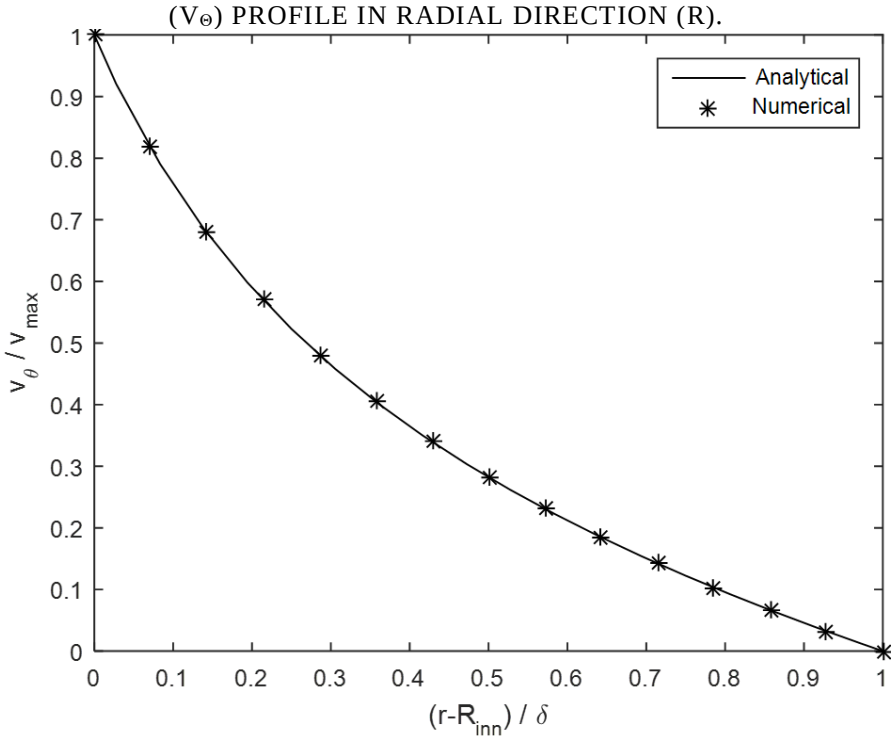

FIGURE 72 - TWO-DIMENSIONAL VALIDATION: TANGENTIAL VELOCITY COMPONENT (V_Θ) PROFILE IN TANGENTIAL DIRECTION (Θ).

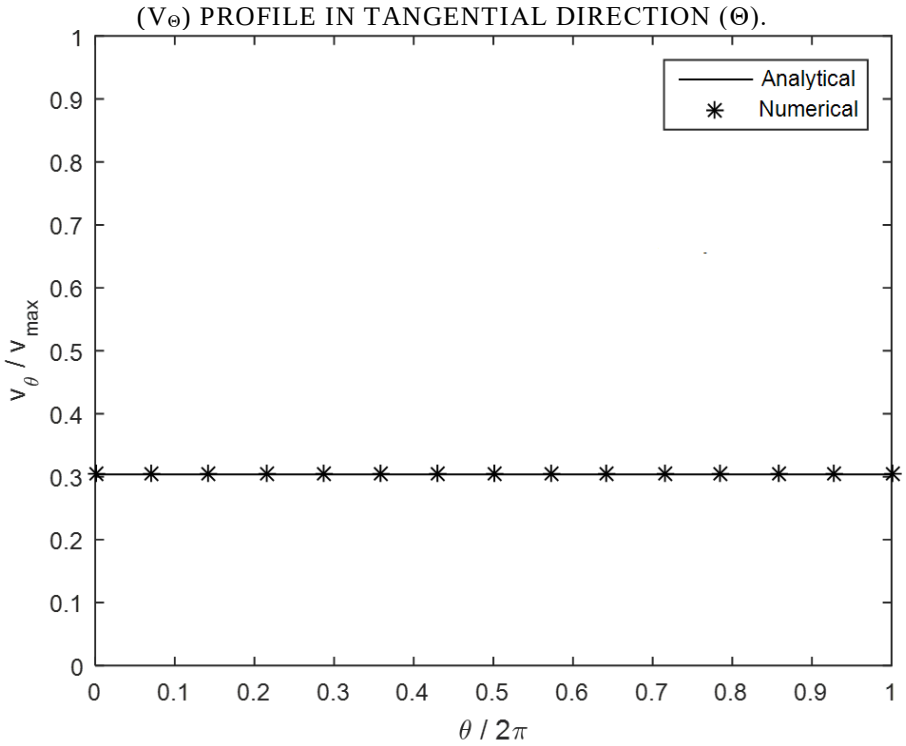

The same configuration of the previous simulation was used in order to perform a comparison between three different solvers: (a) TDMA / CTDMA, (b) BiCGSTAB (without preconditioner), and (c) BiCGSTAB using the TDMA / CTDMA as a preconditioner. For the same convergence criterion (ERR = 10^{-10}), various simulations changing the number of control volumes were performed. The number of control volumes corresponding to the number of nodes on tangential (n_θ) and radial (n_r) directions are shown in Table 23, as well as the computational time to achieve the convergence criterion for the three different solvers.

Figure 73 illustrates Table 23 information and points out that the BiCGSTAB with the CTDMA as preconditioner is the fastest method (between the three mentioned) for this simulation, while the TDMA/CTDMA spends almost three times more the CPU time in the 150 x 150 grid case. This comparison was used as the basis for choosing the BiCGSTAB, using the TDMA/CTDMA (preconditioner), as the main solver for both two-dimensional and three-dimensional simulations.

TABLE 23 - COMPUTATIONAL CONVERGENCE TIME COMPARISON.

Bidimensional Grid (n_θ x n_r)	**Control Volumes Number**	**CPU time until convergence (s)**		
		CTDMA	**BiCGSTAB (alone)**	**BiCGSTAB – TDMA**
150 x 150	22500	31339.8	23970.9	10906.2
100 x 100	10000	5438.4	3886.0	2143.9
75 x 75	5625	1652.2	1294.1	659.6
50 x 50	2500	307.6	225.7	119.8
45 x 45	2025	193.7	149.5	76.9
40 x 40	1600	123.9	94.6	49.3
35 x 35	1225	72.4	55.7	28.2
30 x 30	900	38.0	29.6	15.0
25 x 25	625	18.4	16.1	7.9
20 x 20	400	7.2	7.2	3.7
15 x 15	225	2.8	3.3	1.2
10 x 10	100	0.6	1.1	0.5
5 x 5	25	0.3	0.3	0.3

FIGURE 73 - COMPUTATIONAL TIME COMPARISON.

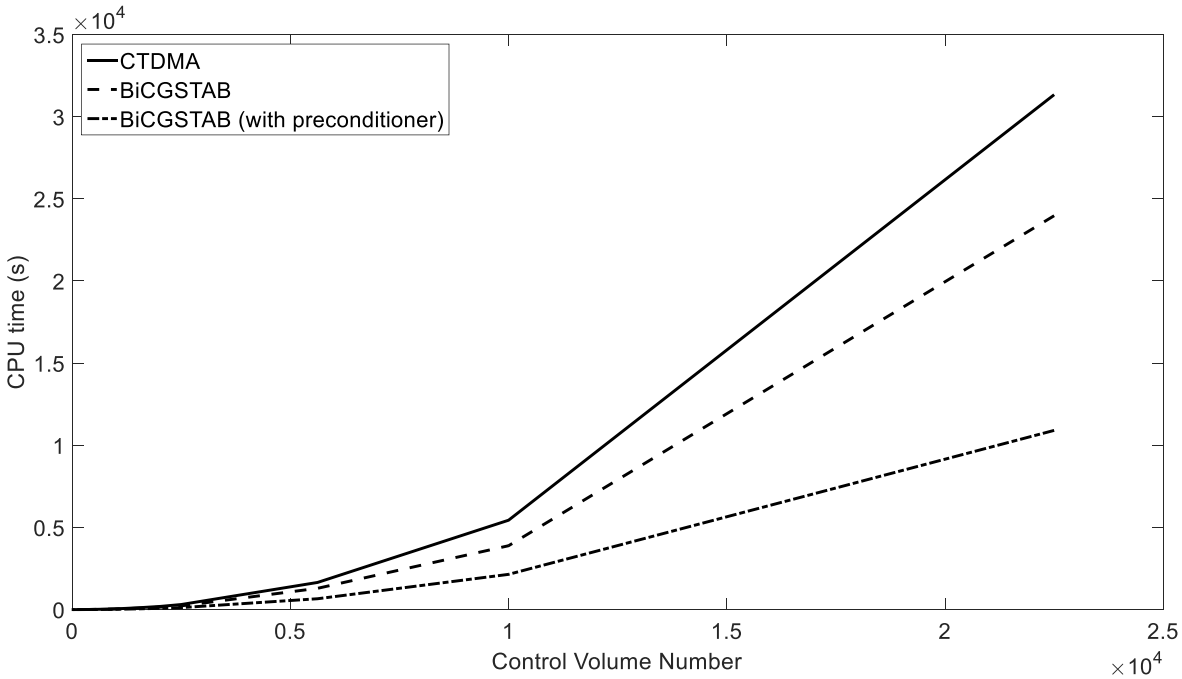

5.1.2 Three-dimensional Results Verification

The simulation results for the Newtonian fluid were verified against the numerical and experimental database from Watanabe et al. (2003). In that work, numerical results and experimental measurements concerning three different concentrations of an aqueous solution of glycerin (60%, 70%, and 80%) for two different wall types (smooth and water-repellent) were conducted. For the present verification, only the results concerning smooth walls were taken into account.

The two concentric cylinders geometric parameters in this simulation are the following: R_{inn} = 0.081 m and R_{out} = 0.0965 m, leading to radius ratio and gap of respectively k = 0.839 and δ = 0.0155 m. The fluid column height *h* is H = 0.240 m, thus the aspect ratio Γ = 15.5.

Considering the above-mentioned geometry, Watanabe et al. (2003) performed some experiments for the all three Newtonian fluids with Reynolds number in the range of 10 to 25. The fluids thermophysical properties are summarized in Table 24.

TABLE 24 - PHYSICAL PROPERTIES OF THE AQUEOUS SOLUTION OF GLYCERIN

Fluid concentration in weight (%)	**Density (kg/m^3)**	**Viscosity (Pa·s)**	**Kinematic viscosity (m^2/s)**	**Temperature (°C)**
60	1.157	13.1×10^{-3}	11.3×10^{-6}	15
70	1.185	28.1×10^{-3}	23.7×10^{-6}	15
80	1.212	72.2×10^{-3}	59.6×10^{-6}	16

Source: (Watanabe at al., 2003)

The results obtained by Watanabe et al. comparing the experimental measurements and the analytical solution for the dimensionless tangential velocity component values are illustrated in Figure 74.

FIGURE 74 - TANGENTIAL VELOCITY COMPONENT PROFILES FOR ROTATING SMOOTH-WALL INNER CYLINDER.

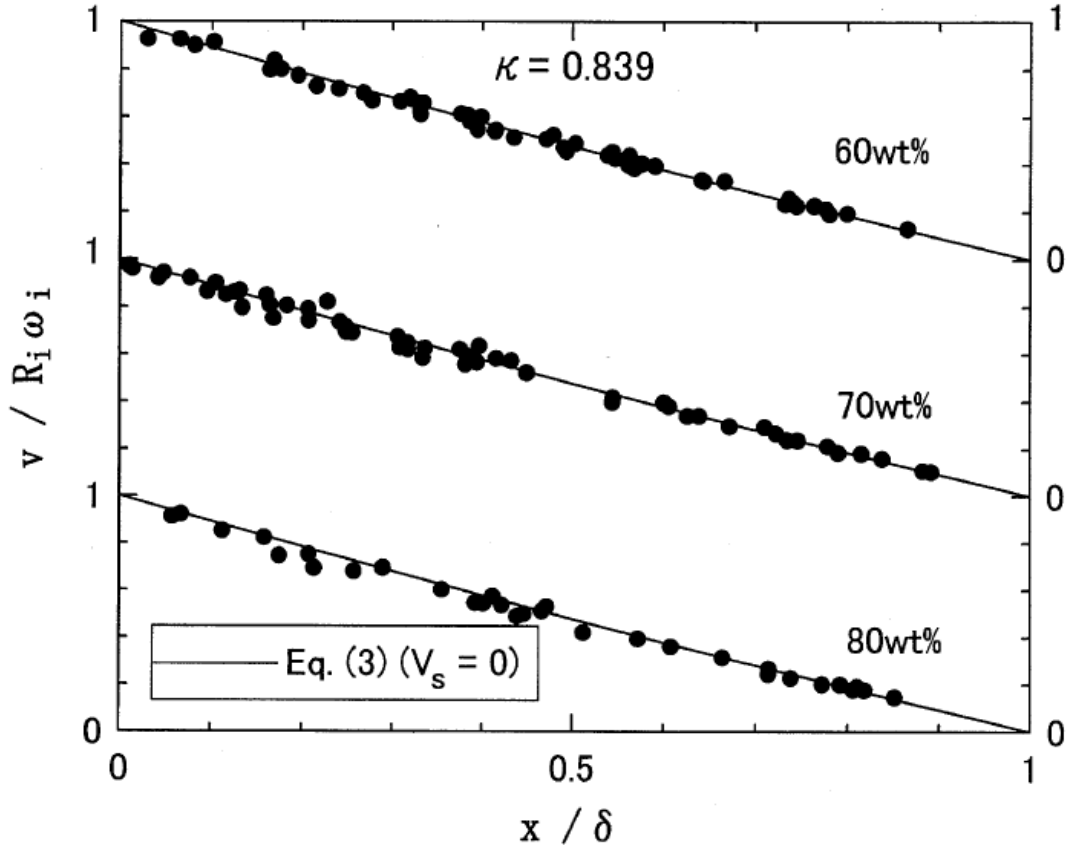

SOURCE: WATANABE ET AL. (2003)

Watanabe et al. achieved a very good agreement between the experimental and analytical points. Thus, in order to certificate if the present code is able to achieve such good agreement with the analytical solution, some simulations concerning the same geometry were held for all the three fluid concentrations. The conditions are summarized in Table 25 below:

TABLE 25 - SIMULATIONS USING AQUEOUS SOLUTION OF GLYCERIN DIMENSIONLESS NUMBERS.

Fluid concentration (%)	**Inner cylinder velocity (rad / s)**	**Reynolds number**	**Taylor number**
60	$\frac{1.5}{30}\pi$	17.42	58.06
70	$\frac{2.5}{30}\pi$	13.86	36.76
80	$\frac{11}{30}\pi$	24.27	112.79

Figure 75 shows the results of the tangential velocity component profiles obtained through the simulations realized using the aqueous solutions of glycerin (60%, 70%, and 80%) until convergence. All three simulations show a good agreement with the analytical solution, the results plotted in the figures were obtained in the height of h = 0.120 m, in order to avoid the bottom and top wall effects. The convergence criterion used in this simulation was 10^{-10} for both mass and momentum residues and the applied mesh has 25 x 25 x 25 nodal points.

Watanabe et al. (2003), also performed some numerical simulation and experiments in order to compare the flow behavior through some PIV measurements and numerical contour plots. The fluid applied in this case was the aqueous solution of glycerin with 80% of weight concentration. The outer radius applied has the value $R_{out} = 0.120$ m, which changes some geometric parameters: $k = 0.675$, $\delta = 0.039$ m and $\Gamma = 6.15$. The Reynolds number utilized is 300, thus the inner cylinder velocity is $\omega = 1.8\,\pi\,\mathrm{rad}/s$ and Taylor number is 43297.

Figure 76 compares the results obtained with the present work simulation (right side) with the one obtained by Watanabe et al., (2003). The streamlines obtained by Watanabe et al. show the three Taylor-cells in half cylinder length. One can observe a great agreement between the positions of the Taylor cells from both works, despite the difference of the streamlines values.

Figure 77, on the other hand, compares the photographs of the Taylor-cells with the flow direction obtained in this work. Both demonstrated that for the first Taylor-cell, near the bottom wall, the fluid moves from the outer cylinder to the inner cylinder in a counterclockwise orientation.

FIGURE 75 - TANGENTIAL VELOCITY COMPONENT PROFILE OF THE AQUEOUS SOLUTION OF GLYCERIN DIFFERENT CONCENTRATIONS.

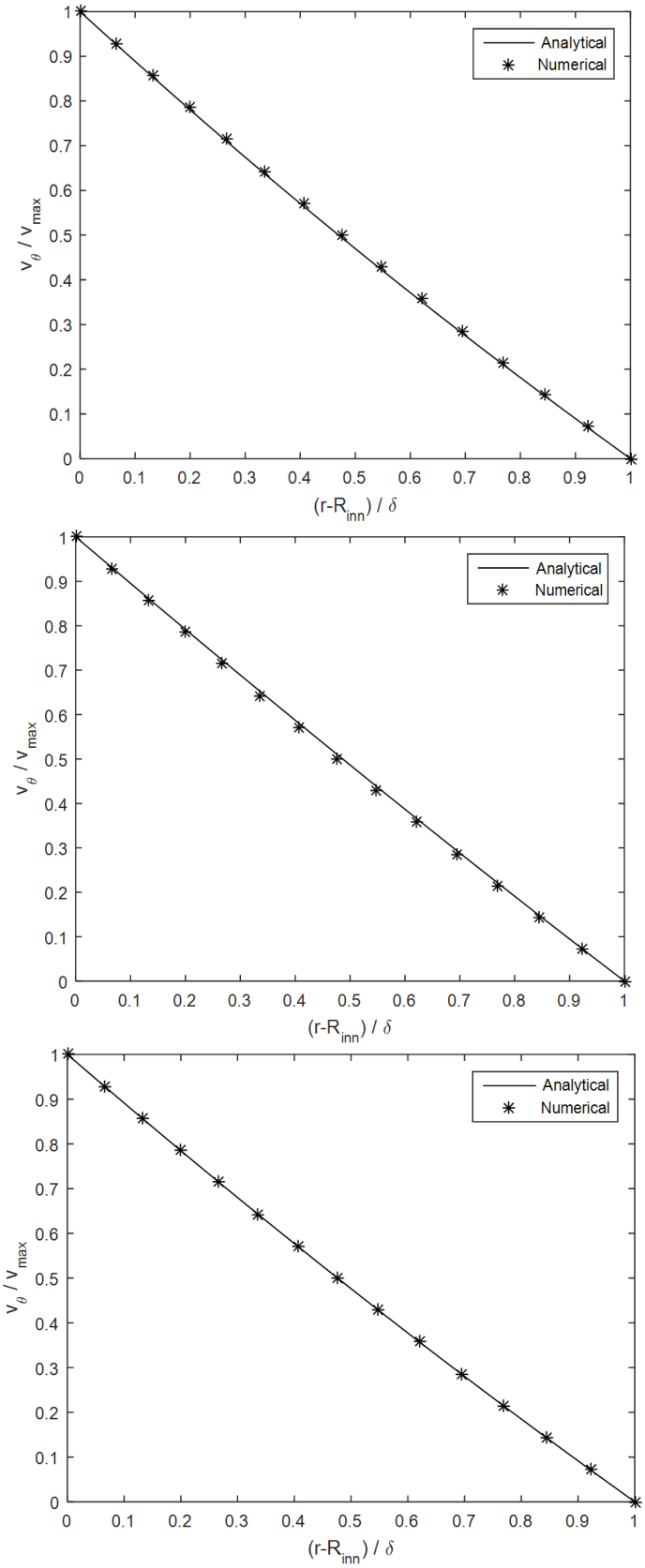

(A)

(B)

(C)

(A) 60%, (B) 70% AND (C) 80%

FIGURE 76 - STREAMLINES CONTOURS COMPARISON.

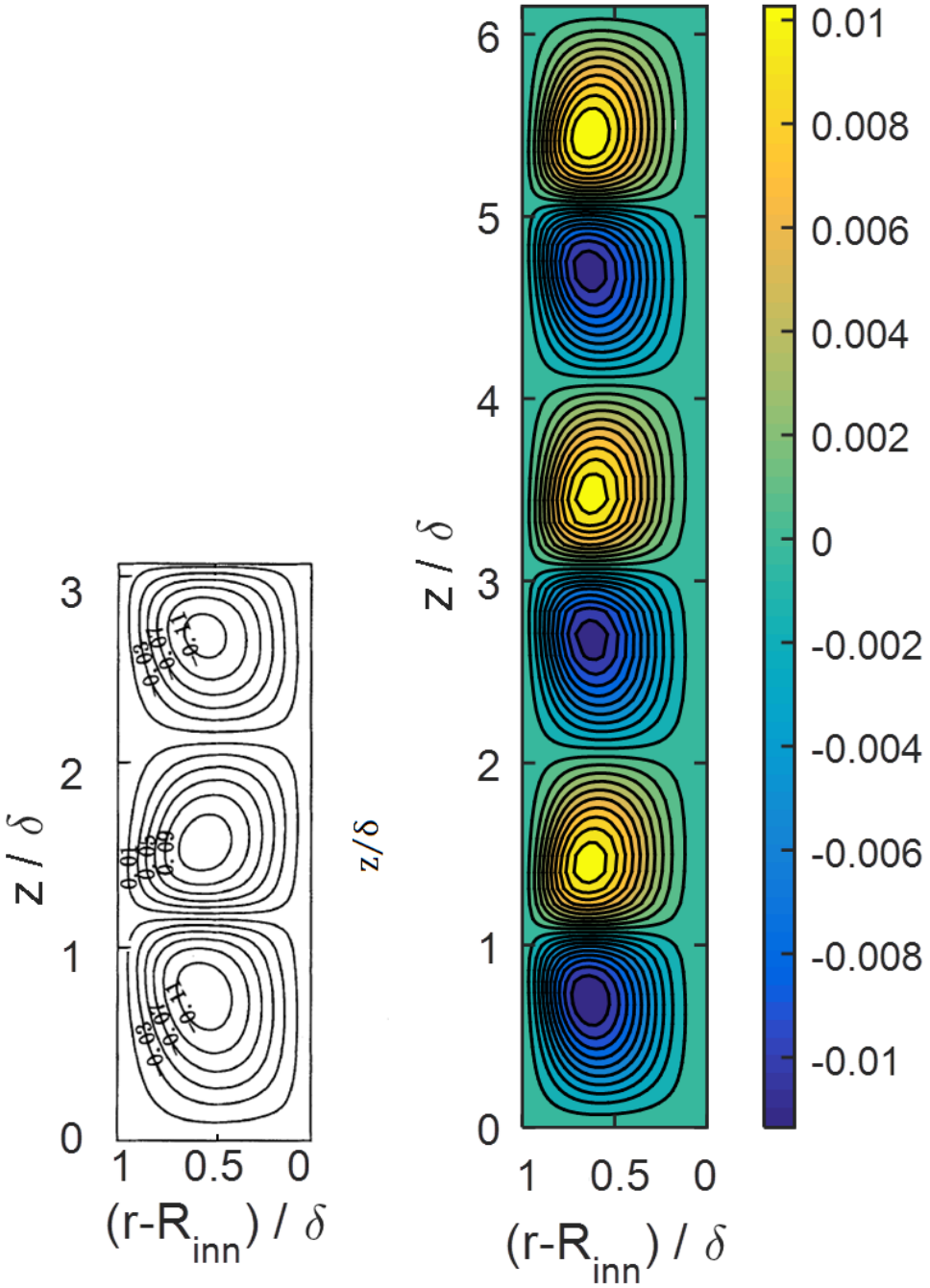

(A) (B)

(A) BY WATANABE ET AL., (2003), AND (B) SIMULATION RESULT

FIGURE 77 - TAYLOR-CELL DIRECTIONS COMPARISON.

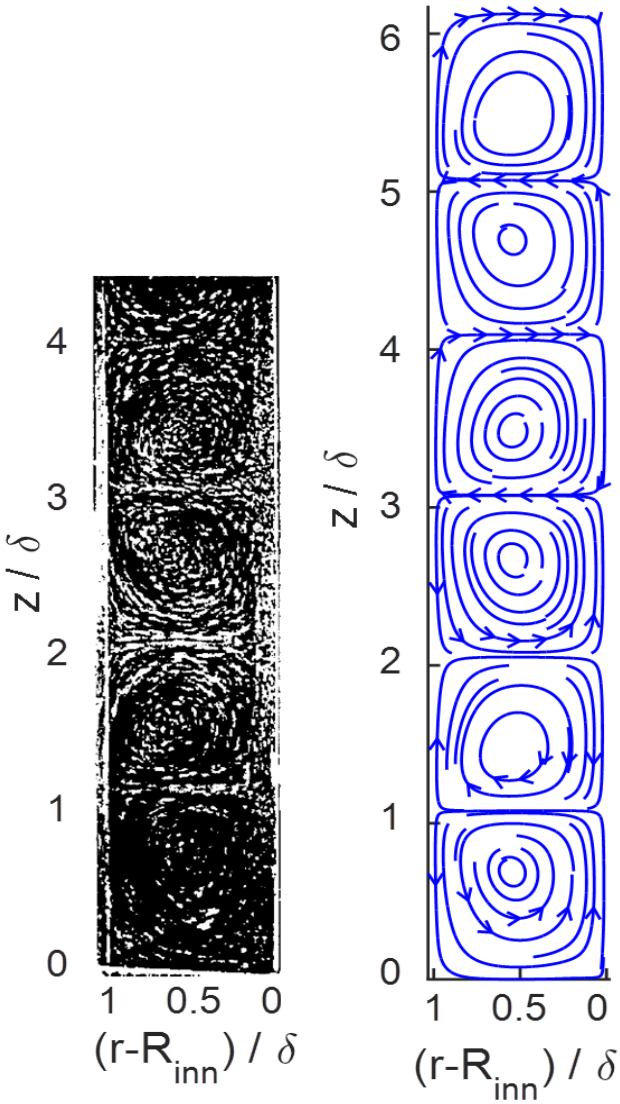

(A) (B)

(A) BY WATANABE ET AL., (2003), AND (B) SIMULATION RESULT

In the case of the non-Newtonian fluids, the verification was performed in two different ways: (i) through steady-state flow simulations, comparing the tangential velocity component profile at the half-height of the cylinders with the analytical solution, and (ii) performing a qualitative comparison with the results obtained by Escudier (1995) in a supercritical experiment (high Reynolds and Taylor numbers values). While the former way of comparison regards to a steady-state laminar flow simulation, the latter is considered supercritical as the author observed that, for that specific geometry and fluid, its critical Taylor number is 10000.

Firstly, two geometries with different radius gaps were analyzed in order to compare the results between three different fluids: (i) shear-thinning Power-Law fluid, (b) Newtonian fluid

and (iii) shear-thickening Power-Law fluid. For all the simulations, in steady-state regime, the outer radius is $R_{out} = 0.12$ m, thus the discrepancies between the two geometries are the following: (i) $R_{inn} = 0.06$ m, $H = 0.24$ m, $\delta = 0.06$ m, $k = 0.5$ and $\Gamma = 4$, while (ii) $R_{inn} = 0.114$ m, $H = 0.24$ m, $\delta = 0.006$ m, $k = 0.95$ and $\Gamma = 4$. The former geometry is considered wide-gap Taylor-Couette geometry, whereas the latter is a narrow-gap one. The utilized mesh has 50 x 50 x 70 nodal points in tangential, radial, and axial axis, respectively. The six different simulations information are summarized in Table 29.

TABLE 26 - THREE-DIMENSIONAL SIMULATIONS PROPERTIES.

Simulation	**k**	**Type**	**Power-Law index (n)**	**Flow Consistency (m)**	**ω_{inn} (rad/s)**	**Reynolds**	**Taylor**
(a)	0.50	Power-Law	0.5	1	$\pi/8$	1.830	3.35
(b)	0.50	Newtonian	1.0	1	$\pi/8$	1.410	2.00
(c)	0.50	Power-Law	1.5	1	$\pi/8$	1.520	2.30
(d)	0.95	Power-Law	0.5	1	$\pi/8$	0.780	0.03200
(e)	0.95	Newtonian	1.0	1	$\pi/8$	0.270	0.00380
(f)	0.95	Power-Law	1.5	1	$\pi/8$	0.096	0.00048

The main results obtained from the simulations are summarized from Figure 78 to Figure 81. Simulations (a), (b), (c) streamlines contours are observed in Figure 78. One can observe that the Taylor-vortices have different shapes for the different fluids. It is possible to observe the main characteristics of shear-thinning and shear-thickening fluids. While the former leads to higher apparent viscosities values in regions with the lesser shear rates values (i.e., top and bottom walls near the outer cylinder surface), the latter leads to higher apparent viscosities values in regions with the higher shear rates values (i.e., top and bottom walls near the inner cylinder surface).

Figure 80 shows a good agreement between the numerical solution of the tangential velocity profile through the radial direction with the analytical solutions (Equations (2.45) and (2.46)).

Likewise, simulations (d), (e) and (f) streamlines contours are illustrated in Figure 79. One can observe that despite the fact of the Taylor-vortices having similar shapes for both wide-gap and narrow-gap geometries, the streamlines values are smaller for the narrow-gap case, especially for the Newtonian case.

Following the results observed in Figure 80, Figure 81 also shows a very good agreement between the numerical and analytical results. The major difference observed is that for the narrow-gap case the velocity profile, for all the cases, is similar to a straight line.

FIGURE 78 - STREAMLINE CONTOURS COMPARISON BETWEEN (A) SHEAR-THINNING, (B) NEWTONIAN AND (C) SHEAR-THICKENING FLUIDS IN WIDE-GAP GEOMETRY.

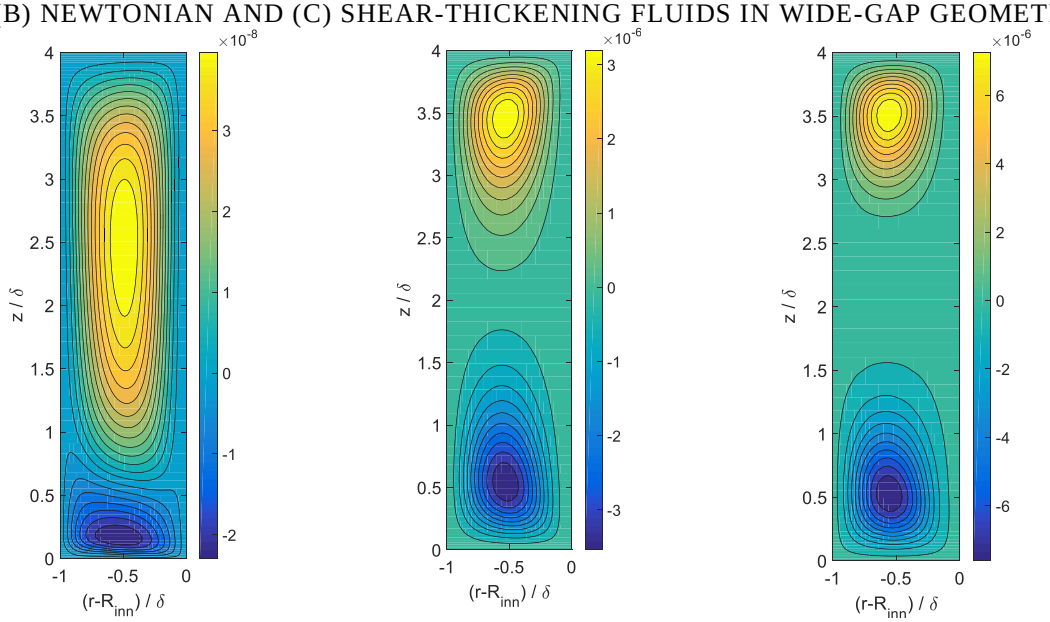

(A) (B) (C)

FIGURE 79 - STREAMLINE CONTOURS COMPARISON BETWEEN (D) SHEAR-THINNING, (R) NEWTONIAN AND (F) SHEAR-THICKENING FLUIDS IN NARROW-GAP GEOMETRY.

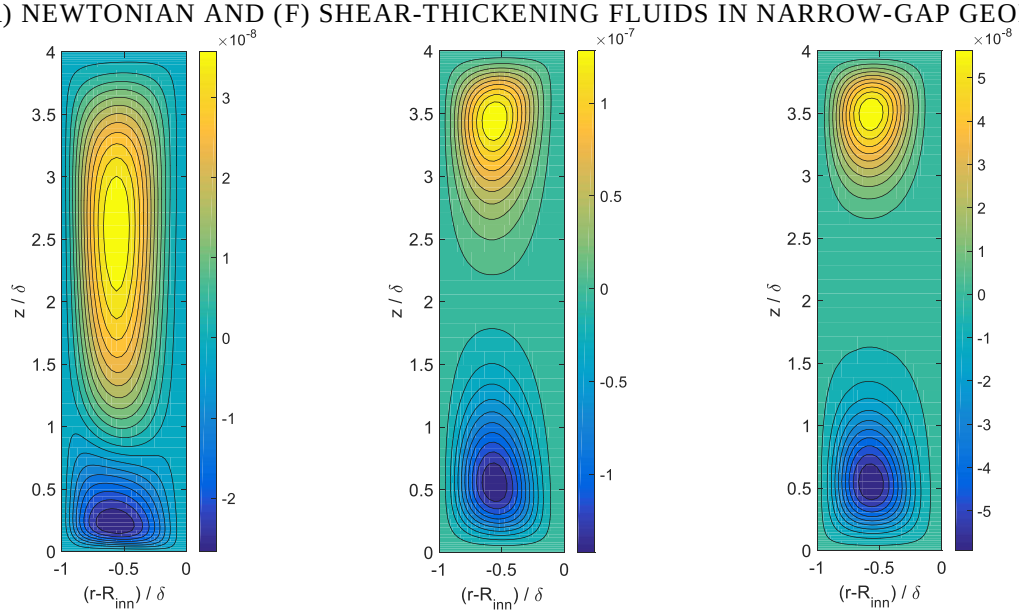

(D) (E) (F)

FIGURE 80 - TANGENTIAL VELOCITY COMPONENT VALIDATION FOR (A) SHEAR-THINNING, (B) NEWTONIAN AND (C) SHEAR-THICKENING FLUIDS IN WIDE-GAP GEOMETRY.

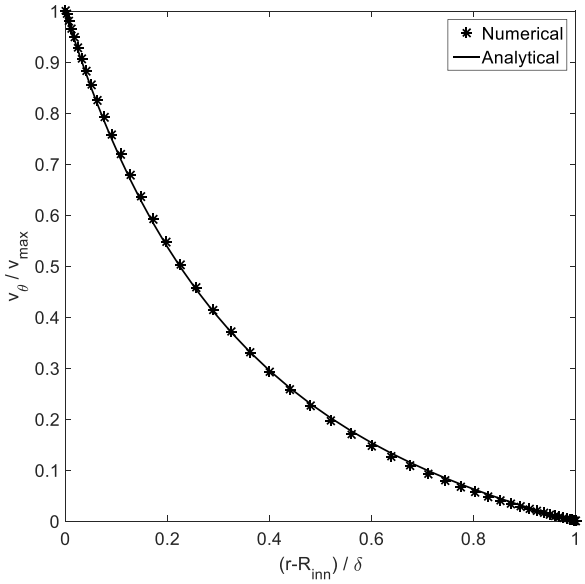

(A)

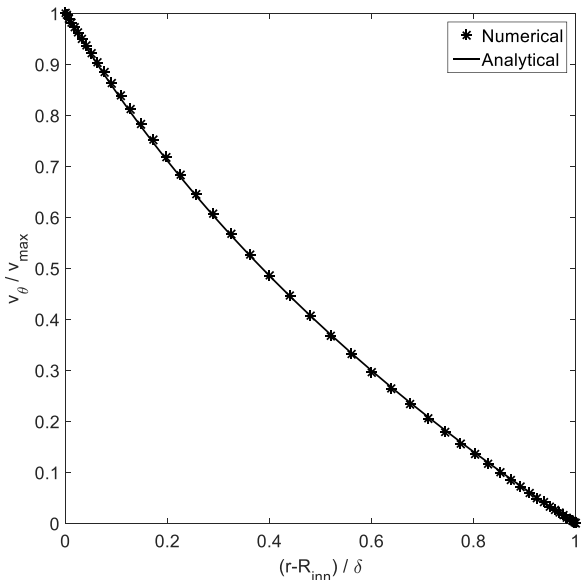

(B)

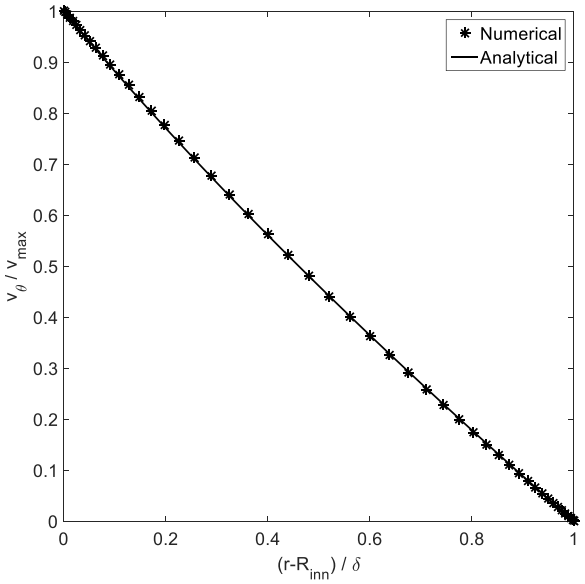

(C)

FIGURE 81 - TANGENTIAL VELOCITY COMPONENT VALIDATION FOR (D) SHEAR-THINNING, (E) NEWTONIAN AND (F) SHEAR-THICKENING FLUIDS IN NARROW-GAP GEOMETRY.

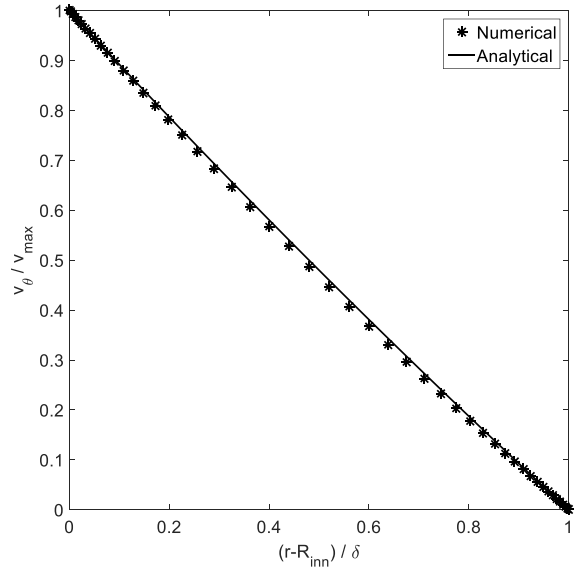

(D)

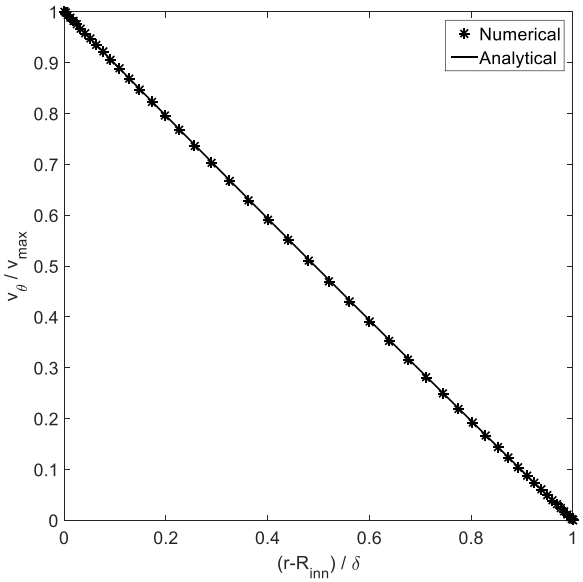

(E)

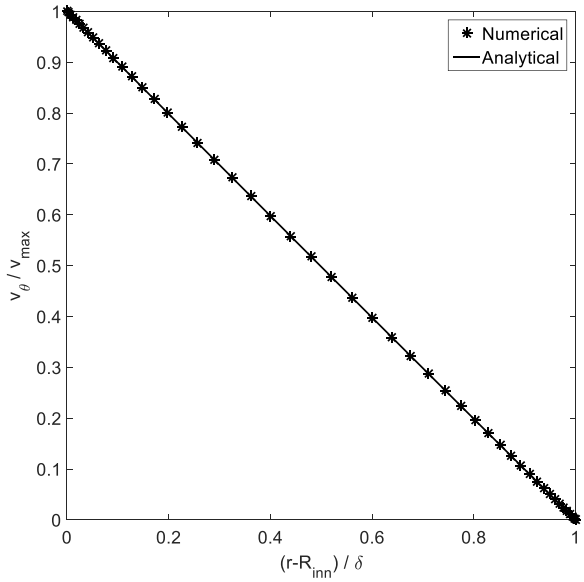

(F)

Additionally, a mesh size comparison was held regarding the simulation (a), while holding the nodal points number at the tangential and axial direction, three different simulations were performed using three different number of nodal point at radial direction (n_r). The RMS deviation values for each simulation are also shown in the graphs (Equation 3.53). The RMS deviation values in function of the number of nodal points in the radial direction are presented in Figure 82. One can observe that, for this specific simulation, all the values are acceptable (for a convergence criterion that is less than 10^{-3}). For this reason, the value $n_r = 50$ was used also in simulations (b), (c), (d), (e) and (f). Figure 83 shows the comparison between numerical and analytical solutions for (i) $n_r = 25$, (ii) $n_r = 50$ and (iii) $n_r = 100$.

FIGURE 82 - RMS DEVIATION AGREEMENT BETWEEN NUMERICAL RESULTS AND ANALYTICAL SOLUTION IN FUNCTION OF THE RADIAL NODAL POINTS.

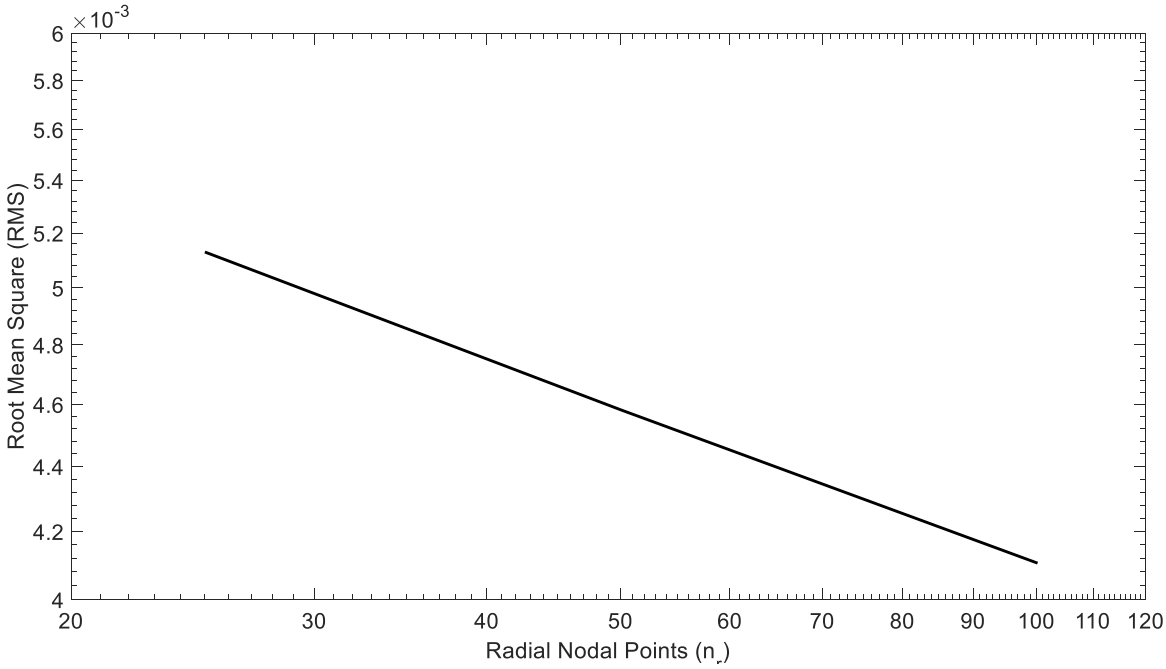

FIGURE 83 - RMS DEVIATION VALUES COMPARISON BETWEEN SIMULATION WITH (A) 25, (B) 50 AND (C) 100 RADIAL NODAL POINTS.

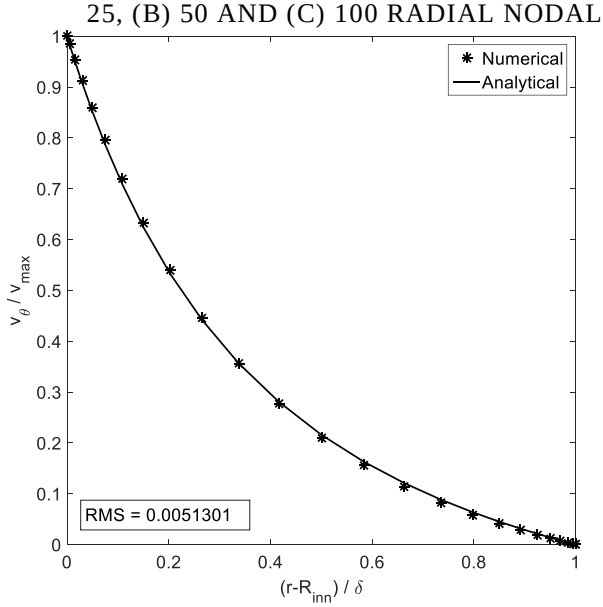

(A)

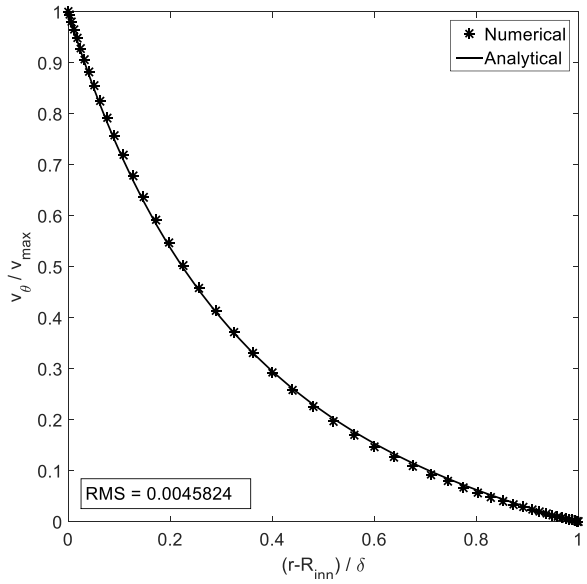

(B)

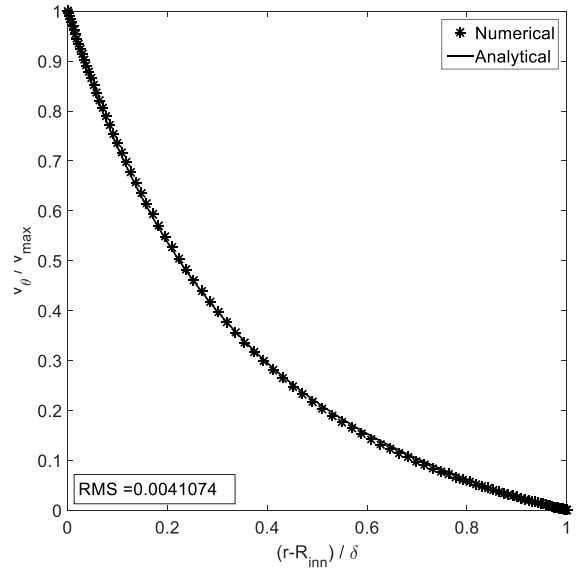

(C)

Furthermore, the simulations regarding Power-Law fluids were also verified against the database from Escudier (1995). In that paper, experimental measurements for an aqueous solution of Xantham gum in a concentric longitudinal annular geometry were carried in order to compare the measurements with a Newtonian fluid and thixotropic shear-thinning fluid measurements. In the present work, only the measurements for the Xantham gum solution were taken into account.

The geometric parameters of the annular section for this work are the following: $R_{inn} = 0.0254$ m, $R_{out} = 0.0502$ m, $k = 0.506$, $\delta = 0.025$ m. While the overall apparatus length is $H = 5.775$ m, thus the aspect ratio is $\Gamma = 233$. Measurements were made at a location of 24 radius gap from the end housing furthest away from the centrebody drive. A laser Doppler anemometer was used to determine the mean flow velocities and the vortex mapping in the axial direction, and it was realized by traversing the probe head along the axis of the annulus at discrete radii within the annulus gap. The Taylor number of the experiments is 46000.

Consequently, the simulations of the present work were made only for an 8 radius gap values in the axial distance due to the fact that the apparatus length is very large and would be necessary a large computational effort to simulate the whole experiment. Besides, the present simulation main objective is to perform only a qualitative comparison, because the present computational code is not aimed to turbulent flows. In order to fit the condition, which is found at the same distance of the experiments measurements from Escudier, the bottom and top boundary conditions of the present simulations were made as symmetric boundary conditions. The convergence criterion used in this simulation was 10^{-3} mass residues and the applied mesh has 50 x 50 x 100 nodal points.

Xantham gum apparent viscosity obeys the following relation:

$$\eta = 1 + (11\dot{\gamma})^{0.437-1} + 0.001 \qquad (5.1)$$

Figure 84 makes a comparison between the numerical results and experimental measurements for the dimensionless tangential velocity component along one Taylor-vortices pair. One can observe that the smaller the relation $(R_{out} - r)/\delta$ the closer to the outer cylinder. Therefore, for the present simulation, a better agreement with the experimental results was observed near the inner cylinder.

FIGURE 84 - TANGENTIAL VELOCITY COMPONENT WITHIN TAYLOR VORTICES FOR XANTHAN GUM COMPARISON WITH THE WORK OF ESCUDIER (1995).

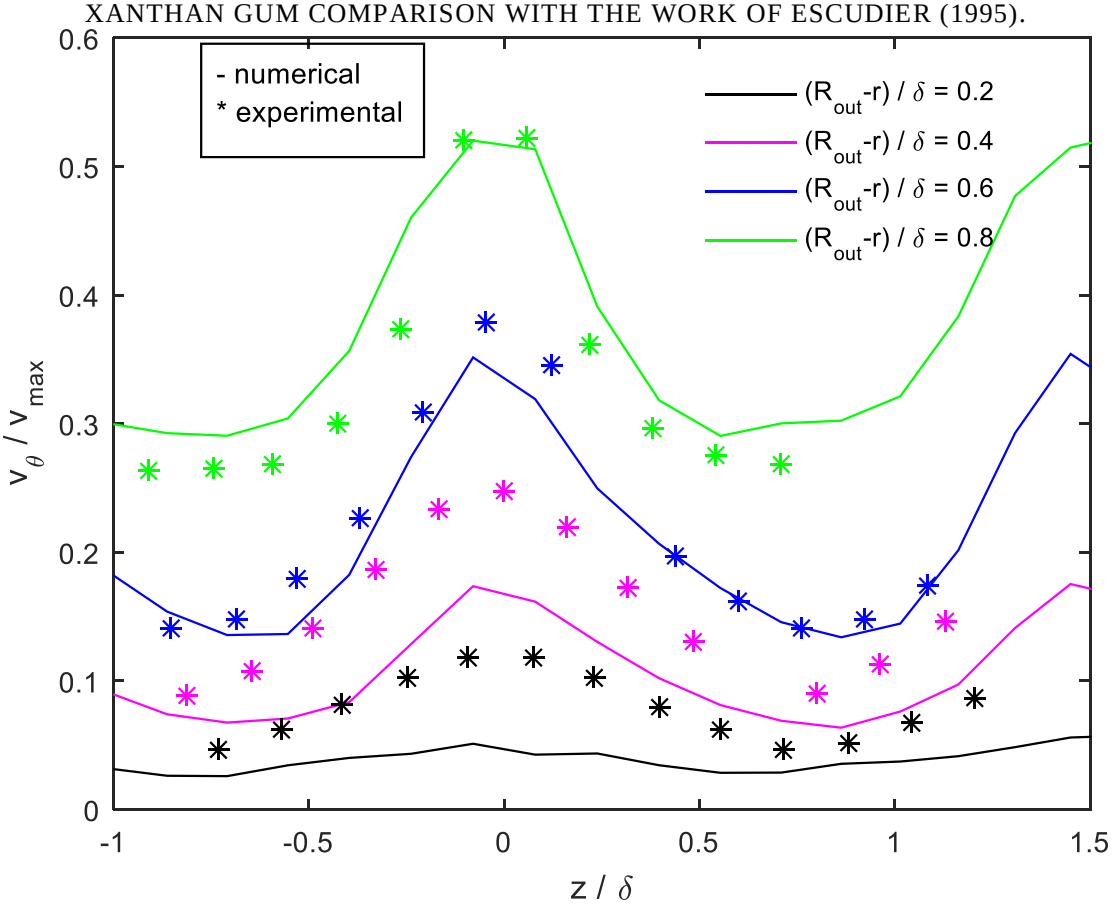

Similarly, Figure 85 shows a comparison between the numerical results and experimental measurements for the dimensionless axial velocity component along one Taylor-vortices pair. The comparison is realized for six different $(R_{out} - r)/\delta$ distance relations: (a) 0.1, (b) 0.2, (c) 0.4, (d) 0.6, (e) 0.8 and (f) 0.86. The same behaviors of the numerical and experimental axial velocity profiles are observed in all the radial points.

FIGURE 85 - AXIAL VELOCITY COMPONENT WITHIN TAYLOR VORTICES FOR XANTHAN GUM COMPARISON.

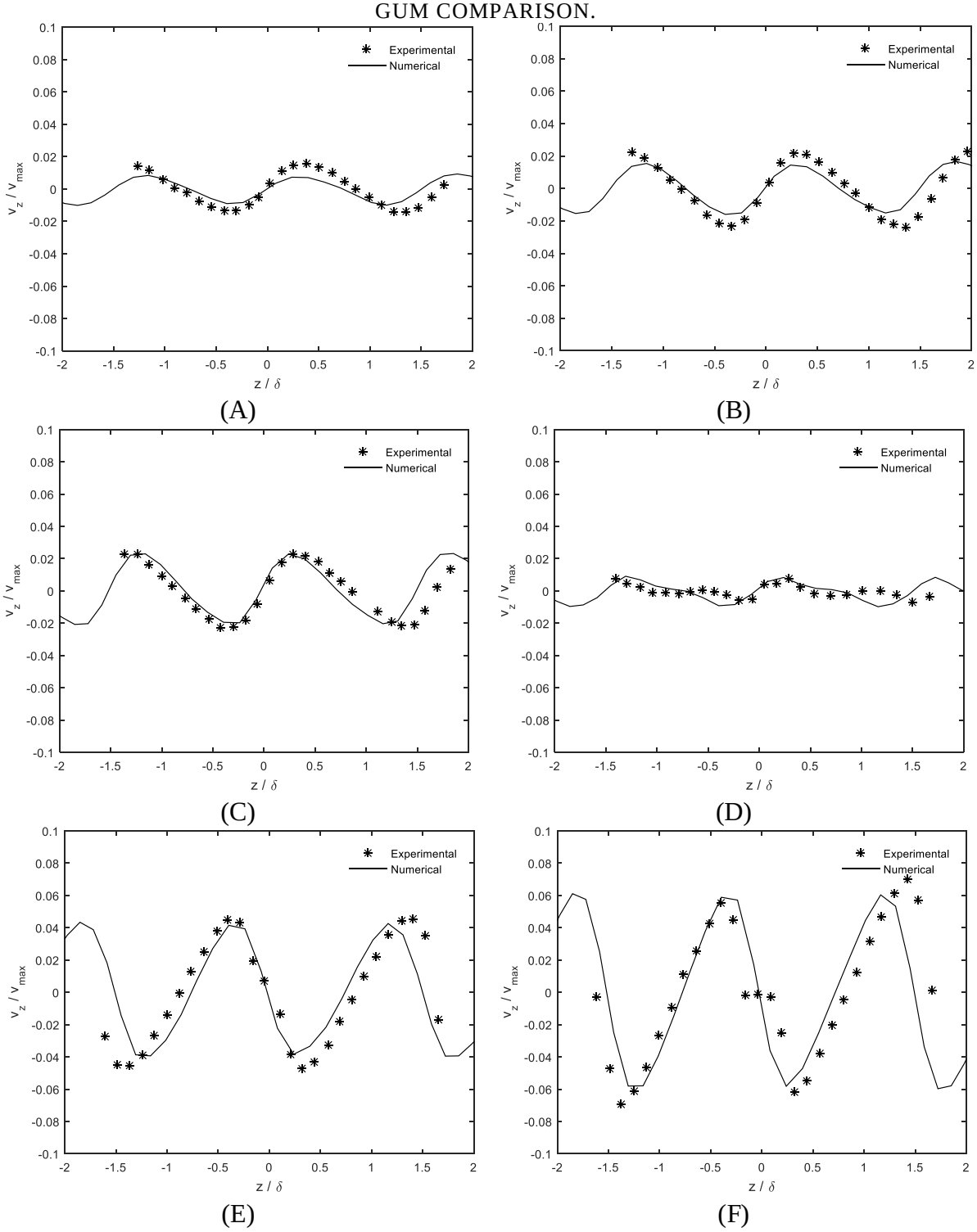

Figure 86 also shows a comparison of the axial velocity component contours within Taylor-vortices between the experimental measurements (top) and the numerical simulation results of this work (bottom). Moreover, Figure 87 shows a similar comparison between the streamline contour patterns. One can see that a similar behavior for both axial velocity and streamline patterns are observed.

FIGURE 86 - AXIAL VELOCITY COMPONENT CONTOUR PLOT COMPARISON.

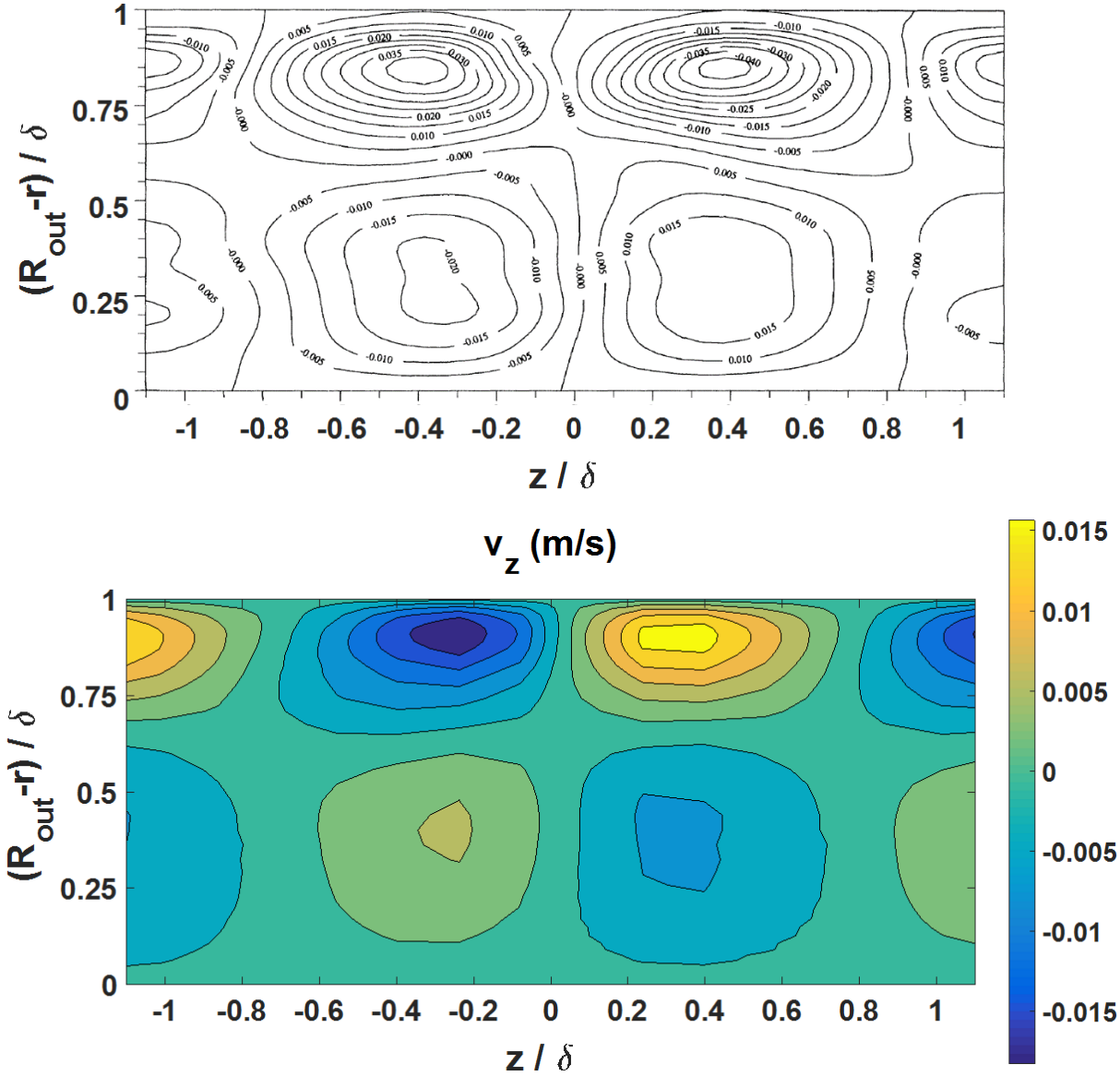

TOP (ESCUDIER, 1995), BOTTOM (PRESENT WORK).

FIGURE 87 - STREAMLINE CONTOURS COMPARISON

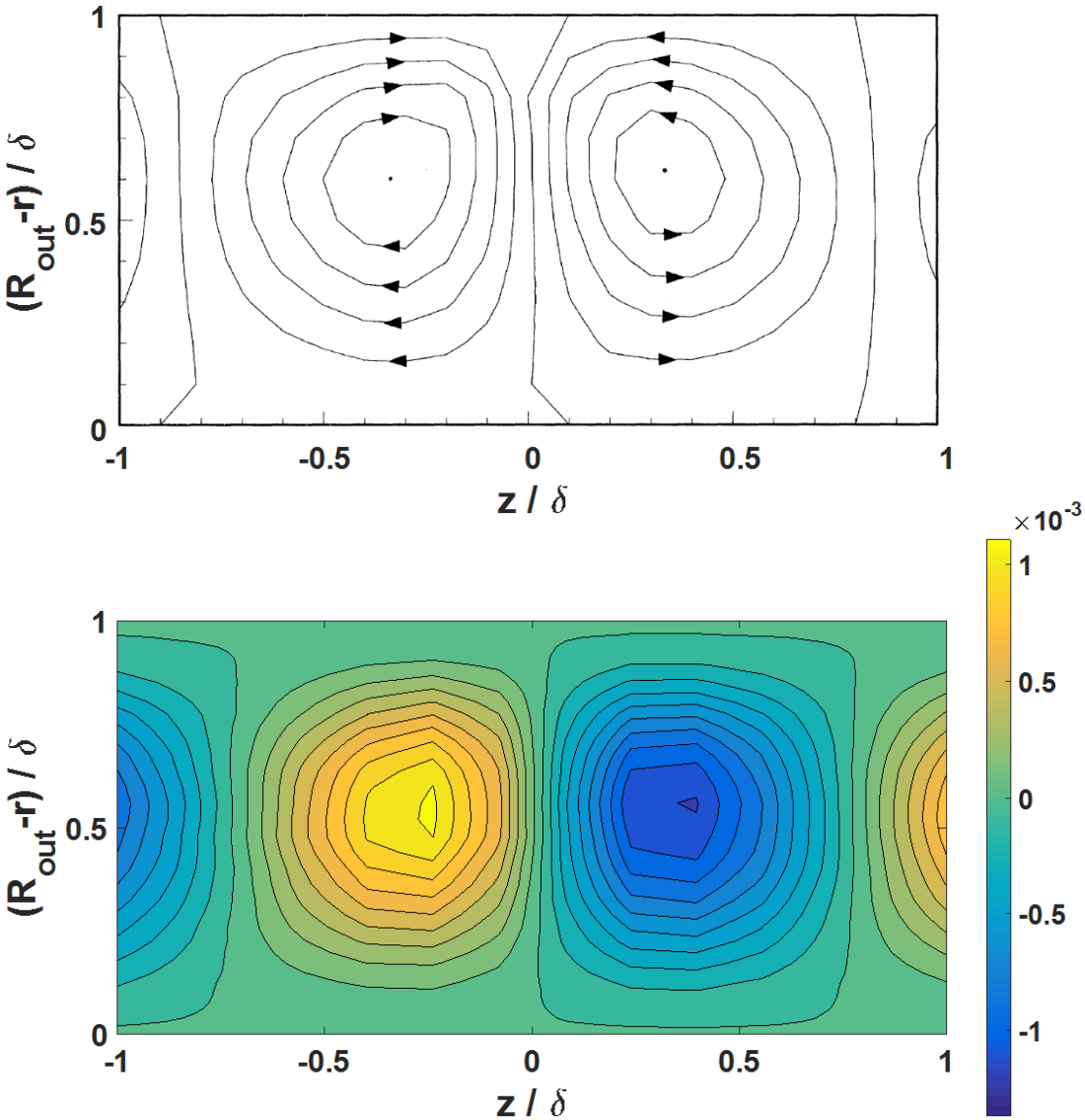

TOP (ESCUDIER, 1995), BOTTOM (PRESENT WORK).

5.2 STEADY-STATE SIMULATIONS

In Chapter 4, it has been discussed that the Robertson-Stiff and Herschel-Bulkley models presented a best fitting regression than the Bingham and Casson NNF models. Accordingly, the Herschel-Bulkley fluid has been chosen to model the behavior of fabric-water solutions through the algorithm presented in Figures 18 and 19.

It should also be noted that the Herschel-Bulkley fluid model parameters obtained by regression were used for the six different fluid suspensions considered in this work: (i) 1.25 kg of cotton fabric, (ii) 2.50 kg of cotton fabric, (iii) 1.25 kg of semi-synthetic fabric, (iv) 2.50 kg of semi-synthetic fabric, (v) 1.25 kg of mixed fabrics, and (vi) 2.50 kg of mixed fabrics. For all

the suspensions, numerical simulations with six different angular velocities for the inner cylinder were used as boundary conditions: (i) 40 rpm, (ii) 60 rpm, (iii) 80 rpm, (iv) 100 rpm, and (v) 120 rpm. Simulations have not been carried out for 20-rpm because of the presence of plug flow (see Tables 27 to 29)

In total, 30 different steady-state simulations were carried out. It is worthy of mention that for all simulations the mass conservation and the θ-axis momentum convergence were achieved before the r and z-axes momentum ones.

Furthermore, the BiCGSTAB method using the CTDMA as preconditioner was used for solving the pressure heptadiagonal linear system for each iteration (Appendixes I and II).

Moreover, a mesh grid with 50, 65 and 50 points in tangential (θ), radial (r) and axial (z) directions, respectively, was implemented. Thus, the tridimensional cylindrical mesh presents a total of 162500 nodal points to represent the geometry described in Chapter 4 (R_{inn} = 110 mm, R_{out} = 269 mm, and H = 316 mm). Also, a concentration factor (ς) of 1.05, see Equations (3.49) and (3.50), was applied for generating the non-uniform grid in the radial and axial directions.

To avoid two discontinuous regions in the flow domain, the Papanastasiou- Herschel-Bulkley Equation with K = 1 is used to model the fluid behavior – Equations (2.13) and (2.16).

Plots of all the shear rate ($\dot{\gamma}_{\theta\theta}$, $\dot{\gamma}_{rr}$, $\dot{\gamma}_{zz}$, $\dot{\gamma}_{r\theta}$, $\dot{\gamma}_{\theta z}$, and $\dot{\gamma}_{rz}$) components and velocities components (v_θ, v_r, and v_z), as well as shear stress components and shear stress tensor modulus, pressure, residues and streamfunction distributions, were analyzed in each iteration to evaluate the flow progress until convergence.

The key point of the streamfunction analysis is to evaluate the secondary flow, the fluid circulation inside the gap concerning the radial and the vertical axis, this understanding of its directions and magnitudes to perform some comparisons.

Torque values are used as the comparison parameter between the simulation results and the experimental data. In the first place, it was mentioned that the relation between the torque transmitted to the fluid stream and shear stress on the inner cylinder surface relation is as follows:

$$|\tau_{inn}| = \frac{T}{2\pi R_{inn}^2 H} \tag{5.2}$$

The equation above is accurate only when all shear and normal stress components, but the $\tau_{r\theta}$ one is neglected, together with all the end effects. However, the aspect ratio in this work is not high enough to neglect end effects ($\Gamma \approx 2$) and the water-fluid suspension is not uniformed to neglect all the stress components too.

For the numerical computation of the torque on the inner cylinder surface is calculated by the following equation:

$$T = \int_0^{2\pi} \int_0^{H} |\tau| 2R_{inn} dz d\theta \tag{5.3}$$

In order to evaluate the torque, two different calculations were proposed: (i) complete torque calculation and (ii) simplified torque calculation. The former considers all the shear stress components ($\tau_{\theta\theta}$, τ_{rr}, τ_{zz}, $\tau_{r\theta}$, $\tau_{\theta z}$, and τ_{rz}) in order to evaluate the shear stress near the inner cylinder surface, while the latter only consider the $\tau_{r\theta}$ shear stress component. One can note that as the integration limits of Equation (5.2) vary from the bottom to the top basis of the geometry, the end-effects are considered in both calculations.

Figure 88 depicts the comparison of the experimental torques (solid lines) for fabric-water suspensions (1.25 kg and 2.50 kg of cotton fabric) with the numerical torque, evaluated by Equation (5.2) represented by symbols (circle for complete torque calculation and square for the simplified one) in function of the velocity. In addition, two dashed lines with ± 20% of tolerance were plotted together with the experimental measurement spline. One can note that for the lighter suspension, the numerical torque values for 40 rpm condition do not fit the tolerance boundary, while it fits the boundaries for higher velocities. The lighter suspension presents a Power-Law index parameter (n) of 1.02, thus showing the Newtonian-like behavior also in the plot, while that for the heavier suspension n = 1.17, which reflects on the shear-thickening behavior.

FIGURE 88 - COMPARISON OF THE EXPERIMENTAL TORQUE MEASUREMENTS WITH NUMERICAL TORQUE RESULTS FOR COTTON FABRIC-WATER SOLUTIONS.

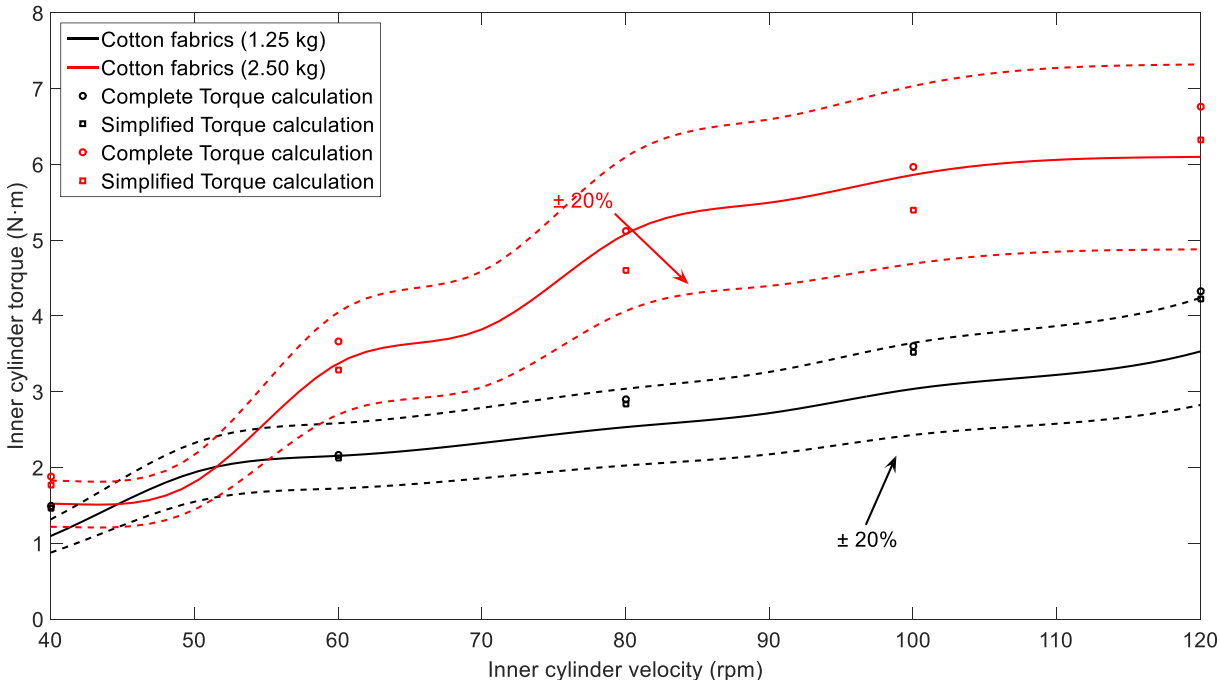

Similarly, Figure 89 shows the comparison of the measured values with the numerical torque calculation for fabric-water suspensions for 1.25 and 2.50 kg of semi-synthetic fabric mass in function of ω_{inn} (rpm). Again, the dashed lines with ± 20% of tolerance from the experimental values were plotted again. Contrary to the cotton fabric case, the lighter suspension presents a larger difference between the two torque calculation approaches, thus showing that not only the $\tau_{r\theta}$ shear stress component affects the fluid flow. The torque calculations for the heavier fluid do not fit very well the tolerance boundaries for all the ω_{inn} values but 20 rpm. However, in that case, the values for the different torque calculations approaches are more similar. The Newtonian-like behavior of the heavier suspension is demonstrated on the plot (n is nearly the unit), while that for the lighter suspension a more shear-thickening behavior is observed (n = 1.59), because of the torque tendency for slower velocities.

FIGURE 89 - COMPARISON OF THE EXPERIMENTAL TORQUE MEASUREMENTS WITH NUMERICAL TORQUE RESULTS FOR SEMI-SYNTHETIC FABRICS AND WATER SOLUTIONS.

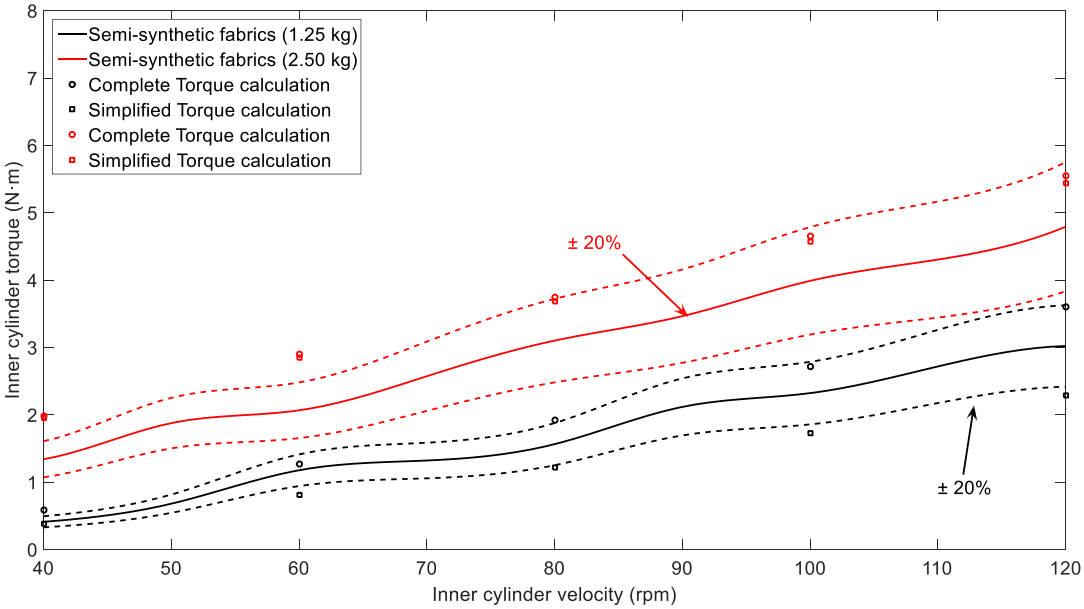

Figure 90 shows the comparison between the experimental torque values (with ± 20% of tolerance dashed lines) and the calculated numerical torques for 1.25 kg and 2.50 kg of mixed fabric amounts (cotton and semi-synthetic). Both fluids fit satisfactorily the tolerance boundaries. For the lighter fluid, only the values for 40 rpm do not fit the boundaries, while for the heavier fluid the numerical calculation fit the boundaries. The difference between the approaches is notable and denotes that other shear rate components also have importance. Similarly to the other fluid suspensions, for the mixed fabric-water ones, both curves show the tendency to a shear-thickening behavior. These behaviors were also observed on the experimental torque and the Herschel-Bulkley parameters obtained by non-linear regression o Chapter 4. The mixed fabric-water suspensions show a combined effect of both cotton and semi-synthetic on the fluid flow.

FIGURE 90 - COMPARISON OF THE EXPERIMENTAL TORQUE MEASUREMENTS WITH NUMERICAL TORQUE RESULTS FOR MIXED FABRIC-WATER SOLUTIONS.

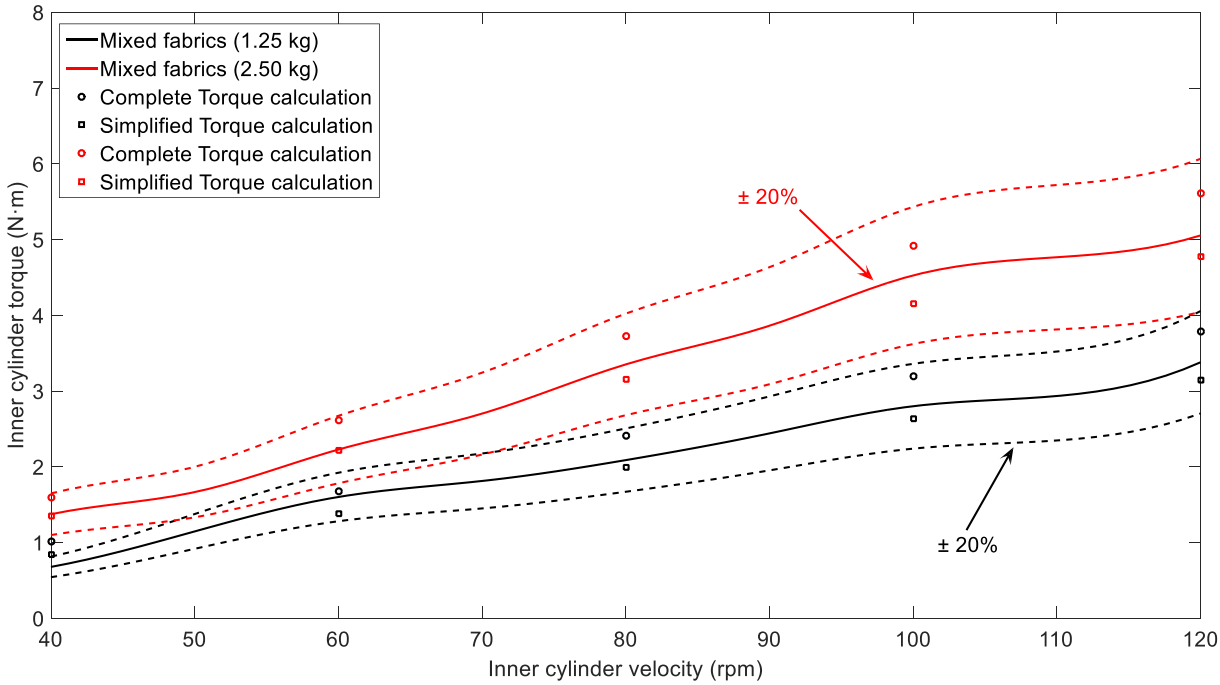

One can note that the difference between the torque calculation approaches is more notable for some fluids, which may vary because of the Herschel-Bulkley parameters and the flow behavior change because of the bottom surface end-effects. For that reason, plots of tangential velocities, pressure, shear rate, viscosity, shear stress, and streamlines are presented next for all fluids.

Table 27 summarizes the conditions for the steady-state simulations. Both the Reynolds number (Re) and Taylor numbers (Ta), based on Equations (2.40) and (2.41), were obtained using the shear rates ($\dot{\gamma}$) and viscosity (η) from the regression of the experimental measurements. One can see that the Reynolds values are below the critical values so that all simulations are comprised in the laminar regime. The value of the plug radius (r_o) – Equation (2.63) – is also shown, pointing out that only the 20-rpm inner cylinder velocity condition (1.25 kg cotton fabric-water suspension) there was a presence of a plug flow as the plug radius is smaller than the outer cylinder radius (R_{out}), which is 269 mm, reason why 20-rpm condition has not been performed.

TABLE 27 - CONDITIONS OF COTTON FABRIC-WATER SIMULATIONS.

	1.25 kg of cotton fabric					2.50 kg of cotton fabric				
ω_{inn} (rpm)	$\dot{\gamma}$ (s^{-1})	η (Pa·s)	Re	Ta	r_0 (mm)	$\dot{\gamma}$ (s^{-1})	η (Pa·s)	Re	Ta	r_0 (mm)
40	8.91	5.20	14.00	409.24	1181.4	7.34	8.75	8.32	144.67	885.31
60	17.43	5.24	20.83	906.83	2322.2	14.62	9.79	11.16	260.11	1962.3
80	20.43	5.26	27.72	1604.9	2731.0	20.75	10.39	14.03	411.03	2954.6
100	24.43	5.27	34.55	2494.4	3274.3	23.44	10.60	17.17	616.28	3408.1
120	28.34	5.28	41.37	3575.4	3808	24.24	10.66	20.49	877.39	3546.6

Table 28, on the other hand, summarizes the flow conditions for the semi-synthetic fabric-water suspension. One can see that there is the presence of plug flow for 20 and 40-rpm simulations for the 2.50 kg of semi-synthetic fabric-water suspension flows. However, both plug radius values are closer to the outer cylinder radius, thus the plug flow comprehends just a small portion of the gap. The values of Reynolds and Taylor number are not high either.

TABLE 28 - CONDITIONS OF SEMI-SYNTHETIC FABRIC-WATER SIMULATIONS.

	1.25 kg of semi-synthetic fabric					2.50 kg of semi-synthetic fabric				
ω_{inn} (rpm)	$\dot{\gamma}$ (s^{-1})	η (Pa·s)	Re	Ta	r_0 (mm)	$\dot{\gamma}$ (s^{-1})	η (Pa·s)	Re	Ta	r_0 (mm)
40	6.42	2.69	27.10	1533.8	517.0	8.39	6.69	10.89	247.9	245.0
60	12.68	3.94	27.72	1605.9	1482.1	13.24	6.58	16.60	575.8	377.8
80	15.17	4.37	33.35	2323.1	1968.7	20.15	6.52	22.33	1041.5	567.1
100	19.50	5.05	36.07	2718.4	2922.1	26.01	6.50	28.00	1638.2	729.3
120	23.04	5.56	39.30	3226.6	3803.1	31.30	6.49	33.66	2367.1	876.0

Similarly, Table 29 summarizes the flow conditions for the mixed fabric-water suspension simulations. Similar to the other fabrics, the Reynolds and Taylor numbers are not high enough to characterize a turbulent flow regime because the fluid is very viscous. In this table, only the 20-rpm condition indicates the presence of a plug flow for 1.25 kg of semi-synthetic fluid suspension, but the plug radius value is close to the outer cylinder radius.

TABLE 29 - CONDITIONS OF MIXED FABRIC-WATER SIMULATIONS.

	1.25 kg of mixed fabric					2.50 kg of mixed fabric				
ω_{inn} (rpm)	$\dot{\gamma}$ (s^{-1})	η (Pa·s)	Re	Ta	r_0 (mm)	$\dot{\gamma}$ (s^{-1})	η (Pa·s)	Re	Ta	r_0 (mm)
40	7.15	3.99	18.25	696.17	464.13	8.81	6.61	11.02	253.93	574.96
60	14.33	4.75	23.02	1107.4	1095.3	13.07	7.23	15.12	477.73	932.21
80	17.67	5.01	29.07	1765.7	1427.8	18.20	7.81	18.65	726.99	1402.4
100	22.29	5.33	34.19	2441.9	1914.3	23.20	8.27	22.01	1011.7	1894.0
120	25.86	5.54	39.44	3250.3	2310.7	25.34	8.45	25.85	1396.2	2114.7

5.2.1 Inner Cylinder Angular Velocity of 40 rpm

For 40 rpm, there are no significant differences, at sight, between the six fabric-water suspensions for tangential velocity and pressure plots. Consequently, Figure 91 depicts the plots of the (a) tangential velocity v_θ (m/s) and (b) pressure p (Pa) representing all the six fluids. The maximum velocity, demonstrated at the inner cylinder wall, is the same for all fluid suspensions. There are only slight differences between the velocity propagation in radial direction depending on the fluid parameters, despite it is nearly indistinguishable by perception. It is important to emphasize that the pressure was not computed as the absolute, but zero-referenced differential pressure. One can note that, as the inner cylinder velocity is relatively slow, the represented pressure difference between the bottom and top surfaces are almost equal to the hydrostatic pressure difference ($p_{h=0} = p_{h=H} + \rho gH$).

One can note that the plots presented are represented in an r-z section for $\theta = 180^o$ (π rad), thus the left corner of the plots corresponds to the inner cylinder surface. This pattern will be used in all plots henceforth.

FIGURE 91 - TANGENTIAL VELOCITY (VΘ) AND PRESSURE FIELD (P) FOR 40 RPM IMPOSED VELOCITY.

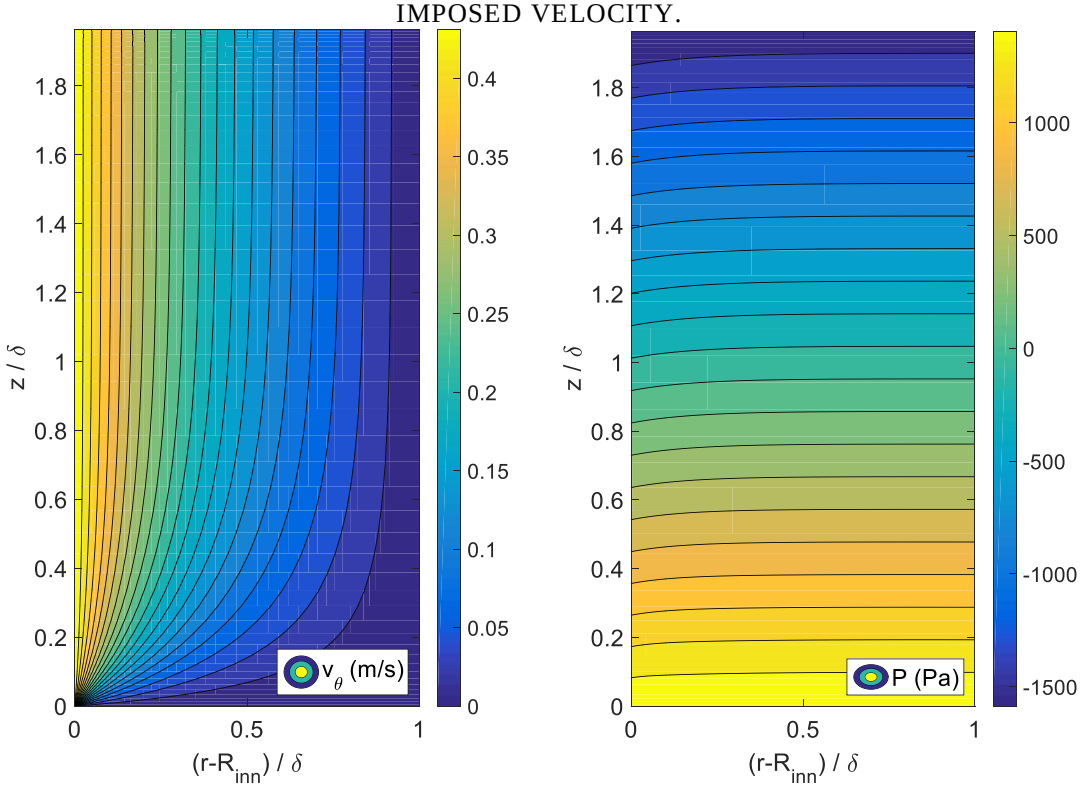

(A) (B)

Figure 92 represents the dynamic viscosity (η) for the six different fluid suspensions for 40 rpm. For the cases where the Power-Law indexes (n) is closer to unity, 1.25 kg of cotton and 2.50 kg of semi-synthetic fabric-water suspensions. On the other hand, because of the higher variation of the shear rates within the gap, the main variation of the viscosity is noticeable for the suspensions where the Power-Law index is higher. One can mention that the maximum viscosity value is higher for the heavier fluids, except for the semi-synthetic fabric-water suspension, where the heavier fluid presents a Newtonian fluid-like behavior with higher flow consistency index (m) and yield stress values (τ_0) however.

FIGURE 92 - APPARENT VISCOSITY (H) FIELD FOR A 40 RPM IMPOSED VELOCITY CONSIDERING A SUSPENSION WITH (A) 1.25KG OF COTTON, (B) 2.50KG OF COTTON, (C) 1.25KG OF SEMI-SYNTHETIC, (D) 2.50KG OF SEMI-SYNTHETIC, (E) 1.25 OF MIXED AND (F) 2.50 OF MIXED FABRICS.

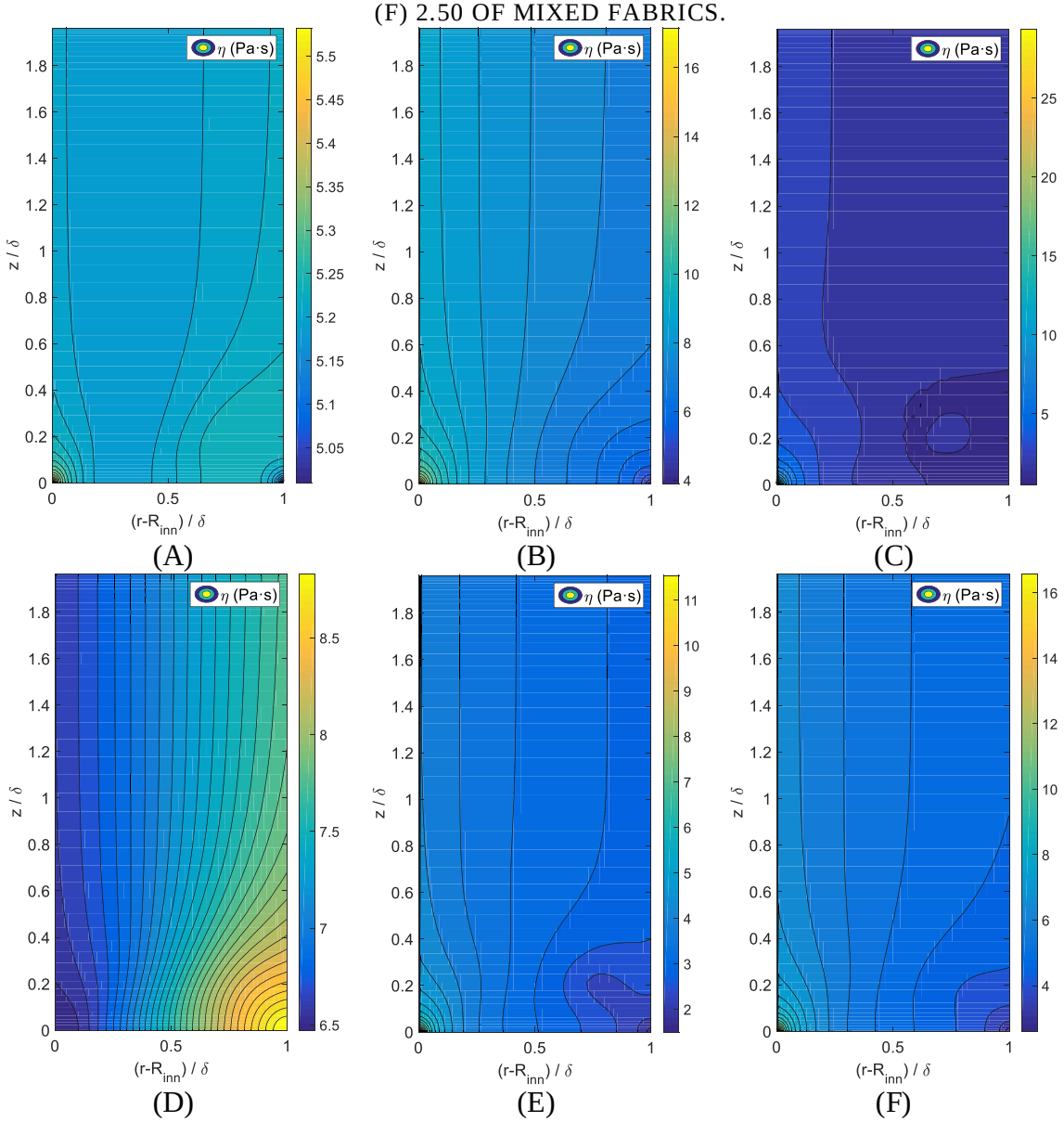

One can note that in the case of 2.50 kg of semi-synthetic fabric-water suspension, contrary to the other fluids, the maximum viscosity is found on the bottom corner with the outer cylinder, where the minimum shear rate value is found. This behavior can be better observed in Figure 93. The fluid suspension has the following parameters for the Herschel-Bulkley fluid, n = 1.006, m = 6.271 Pa·s^n and τ_0 = 2.808 Pa. Thus, Figure 93 represents the rheological curve of the fluid in function of the maximum and minimum shear rate values found in the simulation ($4.57 \cdot 10^2$ and $4.63 \cdot 10^{-3}$) for the *real* Power-Law index and another index (n = 1.05). So, one can observe that the higher index represents a more shear-thickening behavior, the viscosity increases with the shear rate, as for the smaller index it has a Newtonian-like behavior. However,

for the minimum shear rate value, the viscosity tends to the infinity because of the presence of yield stress. That is the reason because such an unexpected behavior showed up on simulation.

FIGURE 93 - APPARENT VISCOSITY (H) CURVES FOR DIFFERENT POWER-LAW INDEX (N) CONCERNING THE 2.50KG OF SEMI-SYNTHETIC FABRIC-WATER SUSPENSION.

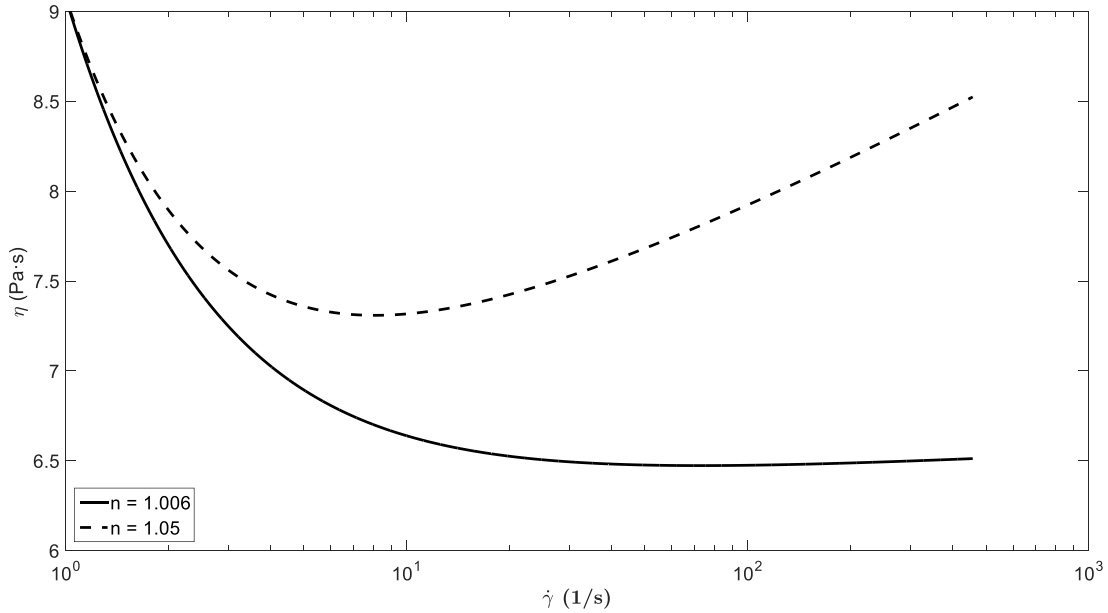

Figure 94 represents the stream function behaviors for the different fluid suspensions. One can note that there is still only one Taylor cell for all simulations, different from Newtonian fluids, where more cells can appear depending on the Reynolds number and geometrical aspects (WATANABE et al., 2003). There are only minor differences between the stream function intensities, which may vary according to the viscosity distribution across the gap, which can enhance or decrease either radial or axial velocity components. The center of Taylor-Couette cells denotes the center of rotation of the secondary flow within the gap. Also, the magnitude of the stream function denotes the influence of the secondary flow on the main flow. The higher the stream function magnitude the higher its influence. For all cases, the secondary flow goes upward near the inner cylinder and downwards near the outer cylinder surface.

FIGURE 94 - STREAM FUNCTION (Ψ) FIELD FOR A 40 RPM IMPOSED VELOCITY CONSIDERING A SUSPENSION WITH (A) 1.25KG OF COTTON, (B) 2.50KG OF COTTON, (C) 1.25KG OF SEMI-SYNTHETIC, (D) 2.50KG OF SEMI-SYNTHETIC, (E) 1.25 OF MIXED AND (F) 2.50 OF MIXED FABRICS.

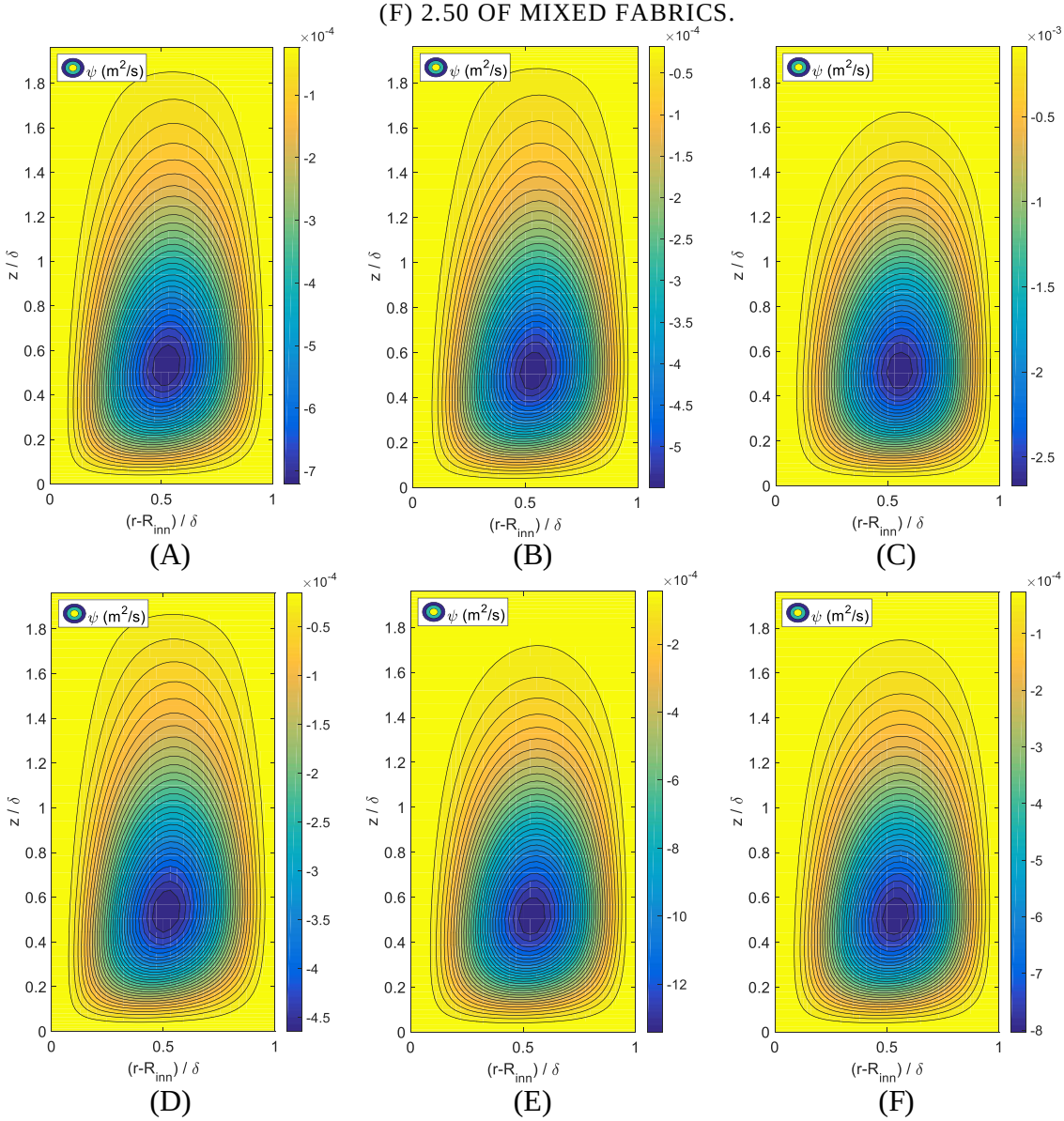

5.2.2 Inner Cylinder Angular Velocity of 60 rpm

Figure 95 depicts the plots of the (a) tangential velocity v_θ (m/s) and (b) pressure p (Pa) representing one of the six suspension fluids for ω_{inn} of 60 rpm. There is no significant change in the tangential velocity propagation across the gap. Moreover, the pressure distribution shows a more apparent influence of the inner cylinder velocity on it as there is a discontinuity of the pressures isolines near the cylinder surface.

FIGURE 95 - TANGENTIAL VELOCITY (VΘ) AND PRESSURE FIELD (P) FOR A 60 RPM IMPOSED VELOCITY.

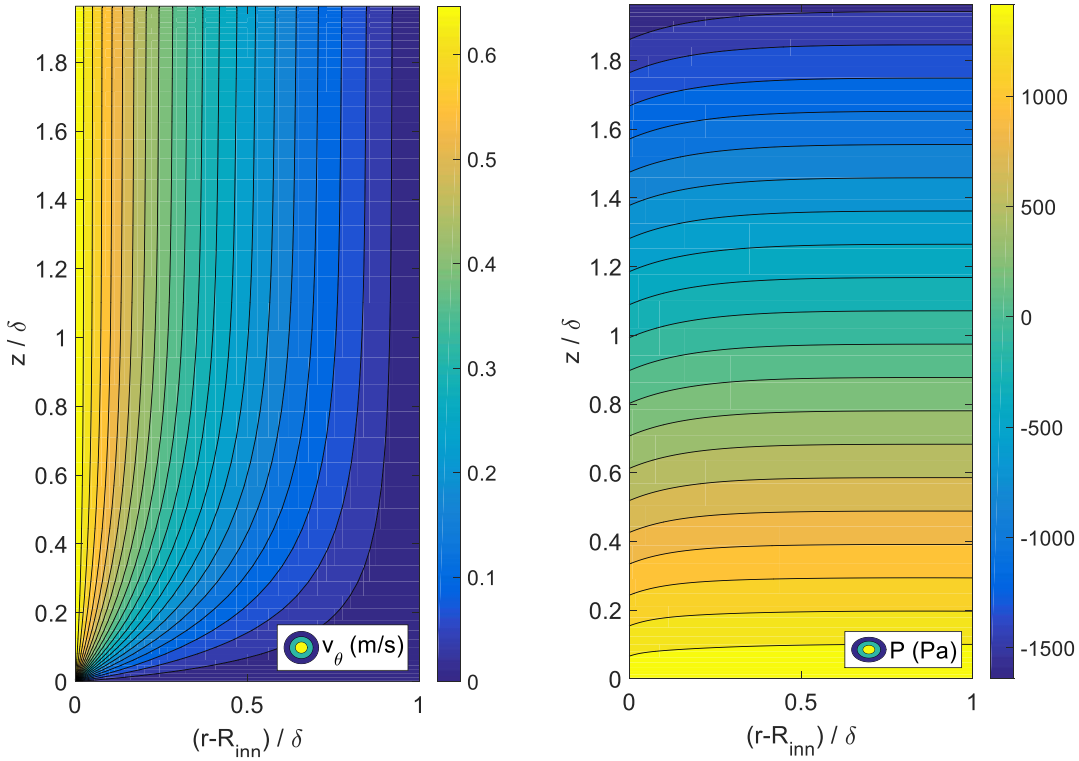

(A) (B)

Furthermore, Figure 96 represents the apparent viscosity (η) for all six fluid suspensions. One can note that there is a small difference between the fluids with the smaller Power-Law indexes (n), which varies from 9 to 6.5 Pa·s for the fluid with the 2.50 kg of fabric-water suspension and 5.55 to 5 Pa·s for the 1.25 kg of cotton fabric-water suspension.

FIGURE 96 - APPARENT VISCOSITY (H) FIELD FOR A 60 RPM IMPOSED VELOCITY CONSIDERING A SUSPENSION WITH (A) 1.25KG OF COTTON, (B) 2.50KG OF COTTON, (C) 1.25KG OF SEMI-SYNTHETIC, (D) 2.50KG OF SEMI-SYNTHETIC, (E) 1.25 OF MIXED AND (F) 2.50 OF MIXED FABRICS.

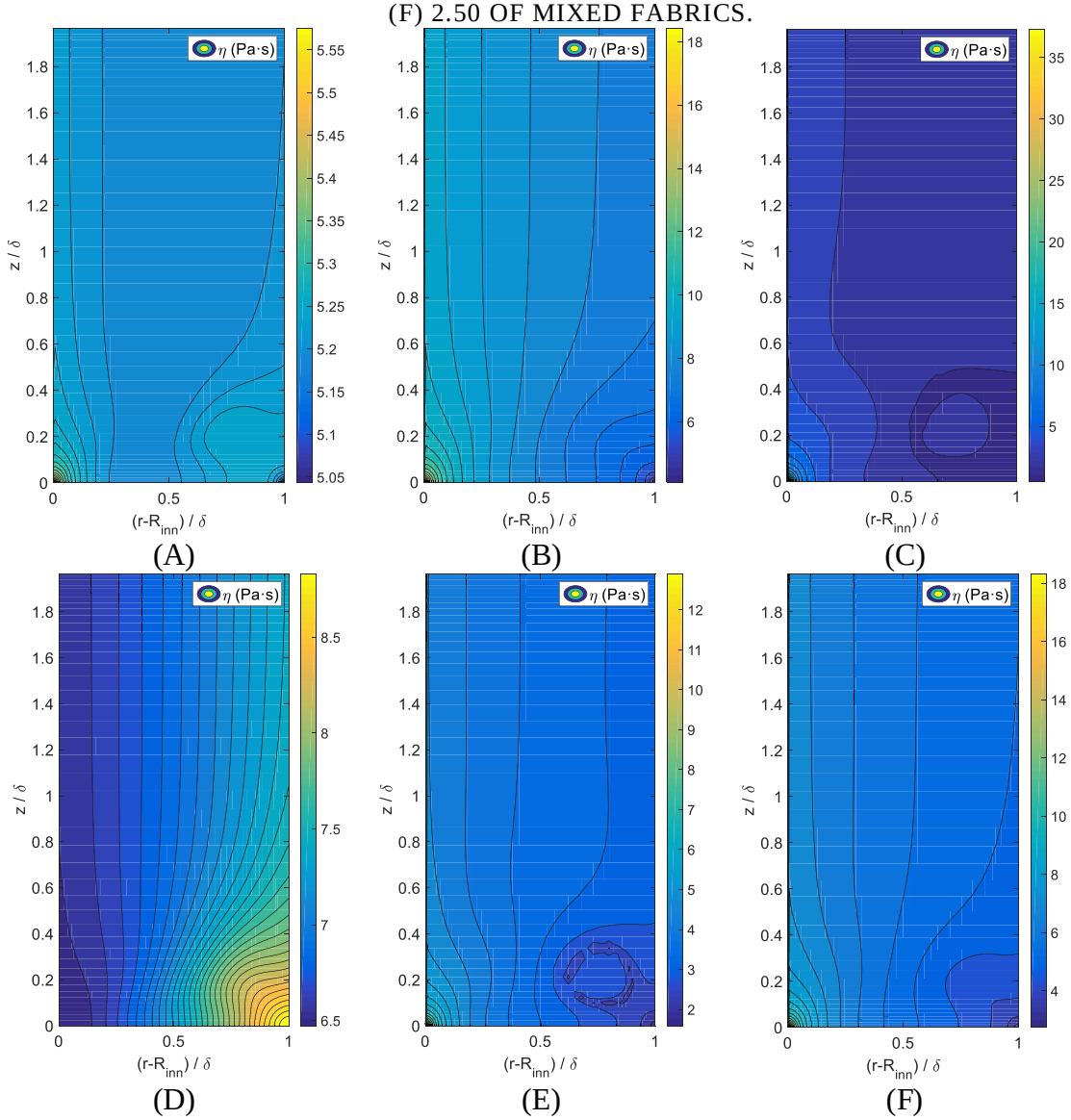

Figure 97 represents the stream function distribution across the gap for different fluid suspensions. Because of the non-Newtonian behavior of the suspensions, only one cell of circulation of the second flow is observed as well (Taylor-cell) in the same direction as the slower inner cylinder velocities cases. There are some minor differences concerning the center of the cell and the magnitude of the stream function which is defined according to the fluid properties but still, demonstrates that the second flow is weaker than the magnitude of the primary flow (tangential velocity).

FIGURE 97 - STREAM FUNCTION (Ψ) FIELD FOR A 60 RPM IMPOSED VELOCITY CONSIDERING A SUSPENSION WITH (A) 1.25KG OF COTTON, (B) 2.50KG OF COTTON, (C) 1.25KG OF SEMI-SYNTHETIC, (D) 2.50KG OF SEMI-SYNTHETIC, (E) 1.25 OF MIXED AND (F) 2.50 OF MIXED FABRICS.

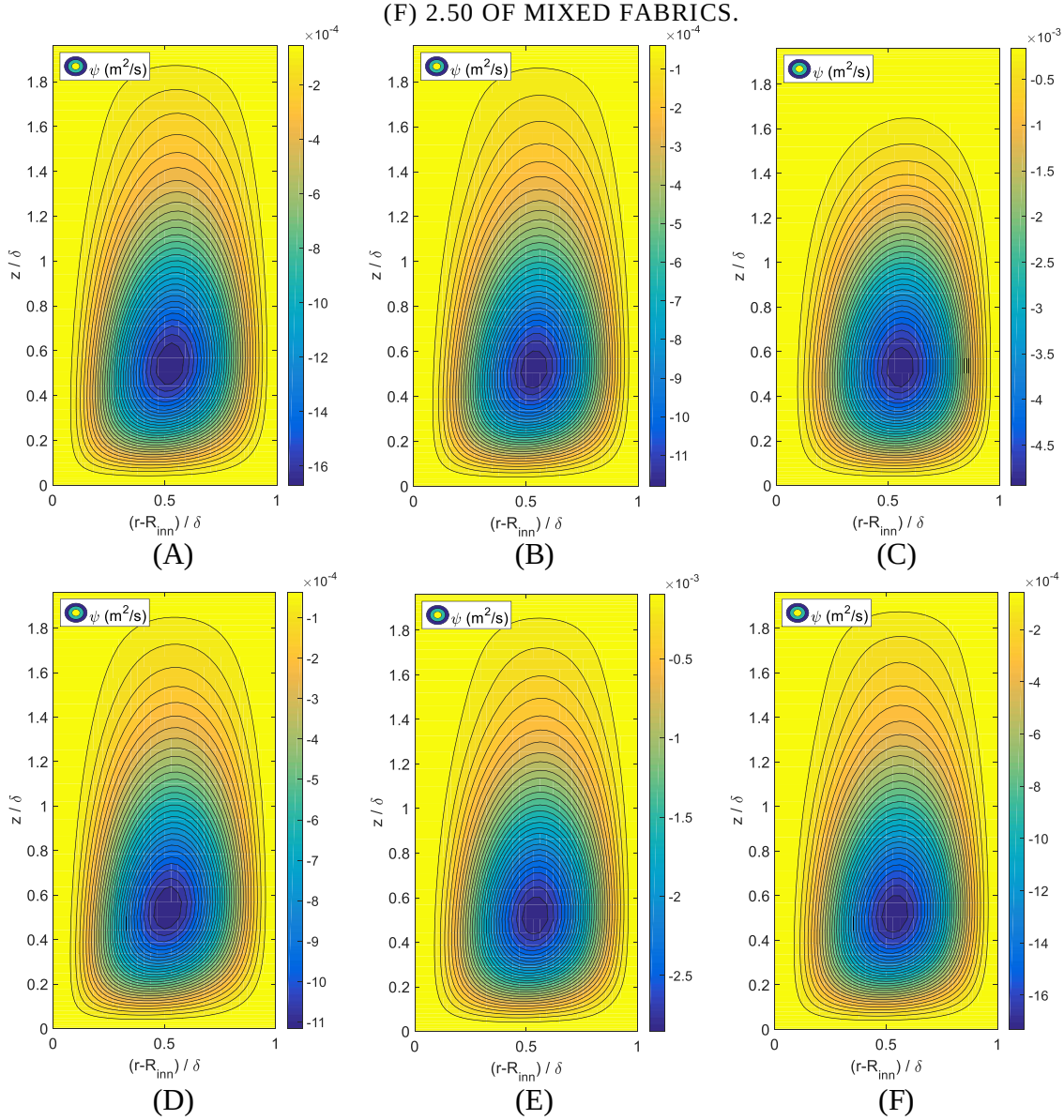

5.2.3 Inner Cylinder Angular Velocity of 80 rpm

Figure 98 represents the (a) tangential velocity v_θ (m/s) and (b) pressure p (Pa) distribution plotted across the gap between the cylinders. As one can see, the propagation of the tangential velocity does not change significantly between the fluids, for this reason, only one of them has been plotted representing all fluid suspensions. The same analysis can be extended to the pressure distribution, which one can see the growing influence of the inner cylinder velocity boundary into it, thus changing the pressure isolines near the inner cylinder surface.

FIGURE 98 - TANGENTIAL VELOCITY (VΘ) AND PRESSURE FIELD (P) FOR A 80 RPM IMPOSED VELOCITY.

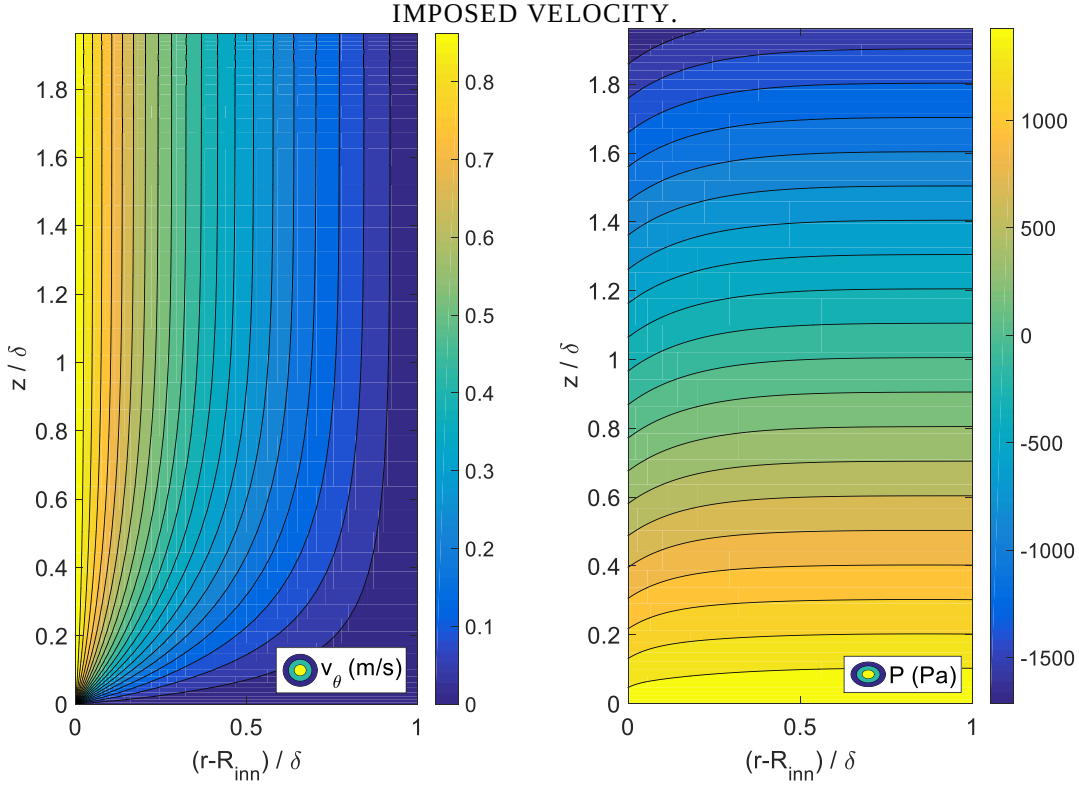

(A) (B)

Figure 99 represents the apparent viscosity(η) for all six different fluid suspensions. One can see that if compared to the water dynamic viscosity (μ), which is near 10^{-3} Pa·s at 20°C, the viscosity of the suspension is thousands of times higher, approaching that of glycerin. It can demonstrate the influence of the presence of fabrics inside washing machines. The fabric tissues used in these tests do not affect the fluid density significantly because their volume compared with the water is minimum, besides being lighter than the water. The main influence of the fabrics is in the way how the fluids behave when an external torque is imposed on it, and it can be seen that the quantities of tissues and fabric kind have a quite influence on its distribution.

FIGURE 99 - APPARENT VISCOSITY (H) FIELD FOR AN 80 RPM IMPOSED VELOCITY CONSIDERING A SUSPENSION WITH (A) 1.25KG OF COTTON, (B) 2.50KG OF COTTON, (C) 1.25KG OF SEMI-SYNTHETIC, (D) 2.50KG OF SEMI-SYNTHETIC, (E) 1.25 OF MIXED AND (F) 2.50 OF MIXED FABRICS.

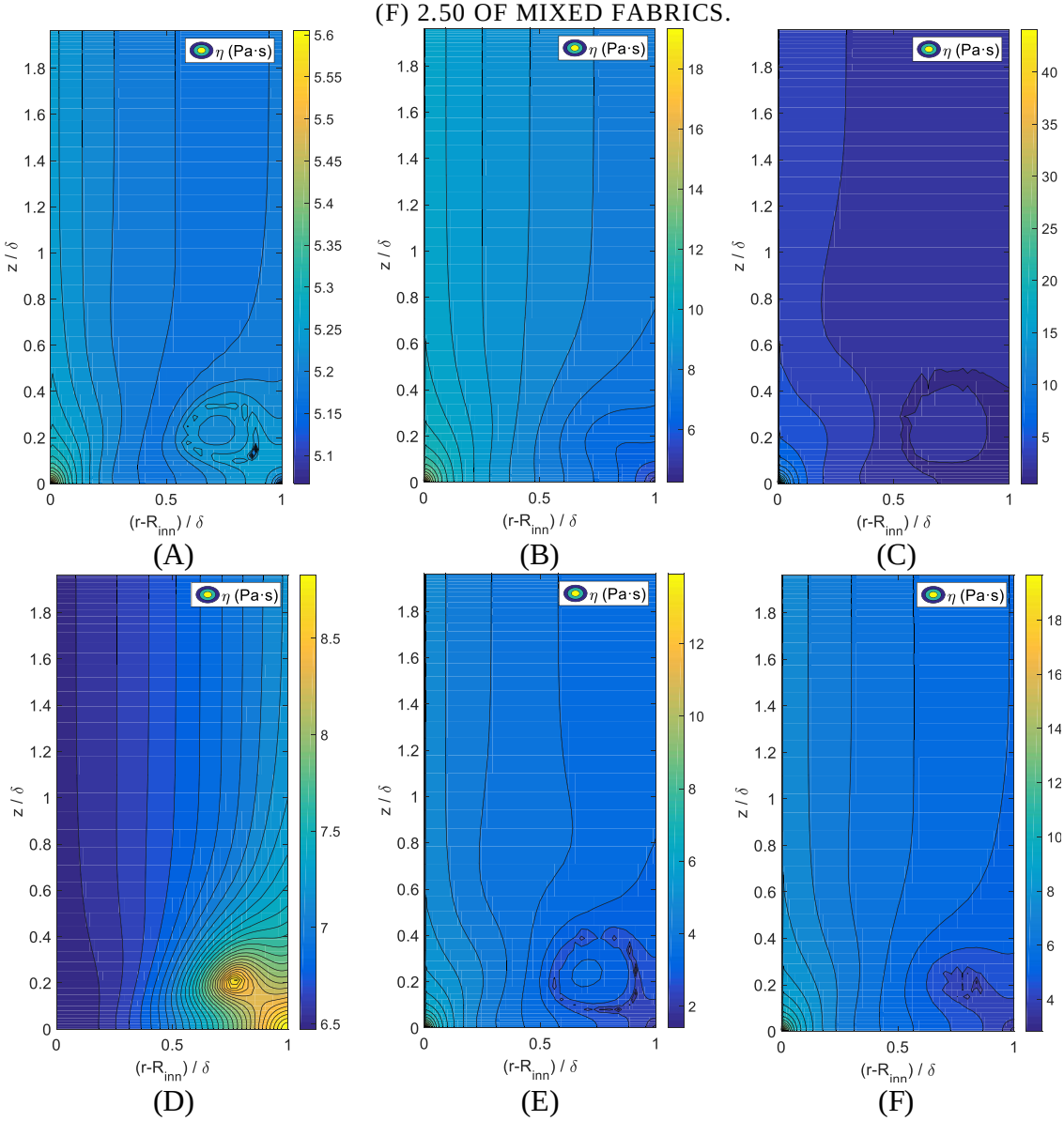

Figure 100 represents the stream function (ψ) distribution across the gap for the six different fluid suspensions. One can see that there is only one cell of recirculation, despite the higher velocities on the inner cylinder. In this case, the magnitude of the secondary flow is higher than the ones found on the 60-rpm inner cylinder velocity condition. The direction of the secondary flow did not change either.

FIGURE 100 - STREAM FUNCTION (Ψ) FIELD FOR AN 80 RPM IMPOSED VELOCITY CONSIDERING A SUSPENSION WITH (A) 1.25KG OF COTTON, (B) 2.50KG OF COTTON, (C) 1.25KG OF SEMI-SYNTHETIC, (D) 2.50KG OF SEMI-SYNTHETIC, (E) 1.25 OF MIXED AND (F) 2.50 OF MIXED FABRICS.

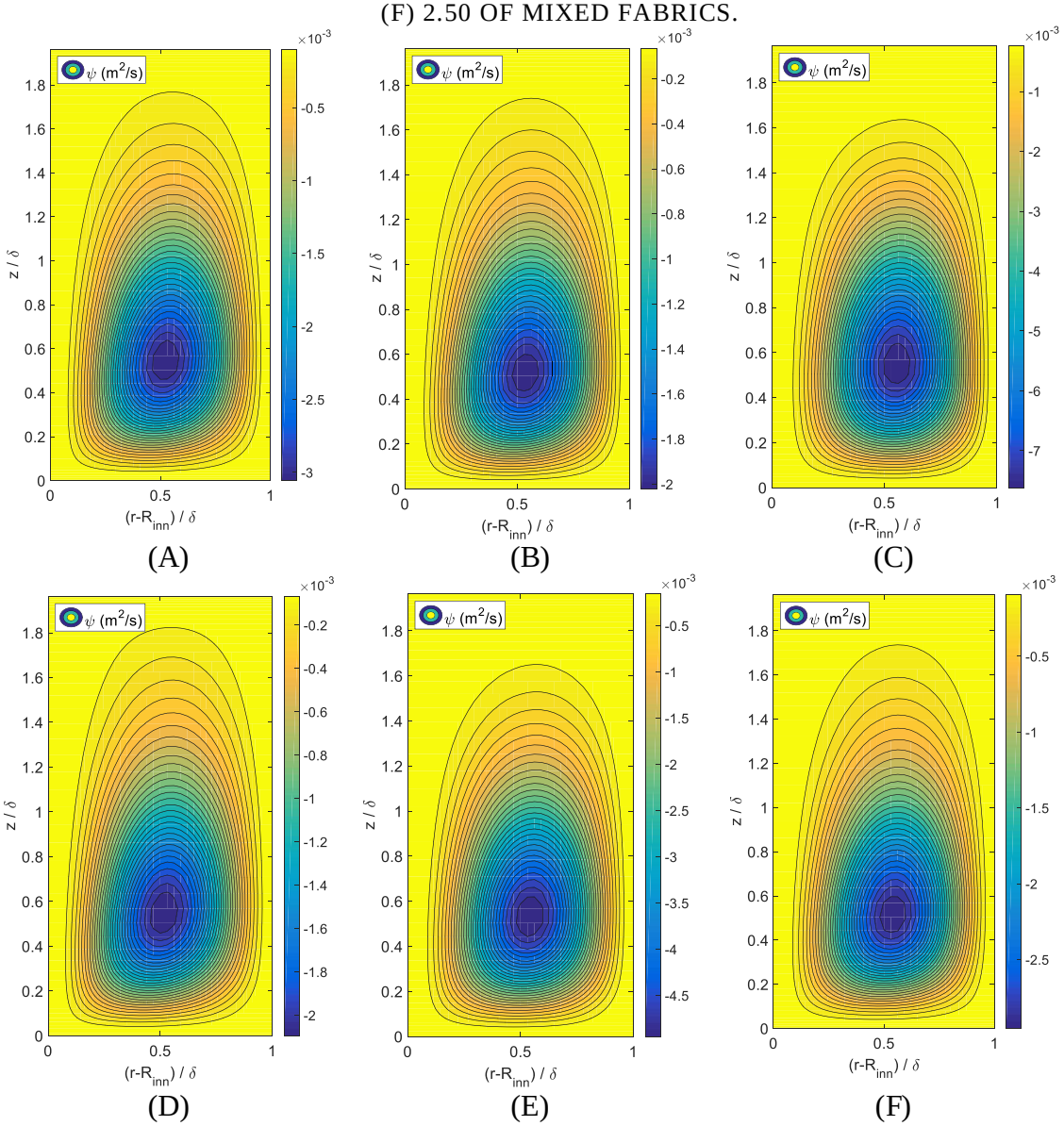

5.2.4 Inner Cylinder Angular Velocity of 100 rpm

Figure 101 depicts the plot of the (a) tangential velocity v_θ (m/s) and (b) pressure p (Pa) distribution plotted across the gap between the cylinders, where there are no visual differences between these six fluid suspensions distributions. As one can see the maximum velocity is achieved near the inner cylinder surface ($\omega_{inn} \cdot R_{inn}$ = 1.152 m/s). Also, the influence of the growing inner cylinder velocity on the pressure distribution becomes more noteworthy as it deflects this distribution near the left-top boundary.

FIGURE 101 - TANGENTIAL VELOCITY (VΘ) AND PRESSURE FIELD (P) FOR A 100 RPM IMPOSED VELOCITY.

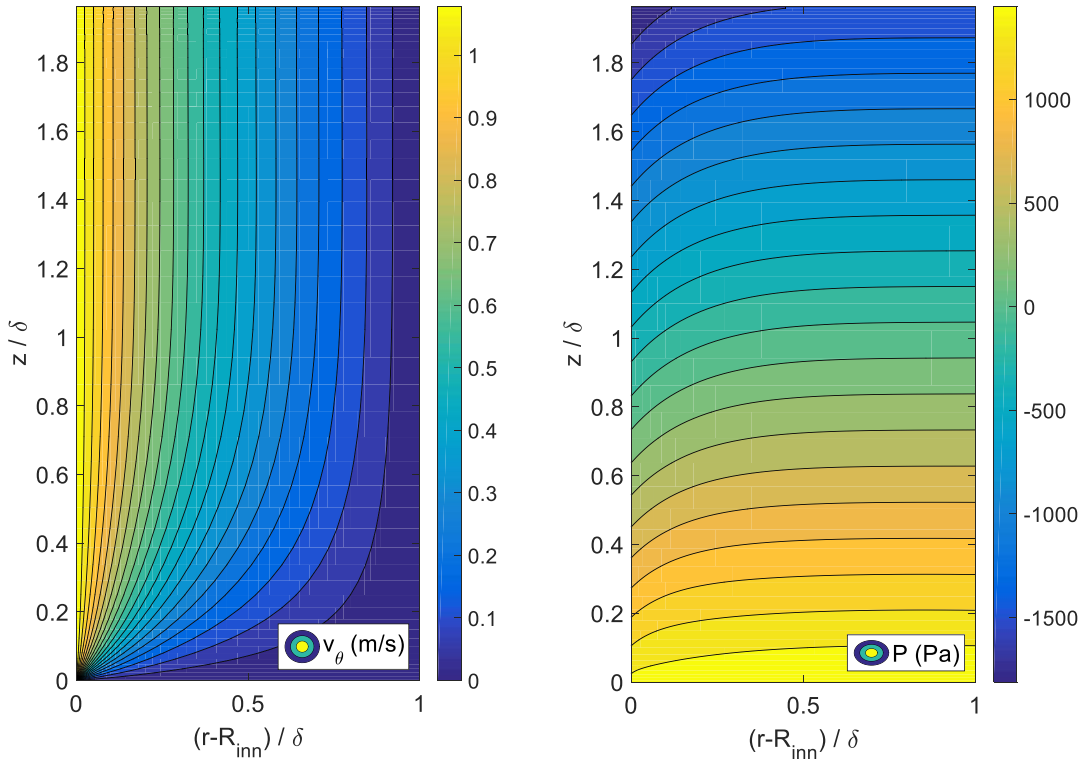

(A) (B)

Figure 102 depicts the apparent viscosity (η) for all six fluid suspensions. One can see that for the fluids with Newtonian-like behavior, the maximum and the minimum have not changed much in all ω_{inn} imposed conditions. Moreover, the main difference between the maximum and the minimum viscosity along the distribution is due to the shear stress influence. However, the fluids that present a high viscosity near the left-bottom end wall also presents a strong variation of the viscosity variation. Thus, one can note that the most important characteristic is the viscosity distribution across the whole gap, not only where the end-effects occur.

FIGURE 102 - APPARENT VISCOSITY (H) FIELD FOR AN 100 RPM IMPOSED VELOCITY CONSIDERING A SUSPENSION WITH (A) 1.25KG OF COTTON, (B) 2.50KG OF COTTON, (C) 1.25KG OF SEMI-SYNTHETIC, (D) 2.50KG OF SEMI-SYNTHETIC, (E) 1.25 OF MIXED AND (F) 2.50 OF MIXED FABRICS.

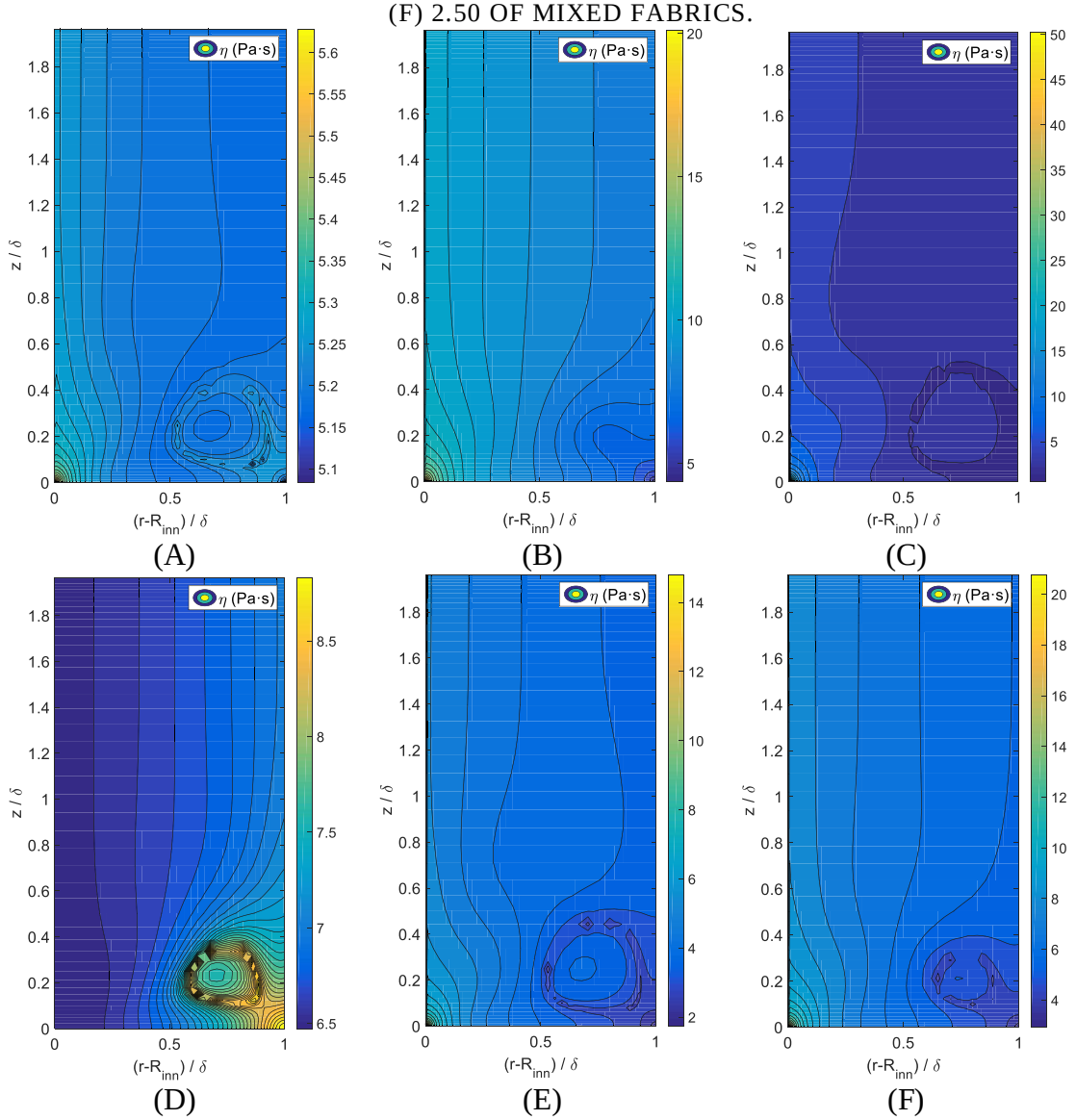

Figure 103 represents the stream function (ψ) distribution across the gap for all fluid suspensions. The presence of only one Taylor-cell (secondary flow recirculation) has not changed, despite some variations on the eye of recirculation position and the higher stream function intensity when compared to the slower cases.

FIGURE 103 - STREAM FUNCTION (Ψ) FIELD FOR AN 100 RPM IMPOSED VELOCITY CONSIDERING A SUSPENSION WITH (A) 1.25KG OF COTTON, (B) 2.50KG OF COTTON, (C) 1.25KG OF SEMI-SYNTHETIC, (D) 2.50KG OF SEMI-SYNTHETIC, (E) 1.25 OF MIXED AND (F) 2.50 OF MIXED FABRICS.

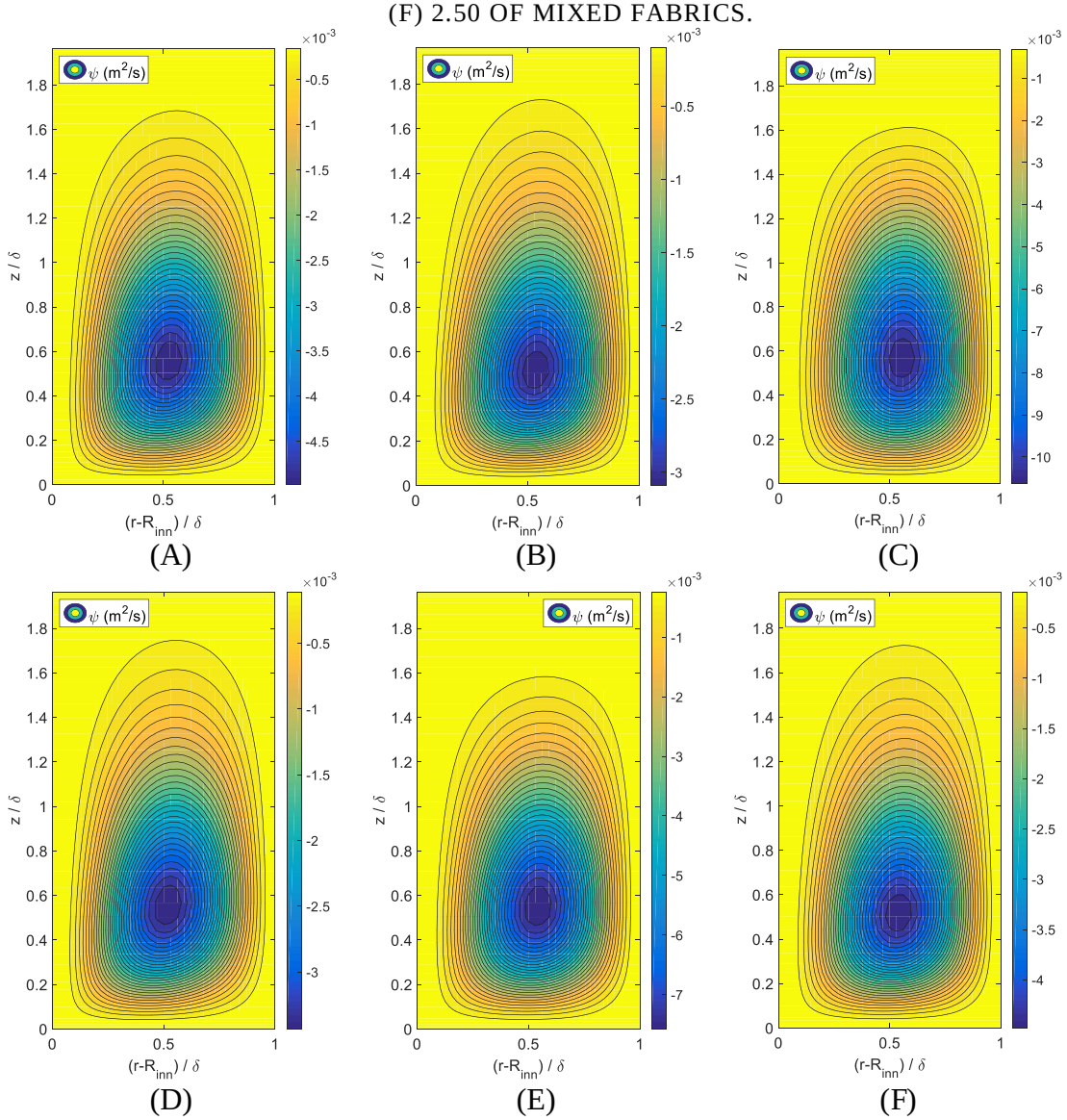

5.2.5 Inner Cylinder Angular Velocity of 120 rpm

Figure 104 represents the plotted distribution of the (a) tangential velocity v_θ (m/s) and (b) pressure p (Pa) for one fluid suspension representing all six fabric-water suspensions. In this case, where the inner cylinder surface velocity is the maximum, the deflection on the pressure distribution maximized near its surface as well.

FIGURE 104 - TANGENTIAL VELOCITY (VΘ) AND PRESSURE FIELD (P) FOR A 120 RPM IMPOSED VELOCITY.

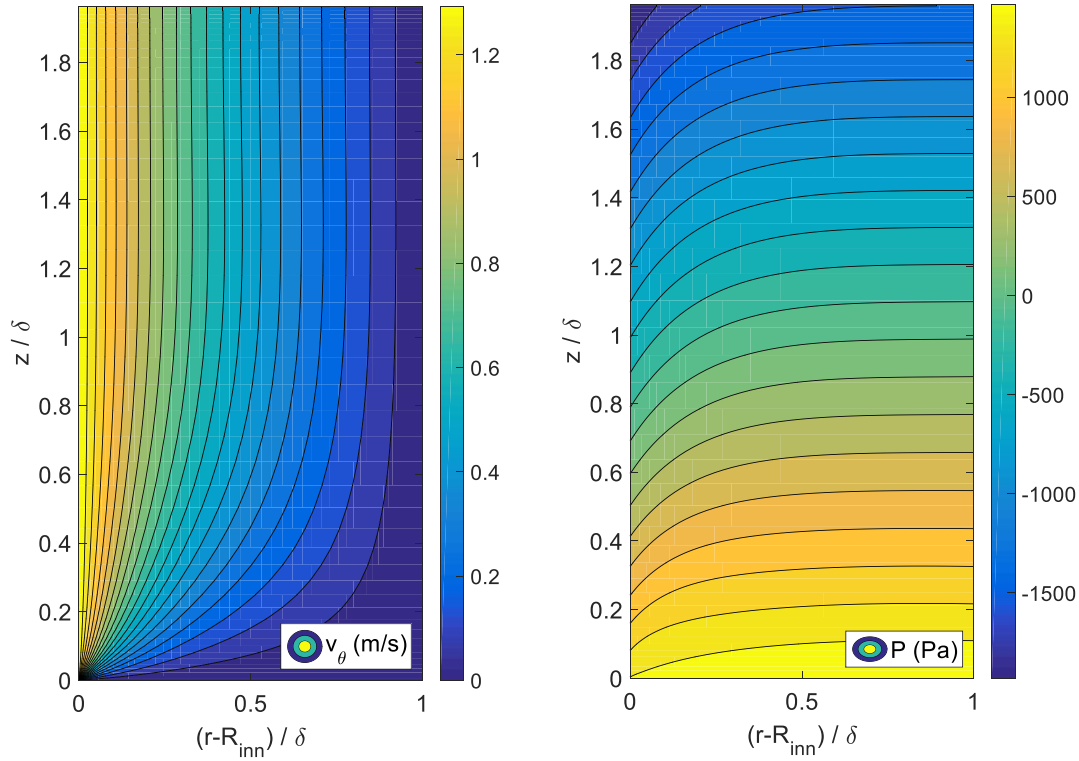

(A) (B)

Figure 105 represents the apparent viscosity (η) for all the six different fluid suspensions. The graphics represent not only the influence of the rheological parameters of the suspensions, given by the Herschel-Bulkley model but also the differences between the fabric kinds and tissues quantities in each suspension. For the cotton fabric case, the lighter suspension presents a Newtonian-like behavior and smaller yield stress and Power-Law consistency index compared to the heavier suspension, which can be observed in the other viscosities graphs for all velocities. On the other hand, for the semi-synthetic fabric the heavier fluid also presents a higher m-parameter and yield stress, but in this case, a Newtonian-like behavior which could be explained by the great concentration of fabric tissues near the inner cylinder wall that influence the suspension behavior. Finally, for the mixed fluids, both heavier and lighter presents similar shear-thickening Power-Law index (n) and greater m-parameter and yield stress for the heavier fluid.

FIGURE 105 - APPARENT VISCOSITY (H) FIELD FOR AN 120 RPM IMPOSED VELOCITY CONSIDERING A SUSPENSION WITH (A) 1.25KG OF COTTON, (B) 2.50KG OF COTTON, (C) 1.25KG OF SEMI-SYNTHETIC, (D) 2.50KG OF SEMI-SYNTHETIC, (E) 1.25 OF MIXED AND (F) 2.50 OF MIXED FABRICS.

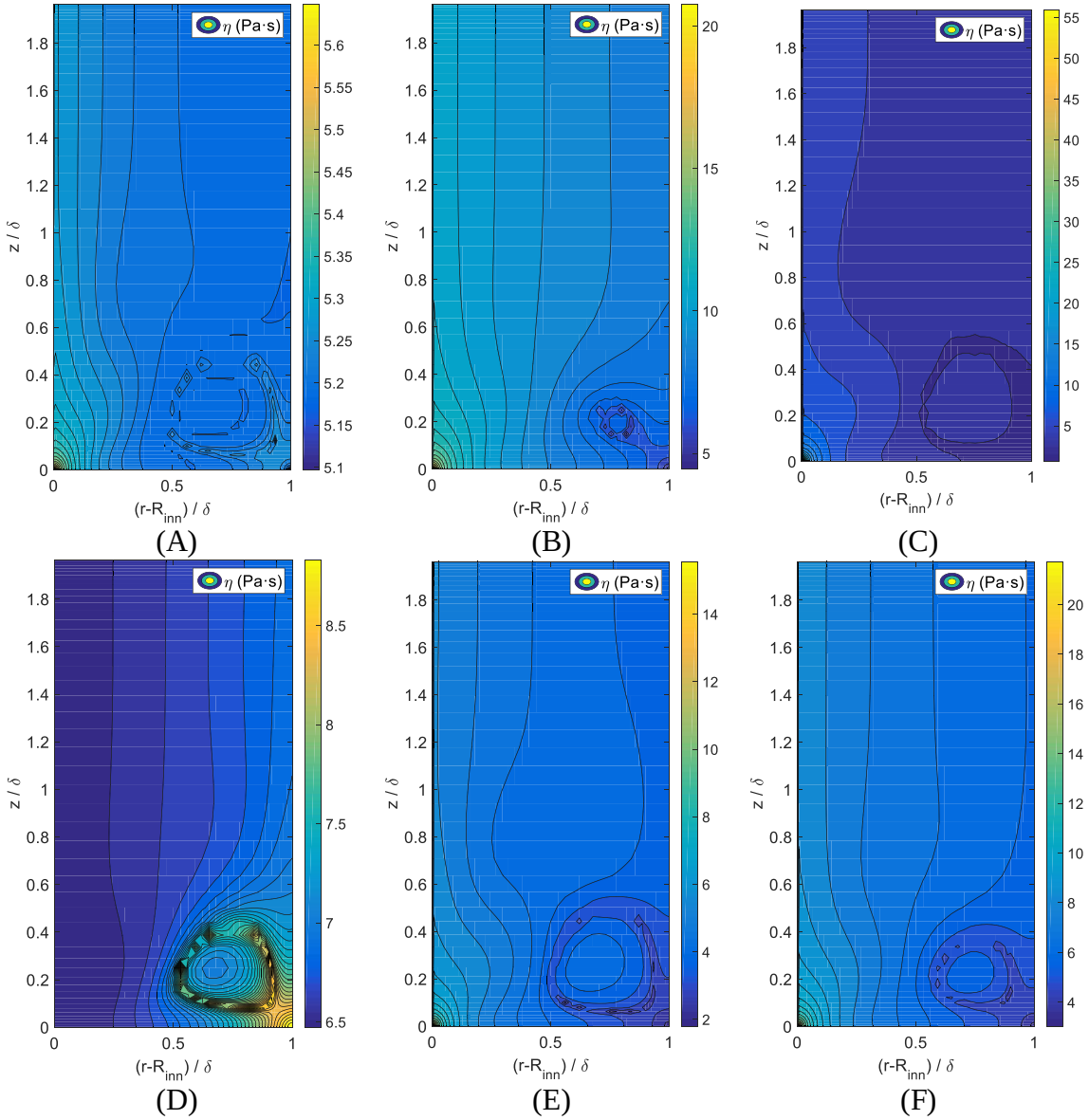

Figure 106 represents the stream function (ψ) distribution across the gap for all the fluid suspensions. On the literature review concerning the instabilities on the Taylor-Couette flow it has been mentioned how the increasing on the Reynolds number (or the inner cylinder imposed velocity) enhances the secondary flow influence than increasing the number of recirculation cells (depending on the geometry) and also impacts on the primary flow behavior. However, for these suspensions, the rheological parameters point out that they are very viscous fluids, thus the appearance of instabilities is retarded, as one can see on all graphical visualization of the stream functions.

FIGURE 106 - STREAM FUNCTION (Ψ) FIELD FOR AN 120 RPM IMPOSED VELOCITY CONSIDERING A SUSPENSION WITH (A) 1.25KG OF COTTON, (B) 2.50KG OF COTTON, (C) 1.25KG OF SEMI-SYNTHETIC, (D) 2.50KG OF SEMI-SYNTHETIC, (E) 1.25 OF MIXED AND (F) 2.50 OF MIXED FABRICS.

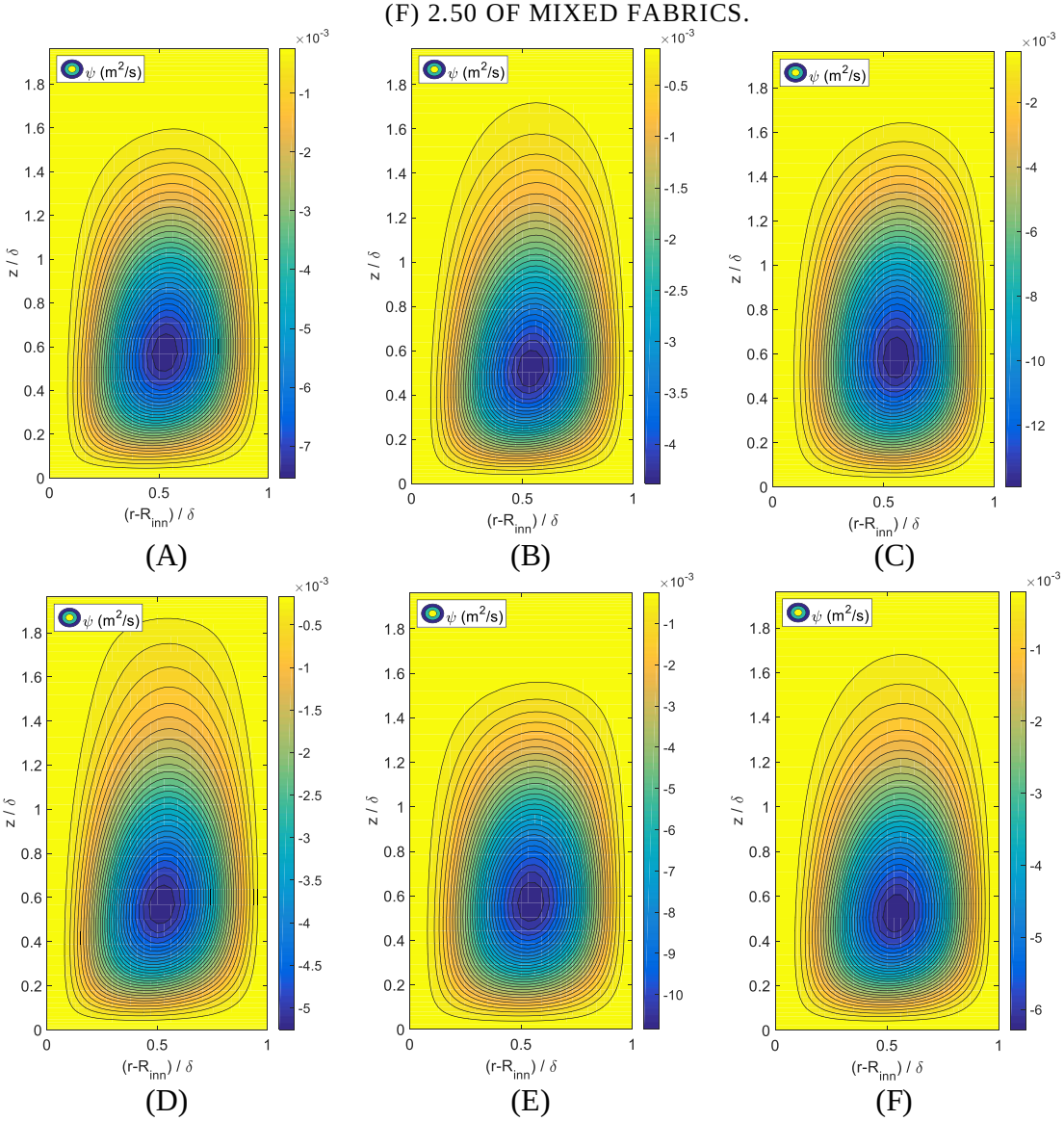

5.2.6 End-Effect Analysis

End-effects were computed on the torque calculations and also in the experimental measurements as well. It is important to mention that the geometry aspect ratio (Γ), which is not high enough to avoid the impact of end-effects on measurement, is similar to the ones found in real washing machines. One can note that the faster is the inner cylinder tangential velocity, the higher is the influence of the end walls and the end-effects influence in numerical calculation and experimental measurements. One can see, by checking the rheological parameters of the fluids (Table 19), that the higher the Power-Law index parameter (n) the higher the maximum shear-stress value and the end-effect impact in the fluid flow. Not only

the n-parameter enhances the end-effect, but also the yield stress (τ_0) and the flow consistency index (m).

Table 30 summarizes the maximum shear-stress found for each numerical simulation. In a coaxial Couette geometry, the maximum shear stress occurs due to the contribution from the portion of the flow which is influenced by the solid bottom surface. The growth of the tensor magnitude across the gap is related to the rheological properties. For example, despite being the lighter, the semi-synthetic fabric-water fluid suspension presents a higher maximum tensor magnitude value than the heavier one. The propagation of shear stresses from the end-effect focuses depends on the rheological parameters for each fluid suspension. Table 31 presents the ratio between the average of the shear stress magnitude in the inner cylinder surface with the maximum magnitude. One can see that it changes significantly with the fabric type, but it does not change very much with the velocities.

TABLE 30 - MAXIMUM SHEAR STRESS TENSOR MAGNITUDE.

	$\lvert\tau\rvert_{max}$ (Pa)					
	Cotton		Semi-synthetic		Mixed	
	1.25 kg	2.50 kg	1.25 kg	2.50 kg	1.25 kg	2.50 kg
40 rpm	2488	7749	12778	2924	5173	7434
60 rpm	3761	12472	24298	4395	8663	12330
80 rpm	5041	17482	38335	5869	12491	17654
100 rpm	6328	22718	54600	7345	16591	23323
120 rpm	7620	28140	72894	8823	20921	29282

TABLE 31 - RATIO BETWEEN AVERAGE AND MAXIMUM SHEAR STRESS ON THE INNER CYLINDER SURFACE.

	$\lvert\bar{\tau}\rvert/\lvert\tau\rvert_{max}$					
	Cotton		Semi-synthetic		Mixed	
	1.25 kg	2.50 kg	1.25 kg	2.50 kg	1.25 kg	2.50 kg
40 rpm	7.589%	5.526%	4.217%	8.041%	4.920%	5.043%
60 rpm	7.576%	5.519%	4.216%	7.970%	4.912%	5.031%
80 rpm	7.580%	5.518%	4.215%	7.936%	4.911%	5.028%
100 rpm	7.586%	5.516%	4.215%	7.921%	4.911%	5.026%
120 rpm	7.596%	5.516%	4.215%	7.905%	4.912%	5.026%

One can still note that the maximum shear stress tensor magnitude is found near the bottom corner with the inner cylinder surface, which denotes the presence of a great end-effect in such a small region. For almost all fluids the shear stress variation changes in a radial way

along the gap. Figure 107 denotes that variation along the axial direction for the ratio of the local shear stress and the maximum one in the inner cylinder surface region. It shows that the fluids with the lower Power-Law index (n) (i.e., 1.25 kg of cotton and 2.50 of semi-synthetic fabric-water suspensions) are the most affected with the end-effects. It occurs because the linear behavior of the shear stress for Newtonian-like fluid flows. While that for a shear-thickening fluid the viscosity on the maximum shear stress region is also maximum, but with the decreasing of the shear stress magnitude leaving the end-effect region the viscosity also decreases, thus suffering less from the end-effects.

FIGURE 107 - RATIO BETWEEN THE SHEAR STRESS ALONG THE INNER CYLINDER SURFACE AND THE MAXIMUM SHEAR STRESS.

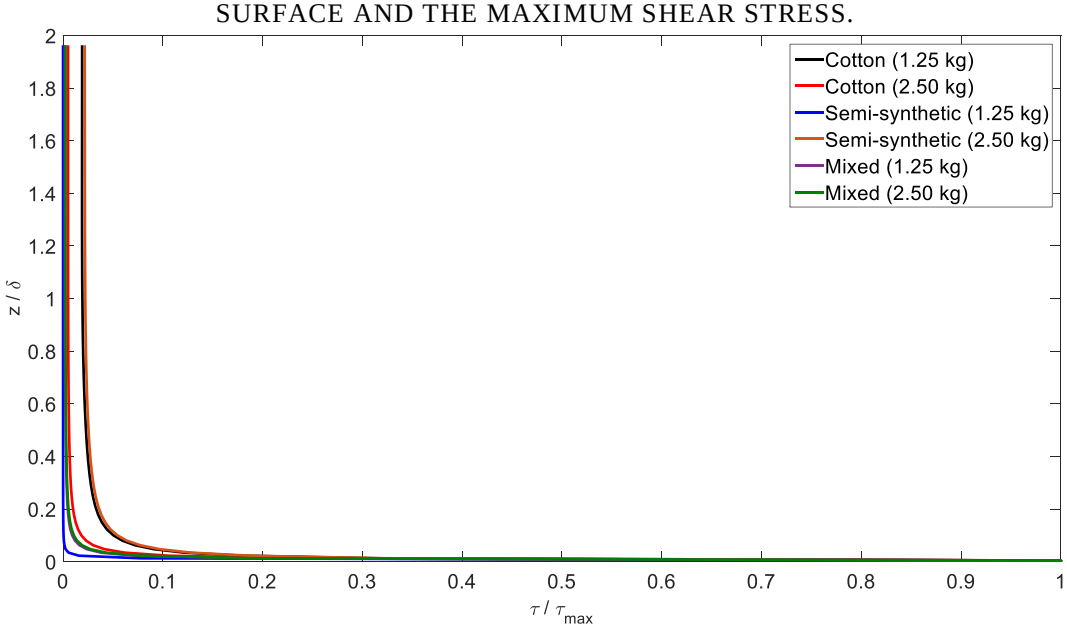

Figure 108 plots the variation along the axial direction for the ratio of the local shear rate and the maximum one in the inner cylinder surface region. One can see some minor differences when comparing to the shear stress behavior. In this case, it occurs because the shear rate is calculated directly with the velocity variation on the region, while that for the shear stress it is more affected with the change on the viscosities.

FIGURE 108 - RATIO BETWEEN THE SHEAR RATE ALONG THE INNER CYLINDER SURFACE AND THE MAXIMUM SHEAR RATE.

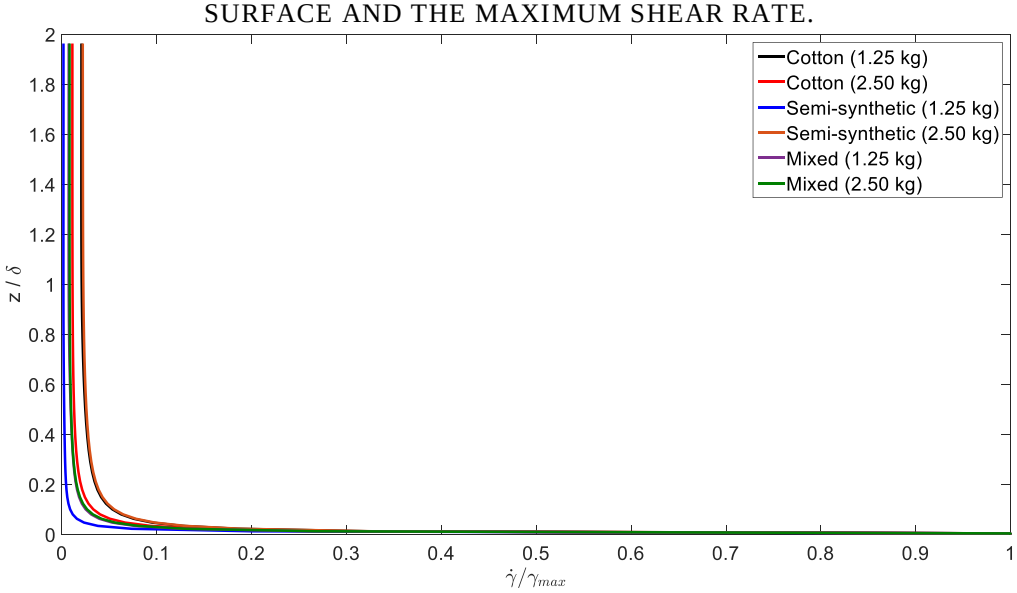

Figure 107 and 108 are depicted for the 120-rpm simulation, but their analyses are extended to the other velocities due to the fact that there are almost no changes between the distribution of the local shear rate and the maximum one, as seen in Table 31.

5.3PERIODIC FLOW SIMULATIONS

Similar to the steady-state simulations the results of the periodic flow simulations were compared against the experimental measurements presented in Chapter 4. The parameters of the Herschel-Bulkley fluid model obtained through the regression of experimental measurements are used in simulations. In the periodic flow simulations, only the two bulks of mixed fabric-water suspensions are used as the working fluid.

Two different tests conditions have been analyzed: (i) statical basis flow, and (ii) rotating basis flow. The former corresponds to the geometry used for steady-state simulations, whereas the latter bottom of the geometry also rotates with the inner cylinder.

For convenience, Figures 31 and 32 are repeated here to facilitate the understanding of the four periodic test conditions.

A time-step (Δt) of 80 milliseconds was applied for all the simulations, following the algorithm depicted in Figure 20. The value of 80 milliseconds was appointed just for the sake of illustrating the fluid flow, without any further evaluation of the best time-step value.

FIGURE 109 - ANGULAR VELOCITY FOR DIFFERENT PERIODIC TESTS.

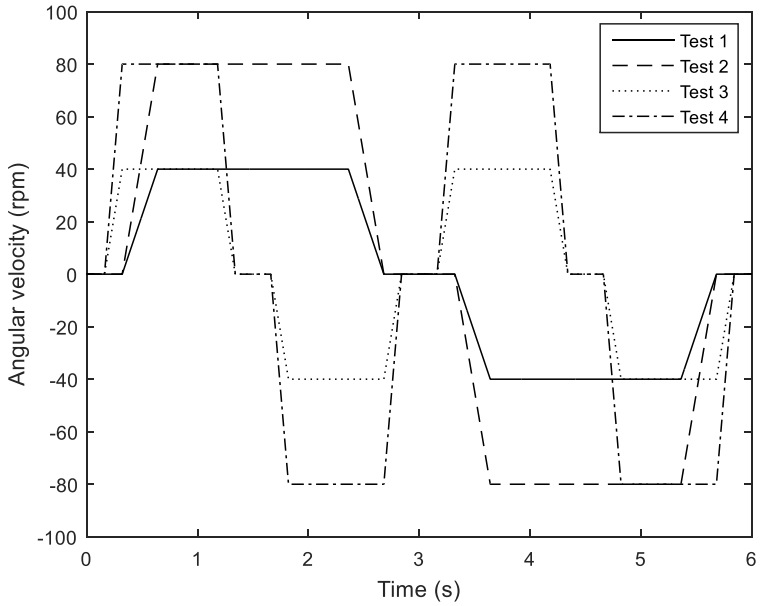

FIGURE 110 - ANGULAR ACCELERATION FOR DIFFERENT PERIODIC TESTS.

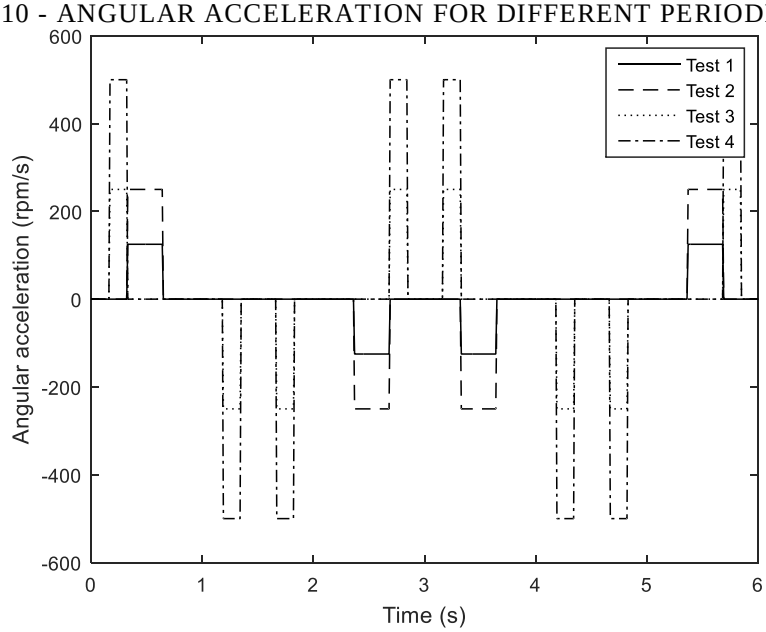

5.3.1 Static Bottom Basis Flow Simulations

In accordance to the steady-state simulations, two different torque calibrations were conducted: One considers all the shear stress components ($\tau_{\theta\theta}$, τ_{rr}, τ_{zz}, $\tau_{r\theta}$, $\tau_{\theta z}$ and τ_{rz}) in order to evaluate the shear stress near the inner cylinder surface, while the another consider the $\tau_{r\theta}$ shear stress component only.

Figure 111 shows the verification of the numerical torque on inner cylinder surface (complete and simplified calculations) compared to the experimental measurement for the Test

1 of 1.25 kg of mixed fabric-water simulations. One can see that the simulated torque values follow the pattern of the experimental measurement. Despite the model cannot specify the torque peaks values when the cylinder is at full velocity, the torque values are similar to the experimental ones for time periods of constant velocity.

FIGURE 111 - TORQUE VERIFICATION OF TEST 1 NON-ROTATING BASIS SIMULATION FOR 1.25 KG OF MIXED FABRIC-WATER SUSPENSION.

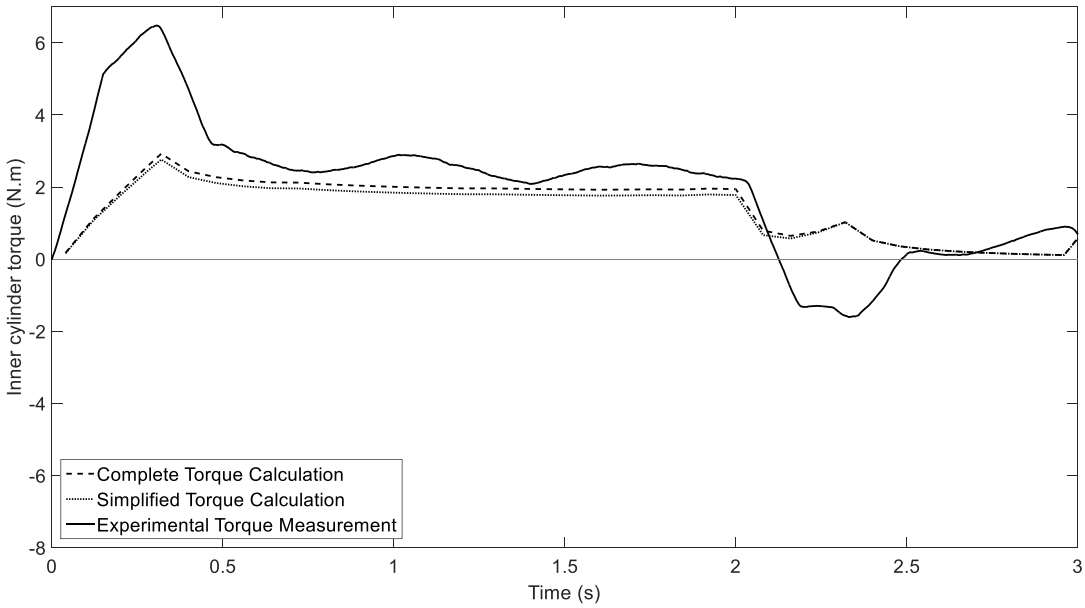

Similarly, Figure 112 shows the verification of the numerical torque on inner cylinder surface (complete and simplified calculations) compared to the experimental torque measurement for the Test 1 of 2.50 kg of mixed fabric-water simulations. The same observations mentioned in the previous figure is extended henceforth. One can see that both numerical and experimental torque values in this case for the heavier suspension.

Figure 113 depicts the verification of the numerical torque on inner cylinder surface (complete and simplified calculations) compared to the experimental torque measurement for the Test 2 of 1.25 kg of mixed fabric-water simulations. In this test, the maximum velocity is 80 rpm, thus a higher torque is expected as well. One can observe a better agreement between numerical and experimental torques in this case.

FIGURE 112 - TORQUE VERIFICATION OF TEST 1 NON-ROTATING BASIS SIMULATION FOR 2.50 KG OF MIXED FABRIC-WATER SUSPENSION.

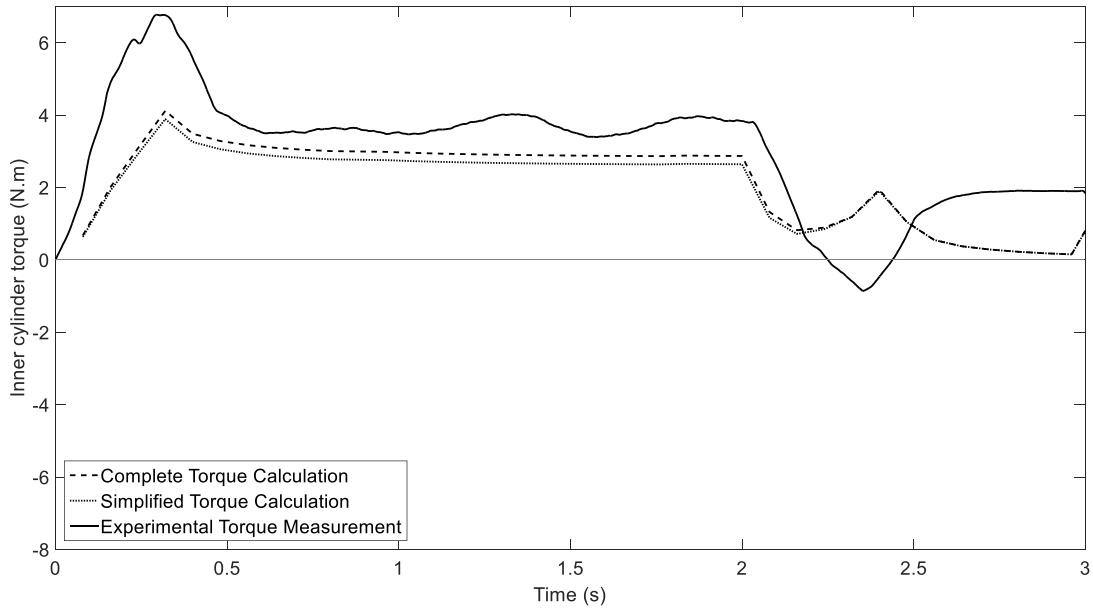

Similarly, Figure 114 shows the verification for the numerical torque values for the Test 2 with 2.50 kg of mixed fabric-water simulations. In the same way, the torque values are higher for the heavier suspension. One can see that the agreement between both numerical and experimental counterparts are quite good for this case too.

FIGURE 113 - TORQUE VERIFICATION OF TEST 2 NON-ROTATING BASIS SIMULATION FOR 1.25 KG OF MIXED FABRIC-WATER SUSPENSION.

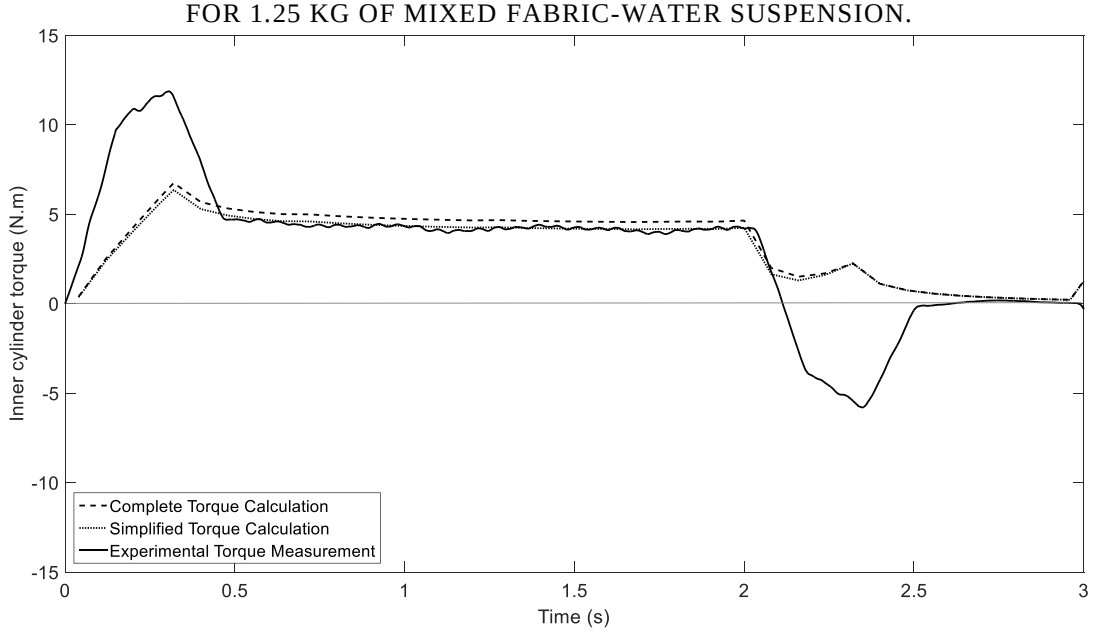

FIGURE 114 - TORQUE VERIFICATION OF TEST 1 NON-ROTATING BASIS SIMULATION FOR 2.50 KG OF MIXED FABRIC-WATER SUSPENSION.

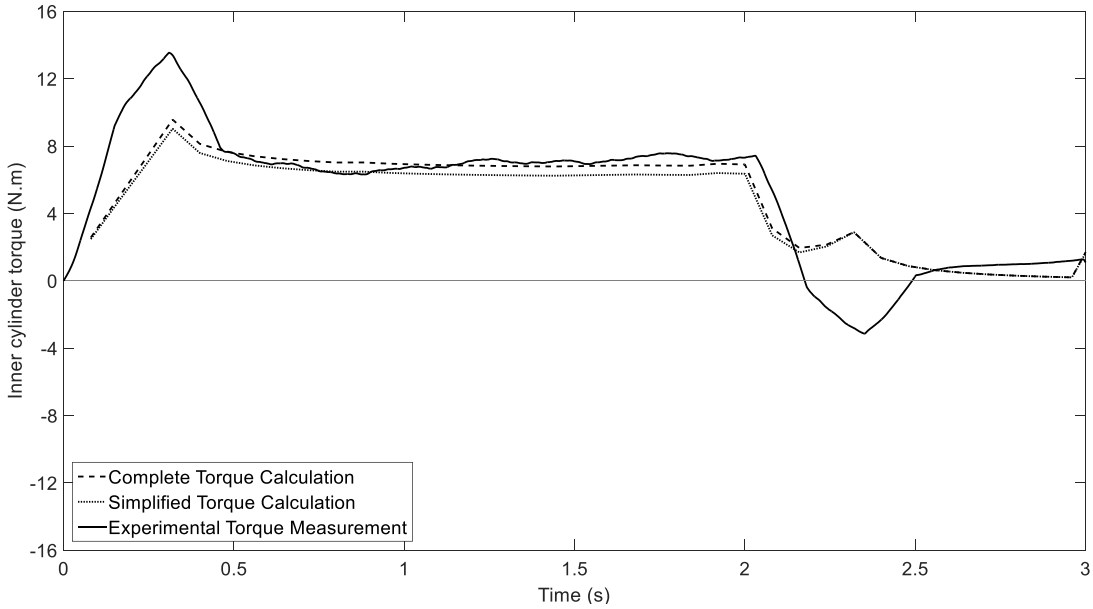

To verify the algorithm consistency for faster responses, 1.25 kg of mixed fabric-water suspension were simulated for Tests 3 and 4. Figure 115 depicts the torque verification for Test 3 and Figure 116 for Test 4. Tests 3 and 4 cycles are half (3 seconds) of the cycle extent of Tests 1 and 2, and the numerical responses for both tests are still in very good agreement with experimental measurements, despite not being able to represent the peaks.

FIGURE 115 - TORQUE VERIFICATION OF TEST 3 NON-ROTATING BASIS SIMULATION FOR 1.25 KG OF MIXED FABRIC-WATER SUSPENSION.

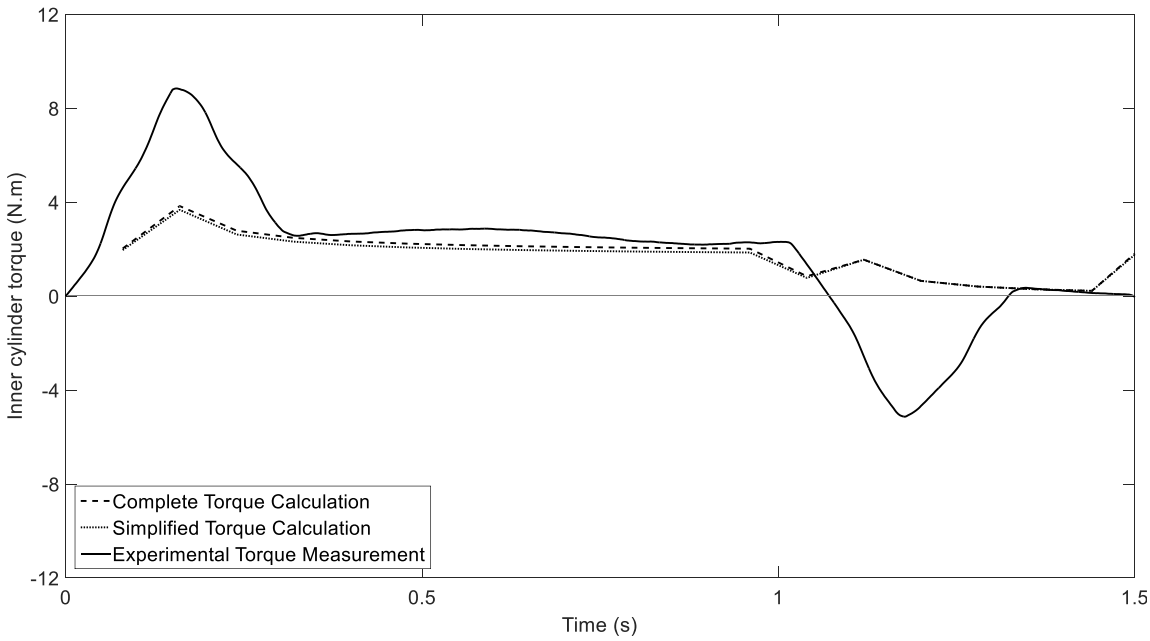

FIGURE 116 - TORQUE VERIFICATION OF TEST 4 NON-ROTATING BASIS SIMULATION FOR 1.25 KG OF MIXED FABRIC-WATER SUSPENSION.

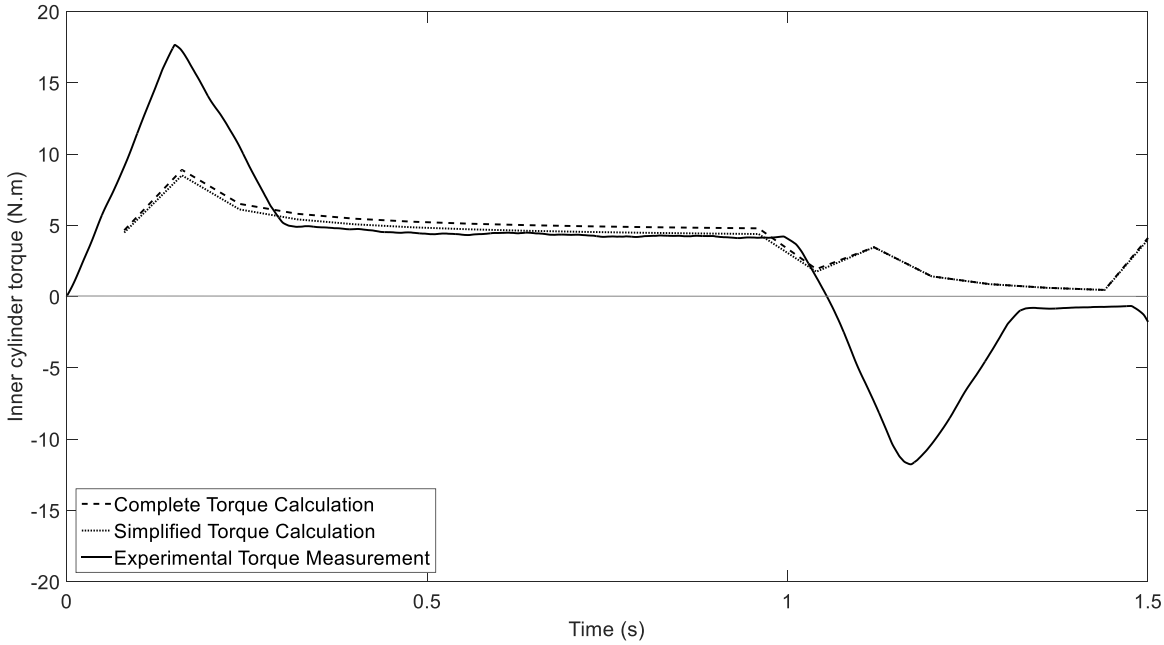

5.3.2 Rotating Bottom Basis Flow Simulations

Previously in Chapter 4, experimental tests concerning a simple arrangement aiming to emulate a top-load washing machine were carried out. Those experimental measurements demonstrated the torque response behavior over time when a rotating bottom basis was put to rotate with the inner cylinder. Nevertheless, the main objective of the simulation results presented below is to illustrate the fluid flow behavior in some critical instants of a washing cycle.

For that reason, the distribution of the tangential velocity (v_θ) and the apparent viscosity (η), as well as the streamlines of the secondary flow (with arrows), are presented for the four tests and the two fluid suspensions (1.25 and 2.50 kg of mixed fabric-water). The critical instants presented on the plots below are, for Tests 1 and 2: (i) 0.32 s, (ii) 2.34 s, (iii) 3.32 s, and (iv) 5.04 s. These times represent, respectively, (i) the instant when the maximum velocity is reached, (ii) when the first deceleration takes place after some time on constant maximum velocity, (iii) when the maximum velocity is reached on contrary direction, and (iv) when the last acceleration of the cycle takes place after some time in constant velocity on contrary direction. While that, for Tests 3 and 4, that were faster cycles, these instants are: (i) 0.16 s, (ii) 1.02 s, (iii) 1.66 s, and (iv) 2.52 s.

All the plots presented are represented in an r-z section for $\theta = 180^{o}$ (π rad). Even though there are flow variations in tangential axis, the differences between angular positions are not important when compared to the radial and axial variations.

Figures 117 to 120 represent the tangential velocity and apparent viscosity distribution, as well as the streamlines of the secondary flow at t = 0.32 s for 1.25 kg of mixed fabric-water suspension on Test 1 (Figure 117), for 2.50 kg of mixed fabric-water suspension on Test 1 (Figure 118), for 1.25 kg of mixed fabric-water suspension on Test 2 (Figure 119) and for 2.50 kg of mixed fabric-water suspension on Test 2 (Figure 120). These graphics represent the instant when the maximum velocity is reached and the torque peak is observed after a swift acceleration. One can see that the distribution of v_θ is quite contrasting with the ones observed in steady-state simulations due to the rotating basis, and the maximum velocity is observed on the corner of the bottom basis with the outer cylinder. The main difference between the tests is the maximum velocity, which is 40-rpm for Test 1 and 80-rpm for Test 2. However, the discrepancy between the velocity distribution across the gap for the two suspensions is almost imperceptible.

The apparent viscosity distribution along the gap is more notable as its changes with the fluid rheological parameters. One can see that for the shear-thickening fluids the maximum viscosity is observed on the place where the shear rate is also maximum and thus the velocity. The heavier suspension presents a wider difference between the maximum and minimum viscosity values, which is enhanced on Test 2 because of the 80-rpm condition. Finally, by observing the streamlines one can note that there is no perceptible discrepancy between them despite some minor changes on the recirculation cell eye position. The main difference is observed when compared with the tests when the bottom basis was static because the recirculation orientation is the opposite. Now, the secondary flow goes upward near the outer cylinder wall and downwards near the inner cylinder wall.

FIGURE 117 - TEST 1 PERIODIC FLOW FOR 1.25 KG OF MIXED FABRIC-WATER SUSPENSION; T = 0.32 S: (A) TANGENTIAL VELOCITY, (B) APPARENT VISCOSITY AND (C) SECONDARY FLOW STREAMLINES.

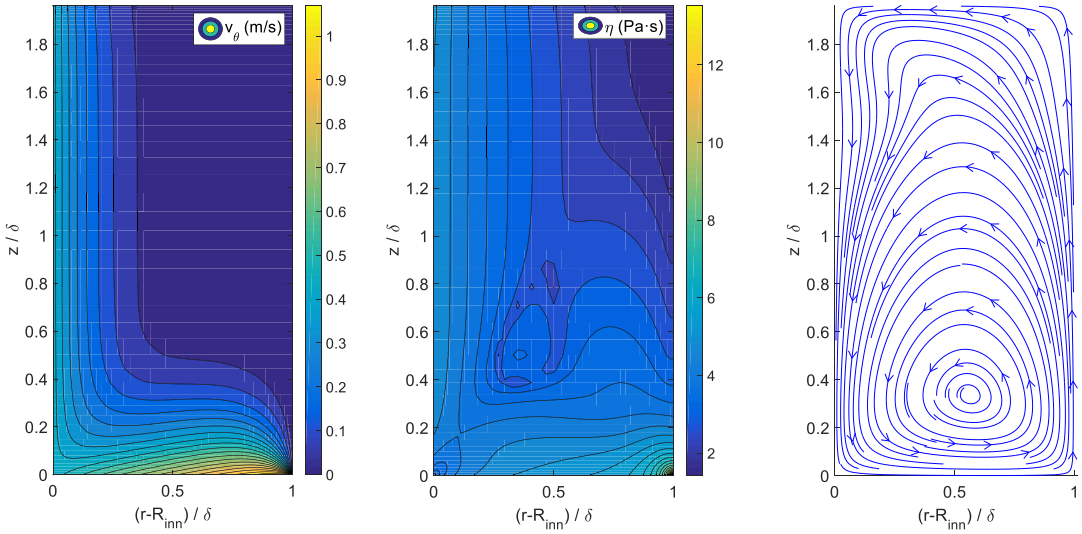

(A) (B) (C)

FIGURE 118 - TEST 1 PERIODIC FLOW FOR 2.50 KG OF MIXED FABRIC-WATER SUSPENSION; T = 0.32 S: (A) TANGENTIAL VELOCITY, (B) APPARENT VISCOSITY AND (C) SECONDARY FLOW STREAMLINES.

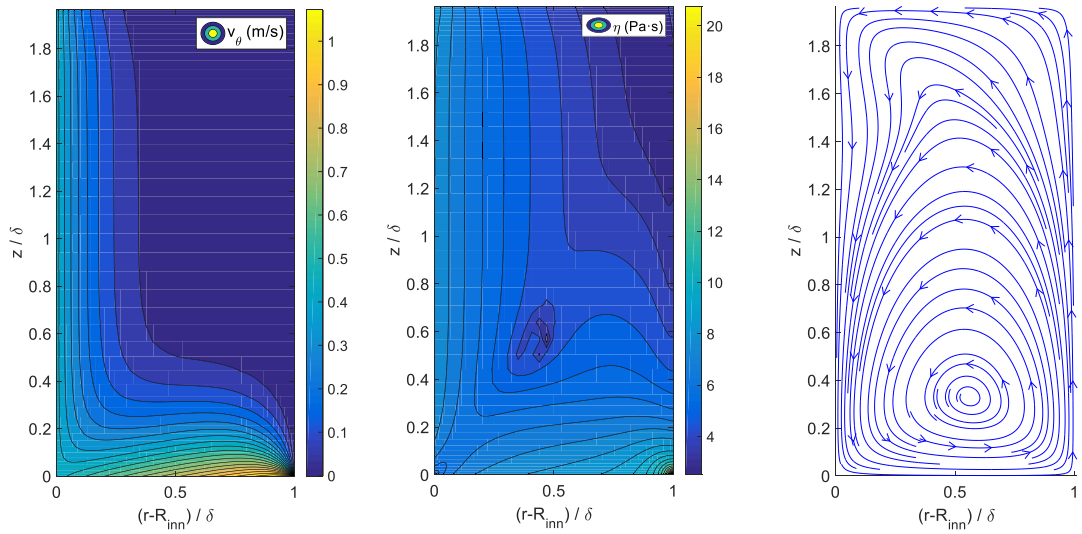

(A) (B) (C)

FIGURE 119 - TEST 2 PERIODIC FLOW FOR 1.25 KG OF MIXED FABRIC-WATER SUSPENSION; T = 0.32 S: (A) TANGENTIAL VELOCITY, (B) APPARENT VISCOSITY AND (C) SECONDARY FLOW STREAMLINES.

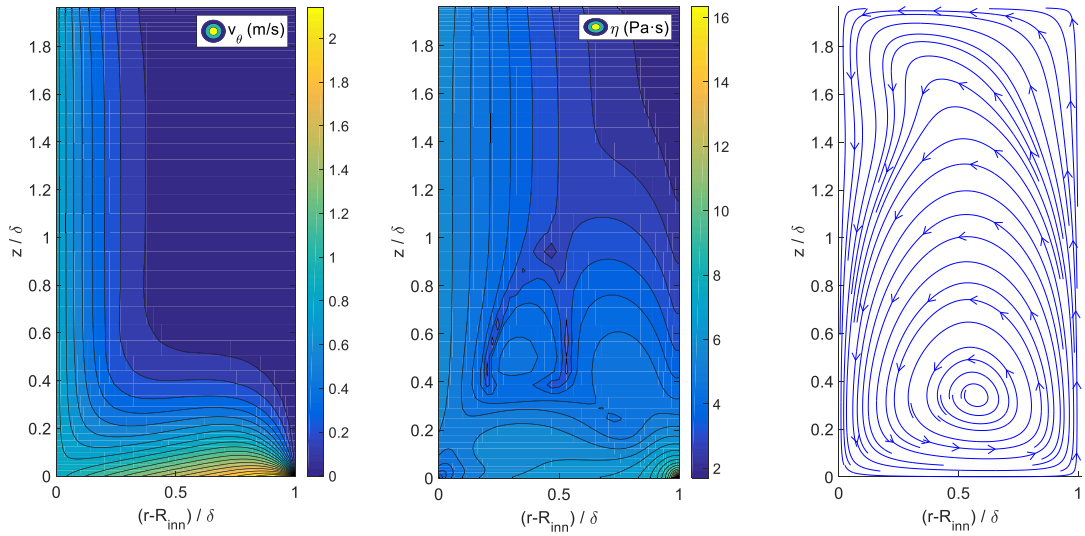

(A) (B) (C)

FIGURE 120 - TEST 2 PERIODIC FLOW FOR 2.50 KG OF MIXED FABRIC-WATER SUSPENSION; T = 0.32 S: (A) TANGENTIAL VELOCITY, (B) APPARENT VISCOSITY AND (C) SECONDARY FLOW STREAMLINES.

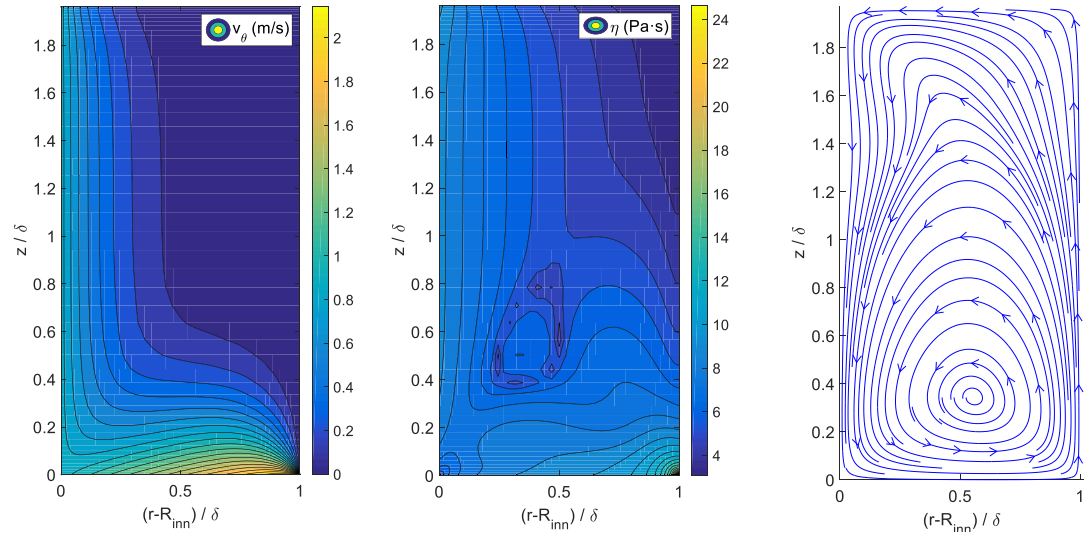

(A) (B) (C)

Subsequently, the distribution of the tangential velocity (v_θ), apparent viscosity (η) and the streamlines of the secondary flow at t = 2.04 s. Figure 121 represents the flow of 1.25 kg of mixed fabric-water suspension on Test 1, Figure 122 represents the heavier suspension also on Test 1, Figure 123 depicts the flow of 1.25 kg of mixed fabric-water suspension on Test 2 and Figure 124 depicts the heavier fluid on Test 2. One can see that after 1.72 seconds of constant velocity of the inner cylinder, the distribution of the tangential velocity across the gap has

spread even more; however, it has not reached the steady-state regime yet. This distribution is more apparent for Test 2 because of the faster-imposed velocity into the flow. The viscosity distribution changed according to the change on velocity fields, as one can see on the graphics. Finally, the streamlines denote a small change of orientation between the fluids and the tests when compared to the previous moment, but the secondary flow magnitude is greater.

FIGURE 121 - TEST 1 PERIODIC FLOW FOR 1.25 KG OF MIXED FABRIC-WATER SUSPENSION; T = 2.04 S: (A) TANGENTIAL VELOCITY, (B) APPARENT VISCOSITY AND (C) SECONDARY FLOW STREAMLINES.

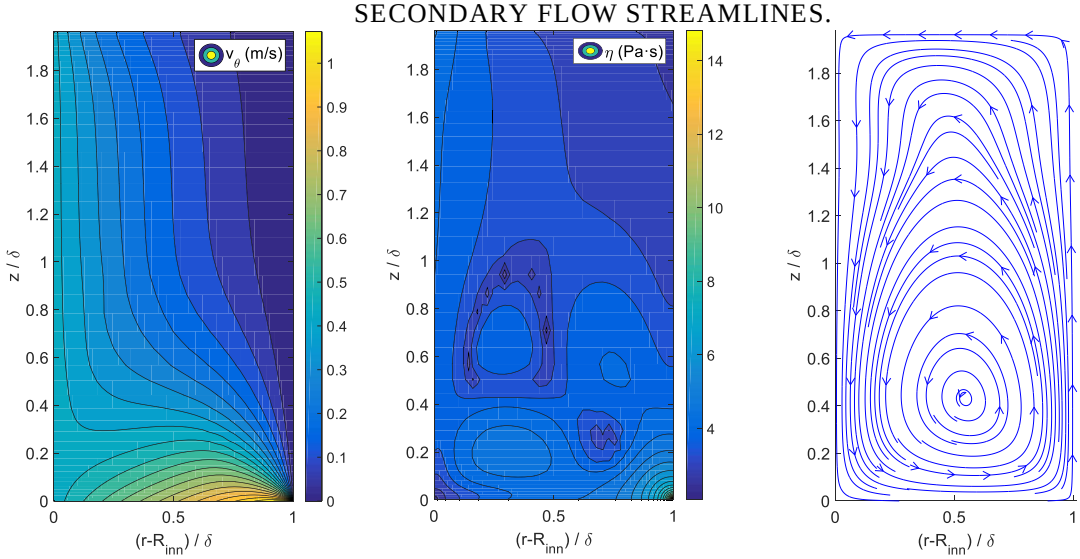

(A) (B) (C)

FIGURE 122 - TEST 1 PERIODIC FLOW FOR 2.50 KG OF MIXED FABRIC-WATER SUSPENSION; T = 2.04 S: (A) TANGENTIAL VELOCITY, (B) APPARENT VISCOSITY AND (C) SECONDARY FLOW STREAMLINES.

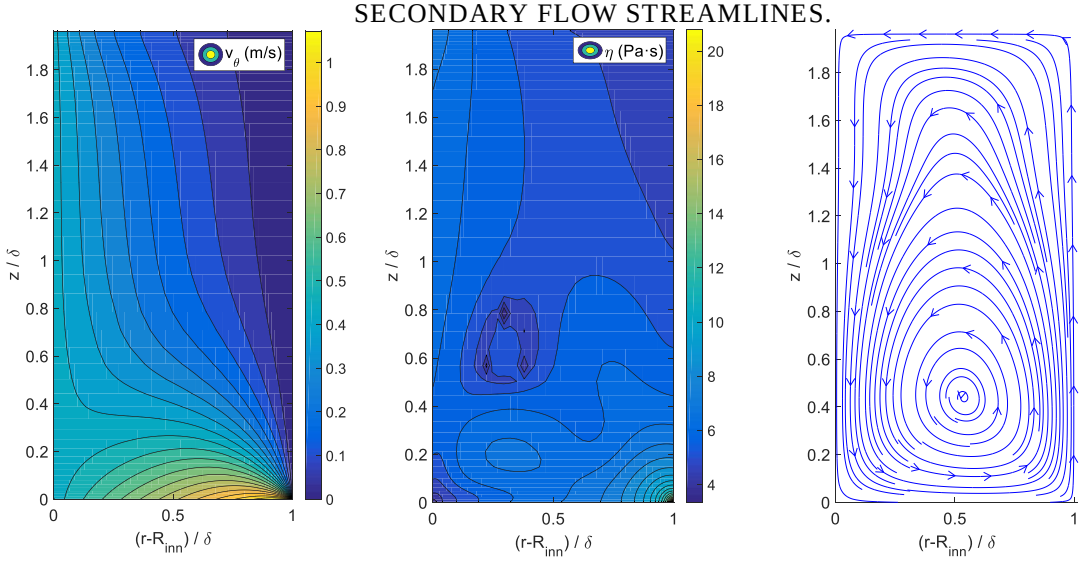

(A) (B) (C)

FIGURE 123 - TEST 2 PERIODIC FLOW FOR 1.25 KG OF MIXED FABRIC-WATER SUSPENSION; T = 2.04 S: (A) TANGENTIAL VELOCITY, (B) APPARENT VISCOSITY AND (C) SECONDARY FLOW STREAMLINES.

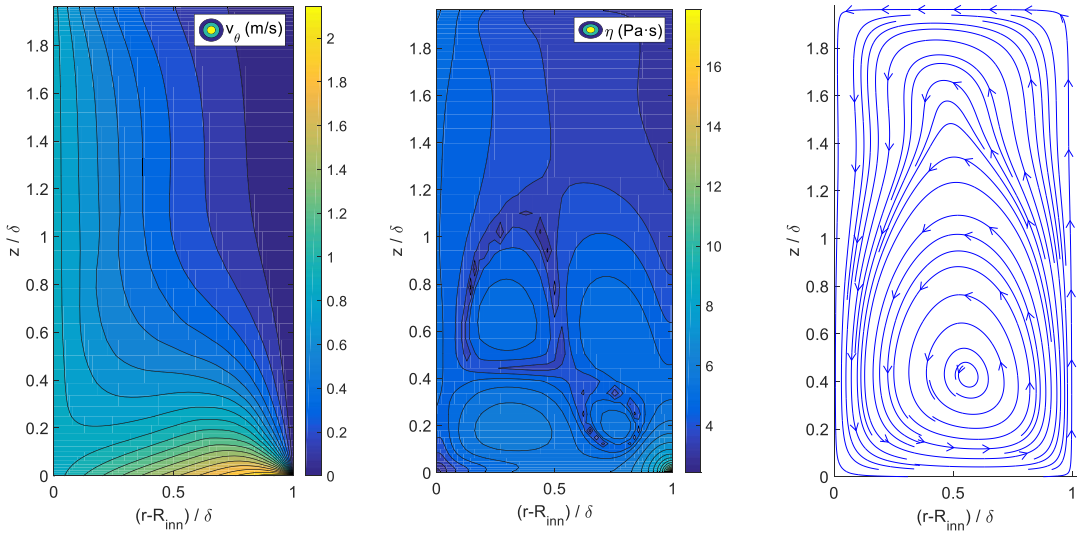

(A) (B) (C)

FIGURE 124 - TEST 2 PERIODIC FLOW FOR 2.50 KG OF MIXED FABRIC-WATER SUSPENSION; T = 2.04 S: (A) TANGENTIAL VELOCITY, (B) APPARENT VISCOSITY AND (C) SECONDARY FLOW STREAMLINES.

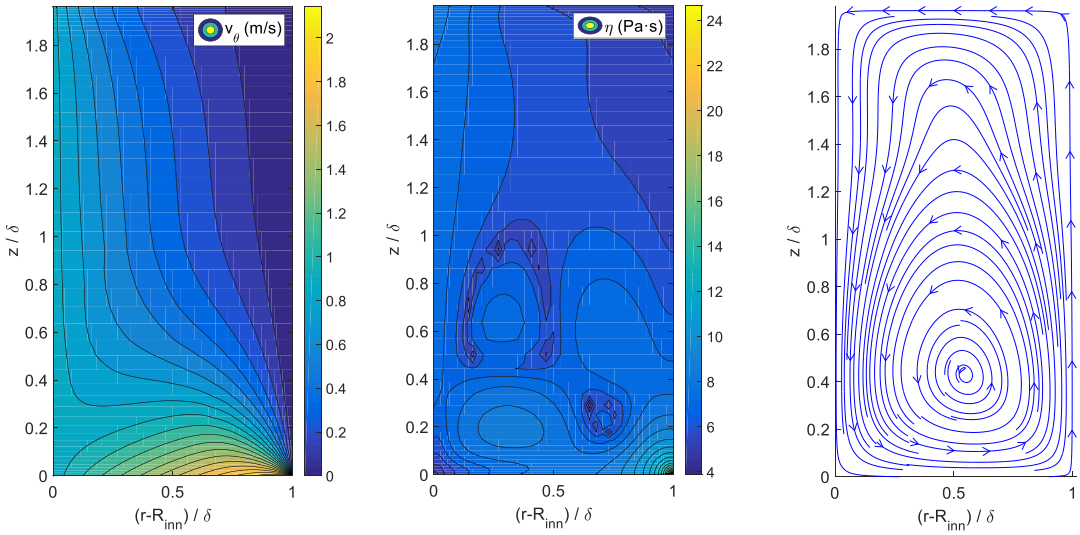

(A) (B) (C)

Then, for t = 3.32 seconds, the graphics concerning the variation of tangential velocity, apparent viscosity, and streamlines on the r-z section plane (θ = 180°) are depicted below from Figure 125 to Figure 128 with the same sequence of fluid suspensions and tests made previously. This time is related to the moment where the maximum velocity is reached in the contrary direction, after periods of deceleration and time-off period. Compared to the first acceleration period, when the fluid was static at the beginning, in this case when the fluid

experiences this acceleration on contrary velocity the fluid flow was still rotating in the previous direction, thus requiring a higher torque from the inner cylinder to the fluids for inverting rotation direction. It was also perceived on the experimental measurements that second torque peak magnitude was greater than the first one. For that reason, one can see on the graphics below that the maximum velocity modules are higher than the ones for t = 0.32 s. The distribution of the plots below is similar to the ones observed before. For the apparent viscosity, its values are similar when compared to the flow on contrary direction with some minor differences because of the relevance of other shear rates components due to the variations in velocity. Finally, there are no changes in the direction of the recirculation cells but some minor variation on the position of the recirculation eye.

FIGURE 125 - TEST 1 PERIODIC FLOW FOR 1.25 KG OF MIXED FABRIC-WATER SUSPENSION; T = 3.32 S: (A) TANGENTIAL VELOCITY, (B) APPARENT VISCOSITY AND (C) SECONDARY FLOW STREAMLINES.

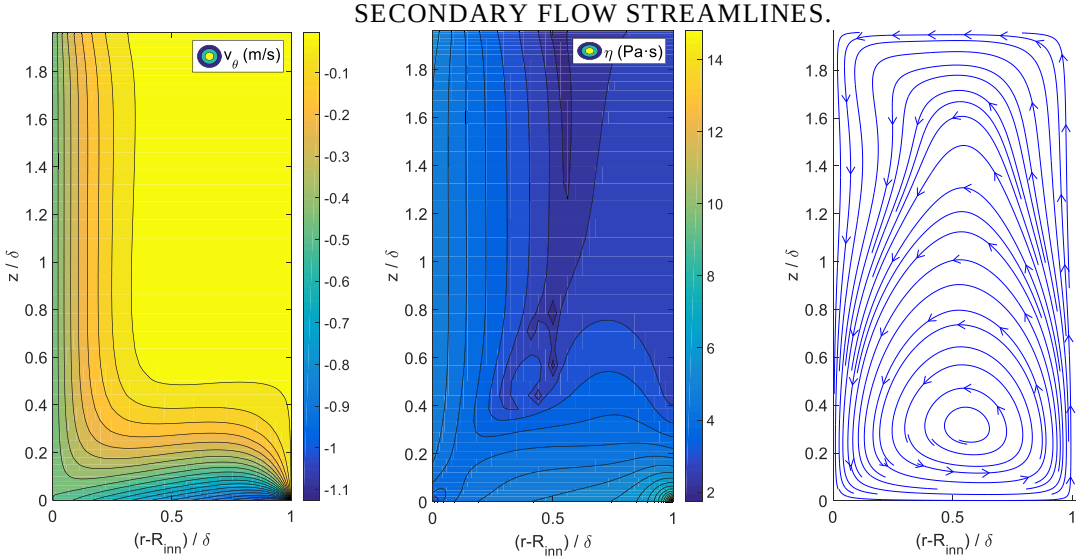

(A) (B) (C)

FIGURE 126 - TEST 1 PERIODIC FLOW FOR 2.50 KG OF MIXED FABRIC-WATER SUSPENSION; T = 3.32 S: (A) TANGENTIAL VELOCITY, (B) APPARENT VISCOSITY AND (C) SECONDARY FLOW STREAMLINES.

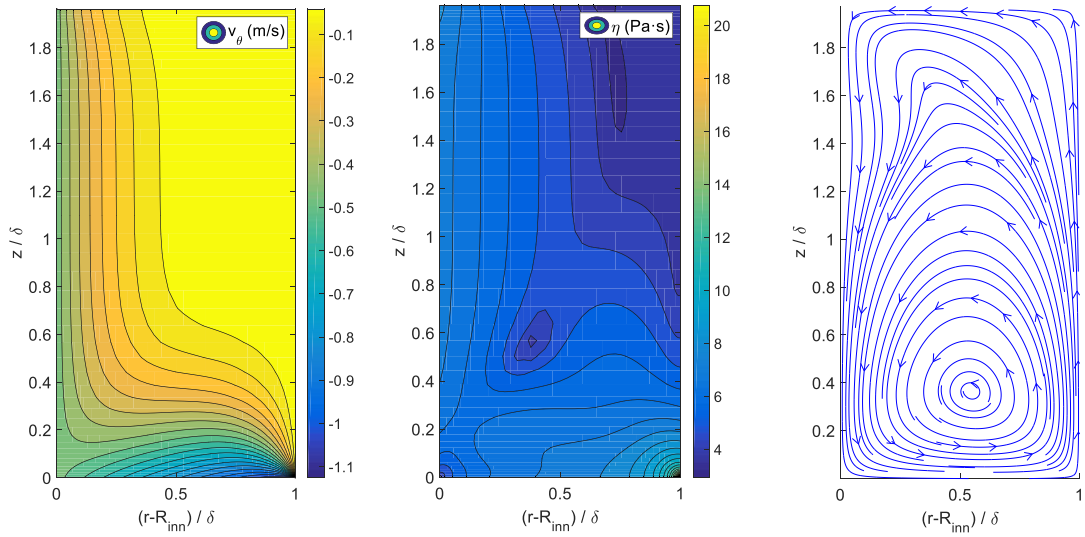

(A) (B) (C)

FIGURE 127 - TEST 2 PERIODIC FLOW FOR 1.25 KG OF MIXED FABRIC-WATER SUSPENSION; T = 3.32 S: (A) TANGENTIAL VELOCITY, (B) APPARENT VISCOSITY AND (C) SECONDARY FLOW STREAMLINES.

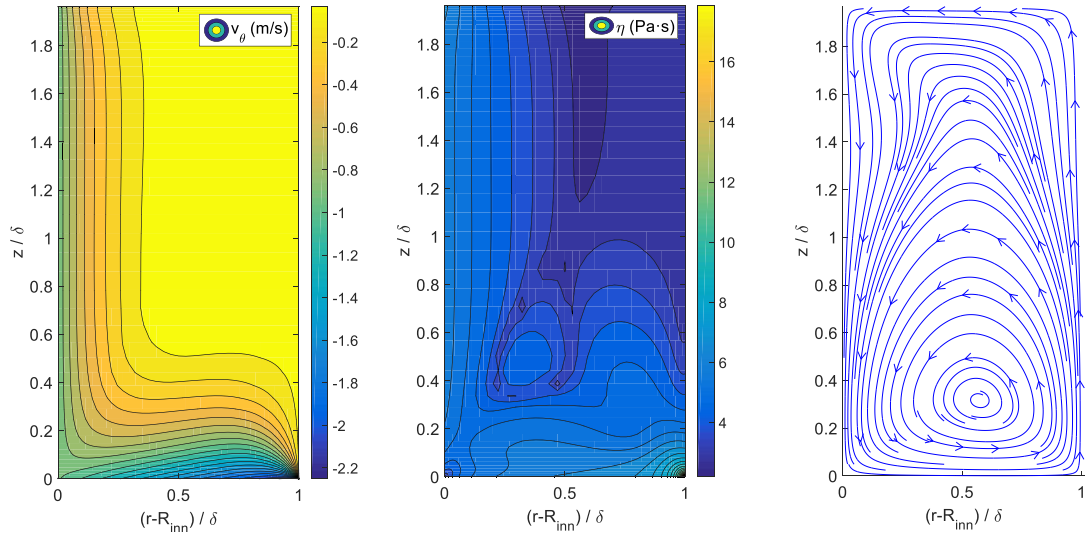

(A) (B) (C)

FIGURE 128 - TEST 2 PERIODIC FLOW FOR 2.50 KG OF MIXED FABRIC-WATER SUSPENSION; T = 3.32 S: (A) TANGENTIAL VELOCITY, (B) APPARENT VISCOSITY AND (C) SECONDARY FLOW STREAMLINES.

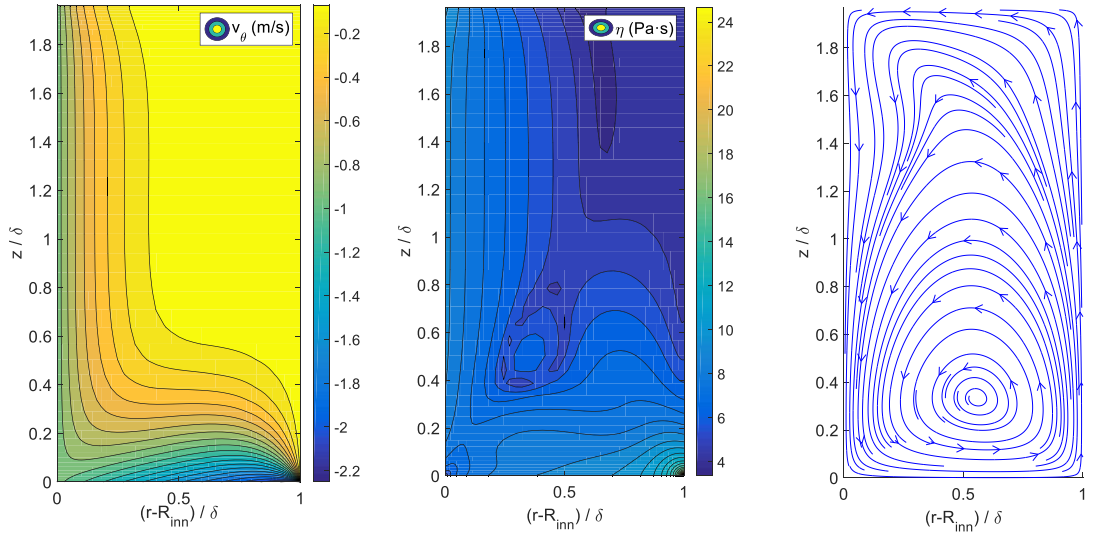

(A) (B) (C)

Finally, for t = 5.04 seconds, the following graphics depicts the distribution of the tangential velocity and the apparent viscosity as well as the streamlines of the secondary flow. The plots are represented from Figure 129 to Figure 132 with the same organization of fluid suspensions and tests made previously. At this instant, this tangential velocity is more spread across the gap, similar to the distribution at t = 2.04 s. The viscosity also has changed and is more spread, as well as the streamlines.

FIGURE 129 - TEST 1 PERIODIC FLOW FOR 1.25 KG OF MIXED FABRIC-WATER SUSPENSION; T = 5.04 S: (A) TANGENTIAL VELOCITY, (B) APPARENT VISCOSITY AND (C) SECONDARY FLOW STREAMLINES.

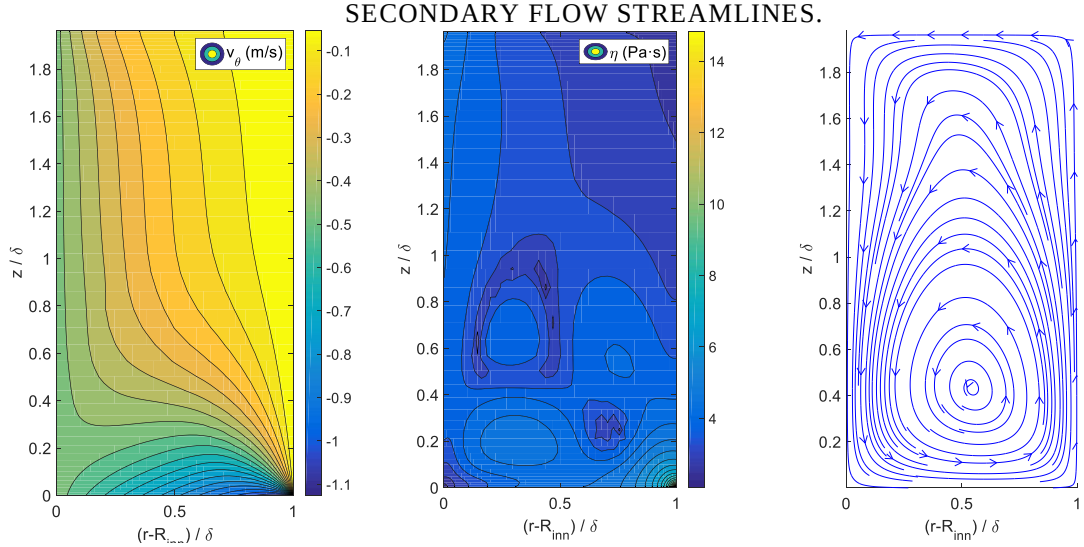

(A) (B) (C)

FIGURE 130 - TEST 1 PERIODIC FLOW FOR 2.50 KG OF MIXED FABRIC-WATER SUSPENSION; T = 5.04 S: (A) TANGENTIAL VELOCITY, (B) APPARENT VISCOSITY AND (C) SECONDARY FLOW STREAMLINES.

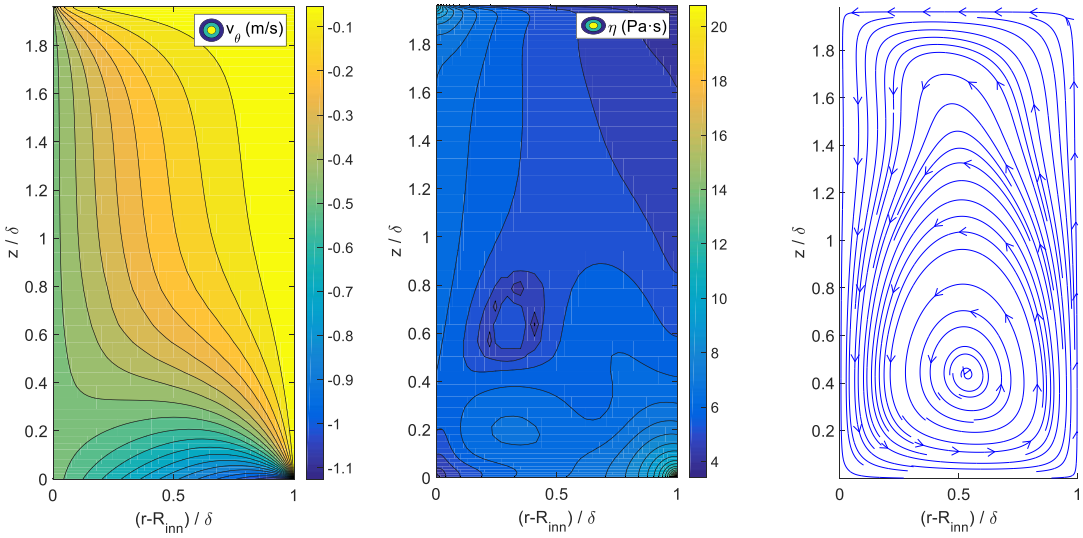

(A) (B) (C)

FIGURE 131 - TEST 2 PERIODIC FLOW FOR 1.25 KG OF MIXED FABRIC-WATER SUSPENSION; T = 5.04 S: (A) TANGENTIAL VELOCITY, (B) APPARENT VISCOSITY AND (C) SECONDARY FLOW STREAMLINES.

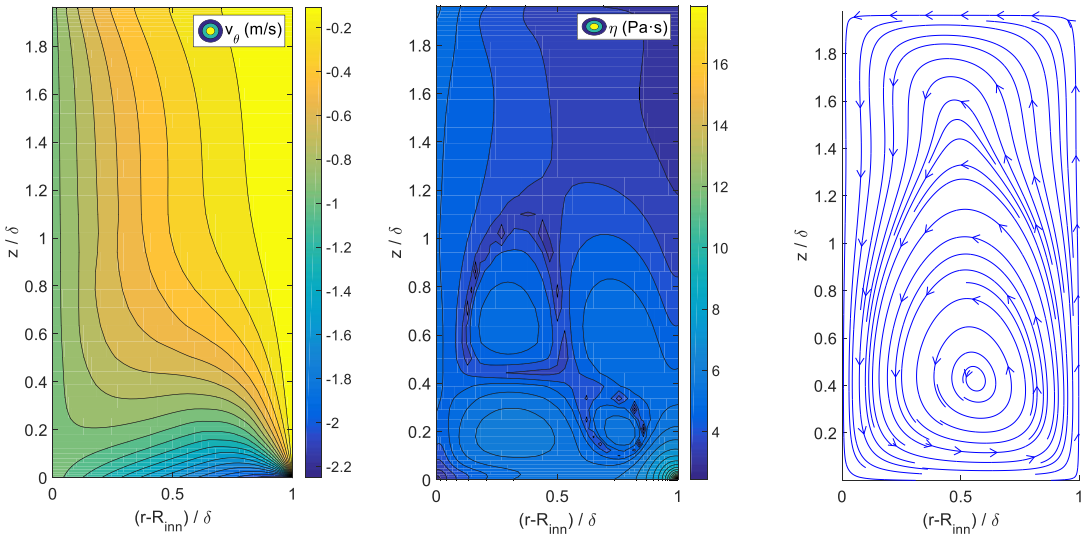

(A) (B) (C)

FIGURE 132 - TEST 2 PERIODIC FLOW FOR 2.50 KG OF MIXED FABRIC-WATER SUSPENSION; T = 5.04 S: (A) TANGENTIAL VELOCITY, (B) APPARENT VISCOSITY AND (C) SECONDARY FLOW STREAMLINES.

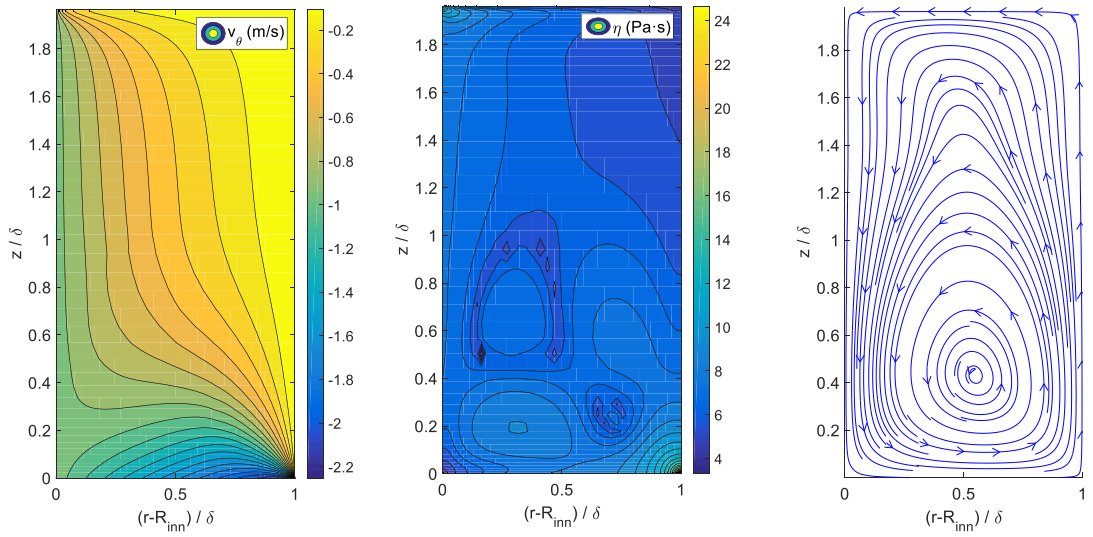

(A) (B) (C)

In addition, the graphics concerning the Tests 3 and 4 are presented below. For Tests 3 and 4 all the times (acceleration, deceleration, time on and time off) are cutted in half. Thus, it is expected that swifter accelerations and decelerations result in more torque transmitted to the fluid flow and that shorter time-spans in constant velocities result in a fluid flow more distant to the steady-state flow regime.

Figures 133 to 136 represent the tangential velocity and the apparent viscosity distribution, as well as the streamlines of the secondary flows at t = 0.16 s for the lighter fluid suspension (1.25 kg of mixed fabric-water fluid suspension) and the heavier suspension (2.50 kg of the same fabrics) concerning the Tests 3 and 4. Comparing the v_θ distribution across the gap with the ones for Tests 1 and 2, one can see that velocity spread across the gap is less intense than for the previous tests, as the isolines are much closer to the location of maximum velocity. It occurs because of the shorter time of acceleration.

Moreover, because of this swifter acceleration, the viscosities distribution is also different from the previous tests, as the difference between maximum and minimum velocities are tighter, as well as the isolines distribution. Finally, the streamlines show that the organization of the secondary flow has not changed at all, but the magnitude of the secondary flow is lower than the previous tests ones.

FIGURE 133 - TEST 3 PERIODIC FLOW FOR 1.25 KG OF MIXED FABRIC-WATER SUSPENSION; T = 0.16 S: (A) TANGENTIAL VELOCITY, (B) APPARENT VISCOSITY AND (C) SECONDARY FLOW STREAMLINES.

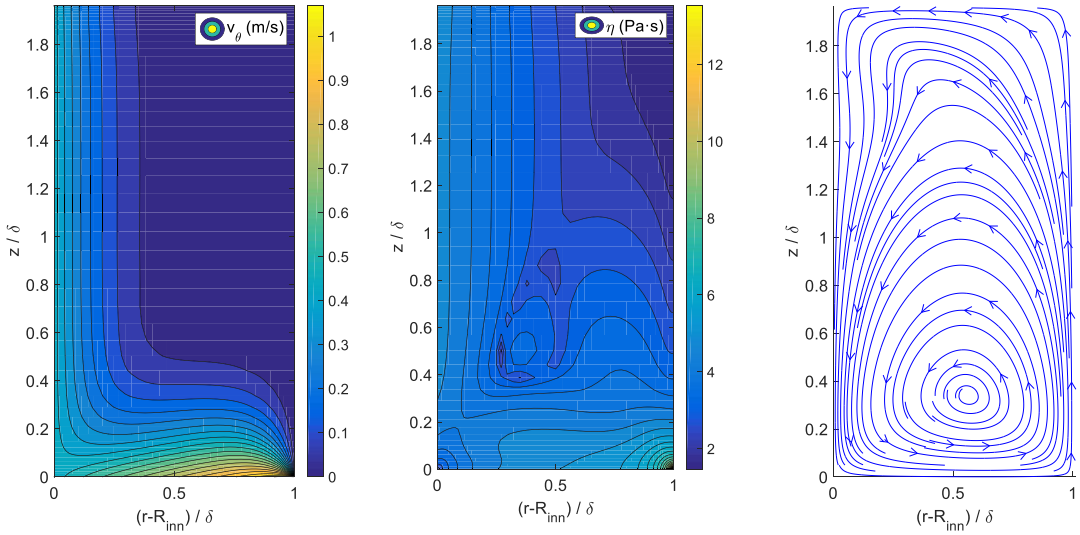

(A) (B) (C)

FIGURE 134 - TEST 3 PERIODIC FLOW FOR 2.50 KG OF MIXED FABRIC-WATER SUSPENSION; T = 0.16 S: (A) TANGENTIAL VELOCITY, (B) APPARENT VISCOSITY AND (C) SECONDARY FLOW STREAMLINES.

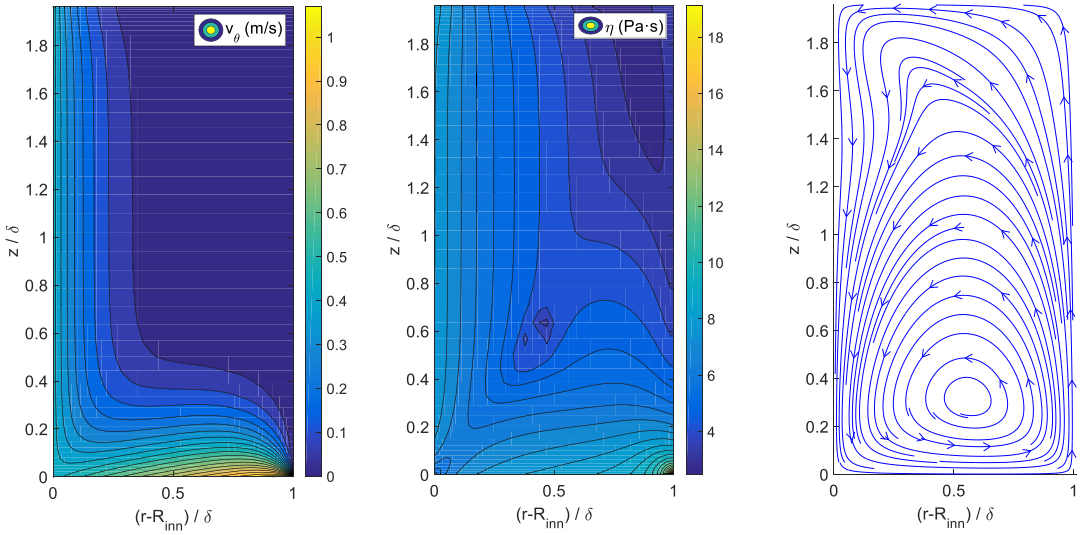

(A) (B) (C)

FIGURE 135 - TEST 4 PERIODIC FLOW FOR 1.25 KG OF MIXED FABRIC-WATER SUSPENSION; T = 0.16 S: (A) TANGENTIAL VELOCITY, (B) APPARENT VISCOSITY AND (C) SECONDARY FLOW STREAMLINES.

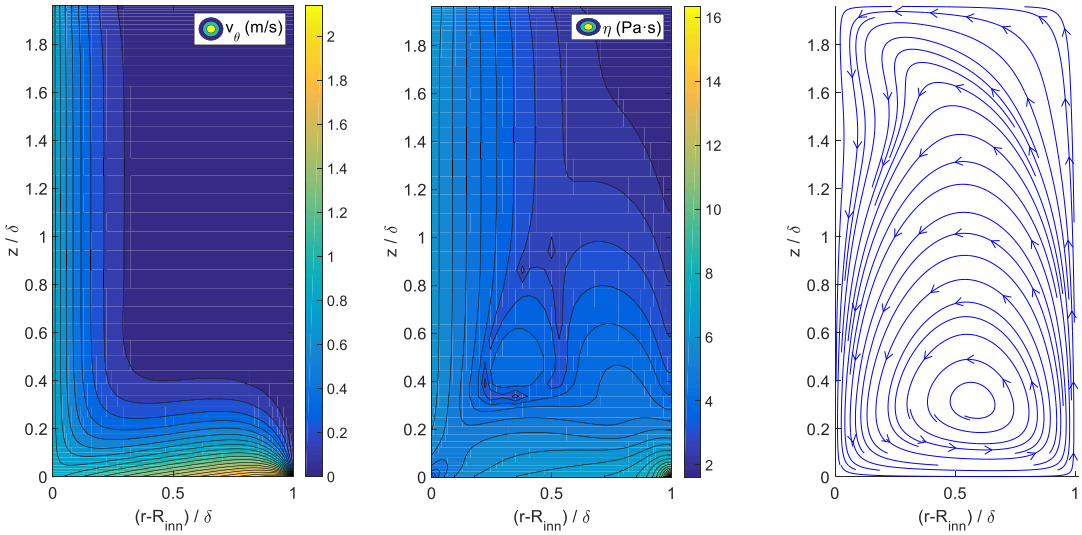

(A) (B) (C)

FIGURE 136 - TEST 4 PERIODIC FLOW FOR 2.50 KG OF MIXED FABRIC-WATER SUSPENSION; T = 0.16 S: (A) TANGENTIAL VELOCITY, (B) APPARENT VISCOSITY AND (C) SECONDARY FLOW STREAMLINES.

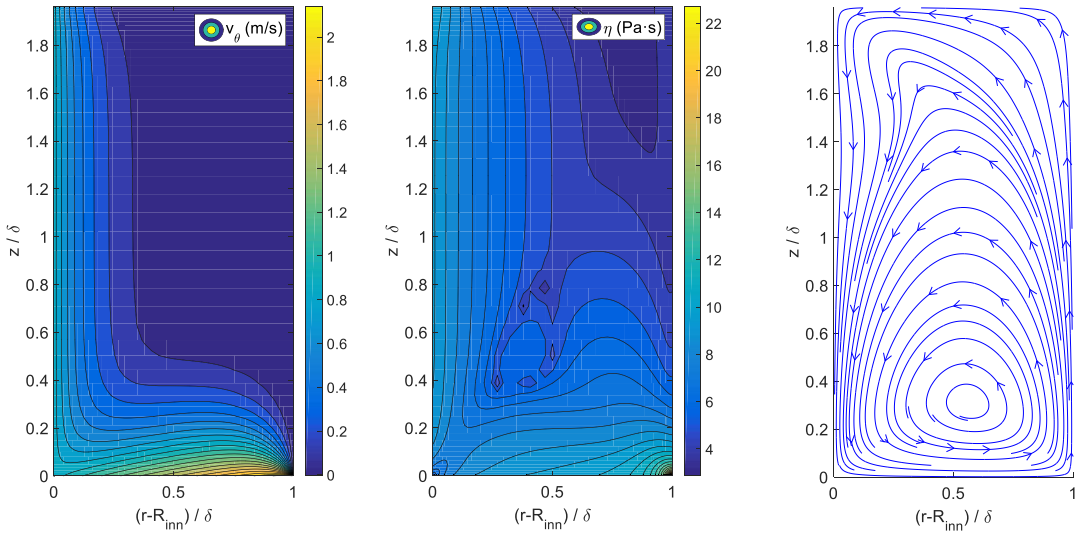

(A) (B) (C)

Subsequently, the distribution of the tangential velocity (v_θ), apparent viscosity (η) and the streamlines of the secondary flow at t = 1.02 s for Tests 3 and 4 are plotted. Figure 137 represents the flow of 1.25 kg of mixed fabric-water suspension on Test 3, Figure 138 represents the heavier suspension also on Test 3. Similarly, Figures 139 and 140 represents the same fluid suspensions for Test 4. At this instant, the velocity of the inner cylinder was maintained constant for 0.86 s, which can be seen on the plots below as the velocity field has spread across the gap,

thus changing the viscosity distribution as well. Because of the shorter period on maximum velocity, the fluid flows are even more distant from the conditions found in steady-state flow regimes. It can be seen, when compared to the plots of Tests 1 and 2, where the velocity field is more distributed, that the both velocities and viscosities are less scattered across the gap. Moreover, streamlines at this moment appear to be more uniform than the previous moment.

FIGURE 137 - TEST 3 PERIODIC FLOW FOR 1.25 KG OF MIXED FABRIC-WATER SUSPENSION; T = 1.02 S: (A) TANGENTIAL VELOCITY, (B) APPARENT VISCOSITY AND (C) SECONDARY FLOW STREAMLINES.

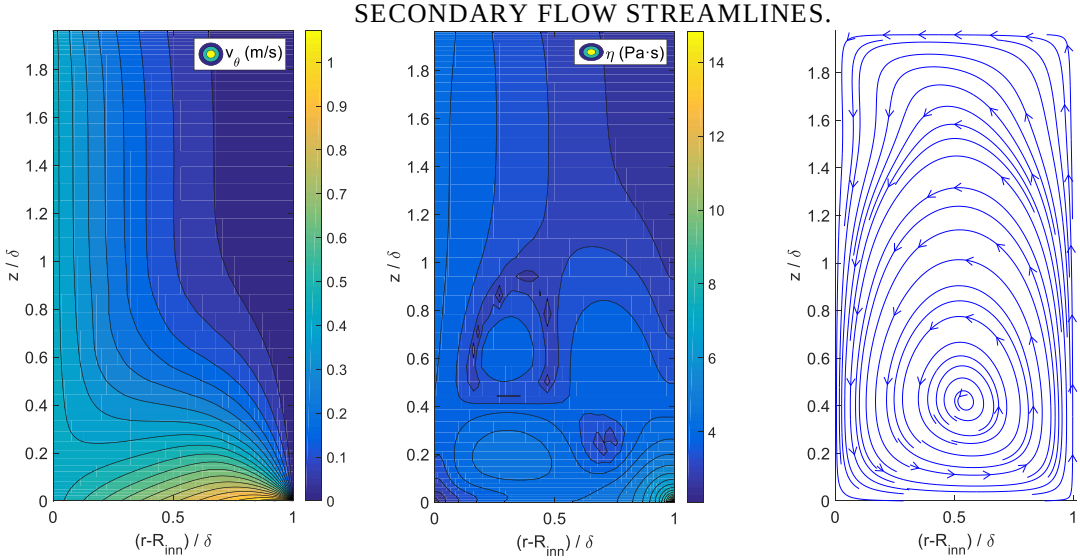

(A) (B) (C)

FIGURE 138 - TEST 3 PERIODIC FLOW FOR 2.50 KG OF MIXED FABRIC-WATER SUSPENSION; T = 1.02 S: (A) TANGENTIAL VELOCITY, (B) APPARENT VISCOSITY AND (C) SECONDARY FLOW STREAMLINES.

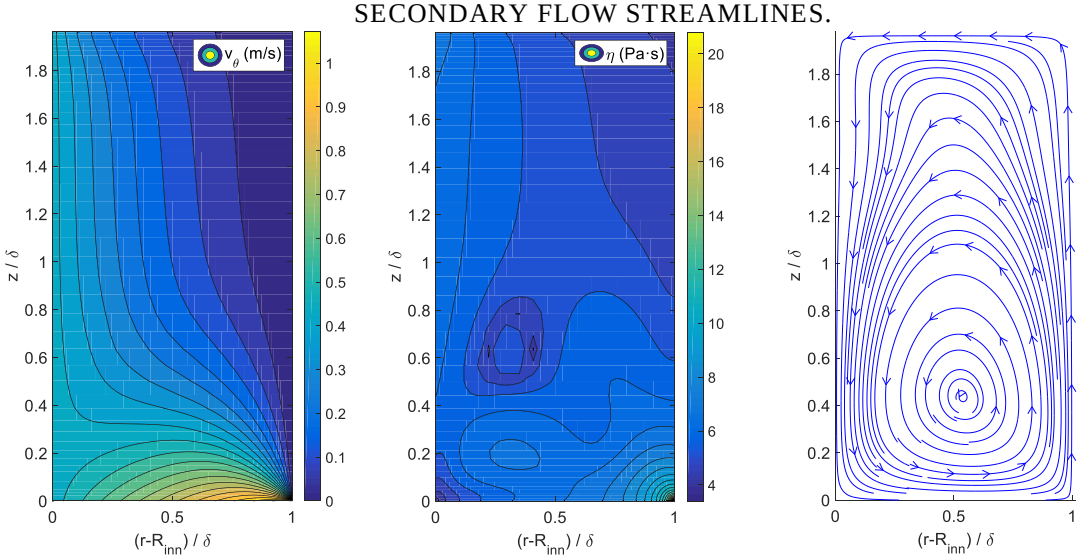

(A) (B) (C)

FIGURE 139 - TEST 4 PERIODIC FLOW FOR 1.25 KG OF MIXED FABRIC-WATER SUSPENSION; T = 1.02 S: (A) TANGENTIAL VELOCITY, (B) APPARENT VISCOSITY AND (C) SECONDARY FLOW STREAMLINES.

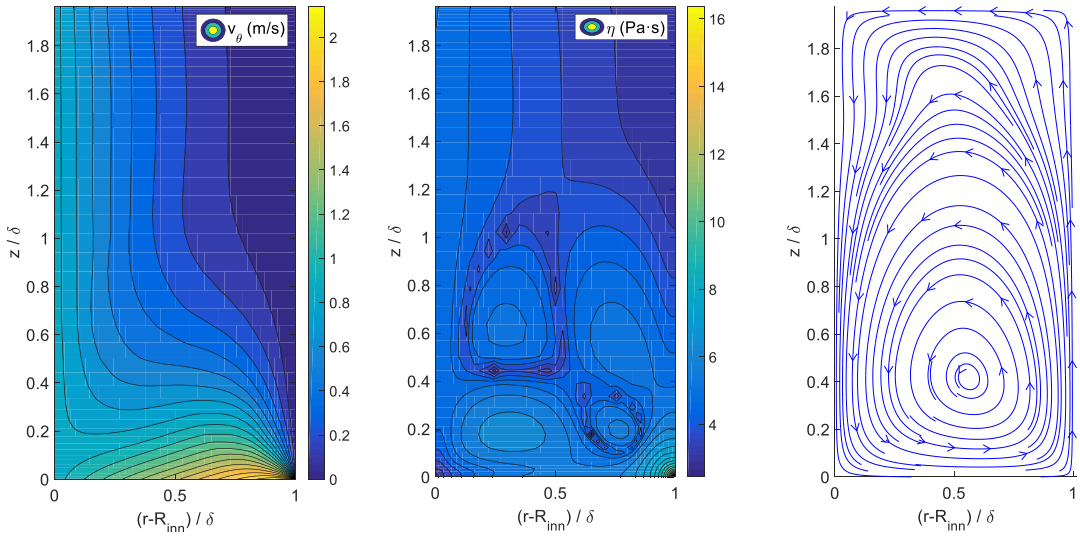

(A) (B) (C)

FIGURE 140 - TEST 4 PERIODIC FLOW FOR 2.50 KG OF MIXED FABRIC-WATER SUSPENSION; T = 1.02 S: (A) TANGENTIAL VELOCITY, (B) APPARENT VISCOSITY AND (C) SECONDARY FLOW STREAMLINES.

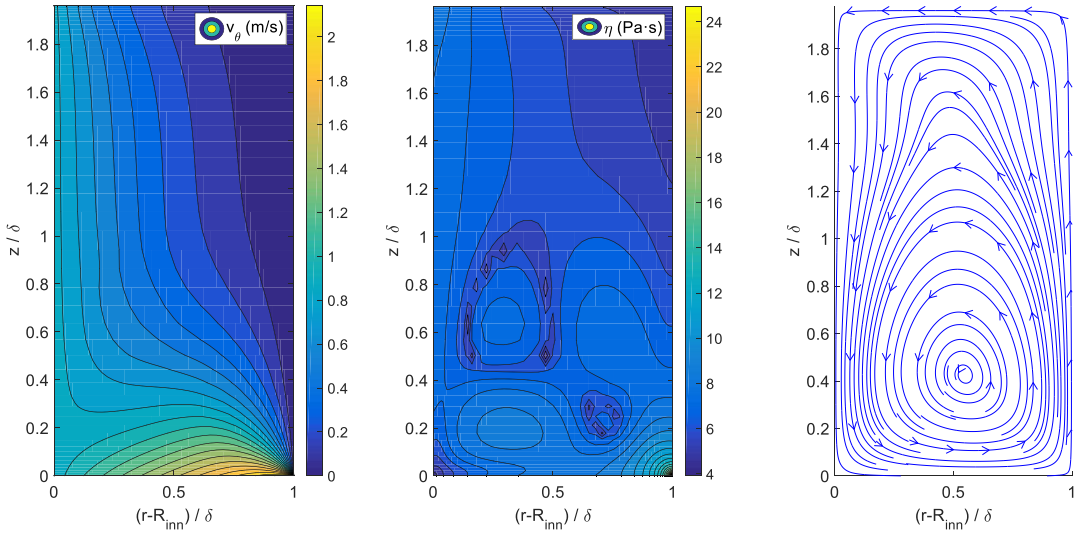

(A) (B) (C)

Yet, for t = 1.66 seconds, the plots concerning the distribution of the tangential velocity and the apparent viscosity, as well as the streamlines are depicted on Figures 141 to 144.

At this instant, the principal differences between the faster cycles and the slower cycles can be noticed easily. The analysis of the tangential velocities plots shows that there are still some portions of the flow with contrary velocity orientation, which denotes that the fluid flow is far from the ones observed in Tests 1 and 2 and that it is more unstable. It can be observed

that the viscosity variation is more concentrated near the inner wall and bottom basis corner, and the streamlines demonstrate an unstable recirculation cell near the open surface.

FIGURE 141 - TEST 3 PERIODIC FLOW FOR 1.25 KG OF MIXED FABRIC-WATER SUSPENSION; T = 1.66 S: (A) TANGENTIAL VELOCITY, (B) APPARENT VISCOSITY AND (C) SECONDARY FLOW STREAMLINES.

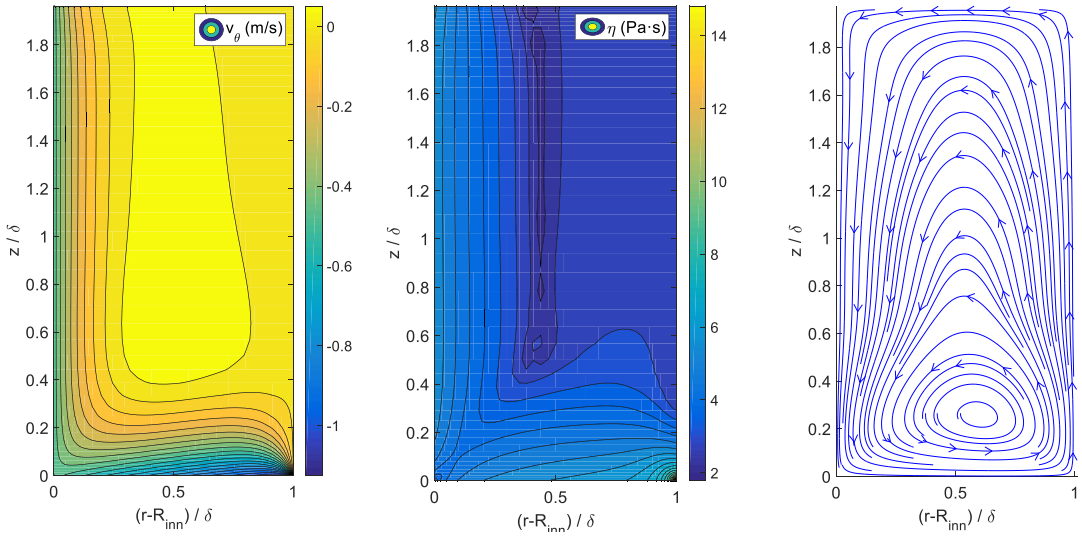

(A) (B) (C)

FIGURE 142 - TEST 3 PERIODIC FLOW FOR 2.50 KG OF MIXED FABRIC-WATER SUSPENSION; T = 1.66 S: (A) TANGENTIAL VELOCITY, (B) APPARENT VISCOSITY AND (C) SECONDARY FLOW STREAMLINES.

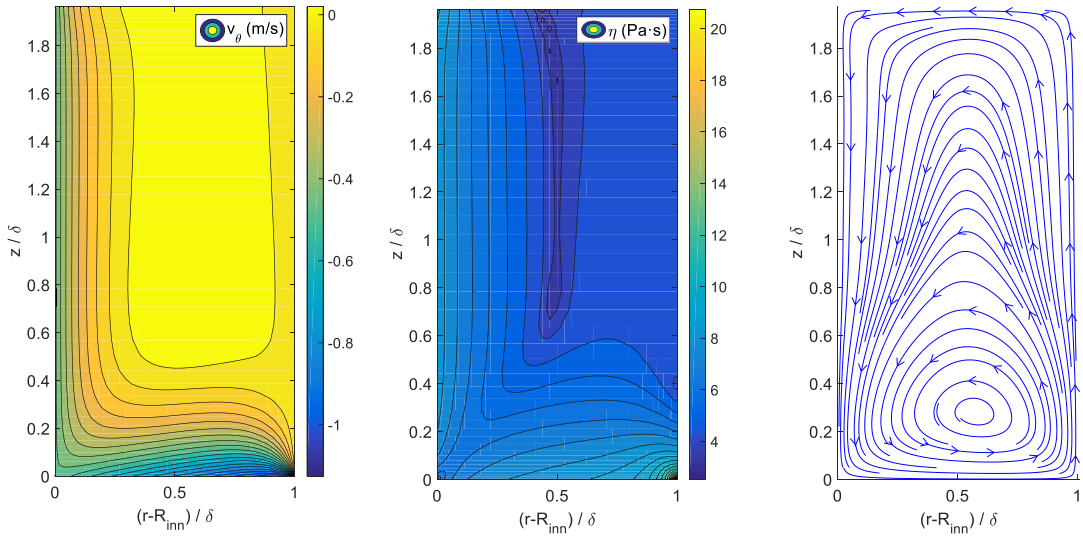

(A) (B) (C)

FIGURE 143 - TEST 4 PERIODIC FLOW FOR 1.25 KG OF MIXED FABRIC-WATER SUSPENSION; T = 1.66 S: (A) TANGENTIAL VELOCITY, (B) APPARENT VISCOSITY AND (C) SECONDARY FLOW STREAMLINES.

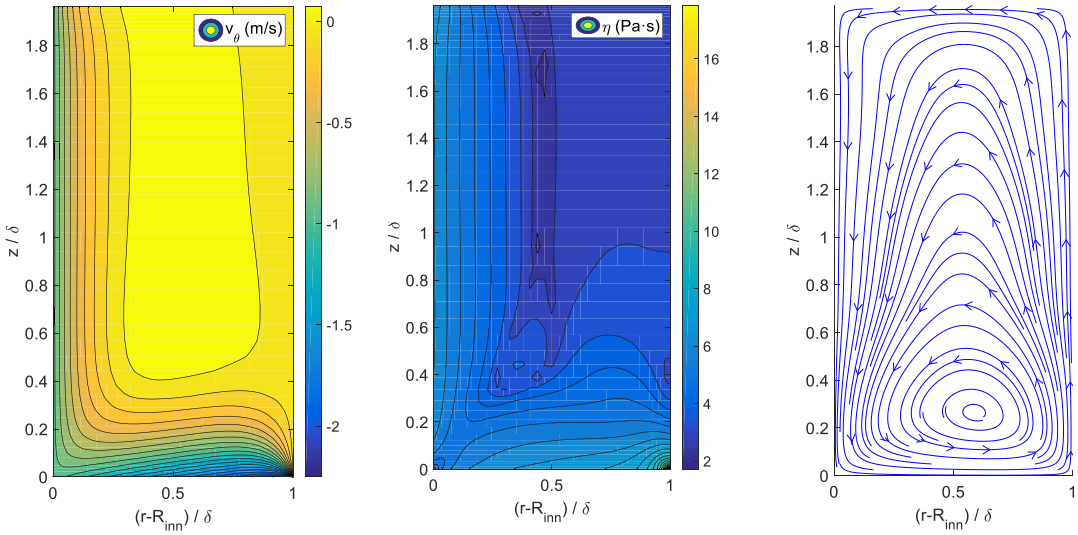

(A) (B) (C)

FIGURE 144 - TEST 4 PERIODIC FLOW FOR 2.50 KG OF MIXED FABRIC-WATER SUSPENSION; T = 1.66 S: (A) TANGENTIAL VELOCITY, (B) APPARENT VISCOSITY AND (C) SECONDARY FLOW STREAMLINES.

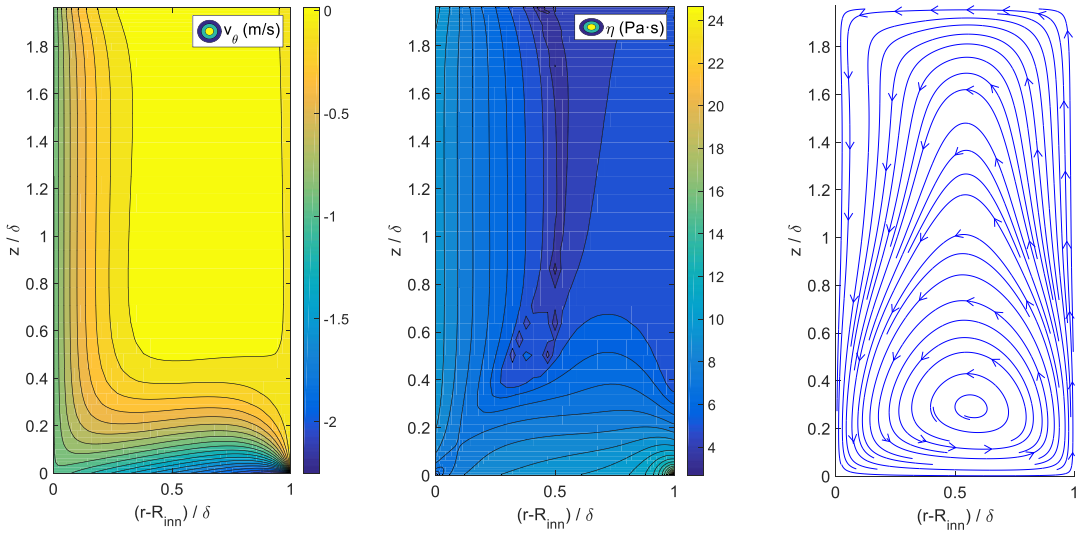

(A) (B) (C)

Finally, for t = 2.52 s, the following plots depict the distribution of the tangential velocity and the apparent viscosity, as well as the streamlines of the secondary flow. The plots are represented from Figure 145 to Figure 148 for the different mixed fabric amounts and Tests (3 and 4).

At this instant, the tangential velocity across the gap is in the same direction as the inner cylinder and the velocity distribution is more distributed because a 0.86 s period has passed by

with constant velocity. Also, the viscosity distribution has changed and it is more similar to the one observed at t = 1.02 s. The streamlines also demonstrate that the secondary flow is more uniformly distributed across the gap than before.

FIGURE 145 - TEST 3 PERIODIC FLOW FOR 1.25 KG OF MIXED FABRIC-WATER SUSPENSION; T = 2.52 S: (A) TANGENTIAL VELOCITY, (B) APPARENT VISCOSITY AND (C) SECONDARY FLOW STREAMLINES.

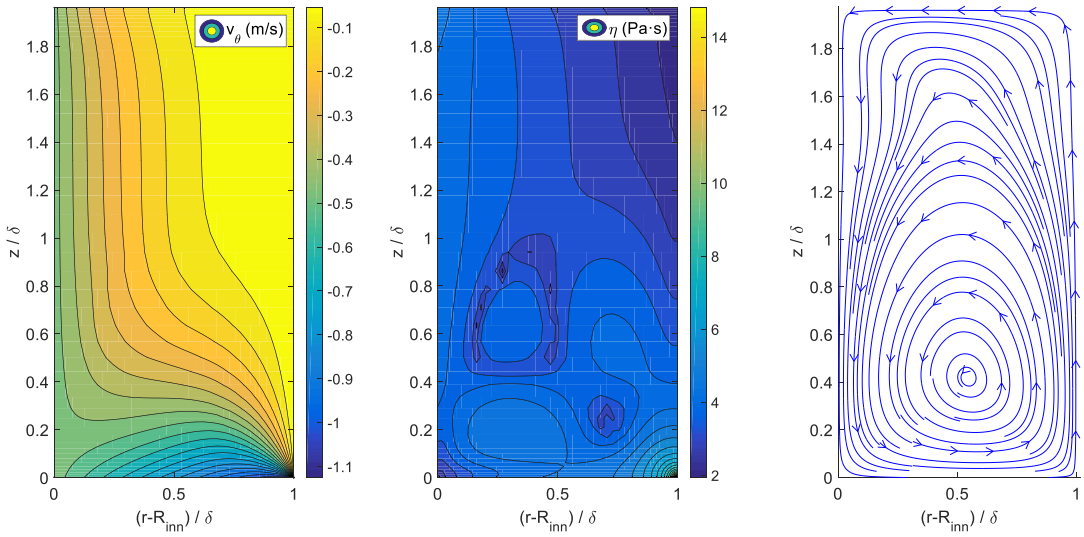

(A) (B) (C)

FIGURE 146 - TEST 3 PERIODIC FLOW FOR 2.50 KG OF MIXED FABRIC-WATER SUSPENSION; T = 2.52 S: (A) TANGENTIAL VELOCITY, (B) APPARENT VISCOSITY AND (C) SECONDARY FLOW STREAMLINES.

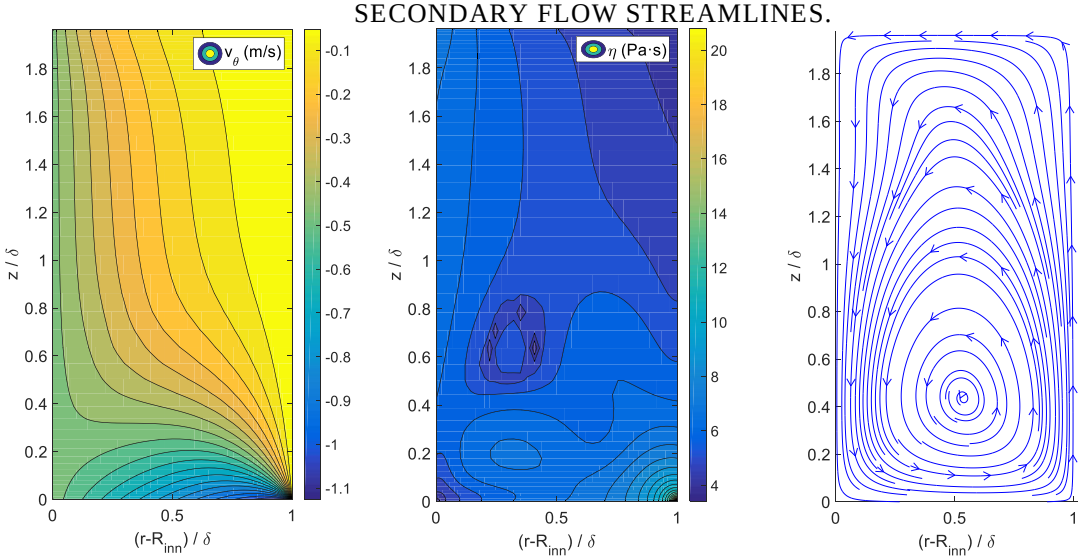

(A) (B) (C)

FIGURE 147 - TEST 4 PERIODIC FLOW FOR 1.25 KG OF MIXED FABRIC-WATER SUSPENSION; T = 2.52 S: (A) TANGENTIAL VELOCITY, (B) APPARENT VISCOSITY AND (C) SECONDARY FLOW STREAMLINES.

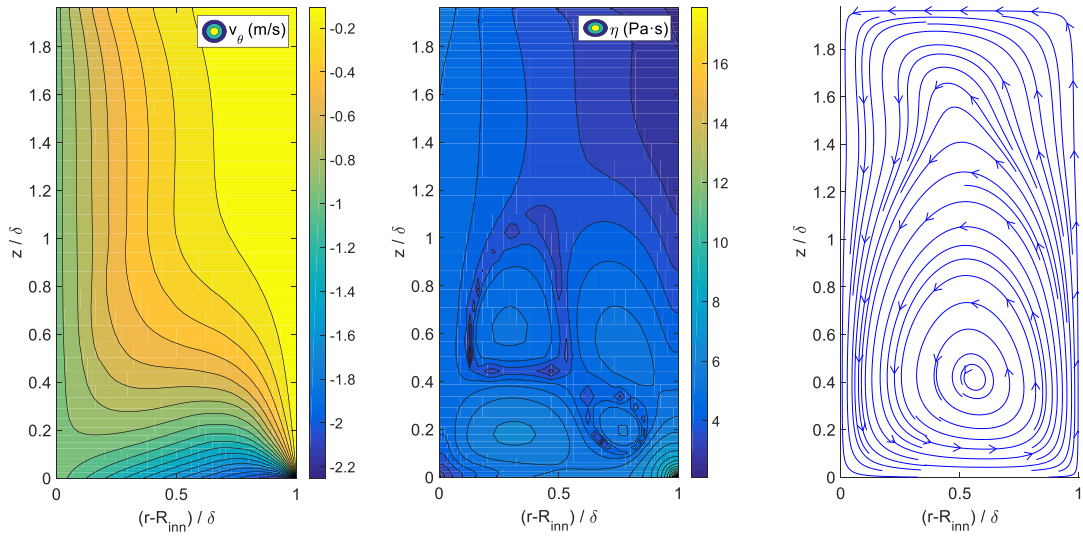

(A) (B) (C)

FIGURE 148 - TEST 4 PERIODIC FLOW FOR 2.50 KG OF MIXED FABRIC-WATER SUSPENSION; T = 2.52 S: (A) TANGENTIAL VELOCITY, (B) APPARENT VISCOSITY AND (C) SECONDARY FLOW STREAMLINES.

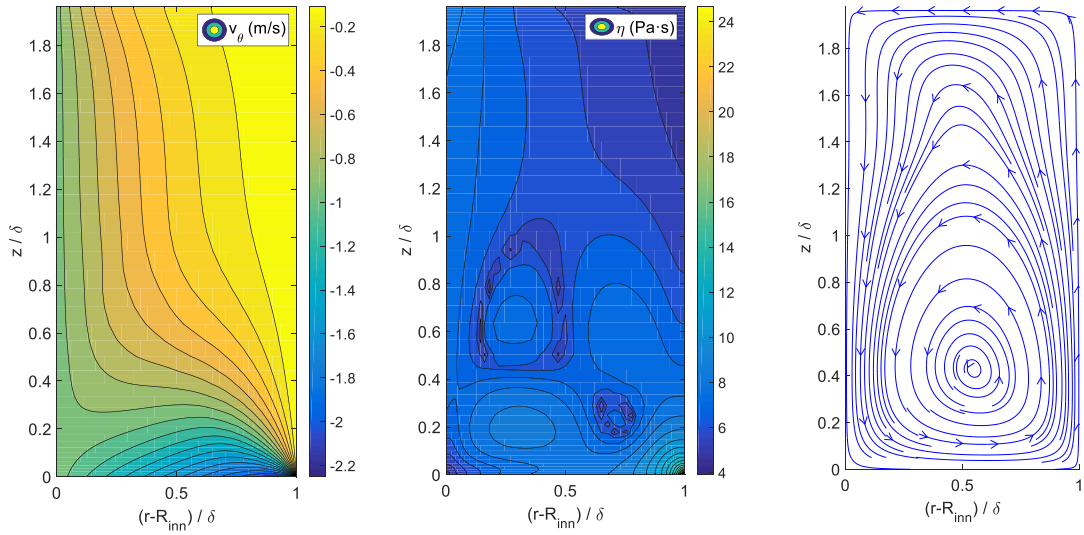

(A) (B) (C)

5.4 CHAPTER SUMMARY

This Chapter presented some numerical simulations concerning the fluid flow of suspensions of fabric-water in a coaxial double cylinder geometry, also known as Taylor-Couette geometry by means of the numerical methodology presented previously in this thesis

and the Herschel-Bulkley NNF model, where the rheological parameters were obtained from experimental raw data and non-linear regression (Chapter 4).

At first, the numerical torque was obtained from different simulations with: different fluid fabric-water suspensions (cotton, semi-synthetic and mixed fabrics), and two different fabric amounts each. These tests were verified through a direct confrontation with the experimental measurements, and it was observed that for most of the simulation results exhibited a satisfactory agreement (±20%) with the experimental torque measurements. This agreement was better for the mixed fabric-water suspensions simulations.

Moreover, the tangential velocity (v_θ), apparent viscosity (η), pressure (p), and streamfunction (ψ) distributions were plotted along the r-z plane for all simulations. It has been observed a presence of end-effects near the corner of the bottom surface and inner cylinder, which is proportional to the maximum shear rate region and the viscosity of the fluid. These end-effects were considered on the numerical torque calculations.

Finally, periodic flow simulations were carried out for two different imposed conditions: (i) non-rotating basis flow and (ii) rotating basis flow. The former results were verified with the experimental measurements of periodic experiments and presented a good agreement for both mixed fabric-water suspensions. The latter was used to observe the behaviors of velocity fields and apparent viscosities for different test conditions and different suspensions.

The periodic flow where the bottom basis rotates with the inner cylinder attempted to emulate a simple operation cycle of a washing machine. It was observed that faster washing cycles enhance the unstable behavior of the principal and secondary flows. In a real washing machine, the flow instability may lead to a higher washing efficiency as the mechanical action has a quite influence on its efficiency. Finally, it was observed that, contrary to the case where the bottom basis is stationary, the direction of the secondary flow goes upward near the outer cylinder wall and downwards near the inner cylinder wall, which may have an influence on the clothes disposal on a real washing machine.

6 CONCLUDING REMARKS

6.1 CONCLUSIONS

The present work discussed the importance of a study for understanding the flow of fabric-water suspensions in a geometry similar to the one found in a top-load washing machine in two fronts: (i) regression of a non-Newtonian model to represent the behavior of the suspensions, and (ii) CFD simulations of the suspensions.

In this fashion, a comprehensive literature review was carried out covering not only different rheometry techniques for Couette-Inverse problems but also providing a deeper understanding of the flow in a coaxial double cylinder cavity (i.e., Taylor-Couette flow) and so the laundry and washing processes.

Based on the literature review and the theoretical background, an experimental methodology was proposed to obtain the rheological behavior of the fabric-water suspensions. Tests with a geometry similar to a real top-load washing machine were carried out varying fabric materials (cotton, semi-synthetic and mixed) for different amounts of fabric and velocities. It was observed that among four different well-known NNF model, the one that best described the suspensions was the Herschel-Bulkley.

A numerical methodology based on CFD techniques was proposed and adopted for steady-state and periodic fluid flows simulations, where the Herschel-Bulkley NNF was used as the working fluid. For steady-state simulations, the results were validated against experimental torque data, where most of the data agreed to within ± 20% tolerance bounds. In the same way, the results for the periodic flow were compared with experimental measurements and showed a good accordance with the torque values over time. Also, periodic flows with a rotating basis were analyzed to emulate a simplified washing machine geometry.

Some difficulties concerning the modeling of such a suspension (fabric-water) have been noticed. The distribution of the fabric tissues within the gap between the cylinders was always non-uniform due to the fabric underwater deformation and the decantation phenomena. Thus, a shear-thickening behavior was observed for almost all suspensions because of the agglomeration of the fabric tissues near the vanes of the inner cylinder surface. Such agglomeration tends to increase the viscosity when both the fabric amount and the velocity increase. Furthermore, the presence of end-effects was reported.

In summary, the key conclusions of this thesis are as follows:

- The Herschel-Bulkley NNF model was used to describe different fabric-water suspensions, each one with their own characteristics because of the three-parameter nature of the model and physical interpretation (sum of yield stress and Power-Law effects);
- The numerical methodology showed reliable results when compared with the experimental data, thus providing information about the suspensions behavior on a geometry that attempts to emulate a washing machine running;
- Cotton and semi-synthetic fabric-water suspensions present different behaviors for different amounts of fabric (changing from Newtonian-like to shear-thickening and *vice-versa*). The mixed fabric-water suspensions presented a more uniform variation of the shear-thickening behavior with the amount of fabric;
- The periodic flows present peaks of torque responses when changing the velocity direction. Such a torque response is due to the efforts for changing the velocities of the fluid flow and the physical structure itself (cylinder and basis);
- The recirculation of the secondary flow, which denotes the fabric rotation inside the washing machine, changes if the bottom basis is rotating or not. Contrary to the cases where the bottom basis are static, if the basis rotates the direction of the secondary flow goes upward near the outer cylinder wall, and downwards near the inner cylinder wall;
- Shorter cycles of agitation tend to promote the instabilities of the fluid flow, which may intensify the mechanical action and the washing efficiency.

This thesis contributed to promoting the study of the flow of fabric-water suspensions within a simplified geometry that attempts to emulate the fluid flow inside the basket of a washing machine by means of a rheometric approach in numerical and experimental counterparts. One can see that this approach does not provide a quite understanding of the behavior of a real fabric in a washing process, but it advances the understanding the behavior of the suspension in the process. It is worthy of note that this thesis provides a simple understanding of a complex fluid flow that involves much more parameters and conditions than the ones taken into account.

6.2 RECOMMENDATIONS

The suggestions for further works are as follows:

- Find a more suitable coaxial double cylinder geometry that minimizes the effects of the immerse fabric distribution and end-effects;
- Extend the conclusions of this thesis to different kinds and forms of fabrics (e.g., real clothes);
- Extend the modeling of suspensions using different NNF models found in literature or elsewhere, and confront with different rheometry techniques, such as the Tikhonov regularization and the wavelet-vaguelette, which give the $\tau(\dot{\gamma})$ curve directly from the raw data without the model limitations;
- Perform some numerical simulations in a commercial CFD package to extend the numerical analyses;
- Use other numerical techniques for modeling a submerged fabric tissue, or a real cloth independently;
- Perform simulations in geometries that can emulate other types of washing machines, such as front-loads and top-loads, with an impeller.

REFERENCES

AHLBERG, J. H.; NILSON, E. N.; WALSH, J. L. **The Theory of Splines and Their Applications**. New York: Academic Press, v. 38, 1967. 284 p.

AHUJA, A.; SINGH, A. Slip velocity of concentrated suspensions in Couette flow. **Journal of Rheology**, v. 53, n. 6, p. 1461-1485, 2009.

AKCABAY, D. T. **Physics Based Washing Machine Simulations**. University of Michigan. Ann Arbor, MI, USA, p. 174. 2007.

AKCABAY, D. T.; DOWLING, D. R.; SCHULTZ, W. W. Clothes washing simulations. **Computers & Fluids**, v. 100, p. 79-94, 1 set. 2014.

ALIBENYAHIA, B. et al. Revisiting the stability of circular Couette flow of shear-thinning fluids. **Journal of Non-Newtonian Fluid Mechanics**, v. 183-184, p. 37-51, set. 2012.

AMOURA, M. et al. Finite element study of mixed convection for non-Newtonian fluid between two coaxial rotating cylinders. **International Communications in Heat and Mass Transfer**, v. 33, n. 6, p. 780-789, jun. 2006.

ANCEY, C. Solving the Couette inverse problem using a wavelet-vaguelette decomposition. **Journal of Rheology**, v. 49, n. 2, p. 441-460, 2005.

ANDERECK, C. D.; LIU, S. S.; SWINNEY, H. L. Flow regimes in a circular Couette system with independently rotating cylinders. **Journal of Fluid Mechanics**, v. 164, p. 155-183, mar. 1986.

BANSAL, P.; VINEYARD, E.; ABDELAZIS, O. Advances in household appliances- A review. **Applied Thermal Engineering**, v. 31, n. 17-18, p. 3748-3760, dez. 2011.

BARNES, H. A. A review of the slip (wall depletion) of polymer solutions, emulsions and particle suspensions in viscometers: its cause, character, and cure. **Journal of Non-Newtonian Fluid Mechanics**, v. 56, n. 3, p. 221-251, mar. 1995.

BARNES, H. A. The yield stress—a review or ‘παντα ρει’—everything flows? **Journal of Non-Newtonian Fluid Mechanics**, v. 81, n. 1-2, p. 133-178, fev. 1999.

BARNES, H. A. Measuring the viscosity of large-particle (and flocculated) suspensions — a note on the necessary gap size of rotational viscometers. **Journal of Non-Newtonian Fluid Mechanics**, v. 94, n. 2-3, p. 213-217, 30 nov. 2000.

BARNES, H. A.; CARNALI, J. O. The vane-in-cup as a novel rheometer geometry for shear thinning and thixotropic materials. **Journal of Rheology**, v. 34, n. 6, p. 841-866, 1990.

BARNES, H. A.; HUTTON, J. F.; WALTERS, K. F. R. S. **An Introduction to Rheology**. Amsterdam: Elsevier, v. 3, 1989. 200 p.

BARNES, H. A.; NGUYEN, Q. D. Rotating vane rheometry — a review, v. 98, n. 1, p. 1-14, 15 mar. 2001.

BINGHAM, E. C. An Investigation of the Laws of Plastic Flow. **Bulletin of the Bureau of Standards**, v. 13, p. 309–353, 1916. Scientific Paper 278.

BINGHAM, E. C. **Fluidity And Plasticity**. New York: McGraw-Hill, 1922.

BIRD, R. B.; ARMSTRONG, R. C.; HASSAGER, O. **Dynamics of Polymeric Liquids - Volume 1 Fluid Mechanics**. New York: John Wiley & Sons, 1987.

BIRD, R. B.; STEWART, W. E.; LIGHTFOOT, E. N. **Transport Phenomena**. 2nd, Revised. ed. Hoboken: John Wiley & Sons, 2006. 895 p.

BITBOL, M.; MILLS, P. The deformation of a viscoelastic sphere in a time dependent shear flow. **Journal de Physique**, 45, n. 16, 1984. 775-780.

BOGER, D. V. Rheology and the resource industries. **Chemical Engineering Science**, v. 64, n. 22, p. 4525-4536, 16 nov. 2009.

BORGIA, A.; SPERA, F. J. Error analysis for reducing noisy wide-gap concentric cylinder rheometric data for nonlinear fluids: Theory and applications. **Journal of Rheology**, v. 34, n. 1, p. 117-136, jan. 1990.

BUSCALL, R.; MCGOWAN, J. I.; MORTON-JONES, A. J. The rheology of concentrated dispersions of weakly attracting colloidal particles with and without wall slip. **Journal of Rheology**, v. 37, n. 4, p. 621-641, 1993.

CALVIMONTES, A. **Topographic characterization of polymer materials at different length scales and the mechanistic understanding of wetting phenomena**. Dresden Technical University. Dresden, Germany, p. 171. 2009.

CAMPOS, L. G. C.; HERMES, C. J. L. Experimental evaluation and transient simulation of detergent transport in household vertical axis washing machines. **Chemical Engineering Research and Design**, v. 109, p. 720-729, maio 2016.

CASSON, N. **Rheology of disperse systems**. Proceedings of a Conference Organized by the British Society of Rheology. Oxford: Pergamon Press. 1959. p. 84–104.

CHANDRASEKHAR, S. The Stability of Viscous Flow between Rotating Cylinders in the Presence of a Magnetic Field. **Proceedings of the Royal Society of London A: Mathematical, Physical and Engineering Sciences**, London, v. 216, n. 1126, p. 293-309, 10 fev. 1953.

CHATZIMINA, M.; GEORGIOU, G.; ALEXANDROU, A. Wall shear rates in circular Couette flow of a Herschel-Bulkley fluid. **Applied Rheology**, v. 19, n. 3, p. 34288, jan. 2009.

CHENG, A. H.-D.; CHENG, D. T. Heritage and early history of the boundary element method. **Engineering Analysis with Boundary Elements**, v. 29, n. 3, p. 268-302, mar. 2005.

CHOW, A. W.; FULLER, G. G. Some experimental results on the development of Couette flow for non-Newtonian fluids. **Journal of Non-Newtonian Fluid Mechanics**, v. 17, n. 2, p. 233-243, 1985.

COLES, D. Transition in circular Couette flow. **Journal of Fluid Mechanics**, Cambridge, v. 21, n. 3, p. 385-425, mar. 1965.

CORONADO, O.; MENDES, P. R. D. S.; CARVALHO, M. D. S. **Stability of viscoplastic flow in annuli with a rotating inner cylinder**. 9th Brazilian Congress of Thermal Engineering and Sciences - ENCIT. Caxambu, MG, Brazil: The Brazilian Society of Mechanical Sciences. 2002. p. 1-10.

COUETTE, M. La viscosité des liquides. **Bulletin des Sciences Physiques**, v. 4, p. 40-62, 123-133, 262-278, 1888. as well as a 47 pages monography of Georges Carré, Paris, 1888.

COUETTE, M. Etudes sur le frottement des liquides. **Annales de Chimie et de Physique**, v. 21, n. VI, p. 433-510, 1890.

COUSSOT, P. et al. Macroscopic vs. local rheology of yield stress fluids. **Journal of Non-Newtonian Fluid Mechanics**, v. 158, n. 1-3, p. 85-90, maio 2009.

DARBY, R. Couette Viscometer Data Reduction for Materials with a Yield Stress. **Journal of Rheology**, v. 29, n. 4, p. 369-378, 1985.

DE WAELE, A. Viscometry and Plastometry. **Journal of the Oil & Colour Chemists Association**, v. 6, p. 33–69, 1923.

DI PRIMA, R. C.; SWINNEY, H. L. Instabilities and transition in flow between concentric rotating cylinders. In: SWINNEY, H. L.; GOLLUB, J. P. **Hydrodynamic Instabilities and the Transition to Turbulence**. Berlin: Springer Berlin Heidelberg, 1985. p. 139-180.

DJERIDI, H.; GABILLET, C.; BILLARD, J. Y. Two-phase Couette–Taylor flow: Arrangement of the dispersed phase and effects on the flow structures. **Physics of Fluids**, v. 16, n. 1, p. 128-139, jan. 2004.

DONNELLY, R. J. Taylor-Couette Flow: The Early Day. **Physics Today**, v. 44, n. 11, p. 32-39, nov. 1991.

DONNELLY, R. J.; SCHWARZ, K. W.; ROBERTS, P. H. Experiments on the Stability of Viscous Flow Between Rotating Cylinders. VI. Finite-Amplitude Experiments. **Proceedings**

of the Royal Society of London A: Mathematical, Physical and Engineering Sciences, v. 283, n. 1395, p. 531-556, 1965.

DONTULA, P.; MACOSKO, C. W.; SCRIVEN, L. E. Origins of concentric cylinders viscometry. **Journal of Rheology**, v. 49, n. 4, p. 807-818, 2005.

DOU, H.-S.; KHOO, B. C.; YEO, K. S. Instability of Taylor–Couette flow between concentric rotating cylinders. **International Journal of Thermal Sciences**, v. 47, n. 11, p. 1422-1435, nov. 2008.

EGER, R. S. **Modelação de escoamentos turbulentos sob a ação de rotação alternada (in portuguese)**. Federal University of Santa Catarina. Florianópolis, SC, Brazil, p. 106. 2010.

ESCUDIER, M. P.; GOULDSON, I. W.; JONES, D. M. Taylor Vortices in Newtonian and Shear-Thinning Liquids. **Proceedings of the Royal Society of London A: Mathematical, Physical and Engineering Sciences**, v. 449, n. 1935, p. 155-176, 1995.

ESCUDIER, M. P.; OLIVEIRA, P. J.; PINHO, F. T. Fully developed laminar flow of purely viscous non-Newtonian liquids through annuli, including the effects of eccentricity and inner-cylinder rotation. **International Journal of Heat and Fluid Flow**, v. 23, n. 1, p. 52-73, fev. 2002.

ESTELLÉ, P.; LANOS, C.; PERROT, A. Processing the Couette viscometry data using a Bingham approximation in shear rate calculation. **Journal of Non-Newtonian Fluid Mechanics**, v. 154, n. 1, p. 31-38, set. 2008.

GOLLUB, J. P.; SWINNEY, H. L. Onset of Turbulence in a Rotating Fluid. **Physical Review Letters**, v. 35, n. 14, p. 927-930, 1975.

HANKS, R. W. Couette Viscometry of Casson Fluids. **Journal of Rheology**, v. 27, n. 1, p. 1-6, 1983.

HARLOW, F. H.; WELCH, E. Numerical Calculation of Time-Dependent Viscous Incompressible Flow of Fluid with Free Surface. **Physics of Fluids**, v. 8, p. 2182-2189, 1965.

HEIRMAN, G. et al. Integration approach of the Couette inverse problem of powder type self-compacting concrete in a wide-gap concentric cylinder rheometer. **Journal of Non-Newtonian Fluid Mechanics**, v. 150, n. 2-3, p. 93-103, abr. 2008.

HEIRMAN, G. et al. Integration approach of the Couette inverse problem of powder type self-compacting concrete in a wide-gap concentric cylinder rheometer: Part II. Influence of mineral additions and chemical admixtures on the shear thickening flow behaviour. **Cement and Concrete Research**, v. 39, n. 3, p. 171-181, mar. 2009.

HERSCHEL, W. H.; BULKLEY, R. Konsistenzmessungen von Gummi-Benzollösungen. **Kolloid-Zeitschrift**, v. 39, n. 4, p. 291–300, ago. 1926.

HUANG, H.; LEE, T. S.; SHU, C. Hybrid lattice Boltzmann finite-difference simulation of axisymmetric swirling and rotating flows. **International Journal for Numerical Methods in Fluids**, v. 53, n. 11, p. 1707-1726, 2007.

IHLE, C. F.; TAMBURRINO, A.; VIVERO, P. Effect of sample manipulation on the Couette rheometry of copper concentrates. **Powder Technology**, v. 239, p. 78-85, maio 2013.

JACOBSEN, R. T. The determination of the flow curve of a plastic medium in a wide gap rotational viscometer. **Journal of Colloid and Interface Science**, 48, n. 3, 1974. 437-441.

JAMES, P. W.; JONES, T. E. R.; HUGHES, J. P. The determination of apparent viscosity using a wide gap, double concentric cylinder. **Journal of Non-Newtonian Fluid Mechanics**, v. 124, n. 1-3, p. 33–41, 15 dez. 2004.

JANÁčOVÁ, D. et al. Computer simulation of washing processes. **International Journal of Mathematical Models and Methods in Applied Sciences**, v. 5, n. 6, p. 1094-1101, 2011.

JASTRZęBSKI, M.; ZAIDANI, H. A.; WROņSKI, S. Stability of Couette flow of liquids with power law viscosity. **Rheologica Acta**, v. 31, n. 3, p. 264-273, 1992.

JENG, J.; ZHU, K.-Q. Numerical simulation of Taylor Couette flow of Bingham fluids. **Journal of Non-Newtonian Fluid Mechanics**, v. 165, n. 19-20, p. 1161-1170, out. 2010.

JOYE, D. D. Shear rate and viscosity corrections for a Casson fluid in cylindrical (Couette) geometries. **Journal of Colloid and Interface Science**, v. 267, n. 1, p. 204-210, 1 nov. 2003.

KELESSIDIS, V. C.; MAGLIONE, R. Modeling rheological behavior of bentonite suspensions as Casson and Robertson–Stiff fluids using Newtonian and true shear rates in Couette viscometry. **Powder Technology**, v. 168, n. 3, 18 out. 2006.

KELESSIDIS, V. C.; MAGLIONE, R. Shear rate corrections for Herschel-Bulkley fluids in Couette geometry. **Applied Rheology**, v. 18, n. 3, p. 3448211, jan. 2008.

KELESSIDIS, V. C.; MAGLIONE, R.; BANDELIS, G. On the end-effect correction for Couette type oil-field direct-indicating viscometers for Newtonian and non-Newtonian fluids. **Journal of Petroleum Science and Engineering**, v. 71, n. 1-2, p. 37-46, mar. 2010.

KHALI, S.; NEBBALI, R.; BOUHADEF, K. Numerical Investigation of Non-Newtonians Fluids Flows between Two Rotating Cylinders Using Lattice Boltzmann Method. **International Journal of Mechanical, Aerospace, Industrial, Mechatronic and Manufacturing Engineering**, v. 7, n. 10, p. 924-930, out. 2013.

KONIJN, B. J.; SANDERINK, O. B. J.; KRUYT, N. P. Experimental study of the viscosity of suspensions: Effect of solid fraction, particle size and suspending liquid. **Powder Technology**, v. 266, p. 61-69, nov. 2014.

KOOS, E. et al. Rheological measurements of large particles in high shear rate flows. **Physics of Fluids**, v. 24, n. 1, p. 01330219, 2012.

KRIEGER, I. M.; MARON, S. H. Direct Determination of the Flow Curves of Non-Newtonian Fluids. **Journal of Applied Physics**, v. 23, n. 1, p. 147-149, jan. 1952.

LASKAR, A. I.; BHATTACHARJEE, R. Torque–speed relationship in a concrete rheometer with vane geometry. **Construction and Building Materials**, v. 25, n. 8, p. 3443-3449, ago. 2011.

LEONG, Y. K.; YEOW, Y. L. Obtaining the shear stress shear rate relationship and yield stress of liquid foods from Couette viscometry data. **Rheologica Acta**, v. 42, n. 4, p. 365-371, jul. 2003.

LOCKETT, T. J.; RICHARDSON, S. M.; WORRAKER, W. J. The stability of inelastic non-Newtonian fluids in Couette flow between concentric cylinders: a finite-element study. **Journal of Non-Newtonian Fluid Mechanics**, v. 43, n. 2-3, p. 165-177, jul. 1992.

MACHADO, D. J. **Estudo experimental do escoamento periódico de água em lavadoras de eixo vertical**. Federal University of Paraná. Curitiba, PR, Brazil, p. 35. 2014.

MALISKA, C. R. **Transferência de Calor e Mecânica dos Fluidos Computacional**. Rio de Janeiro: LTC - Livros Técnicos e Científicos Editora S.A., 1995.

MALISKA, C. R.; RAITHBY, G. D. A method for computing three dimensional flows using non-orthogonal boundary-fitted co-ordinates. **International Journal for Numerical Methods in Fluids**, v. 4, n. 6, p. 519-537, jun. 1984.

MALLOCK, A. Determination of the viscosity of water. **Proceedings of the Royal Society of London**, v. 45, p. 126-132, 1888.

MARCHESINI, F. H. et al. Rheological characterization of yield-stress materials: Flow pattern and apparent wall slip. **Applied Rheology**, v. 25, n. 5, p. 39-48, 2015.

MARCUS, P. S. Simulation of Taylor-Couette flow. Part 2. Numerical results for wavy-vortex flow with one travelling wave. **Journal of Fluid Mechanics**, v. 146, p. 65-113, 9 set. 1984.

MAXWELL, L. **Who Invented the Electric Washing Machine? An Example of How Patents Are Misused by Historians**. [S.l.], p. 18. 2009.

MEYER-SPASCHE, R.; KELLER, H. B. Computations of the axisymmetric flow between rotating cylinders. **Journal of Computational Physics**, v. 35, n. 1, p. 100-109, 1980.

MITSOULIS, E. Flows of viscoplastic materials: models and computations. **Rheology reviews**, v. 2007, p. 135-178, 2007.

MORINISHI, Y.; VASILYEV, O. V.; OGI, T. Fully conservative finite difference scheme in cylindrical coordinates for incompressible flow simulations. **Journal of Computational Physics**, v. 197, n. 2, p. 686-710, 1 jul. 2004.

NEWTON, S. I. **Mathematical Principles of Natural Philosophy and His System of the World**. Tradução de Andrew Motte. Oakland: University of California Press, 1946.

NGUYEN, Q. D.; BOGER, D. V. Yield Stress Measurement for Concentrated Suspensions. **Journal of Rheology**, v. 27, n. 4, p. 321-349, 1983.

NGUYEN, Q. D.; BOGER, D. V. Direct yield stress measurement with the vane method. **Journal of Rheology**, v. 29, n. 3, p. 335-347, 1985.

NGUYEN, Q. D.; BOGER, D. V. Characterization of yield stress fluids with concentric cylinder viscometers. **Rheologica Acta**, v. 26, n. 6, p. 508-515, 1987.

OPPENHEIM, A. V.; SCHAFER, R. W.; BUCK, J. R. **Discrete-Time Signal Processing**. 2nd. ed. Upper Saddle River: Prentice Hall, 1999.

OSTWALD, W. Ueber die Geschwindigkeitsfunktion der Viskosität disperser Systeme. I. **Kolloid-Zeitschrift**, v. 36, n. 2, p. 99–117, fev. 1925.

OVARLEZ, G. et al. Wide-gap Couette flows of dense emulsions: Local concentration measurements, and comparison between macroscopic and local constitutive law measurements through magnetic resonance imaging. **Physical Review E**, v. 78, n. 3, p. 03630713, 2008.

PAPANASTASIOU, T. C. Flows of Materials with Yield. **Journal of Rheology**, v. 31, n. 5, p. 385-404, 1987.

PATANKAR, S. **Numerical Heat Transfer and Fluid Flow**. 1. ed. New York: Hemisphere Publishing Co., 1980. 214 p. Hemisphere Series on Computational Methods in Mechanics and Thermal Science.

PESKIN, C. S. The Immersed Boundary Method. **Acta Numerica**, 11, 2002. 479-517.

PIAU, J.-M.; PIAU, M. Letter to the Editor: Comment on “Origin of concentric cylinder viscometry” [J. Rheol.49, 807–818 (2005)]. The relevance of the early days of viscosity, slip at the wall, and stability in concentric cylinder viscometry. **Journal of Rheology**, v. 49, n. 6, p. 1539-1550, 2005.

POTANIN, A. 3D simulations of the flow of thixotropic fluids, in large-gap Couette and vane-cup geometries. **Journal of Non-Newtonian Fluid Mechanics**, v. 165, n. 5-6, p. 299-312, mar. 2010.

RAYLEIGH, L. Further remarks on the stability of viscous fluid motion. **Philosophical Magazine**, v. 28, n. 6, p. 609-619, 1914.

ROBERTSON, R. E.; STIFF, H. A. An Improved Mathematical Model for Relating Shear Stress to Shear Rate in Drilling Fluids and Cement Slurries. **Society of Petroleum Engineers Journal**, v. 16, n. 01, p. 31-36, fev. 1976.

SAAK, A. W.; JENNINGS, H. M.; SHAH, S. P. The influence of wall slip on yield stress and viscoelastic measurements of cement paste. **Cement and Concrete Research**, v. 31, n. 2, p. 205-212, fev. 2001.

SCHAEFFER, J. C. **Die bequeme und höchstvortheilhafte Waschmaschine. Wie solche in den damit gemachten Versuchen bewährt gefunden und damit dieselbe um so sicherer und nützlicher gebraucht werden könne hin und wieder abgeändert und verbessert worden ; Nebst einer Kupfertaf**. Frankfurt: [s.n.], 1767. Disponivel em: <http://nbn-resolving.de/urn:nbn:de:bvb:210-14-008994946-2>.

SCHOWALTER, W. R. **Mechanics of Non-Newtonian Fluids**. 1st. ed. Oxford: Pergamon Press, 1978. 300 p.

SCHRAMM, G. **A Practical Approach to Rheology and Rheometry**. 2nd. ed. [S.l.]: Gebrueder Haake, 1994. 290 p.

SCIENCE Direct. **Science Direct**, 2017. Disponivel em: <http://www.sciencedirect.com>. Acesso em: 08 March 2017.

SÉRGIO, A. et al. The design of a washing machine prototype. **Materials & Design**, v. 24, n. 5, p. 331-338, ago. 2003.

SINEVIC, V.; KUBOI, R.; NIENOW, A. W. Power numbers, Taylor numbers and Taylor vortices in viscous newtonian and non-newtonian fluids. **Chemical Engineering Science**, v. 41, n. 11, p. 2915-2923, 1986.

SMIESZEK, M.; EGBERS, C. Flow structures and stability in Newtonian and non-Newtonian Taylor-Couette flow. **Journal of Physics: Conference Series**, v. 14, n. 1, p. 72-77, 2005.

SNABRE, P.; MILLS, P. Rheology of concentrated suspensions of viscoelastic particles. **Colloids and Surfaces A: Physicochemical and Engineering Aspects**, v. 152, n. 1-2, p. 79-88, jul. 1999.

SNYDER, H. A. Stability of Rotating Couette Flow. II. Comparison with Numerical Results. **Physics of Fluids**, Melville, v. 11, n. 8, p. 1599-1605, 1968.

SPARROW, E. M.; MUNRO, W. D.; JONSSON, V. K. Instability of the flow between rotating cylinders: the wide-gap problem. **Journal of Fluid Mechanics**, v. 20, n. 01, p. 35-46, 9 set. 1964.

STALMANS, M. **History of Washing**. Brussels, Belgium. 2008.

STOKES, G. G. **Mathematical and Physical Papers**. Cambridge: Cambridge University Press, v. 1, 1880.

STOKES, G. G. **Mathematical and Physical Papers**. Cambridge: Cambridge University Press, v. 5, 1905.

TAKEDA, Y. Quasi-periodic state and transition to turbulence in a rotating Couette system. **Journal of Fluid Mechanics**, v. 389, p. 81-99, 6 jun. 1999.

TAMANO, S. et al. Numerical simulation of confined swirling flow of viscoelastic fluid due to partially rotating disc. **Nihon Reoroji Gakkaishi**, v. 38, n. 1, p. 9-16, 2010.

TAYLOR, G. I. Stability of a Viscous Liquid Contained between Two Rotating Cylinders. **Philosophical Transactions of the Royal Society of London A: Mathematical, Physical and Engineering Sciences**, London, v. 223, p. 289-343, 1923.

THOMAS, L. H. **Elliptic Problems in Linear Differential Equations over a Network**. New York. 1949.

TRISMOSIN, S. **Splendor Solis**. Nuremberg: [s.n.], 1582.

VAN DEN BREKEL, D. M. **Hydrodynamics and mass transfer in domestic drum-type fabric washing machine**. Technical University Delft. Delft, Netherlands. 1987.

VAN DER VORST, H. A. Bi-CGSTAB: A Fast and Smoothly Converging Variant of Bi-CG for the Solution of Nonsymmetric Linear Systems. **SIAM Journal on Scientific and Statistical Computing**, v. 13, n. 2, p. 631–644, 1992.

VERSTEEG, H.; MALALASEKERA, W. **An Introduction to Computational Fluid Dynamics:** The Finite Volume Method. 2nd. ed. Harlow: Pearson Education Limited, 2007. 520 p.

WALLEVIK, O. H. et al. Avoiding inaccurate interpretations of rheological measurements for cement-based materials. **Cement and Concrete Research**, v. 78, n. A, p. 100-109, dez. 2015.

WALOWIT, J.; TSAO, S.; DI PRIMA, R. C. Stability of Flow Between Arbitrarily Spaced Concentric Cylindrical Surfaces Including the Effect of a Radial Temperature Gradient. **Journal of Applied Mechanics**, v. 31, n. 4, p. 585-593, 1 dez. 1964.

WATANABE, K. et al. Flow between two coaxial rotating cylinders with a highly water-repellent wall. **AIChE Journal**, v. 49, n. 8, p. 1956-1963, 2003.

WATANABE, T.; TOYA, Y. Vertical Taylor-Couette flow with free surface at small aspect ratio. **Acta Mechanica**, v. 223, n. 2, p. 347-353, 2012.

WEISBERG, A. Y.; KEVREKIDIS, I. G.; SMITS, A. J. Delaying transition in Taylor–Couette flow with axial motion of the inner cylinder. **Journal of Fluid Mechanics**, v. 348, p. 141-151, 10 out. 1997.

WHITAKER, S. **Introduction to Fluid Mechanics**. 2nd. ed. Malabar: Krieger Publishing Company, 1992. 474 p.

WOOD, W. A. **Multigrid Approach to Incompressible Viscous Cavity Flow**. Hampton. 1996.

WU, X.; SWIFT, J. B. Onset of secondary flow in the modulated Taylor-Couette system. **Physical Review A**, v. 40, n. 12, p. 7197-7201, dez. 1989.

YAN, J.; JAMES, A. E. The yield surface of viscoelastic and plastic fluids in a vane viscometer. **Journal of Non-Newtonian Fluid Mechanics**, v. 70, n. 3, p. 237-253, jun. 1997.

YEE, R. P. **Simulação numérica de escoamento bifásico em máquinas de lavar de eixo vertical**. Federal University of Paraná. Curitiba, PR, Brazil, p. 46. 2013.

YEOW, Y. L. et al. Obtaining the shear rate function and the slip velocity function from Couette viscometry data. **Journal of Non-Newtonian Fluid Mechanics**, v. 124, n. 1-3, p. 43-49, 15 dez. 2004.

YEOW, Y. L.; KO, W. C.; TANG, P. P. P. Solving the inverse problem of Couette viscometry by Tikhonov regularization. **Journal of Rheology**, v. 44, n. 6, p. 1335-1351, 11-12 2000.

ZANOTTO, F. **Determinação experimental das características reológicas de misturas água-tecido em geometrias cilíndricas**. Federal University of Paraná. Curitiba, PR, Brazil, p. 47. 2015.

APPENDIX A – THOMAS ALGORITHM

A.1 TDMA

The TDMA (Tridiagonal Matrix Algorithm) method, also known as Thomas algorithm (THOMAS, 1949), is a numerical method based on the Gaussian elimination used to solve a tridiagonal system of equations when the matrix is diagonally dominant or symmetric positive definitive. Considering a discretized linear equation system as follows:

$$-a_i x_{i-1} + b_i x_i - c_i x_{i+1} = d_i \tag{A.1}$$

Likewise, in the matricial form:

$$\begin{bmatrix} b_1 & c_1 & 0 & \cdots & 0 & 0 \\ a_2 & b_2 & c_2 & \cdots & 0 & 0 \\ 0 & a_3 & b_3 & \cdots & 0 & 0 \\ \vdots & \vdots & \vdots & \ddots & \vdots & \vdots \\ 0 & 0 & 0 & \cdots & b_{n-1} & c_{n-1} \\ 0 & 0 & 0 & \cdots & a_n & b_n \end{bmatrix} \begin{bmatrix} x_1 \\ x_2 \\ x_3 \\ \vdots \\ x_{n-1} \\ x_n \end{bmatrix} = \begin{bmatrix} d_1 \\ d_2 \\ d_3 \\ \vdots \\ d_{n-1} \\ d_n \end{bmatrix} \tag{A.2}$$

The method consists of modifying the above algebraic equations on a forward sweep. Considering a tridiagonal system for n unknowns, an equation with i index can be written as:

$$x_i = A_i x_{i+1} + B_i \tag{A.3}$$

so,

$$x_{i-1} = A_{i-1} x_i + B_{i-1} \tag{A.4}$$

Substituting the Equation (I.4) into the Equation (I.3), one obtains the following equation:

$$x_i = \left(\frac{c_i}{b_i - a_i A_{i-1}}\right) x_{i+1} + \left(\frac{a_i B_{i-1} + d_i}{b_i - a_i A_{i-1}}\right) \tag{A.5}$$

where,

$$A_i = \frac{c_i}{b_i - a_i A_{i-1}} \tag{A.6}$$

$$B_i = \left(\frac{a_i B_{i-1} + d_i}{b_i - a_i A_{i-1}}\right) \tag{A.7}$$

Evaluating the modified coefficients A_i and B_i, it is possible to perform a back substitution using the Equation (I.3). Starting the back substitution with the x_n value, which is a known boundary condition, as below:

$$x_n = B_n \tag{A.8}$$

$$x_1 = B_1 \tag{A.9}$$

In the case of two-dimensional and three-dimensional problems, the matrix will not be three-diagonal anymore. It is called the line-by-line TDMA method (VERSTEEG and MALALASEKERA, 2007). As the boundaries points in all directions are known, one direction is chosen (i.e., west-east, north-south and top-bottom) and the sweeping occurs following this direction. Considering a vertical sweep in the north-south direction of a three-dimensional mesh, the discretized Equation (I.1) can be written as shown below:

$$-A_s\phi_S + A_p\phi_P - A_n\phi_N = A_e\phi_E + A_w\phi_W + A_t\phi_T + A_b\phi_B + B \tag{A.10}$$

The right-hand side of the equation above, and its respective neighbor control volumes nodal points is assumed to be temporarily known. So, the linear system is evaluated starting from the second north-south column, as the first column has known boundary condition. The sweep is done in all the columns (line-by-line), and the results obtained for each column will be used for the next column evaluation. In order to obtain a faster convergence, the sweep can also be performed in the south-north direction.

In order to have the entire mesh covered with all the boundary conditions considered (also to improve the numerical convergence), turning the system more explicit, the sweeping shall be performed in all other directions as well. Thus, the Equation (I.10) can be discretized in other two different manners:

$$-A_w\phi_W+A_p\phi_P-A_e\phi_E=A_n\phi_N+A_s\phi_S+A_t\phi_T+A_b\phi_B+B \quad (A.11)$$

$$-A_b\phi_B+A_p\phi_P-A_t\phi_T=A_n\phi_N+A_s\phi_S+A_e\phi_E+A_w\phi_W+B \quad (A.12)$$

Finally, the TDMA method includes all the boundary conditions and source terms of a three-dimensional mesh. The reason that this method is called line-by-line is because the TDMA method is performed in all directions in an iterative way.

A.2 CTDMA

The CTDMA (Cyclic Tridiagonal Matrix Algorithm), is a modified case of Gaussian elimination (AHLBERG, NILSON and WALSH, 1967) used to solve a linear system with cyclic boundary conditions. Considering the following equation:

$$a_i x_i = b_i x_{i+1} + c_i x_{i+1} + d_i \quad (A.13)$$

For i varying from 1 to n-1, the following boundary conditions are known:

$$\text{if } i = 1, x_i = x_{n-1} \quad (A.14)$$

$$\text{if } i = n-1, x_{i+1} = x_1 \quad (A.15)$$

Performing the following transformation:

$$x_i = e_i x_{i+1} + f_i x_{i+1} + g_i \quad (A.16)$$

where,

$$e_1 = b_1/a_1 \quad (A.17)$$

$$f_1 = c_1/a_1 \quad (A.18)$$

$$g_1 = d_1/a_1 \quad (A.19)$$

thus, for i varying from 2 to n-2:

$$e_i = \frac{b_i}{a_i - c_i e_{i-1}} \tag{A.20}$$

$$f_i = \frac{c_i f_{i-1}}{a_i - c_i e_{i-1}} \tag{A.21}$$

$$g_1 = \frac{d_{i+} c_i g_{i-1}}{a_i - c_i e_{i-1}} \tag{A.22}$$

The value of x_{n-1} is obtained by replacing the i index in Equation (I.13) with i = n-1, then solving x_1 using Equation (I.16) in terms of x_2 and x_{n-1}. Then for x_2 in terms of x_3 and x_{n-1}, and so on until x_{n-1} is the only unknown of the system. Considering the following terms:

$$p_1 = a_{n-1} \tag{A.23}$$

$$q_1 = b_{n-1} \tag{A.24}$$

$$r_1 = d_{n-1} \tag{A.25}$$

then, for i varying from 2 to n-1:

$$p_i = p_{i-1} - q_{i-1} f_{i-1} \tag{A.26}$$

$$q_i = q_{i-1} e_{i-1} \tag{A.27}$$

$$r_i = r_{i-1} - q_{i-1} g_{i-1} \tag{A.28}$$

$$x_{n-1} = \frac{(q_{n-2} + c_{n+1}) g_{n-2} + r_{n-2}}{p_{n-2} - (q_{n-2} + c_{n+1})(e_{n-2} + f_{n-2})} \tag{A.29}$$

thus, Equation (I.16) is used to evaluate the system for i varying from n-2 to 1 by back-substitution.

APPENDIX B – BICGSTAB

The BiCGSTAB (Biconjugate gradient stabilized method) is an iterative method used for solving a linear system, developed by H. A. van der Vorst (1992). It is a variant of the biconjugate gradient method (BiCG) with faster convergence. Moreover, the BiCGSTAB method can be evaluated with or without preconditioners. In the present work, the TDMA method is used as the preconditioner for the BiCGSTAB method. Thus, considering a discretized linear equation system as follows:

$$Ax = D \tag{B.1}$$

The initial residue r_0 is calculated using the initial guess x_0 (or the previous value) as follows:

$$r_0 = D - Ax_0 \tag{B.2}$$

The initial guesses of ρ, α and ω are considered. As well as the initial guess of v and p vectors.

$$\rho_0 = \alpha_0 = \omega_0 = 1 \tag{B.3}$$

$$v_0 = p_0 = 0 \tag{B.4}$$

For i = 1, 2, 3...

$$\rho_i = r_0^T r_{i-1} \tag{B.5}$$

$$\beta = \frac{i}{\rho_{i-1}} \frac{\alpha_i}{\omega_{i-1}} \tag{B.6}$$

$$p_i = r_{i-1} + \beta_i (p_{i-1} - \omega_{i-1} v_{i-1}) \tag{B.7}$$

The preconditioner K is used to evaluate the value of $\hat{p}$

$$K\hat{p} = p_i \tag{B.8}$$

then,

$$v_i = A\hat{p} \tag{B.9}$$

$$\alpha_i = \frac{\rho_i}{r_0^T v_i} \tag{B.10}$$

$$s_i = r_{i-1} - \alpha_i v_i \tag{B.11}$$

In the same way of the Equation (II.8), the preconditioner K is also used to evaluate the value of $\hat{s}$.

$$K\hat{s} = s_i \tag{B.12}$$

thus,

$$t_i = A\hat{s} \tag{B.13}$$

$$\omega_i = \frac{t_i^T s_i}{t_i^T t_i} \tag{B.14}$$

$$x_i = x_{i-1} + i\hat{p} + \omega_i \hat{s} \tag{B.15}$$

Finally, the residue r_i is evaluated as follows:

$$r_i = s_i - \omega_i t_i \tag{B.16}$$

If the norm of the residue is smaller than the convergence criterion the algorithm stops and the value x_i is considered as the solution of the system. If not, it returns to the Equation (II.5).

APPENDIX C – ANALYTICAL SOLUTIONS

Analytical solutions for a laminar-steady flow between two long concentric cylinders, where the is no wall slip and that cylinder height is sufficient to avoid boundary wall effects on the bottom and top boundaries, were presented in chapter 2 for incompressible Newtonian fluids and Power-Law non-Newtonian fluids (Figure 13). Moreover, the Reiner-Riwlin Equation (2.86), which relates the torque of the inner cylinder to the angular velocity of a Bingham fluid, and an adapted Equation (2.102) for a Herschel-Bulkey were also presented. All those equations derivations are depicted below.

C.1 NEWTONIAN FLUID

Considering a laminar steady-state flow, where the cylinder height is sufficient to avoid the bottom and top boundary walls effects, the analytical solution for the tangential velocity is achieved close to the half-height of the cylinders, as shown in the top view of Figure 13. In this case, both axial and radial velocities are considered negligible when compared to the tangential one.

Considering a Newtonian fluid, the analytical solution for the tangential velocity is:

$$\frac{\partial v_\theta}{\partial \theta} = 0 \tag{C.1}$$

Also, the pressure difference is dependent only of the tangential velocity and radial position.

$$\frac{\partial p}{\partial r} = \frac{\rho v_\theta^2}{r} \tag{C.2}$$

Thus, Equation (2.36) is simplified to:

$$\frac{\partial^2 v_\theta}{\partial r^2} + \frac{\partial}{\partial r}\left(\frac{v_\theta}{r}\right) = 0 \rightarrow \frac{\partial}{\partial r}\left(\frac{1}{r}\frac{\partial (r v_\theta)}{\partial r}\right) \tag{C.3}$$

Integrating both sides of the equation in the radial axis gives

$$\int_r \frac{\partial}{\partial r}\left(\frac{1}{r}\frac{\partial(rv_\theta)}{\partial r}\right) = \int_r 0 \tag{C.4}$$

So, the constant of integration C_1 appears.

$$\frac{1}{r}\frac{\partial(rv_\theta)}{\partial r} = C_1 \tag{C.5}$$

Rearranging the equation and integrating it for the second time gives:

$$\int_r \frac{\partial(rv_\theta)}{\partial r} = \int_r rC_1 \tag{C.6}$$

Now, there are two constants of integration that should be solved in order to obtain the analytical solution.

$$rv_\theta = \frac{r^2C_1}{2} + C_2 \tag{C.7}$$

Isolating the tangential velocity on the left side of the equation leads to:

$$v_\theta(r) = \frac{rC_1}{2} + \frac{C_2}{r} \tag{C.8}$$

One can note that the constants of integration above will be found if correct boundary conditions are applied, which are:

i. At $r = R_{inn} \rightarrow v_\theta = R_{inn}\omega_{inn}$
ii. At $r = R_{out} \rightarrow v_\theta = R_{out}\omega_{out}$

Finally, a set of two equations are obtained.

$$\omega_{inn}R_{inn} = R_{inn}C_1 + \frac{C_2}{R_{inn}} \tag{C.9}$$

$$\omega_{out}R_{out} = R_{out}C_1 + \frac{C_2}{R_{out}} \tag{C.10}$$

So, the constants of integration are depicted as follows:

$$C_1 = \frac{\omega_{out}R_{out}^2 - \omega_{inn}R_{inn}^2}{R_{out}^2 - R_{inn}^2} \tag{C.11}$$

$$C_2 = \frac{R_{inn}^2 R_{out}^2(\omega_{inn} - \omega_{out})}{R_{out}^2 - R_{inn}^2} \tag{C.12}$$

Substituting the values above into the Equation (III.8) gives the analytical solution of the tangential velocity of a Newtonian fluid flowing between two concentric, rotating independently, cylinders.

$$v_\theta(r) = R_{inn}\omega_{inn}\left(\frac{\frac{R_{out}}{r} - \frac{r}{R_{out}}}{\frac{R_{out}}{R_{inn}} - \frac{R_{inn}}{R_{out}}}\right) + R_{out}\omega_{out}\left(\frac{\frac{r}{R_{inn}} - \frac{R_{inn}}{r}}{\frac{R_{out}}{R_{inn}} - \frac{R_{inn}}{R_{out}}}\right) \tag{C.13}$$

In the case where only the inner cylinder rotates and the outer cylinders is static, the equation above can be described as the Equation (2.49)

$$v_\theta(r) = \frac{R_{inn}\omega_{inn}}{1 - k^2}\left(\frac{r}{R_{inn}} - \frac{R_{inn}}{r}\right) \tag{C.14}$$

C.2 POWER-LAW FLUID

For a non-Newtonian Power-Law fluid the hypothesis applied in the Newtonian case is the same. Thus, Equation (2.20) can be simplified in:

$$0 = -\frac{1}{r^2}\frac{\partial(r^2\tau_{r\theta})}{\partial r} \tag{C.15}$$

Where for a Power-Law fluid the Equation (2.8) the only non-vanishing component of the stress tensor are $\tau_{r\theta} = \tau_{\theta r}$.

$$\tau_{r\theta} = m\left[r\frac{\partial}{\partial r}\left(\frac{v_\theta}{r}\right)\right]^n \tag{C.16}$$

Then, combining the two equations above one can obtain the following expression:

$$m\frac{\partial}{\partial r}\left[r^2\left(r\frac{\partial}{\partial r}\left(\frac{v_\theta}{r}\right)\right)^n\right] = 0 \tag{C.17}$$

Similarly, the equation above is integrated into the radial axis

$$\int_r \frac{\partial}{\partial r}\left[r^2\left(r\frac{\partial}{\partial r}\left(\frac{v_\theta}{r}\right)\right)^n\right] = 0 \tag{C.18}$$

Obtaining the first constant of integration C_1.

$$\left(r\frac{\partial}{\partial r}\left(\frac{v_\theta}{r}\right)\right)^n = \frac{C_1}{r^2} \tag{C.19}$$

Rearranging the equation above and re-integrating the equation leads to:

$$\int_r \frac{\partial}{\partial r}\left(\frac{v_\theta}{r}\right) = \int_r \frac{C_1^{\frac{1}{n}}}{r^{\frac{2}{n}+1}} \tag{C.20}$$

Thus, obtaining the second constant of integration C_2. For the sake of simplicity, the term $C_1^{\frac{1}{n}}n/2$ will be depicted as $\mathbb{C}_1$.

$$\frac{v_\theta}{r} = -\frac{C_1^{\frac{1}{n}}n}{2r^{\frac{2}{n}}} + C_2 \rightarrow \frac{v_\theta}{r} = \frac{\mathbb{C}_1}{r^{\frac{2}{n}}} + C_2 \tag{C.21}$$

So, the tangential velocity component can be depicted as:

$$v_\theta(r) = \frac{\mathbb{C}_1}{r^{\frac{2}{n}}} r + C_2 r \tag{C.22}$$

Applying the correct boundary conditions for an inner rotating cylinder and a statical outer cylinder, as follows:

i. At $r = R_{inn} = kR_{out} \rightarrow v_\theta = R_{inn}\omega_{inn}$

ii. At $r = R_{out} \rightarrow v_\theta = 0$

The constants of integration $\mathbb{C}_1$ and C_2 are obtained.

$$\mathbb{C}_1 = \frac{\omega_{inn} R_{out}^{2/n}}{\left(\frac{1}{k}\right)^{2/n} - 1} \tag{C.23}$$

$$C_2 = -\frac{\omega_{inn}}{\left(\frac{1}{k}\right)^{2/n} - 1} \tag{C.24}$$

Substituting the equations above into Equation (III.22) gives the analytical solution for a flowing Power-Law fluid, which is the Equation (2.50).

$$\frac{v_\theta(r)}{\omega_{inn} r} = \frac{(R_{out}/r)^{2/n} - 1}{(1/k)^{2/n} - 1} \tag{C.25}$$

Furthermore, the torque on the inner cylinder can be described on the following expression.

$$T = 2\pi (kR_{out})^2 mH \left(\frac{2\omega_{inn}/n}{1 - k^{2/n}}\right)^n \tag{C.26}$$

C.3 REINER-RIWLIN EQUATION

Invoking the expression which relates the Torque measured in the rotating inner cylinder with the shear stress in a steady-state incompressible flow (2.56) and the model of the Bingham fluid (2.9) and relating them with the shear rate Equation (2.52), one can obtain the following expression.

$$\frac{T}{2\pi r^2 H} = \tau_0 + \mu r \frac{\partial \omega(r)}{\partial r} \tag{C.27}$$

Consequently, rearranging and integrating the equations above with the boundary limits for a no-slip flow gives:

$$\int_{R_{inn}}^{R_{out}} \left(\frac{T}{2\pi r^3 H} - \frac{\tau_0}{r} \right) dr = \mu \int_{-\omega}^{0} d\omega(r) \tag{C.28}$$

One can note that similarly to analysis held in Chapter 2, the inner cylinder velocity is denoted as a negative just for the sake of simplifying the mathematics. Thus, solving the integral above and rearranging the equation to isolate the torque value on the left side of the equations gives (HEIRMAN, VANDEWALLE, et al., 2008):

$$T = \frac{4\pi H \tau_0}{\left(\frac{1}{R_{inn}^2} - \frac{1}{R_{out}^2} \right)} \ln\left(\frac{R_{out}}{R_{inn}} \right) + \frac{\mu 8\pi^2 H}{\left(\frac{1}{R_{inn}^2} - \frac{1}{R_{out}^2} \right)} N = G_B + H_B N \tag{C.29}$$

where Heirman et al., (2008) called G and H as the flow resistance and viscosity factor, respectively, while N is the velocity of the inner cylinder in rps.

The equation above is the so-called Reiner-Riwlin equation, and it can be found in different forms in the literature. In the present work, the approach showed by Heirman et al., was chosen because it could be used to obtain the physical properties of the fluid from regression directly from the torque and velocity experimental measurements. Thus, the yield stress and Newtonian viscosity from the Bingham fluid can be determined respectively by:

$$\tau_0 = \frac{G_B}{4\pi H} \left(\frac{1}{R_{inn}^2} - \frac{1}{R_{out}^2} \right) \frac{1}{\ln\left(\frac{R_{out}}{R_{inn}} \right)} \tag{C.30}$$

$$\mu = \frac{H_B}{8\pi^2 H} \left(\frac{1}{R_{inn}^2} - \frac{1}{R_{out}^2} \right) \tag{C.31}$$

Also, the velocity profile for the Bingham fluid flow in function of the radial position (r) inside the gap can be determined as:

$$v_\theta(r) = \frac{Tr}{4\pi H\mu}\left(\frac{1}{R_{inn}^2} - \frac{1}{r^2}\right) - \frac{\tau_0 r}{\mu}\ln\left(\frac{r}{R_{inn}}\right) \tag{C.32}$$

The equations above are valid only when there is no plug formation in the gap between the cylinders. Otherwise, the upper integration limit on the left size of the equation (III.28) should be replaced with the plug radius r_0.

C.4 REINER-RIWLIN EQUATION ADAPTED TO HERSCHEL-BULKLEY FLUIDS

Likewise, the same approach used for Bingham fluid was held by Heirman et al., (2008) (2009). Hence, a similar Equation (III.27) for a Herschel-Bulkley fluid is demonstrated below:

$$\frac{T}{2\pi r^2 H} = \tau_0 + m\left(r\frac{\partial\omega(r)}{\partial r}\right)^n \tag{C.33}$$

Next, the integration limits applied to the equation are identical to the ones used on Bingham fluids.

$$\int_{R_{out}}^{R_{inn}}\left(\left(\frac{T}{2\pi r^2 Hm} - \frac{\tau_0}{m}\right)^{\frac{1}{n}}\frac{1}{r}\right)dr = \int_{-\omega}^{0} d\omega(r) \tag{C.34}$$

According to Herman et al., (2008), there is no analytical solution to the integral above. Instead, "the solution contains the LerchPhi function $\widehat{\phi}(x, 1, a)$, which is a single-valued, continuous but non-polynomial function on the x-plane all along the interval $x \in]-\infty, 1[$ (for a fixed $a, -a \notin \mathbb{N}$)". This solution is presented below:

$$\left[\begin{array}{l}\left(\frac{T}{2\pi R_{inn}^2 Hm} - \frac{\tau_0}{m}\right)^{\frac{1}{n}}\left[n - \widehat{\phi}\left(1 - \frac{T}{2\pi R_{inn}^2 H\tau_0 m}, 1, \frac{1}{n}\right)\right] - \\ \left(\frac{T}{2\pi R_{out}^2 Hm} - \frac{\tau_0}{m}\right)^{\frac{1}{n}}\left[n - \widehat{\phi}\left(1 - \frac{T}{2\pi R_{out}^2 H\tau_0 m}, 1, \frac{1}{n}\right)\right]\end{array}\right] = 4\pi N \tag{C.35}$$

Similarly, the tangential velocity distribution across the gap is:

$$v_\theta(r) = \frac{r}{2}\left[\begin{array}{c}\left(\frac{T}{2\pi R_{inn}^2 Hm} - \frac{\tau_0}{m}\right)^{\frac{1}{n}}\left[n - \widehat{\phi}\left(1 - \frac{T}{2\pi R_{inn}^2 H\tau_0 m}, 1, \frac{1}{n}\right)\right] - \\ \left(\frac{T}{2\pi r^2 Hm} - \frac{\tau_0}{m}\right)^{\frac{1}{n}}\left[n - \widehat{\phi}\left(1 - \frac{T}{2\pi r^2 H\tau_0 m}, 1, \frac{1}{n}\right)\right]\end{array}\right] \quad \text{(C.36)}$$

One may note that if n=1 the above equations results to the same solutions for Bingham fluids. Thus, Heirman et al., suggested a different approach that is based in the superposition of the flow resistance and the Power-Law effect to solve the Couette inverse problem. This approach is represented below:

$$T = G_{HB} + H_{HB}N^J \quad \text{(C.37)}$$

According to Heirman et al., experiments proved that this superposition of decoupled terms can be used for non-linear cases where $\kappa = R_{out}/R_{inn}$, 1 < J < 1.81 and 1.9 10-4 < Od < 33.4, where Od is the Oldroyd number.

Therefore, the first subfunction for the decoupled solution approach is:

$$T' = G_{HB} \quad \text{(C.38)}$$

where, the solution is the same as presented for Bingham fluid, which is:

$$\tau_0 = \frac{G_{HB}}{4\pi H}\left(\frac{1}{R_{inn}^2} - \frac{1}{R_{out}^2}\right)\frac{1}{\ln\left(\frac{R_{out}}{R_{inn}}\right)} \quad \text{(C.39)}$$

Still, the second subfunction is related to the Power-Law effect, which is presented below:

$$T'' = H_{HB}N^J \quad \text{(C.40)}$$

One can note that the equation above is a representation of Power-Law Fluid Equation (2.8), which can be written as:

$$\frac{T''}{2\pi r^2 H} = m\left(r\frac{\partial\omega(r)}{\partial r}\right)^n \tag{C.41}$$

So, applying the boundary limits into the integration of the equation above:

$$\int_{R_{inn}}^{R_{out}}\left(\left(\frac{T''}{2\pi r^2 Hm}\right)^{\frac{1}{n}}\frac{1}{r}\right)dr = \int_{-\omega}^{0} d\omega(r) \tag{C.42}$$

where the solution is:

$$T'' = \frac{2^{2n+1}\pi^{n+1}Hm}{n^n\left(\frac{1}{R_{inn}^{2/n}} - \frac{1}{R_{out}^{2/n}}\right)^n}N^n = H_{HB}N^J \tag{C.43}$$

thus,

$$n = J \tag{C.44}$$

$$m = \frac{H_{HB}}{2^{2n+1}\pi^{n+1}H}n^n\left(\frac{1}{R_{inn}^{2/n}} - \frac{1}{R_{out}^{2/n}}\right)^n \tag{C.45}$$

Finally, the complete decoupled solution is represented by

$$T = T' + T'' = G_{HB} + H_{HB}N^J \tag{C.46}$$

$$T = \frac{4\pi H\tau_0}{\left(\frac{1}{R_{inn}^2} - \frac{1}{R_{out}^2}\right)}\ln\left(\frac{R_{out}}{R_{inn}}\right) + \frac{2^{2n+1}\pi^{n+1}Hm}{n^n\left(\frac{1}{R_{inn}^{2/n}} - \frac{1}{R_{out}^{2/n}}\right)^n}N^n \tag{C.47}$$

More details of this solution can be found in the two works from Heirman et al., (2008) (2009).